Constraining close binary evolution with post common envelope binaries

vorgelegt von
Diplom-Physiker
Ada Nebot Gómez-Morán
aus Oviedo, Spanien

Von der Fakultät II – Mathematik und Naturwissenschaften
der Technischen Universität Berlin
zur Erlangung des akademischen Grades

Doktor der Naturwissenschaften
– Dr. rer. nat. –

genehmigte Dissertation

Promotionsausschuss:

Vorsitzender: Prof. Dr. M. Dähne
Berichter: PD Dr. A. D. Schwope
Berichter: Prof. Dr. H. Rauer

Tag der wissenschaftlichen Aussprache: 19.05.2010

Berlin 2011

D 83

A mi familia

Zusammenfassung

Doppelsterne die aus einem Weißen Zwerg und einem Hauptreihenstern bestehen (WDMS-Systeme) sind ideal, um aus ihrer Beobachtung aktuelle Theorien der Doppelsternentwicklung abzuleiten. In bislang verfügbaren Stichproben sind alte Doppelsterne mit kalten Weißen Zwergen deutlich unterrepräsentiert. Wir haben eine Durchmusterung durchgeführt, die besonders der Identifizierung und Charakterisierung dieser bislang fehlenden Systeme durch Farbselektion und spektroskopische Identifikation gewidmet war. Die neue Stichprobe umfasst 277 gesicherte WDMS-Systeme und 24 weitere Kandidaten mit unsicherer kompakter Komponente. Die kombinierten Spektren wurden in ihre Komponentenspektren zerlegt und die Sternparameter bestimmt. Die so gefundene Temperarturverteilung der Weißen Zwerge zeigt ein Maximum bei deutlich niedrigeren Temperaturen als bislang verfügbare Stichproben, ist jedoch verträglich mit der Verteilung isolierter Weißer Zwergsterne. Ebenso zeigen die Massenverteilungen einzelner Weißer Zwerge und der neuen WDMS-Stichprobe ein Maximum bei 0.6 Sonnenmassen. Im Vergleich zu früheren enthält die neue Stichprobe einen deutlich höheren Anteil Sterne vom frühen Spektraltyp M, ist aber immer noch nicht vollständig *unbiased*. Es wird eine untere Grenze für die Raumdichte abhängig von der Entfernung von der galaktischen Ebene zu $0.1 - 2 \times 10^{-4}\,\mathrm{pc}^{-3}$ bestimmt. Die räumliche Verteilung der neuen Objekte entspricht einer Skalenhöhe von $\sim 100 - 150\,\mathrm{pc}$ der galaktischen Scheibe.

Mit Hilfe einer Radialgeschwindigkeitsanalyse spektroskopischer Daten wurden enge Doppelsterne identifiziert, die die Entwicklungsphase einer gemeinsamen Einhüllenden durchlaufen haben. Ich bestimme eine sichere untere Grenze von 13% dieser sogenannten *post common envelope binaries - PCEBs* unter den WDMS-Systemen. Der Anteil der PCEBs nimmt deutlich mit abnehmender Masse der Sekundärsterne zu, insbesondere beim Übergang zu vollkonvektiven Begleitsternen. Diese Zunahme bestätigt das bislang umstrittene Modell der unterbrochenen magnetischen Bremsung, wonach der Drehimpulsverlust bei vollkonvektiven Spättypsternen deutlich reduziert werden sollte.

Aus spektroskopischen und photometrischen Folgebeobachtungen wurde die Bahnumlaufzeit von 16 WDMS Doppelsternen im Bereich von P_{orb} 2.8 Stunden bis zu 2 Tagen bestimmt und die Umlaufzeiten aller übrigen PCEBs zumindest eingeschränkt. Es wurden 7 Kandidaten mit langen und 15 Kandidaten mit kurzen Umlaufzeit gefunden. Die beobachtete Verteilung der Umlaufzeiten der PCEBs enthält wesentlich weniger langperiodische Systeme als durch Populationssynthese vorhergesagt wurde. Wahrscheinlich handelt es sich hier um einen Auswahleffekt, für Rückschlüsse auf die Effektivität der common-envelope Phase sind vollständige Stichproben notwendig. Eines der neu gefundenen Systeme zeigt Bedeckungen des Weißen Zwerges durch den Begleiter, dieses System wird in bezug auf die Sternparameter detailliert untersucht.

Es wird des weiteren der Einfluss der Doppelsternnatur auf die stellare Aktivität des Sekundärsterns studiert. Der Anteil aktiver Sterne steigt zu späten Spektraltypen an, im Einklang mit Untersuchungen an Feldsternen. Der Anteil aktiver Sterne unter den frühen M-Sternen ist jedoch signifikant höher als bei den Feldsternen, was auf eine charakteristisch höheres Alter der Feldsterne zurückgeführt werden kann. Die Mehrzahl der PCEB-Systeme enthält aktive Sekundärsterne mit einer größeren Äquivalentbreite der Hα-Linie als bei Feldsternen gefunden wird, eine Tatsache, die zur Suche nach PCEBs unter WDMS-Systemen herangezogen werden kann.

Abstract

White dwarf/main sequence binaries (WDMS) are ideal systems to constrain current theories of binary star evolution. In current samples old binaries containing cold white dwarfs are significantly underrepresented. We performed a survey dedicated to identify and characterize the missing population of old white dwarf/main sequence binaries. A total of 277 white dwarf/main sequence binaries and 24 candidates were identified. We obtain their stellar parameters using a spectral decomposition method. The obtained white dwarf temperature distribution peaks at lower temperatures than previous samples but at the same temperature than the distribution of SDSS single white dwarfs. Compared to previous SDSS WDMS sample, the distribution of secondary star spectral types is slightly broader containing more early M companions, but the SEGUE WDMS population is still biased towards late spectral type secondary stars. The white dwarf mass distribution peaks at $M_{\rm wd} \sim 0.6 \mathrm{M}_{\odot}$ similar to that of single white dwarfs. A lower limit for the space density of $0.1 - 2 \times 10^{-4}$ pc^{-3} was derived, depending on the distance from the galactic plane. The spatial distribution is in agreement with a scale-height of $\sim 100 - 150$ pc.

From a statistical analysis of the radial velocities measured from the SDSS sub-exposures and from own spectroscopic follow-up observations we detect those binaries that have gone through a common envelope phase. I derived a lower limit to the *post-common envelope binary - PCEB* fraction of WDMS binaries of $\sim$ 13 %. The fraction of PCEBs increases with decreasing mass of the secondary star, and has a steep increase at the boundary where the secondary star becomes fully convective. This indicates that the angular momentum loss is less efficient at later spectral types, and according to predictions of binary population synthesis studies, in agreement with the disrupted magnetic braking law.

From spectroscopic and photometric follow-up observations we measured the orbital period of 16 WDMS binaries, in the range 2.8h$< P_{\rm orb} <$ 2d. We constrain further the orbital periods of the remaining PCEBs, finding 7 long orbital period (> 1 day) candidates and 15 short orbital period candidates (< 1 day). The observed orbital period distribution of PCEBs presents a sharp drop around 1 day, even though it is biased towards short orbital periods this drop might indicate a lower efficiency of the CE phase than thought. One of the systems is eclipsing, and we present an in-depth study of its stellar and binary parameters.

We study the influence of binarity in the stellar activity, finding that the fraction of active stars increases with the spectral type, a result found for single field red dwarfs, though we find a higher fraction at earlier spectral types. This result can be explained by the lower age of the WDMS compared with single stars of the same spectral type. The majority of the PCEBs contain active secondaries, and at a given spectral type the EW(Hα) is higher than for wide WDMS binaries.

Contents

List of Figures

List of Tables

Chapter 1

Introduction

Most of the stars in the Galaxy are born in binary or multiple systems (Abt 1983). Many exotic objects like millisecond pulsars, Galactic black hole candidatess, LMXBs, CVs and symbiotic stars, are descendant of binary stars. The standard candles, supernovae type Ia, are also a product of close binary evolution. With the discovery of the first binary pulsar by Russel A. Hulse and Joseph H. Taylor, Jr., Einstein's general relativity prediction on how compact objects loose angular momentum due to gravitational wave emission can be tested against alternative theories. Finding that made Hulse and Taylor win the Nobel Prize in 1993 and with the space mission LISA we will be able to proof. Despite the relevance of binary stars our understanding of their evolution is still incomplete. The mentioned systems have in common that they all went through a common envelope (CE) phase. To answer the main questions of close binary evolution we focus our study in one type of binaries that suffered from a CE phase: white dwarf main sequence binaries (WDMS). We choose these objects becuase they are very numerous, so that we can make a good analysis based on large samples; unlike cataclysmic variables they have no accretion so that we can derive easily the stellar parameters of the two components; and the individual evolution of the components is well understood.

1.1 WDMS components and their individual evolution

To know how the spectral energy distribution (SED) of WDMS binaries is and how they evolve it is needed to know how the SED looks like for the individual components and to understand how the evolution is for single stars. The last becomes evident when asking the question *when do stars enter the CE phase?* This depends on the initial orbital separation and also on the initial masses. Stars on the main sequence expand so to answer this question we need to know how much they do it dependent on their mass. We now proceed to describe the most relevant characteristics of the SED of the red dwarf and the white dwarf and secondly we briefly describe their evolution.

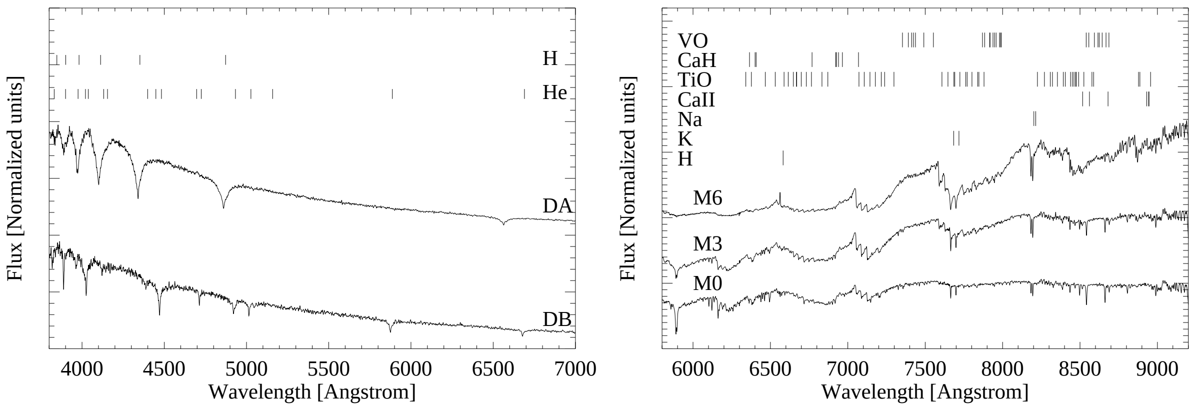

Figure 1.1: DA and DB white dwarf template SDSS spectra with HI and HeI absorption lines marked (left). M0, M3 and M6 templates created with SDSS spectra of red dwarfs with several molecular absorption bands and lines marked (right).

1.1.1 The red dwarf

Low mass stars (<0.5 $M_\odot$) represent a large fraction of all the stars in the Galaxy. Their temperatures and gravity are in the ranges 2800-3800 K and 4.2-5.5 respectively. Due to their low temperatures, their spectral energy distribution is dominated by strong molecular absorption bands of titanium oxide (TiO), vanadium oxide (VO), PC and CaH in the optical, and by H_2O and CO in the infrared, with almost no true continuum present. A detailed list of lines present in their spectra can be found in Kirkpatrick et al. (1991) and some of these molecular bands together with some characteristic lines are shown in Fig. 1.1 for three different spectral types, M0, M3 and M6. The strength of the titanium oxide, the vanadium oxide and the PC bands are correlated with the temperature of the star, and several indexes have beed defined and used to determine the spectral type of this cool stars (Kirkpatrick et al. 1991; Cruz & Reid 2002; Martín et al. 1999).

Evolution of the red dwarf

Evolutionary tracks from Baraffe et al. (1998) are shown in the Hertzsprung-Russel diagram (L-$T_{\rm eff}$ diagram) in the left panel of Fig. 1.2 for three different masses, $M_{\rm sec}$= 0.1 $M_\odot$, $M_{\rm sec}$= 0.3 $M_\odot$, and $M_{\rm sec}$=0.5 $M_\odot$ from left to right. Overplotted are two different isochrones, corresponding to 1 Myr (dotted) and to 1 Gyr (dashed) (we chose for the mixing length parameter α = 1 and Z = 0.02). In the right panel we show the associated change of the radius over the time. There is a pre-main-sequence (MS) contraction that can last from 0.1 Gyr for a 0.5 $M_\odot$ star and up to 1 Gyr for the lower mass. Due to gravitational contraction the central temperature increases and H burning starts, leading the star to a hydrostatic equilibrium if its mass is larger than 0.15 $M_\odot$. Stars below this mass don't reach H burning, since they are too dense and cold their pressure

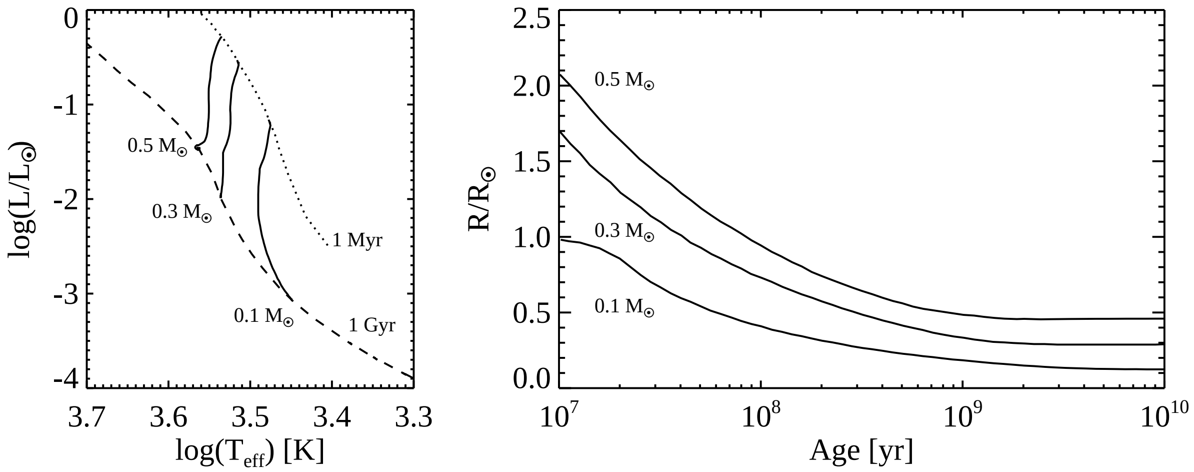

Figure 1.2: Tracks in the $\log L$–$\log T_{\rm eff}$ plane for three different masses, M = 0.5M$_\odot$, 0.3 M$_\odot$ and 0.1 M$_\odot$ from top to bottom (left panel), and associated change in the radius of the star in time (right panel).

is dominated by degenerate electrons, and keep on contracting, until they reach the limit in radius of fully degenerate stars (corresponding to $T_{\rm eff}$= 0 K). For those stars that do reach H burning the presure is governed by its classical value, so that a decrease in radius involves a decrease in luminosity, $L \propto R^2 T_{\rm eff}{}^4$ (from 0.001 Gy to 0.1-1 Gyr). Once the star reaches thermal equilibrium the luminosity will be dominated by nuclear reactions and further evolution of the system becomes very slow (from 0.1-1 Gyr to 10 Gyr). During the pre-MS phase the star moves to higher temperatures and to lower luminosities. The evolution of low mass stars once they are on the MS is very slow. An isochrone of 10 Gy would be at almost the exact position of the 1 Gyr isochrone. A star with a 0.6 M$_\odot$ would increase it's radius by only by a 3 %.

1.1.2 The white dwarf

White dwarfs are the latest stage of the evolution of low and intermediate mass stars, from 0.07 to 8 M$_\odot$ (Fontaine et al. 2001). They have a typical mass of 0.6 M$_\odot$, with sizes typical of planets, making these objects have very high gravities, $\log g \sim 8$. Their luminosities cover a very broad range, from $L \sim 10^2$ L$_\odot$ at the begining of the cooling sequence to $L \sim 10^{-5}$ L$_\odot$ (see Fig. 1.6).

Evolutionary tracks from Salasnich et al. (2000)[1] with Z=0.019 and Y=0.273 are shown in the HR diagram in the left panel of Fig. 1.3 for three masses, M = 2.2 M$_\odot$, 7 M$_\odot$ and 12 M$_\odot$. In the right panel of the same figure we show the associated expansion of the stars. In all cases a star expands by large factors before becoming a WD. A 2.2 M$_\odot$ star will have a radius $\sim$ 30 $R_\odot$ at the tip of the RGB, a star with a mass of 7 M$_\odot$ will have a radius $\sim$ 100 $R_\odot$ at the AGB, while a star with a mass of 12 M$_\odot$ at the AGB will have a radius of up to $\sim$ 1000 $R_\odot$. This tells

[1]http://pleiadi.pd.astro.it/

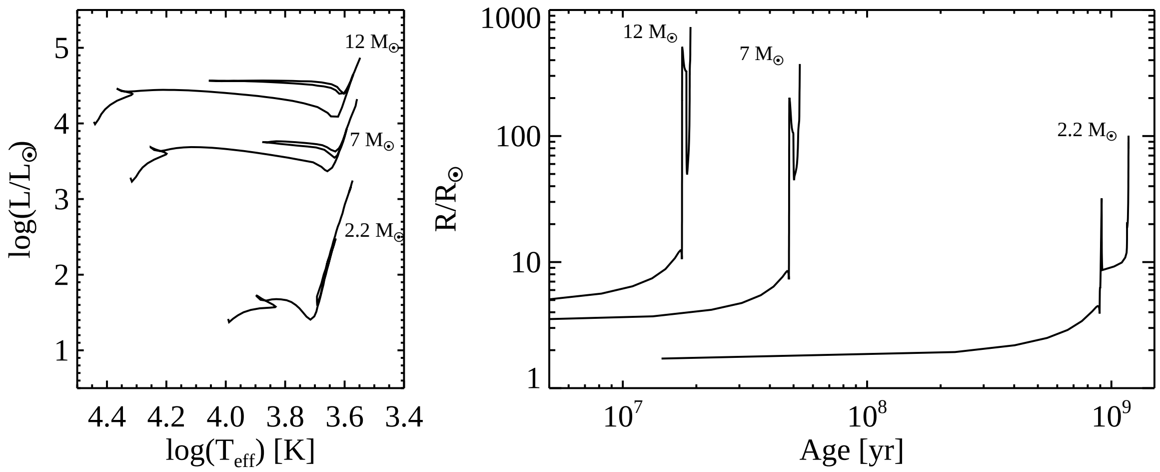

Figure 1.3: Tracks in the $\log L$–$\log T_{\rm eff}$ plane for three different masses, M = 12$M_\odot$, 7 $M_\odot$ and 2.2 $M_\odot$ from top to bottom (left panel), and associated change in the radius of the star in time (right panel).

us the maximum orbital separation allowed for a companion star before filling it's Roche lobe and entering the CE phase. For a secondary star of 0.5 $M_\odot$, this implies that if the binary has a $P_{\rm orb}$<100-200 days (0.5–1 AU) the system will enter a CE phase in the RGB, systems with longer period but shorter than 2 000 days (~ 6 AU) will enter a CE while in the AGB.

A white dwarf is formed once the outer envelope of a star is expelled. The chemical composition of the core depends on the stage the WD was formed. Low mass stars, $M < 2.2$ $M_\odot$ will loose their H envelope in the RGB, so that they don't ignite He. The resulting WD has a core with mainly He in it (He-WD), and has $M_{\rm wd} \sim 0.15 - 0.45$ (the upper limit is defined by the onset of He-flash). It is widely thought that all He-WDs are consequence of binary evolution (Marsh et al. 1995). Intermediate mass stars that loose their envelope during the AGB will have a carbon oxygen core (CO-WD) if they don't start C burning, $M < 6 - 8$ $M_\odot$. The resulting WD has $M_{\rm wd} \sim 0.45 - 1.1$ (the upper limit is defined by the onset of C ignition). Stars with higher masses, up to $\sim$ 12 $M_\odot$ will loose their envelope at the tip of the AGB and will have a core composed of oxygen and neon (ONe-WD) and their mass is in the range $M_{\rm wd} \sim 1.1 - 1.38$ $M_\odot$.

From observations we have learnt that small amounts of H and He are left over after the mass-loss phase during the PN phase (thought to be the precursors of most of the WDs), that suround the core of the WD. The SED of white dwarfs is dominated by the continuum and some absorption lines. If only Balmer lines are present they are classified as DA, DB contain only He and DC show only a continuum. Other white dwarfs have HeII (DO), carbon features (DQ) or some metal lines (DZ) (Sion et al. 1983). Examples of DA and DB white dwarfs are shown in the left panel of Fig. 1.1 with H and He absorption lines marked. We show their location in the color-color diagram in Fig. 1.5 together with the cooling tracks from Wood (1995) (data was taken from Eisenstein et al. (2006)).

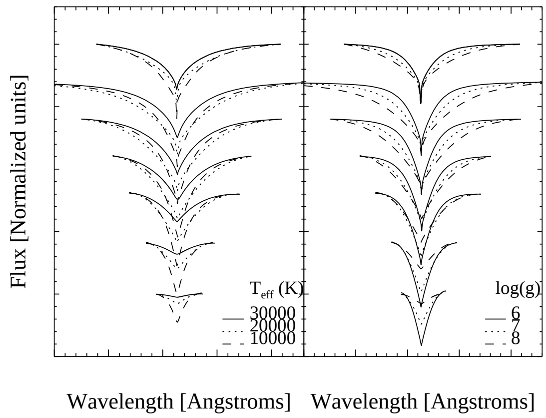

Figure 1.4: Normalized Balmer lines, Hα-H7 as a function of $T_{\rm eff}$ (left) for a DA with $\log g = 8$ and as a function of $\log g$ (right) for a DA with $T_{\rm eff}$= 20 000 K. We used the DA models from Koester et al. (2005).

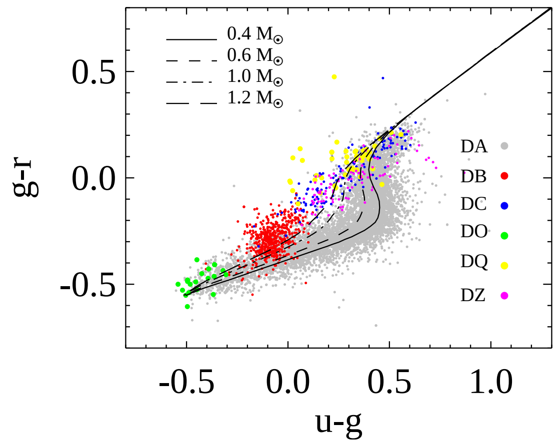

Figure 1.5: Color-color diagram for a sample of WDs from Eisenstein et al. (2006) and cooling tracks (lines) from Wood (1995) for four different DA masses. Different colors are used for WDs of different spectral type.

The equivalent widths of the Balmer lines depend on temperature and gravity and they are used to determine these parameters on DA white dwarfs [2]. In the left panel of Fig. 1.4 we plot the normalized Balmer lines from Hα to H7 from top to bottom for three DAs with effective temperatures of 30000 K (solid line) 20000 K (dotted line) and 10000 K (dashed line), fixing $\log g = 8$. In the right panel of Fig. 1.4 we plot again the normalized Balmer lines but this time for three DAs with same effective temperatures ($T_{\rm eff}$= 20000 K) but different gravity, $\log g = 6$ (solid line), $\log g = 7$ (dotted line) and $\log g = 8$ (dashed line). Colder DAs have deeper lines and, the higher the gravity the broader and shallower the line becomes. This implies that alone with the EW we are not able to discern whether a DA is cold and massive or hot and light, so we need an independent index, for instance the slope of the continuum.

Evolution of the white dwarf

White dwarfs produce no energy by nuclear reaction in their core, and pressure from the degenerate electrons prevents further contraction, and since no other source of energy is available the fate of the WD is to cool. As consequence of degeneracy the temperature is independent of the pressure so they will evolve at constant radius. Degenerate electrons conduct heat very well, so

[2]Different mechanisms are involved in the broadening of spectral lines: i) Natural broadening: electrons stay in a certain level a finite time before they spontaneously decay, and each level has a certain energy given by Heisenberg uncertainty principle, ii) Thermal doppler broadening, iii) Collisional broadening or Stark effect (pressure broadening): line shifting or splitting under the action of an electric field, iv) Zeeman effect: under a magnetic field lines split and if we don't have enough resolution the lines will appear to be one broad line, v) Turbulent broadening, and vi) Rotational broadening. In hot white dwarfs due to the high densities the lines are broadened mostly becuase of the Stark effect.

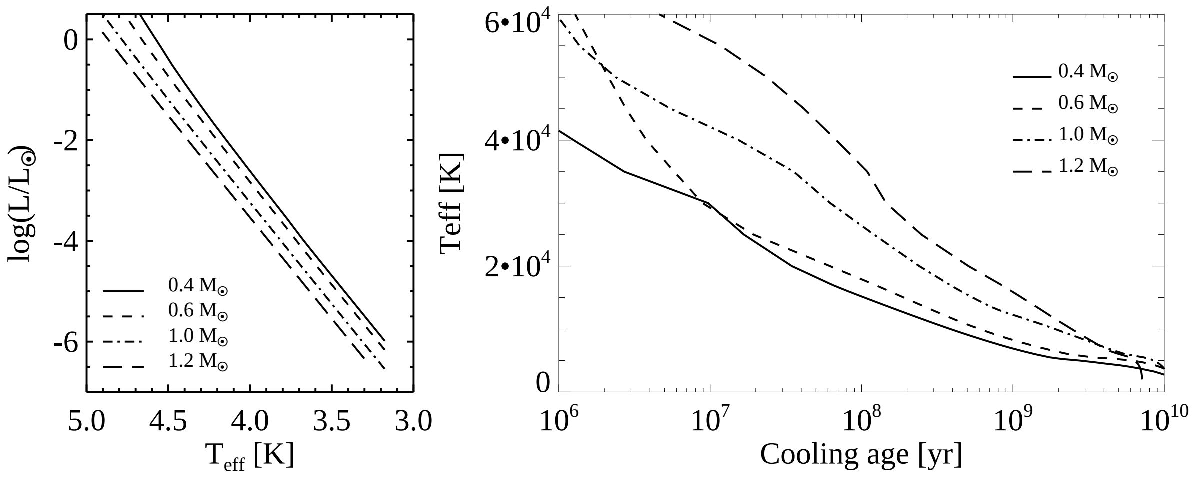

Figure 1.6: HR diagram (left panel) and cooling traks (right) from Wood (1995) for four different DA masses.

that the core is isothermal, and can have temperatures in the range $T_c = 10^6 - 10^7 K$, only in a very thin outer layer the temperature drops to $T_{\rm eff} = 60000 - 6000$ K, giving rise to convection for the cooler WDs. Luminosity is produced by thermal energy from the non-degenarate ions. As the WD cools the ions loose kinetic energy, changing their state from gas to fluid and finally to solid, until the WD becomes a crystalized object, a black dwarf. In the HR diagram shown in the left panel of Fig. 1.6 we plot the evolutionary tracks from Fontaine et al. (2001) [3] for 4 WDs, 0.4 $M_\odot$, 0.6 $M_\odot$, 1 $M_\odot$, and 1.2 $M_\odot$, from left to right. In this double logarithmic representation the luminosity is linear with the temperature and has a slope of ~ -4.

Most of the stars will end up becoming a WD, so that the coolest WDs can be used to estimate the age of a certain population in the Galaxy. The cooling of WDs depends on the thermal energy content of the core and how fast it is transfered from the core, through the envelope to the interstellar medium. Inmediately after the PN phase, WD are hot enough so that they can produce large amounts of neutrinos, taking with them energy and cooling the WD. Once the neutrino cooling phase has finished the cooling age depends only on the thermal energy stored in it's core and the opacity of the outer layers, of the atmosphere (Fontaine et al. 2001). Cooling tracks from Wood (1995) are shown in the right panel of Fig. 1.6 for three different DA masses. We see that the cooling depends on the mass of the white dwarf, so that if we only know the effective temperature $T_{\rm eff}$ we will not be able to discern the cooling age of the WD.

[3]http://www.astro.umontreal.ca/ bergeron/CoolingModels/

1.2 Evolution of close binary stars

The evolution of binaries depends crucially on the initial separation and the stellar masses of the components. If the initial orbital separation of the binary is small enough, as the more massive star evolves, increasing its radius untill it fills its Roche Lobe (region where the material is bound to the gravitational field of the star) when it reaches the Giant Branch or the Asymptotic Giant Branch, matter is transferred to the companion star. If the mass transfer is faster than the thermal time-scale (time a star needs to readjust to thermal equilibrium), the system enters a common envelope phase (CE), where the core of the more massive star, i. e. a white dwarf, and the companion star are surrounded by the envelope of the former. The stars start a spiral-in process, friction between the binary and the non-corotating envelope extract energy and angular momentum from the orbit, leading to a rapid decrease of the orbit. This phase is thought to happen very fast and planetary nebulae with central binary stars are probably the closest objects to the CE phase which are known (see de Marco 2009, for a review on PNe). Further evolution of the system, known as post-common envelope binary (PCEB) is driven by angular momentum loss due to gravitational radiation and to magnetic braking and it may bring the system into a semidetached configuration, i. e. a cataclysmic variable (CV). Both, the energetics of the CE phase and angular momentum loss via a magnetized stellar wind are not well understood and motivated the current project.

1.2.1 Common envelope phase

Although the basic idea of the CE phase has been outlined already 30 years ago (Paczyński 1976), it is still the least understood phase of compact binary evolution. We have learned from theoretical simulations that this phase might be very short ($\sim 10^3$ yrs) (Hjellming & Taam 1991). Because of the short duration the chances of observing a binary during this phase are very small, even worse it would be imposible to see the binary inside the envelope. But simulations make a prediction which can be tested, the outcome of the common envelope phase: elliptical or bipolar planetary nebula with a binary in it's center (Sandquist et al. 1998). And indeed these objects are observed (see de Marco 2009). These are very important findings but with current theories it is not possible to link the initial parameters of the binary with the outcome of the common envelope. Therefore theoretical binary population studies (Willems & Kolb 2004) usually deal with a simple idea: a certain fraction $\alpha_{CE} < 1$ of the binary's binding energy which is released in the spiraling-in process is used to unbind the CE (Webbink 1984):

$$E_{CE} = \alpha_{CE} \Delta E, \tag{1.1}$$

$$-\frac{GM_{1,i}M_{CE}}{\lambda R_{1,i}} = \alpha_{CE} \frac{GM_c M_2}{2} \left(\frac{1}{a_i} - \frac{1}{a_f} \right), \tag{1.2}$$

leading to the relation between inital and final separations

$$a_f = a_i \frac{M_c}{M_{1,i}} \left(1 + \frac{2}{\lambda \alpha_{CE} r_{L,1}} \frac{M_{env}}{M_2} \right), \tag{1.3}$$

where a_i and a_f are the initial and final orbital separation of the binary. $M_{1,i}$ and M_2 are the primary and secondary masses at the start of the CE, M_c is the mass of the primary's core and $r_{L,1}$ is the primary's Roche lobe in units of the binary separation. It is assumed that M_2 does not change during the common-envelope phase. The structural parameter λ is the giant envelope's binding energy parameter, and it's value depends on the initial mass of the primary and it's evolution. The higher the initial mass the deeper the envelope will be when becoming a giant and the less bound it will be to the star, also the moment in which the CE phase starts is important since in the AGB the star has a larger radius and the envelope will be less bound to the core. Some values of the structural parameter can be found in Tauris & Dewi (2001). Davis et al. (2009) have investigated the dependency of α_{CE} on the secondary mass and in contrast with previous works where λ was taken as a constant (typically $\lambda \simeq 0.5$) they calculate it's value from stellar evolution models. They can reproduce most of the PCEBs by models with $\alpha_{CE} > 0.1$, but for one system they find a very high value $\alpha > 3$, which they claim can be explained by another source of energy rather than gravitational potential energy, like for example thermal and ionization energy of the giant's envelope. But this might indicate that there are still some missing ingredients in their recipe.

1.2.2 Post common envelope binaries

Once the common envelope is expelled, the remaining system consist of a main sequence star and a remnant of the more massive star, e.g. a white dwarf, perhaps surrounded by the ejected material that can be ionized forming a planetary nebula (Paczyński 1976; Iben & Livio 1993). Until 2003 there were only about 30 PCEBs with well defined orbital parameters ($P_{\rm orb}$, $M_{\rm sec}$, $M_{\rm wd}$, $T_{\rm eff}$). Schreiber & Gänsicke (2003) studied these systems in detail. They realized that most of the systems contained relatively hot white dwarfs and late-type companions. These biases could be understood as a natural way of discovery, that is as blue objects which later on presented some infrared excess. They calculated the evolutionary state for all the systems, that is their age in terms of CV evolution, noticing that they had only lived a small fraction of their lifes as PCEB. That made them think for the first time that an old population characterized by cold white dwarfs should exist.

Since then, the Sloan Digital Sky Survey turned out to be very efficient at discovering new white dwarf-main sequence binaries (see Silvestri et al. 2006; Rebassa-Mansergas et al. 2007; Heller et al. 2009), but biases towards hot white dwarfs plus secondaries with late spectral types are still present. These biases can be easily understood since the WDMS binaries were discovered as a byproduct of one of the main targets of the SDSS: quasars, which resemble colors of hot white dwarfs plus late secondaries. Among these sample of WDMS binaries a fraction of them, $\sim$ 25% are PCEBs (Willems & Kolb 2004), while the remaining are wide binaries, where the components never interacted and evolved as single stars.

We made a compilation of the published (until the present date, February 2010) WDMS binaries that suffered from a CE phase and in table 1.2.2 we list their orbital periods and stellar parameters. This sample comprises $\sim$ 50, covers a rather narrow range of secondary masses and is dominated by hot white dwarfs and late secondaries, serendipitously discovered in the blue. To constrain better the CE efficiency it is much needed a sample of PCEB covering a large range in both effective temperature and in mass of the secondary.

Table 1.1: Stellar parameters of known close WDMS.

Name	Porb [d]	Sp1	Sp2	$T_{\rm eff}$	$M_{\rm wd}[\mathrm{M}_\odot]$	$M_{\rm sec}[\mathrm{M}_\odot]$	$R_{\rm sec}[R_\odot]$	Ref.
1541-3809	7.7047	DA	dM					[a]
FS Cet	4.23160	DAO	M1-2.5	57000 ± 2000	0.57 ± 0.03	0.39 ± 0.02	0.43 ± 0.02	[b]
J1629+7804	2.89:	DA1	M3/5					[c]
BE UMa	2.291166	DAO	K3-4/5	4750 ± 150	0.59 ± 0.07	0.25 ± 0.08	0.72 ± 0.05	[d]
2147-1405	1.4972	DA	dM					[a]
IN CMa	1.262396	DAO1	M5e/5	52400 ± 1800	0.58 ± 0.03	0.43 ± 0.03	0.47 ± 0.03	[b]
1319-2849	0.8758	DA	dM					[a]
2123-4446	0.8499	DA	dM					[a]
1136+6646AB	0.83607	DAO	K4-7/5	70 000	0.82	0.36		[e]
J1016-0520AB	0.78928	DAO	K5-M2/5	55 000 ± 1000	0.63 ± 0.02	0.15 ± 0.02		[f]
2009+6216	0.741226	DA2	M5/5	25 870	0.61-0.64	0.1845-0.1925		[g]
J1414-0132	0.727	DA	M5	14 065 ± 1452	0.80 ± 0.17			[h]
J0246+0041	0.726	DA	M3	16 600 ± 1600	0.9 ± 0.2	0.38 ± 0.07	0.39 ± 0.08	[i]
J2013+4002	0.705517	DAO	M3-4/5	48 000 ± 900	0.56 ± 0.03	0.23 ± 0.01	0.29 ± 0.01	[b]
EG UMa	0.667579	DA4	M4-5/5	13 125 ± 125	0.63			[j]
J2339-0020	0.6560	DA	M4	13 300 ± 2 800	0.8 ± 0.4	0.32 ± 0.09	0.33 ± 0.10	[i]
UZ Sex	0.597259	DA3	M3-5/5	17 600 ± 2 000	0.65 ± 0.2	0.22 ± 0.05	0.25 ± 0.03	[k]
HZ 9	0.56433	DA2	M5e/5	20 000 ± 2 000	0.51			[l]
V471 Tau	0.521183	DA2	K2/5	34 500 ± 1 000	0.84 ± 0.05	0.93 ± 0.07	0.96 ± 0.04	ecl[m]
J2130+4710	0.521036	DA	M3.5	18 000 ± 1 000	0.554 ± 0.017	0.555 ± 0.023	0.534 ± 0.053	ecl[n]
1334-3237	0.469	DA	K2-M2/5					[o]
J1047+0523	0.382	DA	M5	12 392 ± 1847	0.38 ± 0.20			[h]
1247-1738	0.362	DA	M3-5/5					[o]
DE CVn	0.364139	DA7	M2/5	8 000	0.51 ± 0.02	0.41 ± 0.06	0.37 ± 0.06	ecl[p]
1432-1625	0.350 :	DA	M3-4/5					[o]
GK Vir	0.344331	DAO	M3-5/5	48 800 ± 1 200	0.51 ± 0.04	0.1	0.15	ecl[q]
1042-6902	0.336785	DA3	M5	19 960 ± 400	0.55 ± 0.05	0.14 ± 0.01	0.19 ± 0.02	[b]
J1212-0123	0.335871	DA	M3-5/5	17 700 ± 300	0.47 ± 0.1	0.26-0.29	0.3 ± 0.01	ecl[r]
J1724+5620	0.333019	DA	M3-5	35 800 ± 300	0.42 ± 0.01	0.25-0.38	0.26-0.23	[i]
J0110+1326	0.332687	DA	M3-5/5	25 900 ± 427	0.47 ± 0.2	0.255-0.38	0.262-0.36	ecl[s]
RR Cae	0.303704	DAwk	M3-4/5	7 000	0.44 ± 0.02	0.183 ±0.013	0.188-0.23	ecl[a]
J2125-0107	0.289822	DQZO	M	90 000	0.6	0.4 ± 0.1	0.4 ± 0.1	[t]
CC Cet	0.286654	DA2	M4.5	26 200 ± 2 000	0.40 ± 0.1	0.18 ± 0.05	0.21 ± 0.02	[k]
2313-3303	0.2795	DA	dM					[a]
2154+4048	0.26772	DA2	M3.5/5					[u]
1857+5144	0.266334	DAO	M4-6/5	70 000 – 100 000	0.6-1.0	0.15-0.30		[v]
J0314-0111	0.2633	DA	M4		0.65 ± 0.1	0.32 ± 0.09	0.33 ± 0.1	[i]
LM Com	0.258687	DA	M4+/5	29 300	0.35	0.17	0.22	[w]
BPM 71214	0.201626	DA	K2-M3/5	17 200 ± 1 000	0.77			[x]
J1042+6442	0.197669	WD	M3	9 800				[e2]
J1548+4057	0.185518	DA	M6/5	11 700 ± 820	0.614-0.678	0.146-0.201	0.166-0.196	ecl[s]
MS Peg	0.173666	DA2	M3-5/5	22 170	0.48 ± 0.02	0.22 ± 0.02	0.27 ± 0.02	[w]
J1529+0020	0.1651	DA	M5	14 100 ± 500	0.40 ± 0.04	0.25 ± 0.12	0.26 ± 0.13	[i]

Table 1.1: continued.

Name	Porb [d]	Sp1	Sp2	$T_{\rm eff}$	$M_{\rm wd}[{\rm M}_\odot]$	$M_{\rm sec}[{\rm M}_\odot]$	$R_{\rm sec}[R_\odot]$	Ref.
IR Peg	0.164	DO1	M3/5		0.61 ± 0.02			[y]
QS Vir	0.150758	DA	M2-5/5	14 085 ± 100	0.78 ± 0.04	0.43 ± 0.04	0.42 ± 0.02	ecl[z]
J0908+0604	0.149438	DA2.8	M3/5	17 500 ± 500	0.35 ± 0.04	0.32	0.33	ecl[a2]
LTT 560	0.148	D	M5/5	∼ 7500	0.52 ± 0.12	0.19 ± 0.05	0.11	[b2]
J1151-0007	0.1416	DA	M6/5	10 400 ± 200	0.6 ± 0.1	0.19 ± 0.08	0.19 ± 0.1	[i]
J0303+0054	0.134438	DC	M4-5/5	¡8000	0.878-0.946	0.224-0.282	0.246-0.27	ecl[s]
NN Ser	0.130080	DAO1	M4.75/5	55 000 ± 8000	0.54 ± 0.05	0.15 ± 0.008	0.174 ±0.009	ecl[c2]
J1435+3733	0.125630	DA3.6	M4-5/5	12 500 ± 488	0.48-0.53	0.19-0.246	0.218-0.244	ecl[s]
2237+8154	0.123681	DA	M3.5	11 500 ± 1 500	0.47-0.67	0.2-0.4		[d2]
1606+0153	0.1182	DA	dM					[a]
J0052-0053	0.11396	DA	M4	16 000 ± 4400	1.2 ± 0.4	0.32 ± 0.09	0.33 ± 0.1	[i]
HR Cam	0.103063	DA2.7	M/5	19 000	0.41 ± 0.01	0.096 ± 0.004	0.125 ± 0.02	[f2]
0137 3457	0.0803	DA	L8		0.39	0.053 ± 0.0006		[g2]

a) Maxted et al. (2007) b) Kawka et al. (2008) c) Fuhrmeister & Schmitt (2003) d) Shimanskii et al. (2008) e) Sing et al. (2005) f) Vennes et al. (1999) g) Morales-Rueda et al. (2005) h) Schreiber et al. (2008) i) Rebassa-Mansergas et al. (2008) j) Shimanskii & Borisov (2002) k) Saffer et al. (1993) l) Stauffer (1987) m) O'Brien et al. (2001) n) Maxted et al. (2004) o) Tappert et al. (2009) p) van den Besselaar et al. (2007) q) Fulbright et al. (1993) r) Nebot Gómez-Morán et al. (2009) s) Pyrzas et al. (2009) t) Nagel et al. (2006) u) Hillwig et al. (2002) v) Aungwerojwit et al. (2007) w) Shimansky et al. (2003) x) Kawka et al. (2002) y) Kawaler et al. (1995) z) O'Donoghue et al. (2003) a2) Drake et al. (2009) b2) Tappert et al. (2007) c2) Haefner et al. (2004) d2) Gänsicke et al. (2004) e2) Maxted et al. (2009) f2) Maxted et al. (1998) g2) Maxted et al. (2006)

1.2.3 Evolution into CVs

Further evolution of the system, driven by angular momentum loss due to gravitational wave radiation (GR) and magnetized stellar wind, magnetic braking (MB), will bring the system into semicontact. The secondary star fills it's Roche lobe, and mass transfer starts, forming a CV. The evolutionary time scale for a PCEB to become a CV can be determined by the sum of the GR time scale and the MB time scale, for which we have to assume a certain AML prescription. While GR is well established, MB is still in debate. CVs evolve from long to short orbital periods. At long orbital periods, $P_{\rm orb}>$ 3 hours, the secondary stars are sufficiently massive so as to have a radiative core and angular momentum via MB is supposed to be efficient. Once the donor secondary star becomes fully convective, $P_{\rm orb}\simeq$ 3 hours, magnetic braking is not efficient and the AML via MB stops. The secondary then has time to relax to its thermal equilibrium and mass transfer ceases, becoming a detached CV. The only mechanism leading to AML is emission of gravitational waves. Evolution happens in a much longer time scale giving rise to the observed orbital period gap. At $P_{\rm orb}\sim$ 2 hours the secondary star fills its Roche lobe again and mass transfer restarts, so that a CV is again visible. The orbital period continues decreasing until the secondary star becomes a degenerate brown dwarf at around 80 minutes, and at this point the orbital period starts to increase, this systems are known as bouncers. This is the so called disrupted magnetic braking law (DMB) and was firstly proposed by Verbunt & Zwaan (1981). The DMB was put into question since although it could explain the observed mentioned gap, observations of single low mass stars do not show any evidence for such a discontinuity (Pinsonneault et al. 2002). Also DMB predicts a minimum $P_{\rm orb}$ 10% shorter than the observed value and also a pile-up and spike of systems at short orbital periods. Other magnetic braking laws have been proposed, but none of them can explain the presence of a gap in the CV $P_{\rm orb}$ distribution. Recently Gänsicke et al. (2009) have discovered the spike of CV at short orbital period, demonstrating that our picture of the CV orbital period was not complete and pointing again to the validity of the DMB.

1.2.4 Aim and layout of the thesis

The work presented in this thesis forms part of a large collaboration that has been working in the last years looking for answers to the main questions of close binary evolution: *What is the efficiency of the CE phase removing AM from the orbit? What is the strength of magnetic braking, and does MB get disrupted when the secondary star becomes fully convective?* The work presented in this thesis focuses in a well defined sample of WDMS, representing the older population of WDMS binaries. By finding the PCEBs among the WDMS binary sample, measuring their stellar and binary parameters and comparing with the outcome of binary population synthetic studies we aim to answer these questions.

This thesis is structured in the following way. We firstly describe the first dedicated WDMS binary survey, with a detailed analysis of all the systems found, meaning that we estimate fundamental stellar parameters and compare with other studies of WDMS. This sample combined with the most complete SDSS-database from Rebassa-Mansergas et al. (2009) provides the database for testing the current prescriptions of the CE phase and for constraining magnetic braking. We examine the systems and look for those that went through a CE phase, and estimate the orbital period of some of them. We analyze the activity-binarity relation searching for a possible enhancement in close binaries. We describe in detail the relevance of eclipsing binaries and analyze a serendipitously discovered one. We finish by summarizing the main results. Individual chapters are organized like normal journal papers becuase they either are published as such or will be submitted soon.

Chapter 2

White dwarf/main sequence binaries identified within SEGUE

White dwarf/main sequence binaries (WDMS) are ideal systems to constrain current theories of binary star evolution. In current samples of these systems old binaries containing cold white dwarfs are significantly underrepresented. As partners of SEGUE we performed a survey especially dedicated to identify and characterize the missing population of old white dwarf/main sequence binaries. On 240 spectroscopic plates our color selection algorithm selected 9531 candidates of which 431 have been observed spectroscopically. Among these we find 277 white dwarf/main sequence binaries and 24 candidates resulting in a success rate of $\sim$ 70%. For the identified binaries we obtain the stellar parameters, such as the spectral types of the main sequence secondary stars, the distances, the white dwarf temperatures, and the masses using a spectral decomposition method. The obtained white dwarf temperature distribution peaks at lower temperatures than previous samples but at the same temperature as the distribution of SDSS single white dwarfs. Compared to previous WDMS sample, the SEGUE WDMS distribution of secondary star spectral types is slightly broader containing more early M companions. Although covering a larger parameter space than previous samples, the SEGUE WDMS population is still biased towards late spectral type secondary stars. The white dwarf mass distribution peaks at $M_{\rm wd} \sim 0.6 M_{\odot}$ similar to that of single white dwarfs but contains significantly more high mass white dwarfs. The distances to the WDMS in our sample range from 50 to 1500 pc. For the space density of WDMS we derive a lower limit of $0.1 - 2 \times 10^{-4}\,\mathrm{pc}^{-3}$ depending on the distance from the galactic plane. The spatial distribution of the SEGUE WDMS sample is in agreement with a typical scale-height of $\sim 100 - 150$ pc.

2.1 Introduction

WDMS represent the most numerous compact binaries in the universe. The population of WDMS binaries consists of two types of systems which differ due to their evolutionary history. According to recent binary population synthesis calculations more than 75% are wide binaries in which the stellar components evolve like single stars (Willems & Kolb 2004). Virtually all of the remaining $\lesssim 25\%$ suffered from common envelope evolution when the more massive star left the main sequence. This population of PCEBs represents the largest population of close compact binaries.

The first survey identifying large numbers of WDMS is the Sloan Digital Sky Survey (SDSS): based on SDSS imaging and some DR 1[1] spectra Smolčić et al. (2004) identified a new stellar locus in color-color diagrams, i.e. the WDMS binary bridge. Later, the SDSS turned out to be also very efficient in spectroscopically identifying new unresolved WDMS binaries, e.g. Silvestri et al. (2006) published a list of $\sim$ 747 new WDMS binary systems found in SDSS/DR4 and later Silvestri et al. (2007) published a list of more than 1200 systems based on SDSS/DR5. The latest and biggest compilation based in the DR 6 has been done by Rebassa-Mansergas et al. (2009). A significant fraction of these WDMS are PCEBs. These large WDMS sample hide a significant fraction of PCEBs. Since 2007 we run an extensive follow-up program of WDMS discovered by the SDSS to identify a large sample of PCEBs (Rebassa-Mansergas et al. 2007, 2008; Schreiber et al. 2008; Nebot Gómez-Morán et al. 2009; Pyrzas et al. 2009). The final goal of this project is to derive clear constraints on theories of magnetic braking and common envelope evolution as suggested by Schreiber & Gänsicke (2003); Nelemans & Tout (2005); Politano & Weiler (2006); Davis et al. (2008, 2009). To obtain the desired constraints it is essential that the used sample of WDMS binaries covers a large range of secondary star spectral types and white dwarf temperatures to avoid obtaining a biased sample of PCEBs.

In this chapter we describe a WDMS survey we carried out as a part of SEGUE (Yanny et al. 2009). It has been especially designed to identify the old population of WDMS binaries that is underrepresented in previous samples. The outline of the chapter can be described as follows. In Sect. 2.2 we discuss color selection algorithms of WDMS and present our criteria to identify systems containing cold white dwarfs before we present the final SEGUE-WDMS sample in Sect. 2.3. Then we derive the stellar parameters of the WDMS binaries using a spectral decomposition method in Sect. 2.4 and discuss the obtained distributions (Sect. 2.5). Finally, in Sect. 2.6 and 2.7 we analyze the completeness of our survey and derive constraints on the space density and the scale height of the WDMS population in our galaxy.

2.2 White dwarf/main sequence binary color selection

Since the identification of the WDMS bridge (Smolčić et al. 2004), several attempts have been made to develop color selection criteria to select WDMS candidates using the *ugriz* magnitudes provided by the SDSS. In the following we review those critically and present our own selection criteria especially designed to identify old WDMS.

[1]DR 1 is the first data release of the SDSS, the most recent one is the seventh. The DR 7 includes 11 663 deg^2 of imaging data with five-band photometry for 357 million distinct objects, and spectroscopy over 9 380 deg^2 with around 1.6 million spectra of galaxies (930 000), quasars (120 000) and stars (460 000).

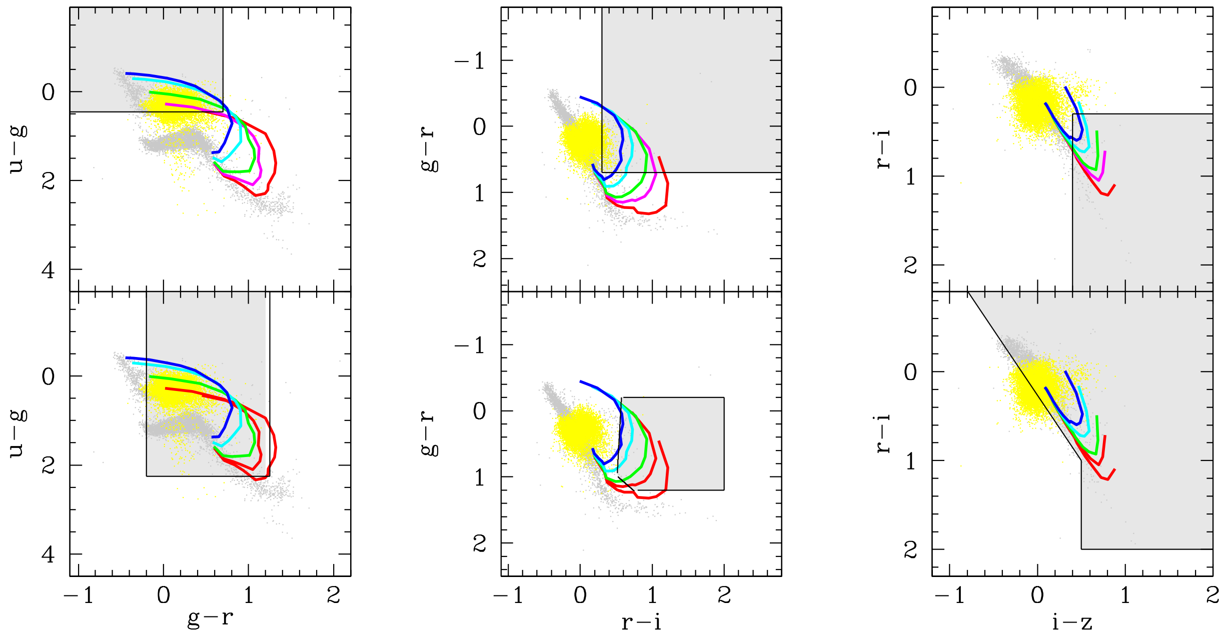

Figure 2.1: *ugriz* color-color diagrams to discuss WDMS target selection algorithms. Quasars and single stars are shown in yellow and grey respectively. Based on data provided by Pickles (1998), Bergeron (private communication), and using the empirical color transformations presented by Jordi et al. (2006), we calculated colors for WDMS binaries. The calculated colors cover the spectral types from K0 to M6 for the main sequence star and effective temperatures of the white dwarf from 6000 to 60 000 K. In the above color-color diagrams tracks from K0 to M6 are shown for five effective temperatures of the white dwarf: 40 000 K (blue), 30 000 K (cyan), 20 000 K (green), 15 000 K (magenta), 10 000 K (red). Grey shaded in the upper panels are the color cuts used by Raymond et al. (2003) and Silvestri et al. (2006) until 2005. Obviously these cuts lead to the detection of only a small part of the WDMS population as especially the "blue" cut (left panel) selects mainly systems with hot white dwarfs ($T_{\rm eff,WD} \gtrsim 15\,000$ K) and/or late type secondary stars (later than ~ M3). Our SEGUE-WDMS color cuts are especially designed to identify WDMS systems containing cold white dwarfs (grey shaded region in the bottom panels) and select most WDMS with cold white dwarf $T_{\rm eff,WD} \lesssim 20\,000$ K. However, for $T_{\rm eff,WD} \lesssim 10\,000$ K and/or very early spectral types (earlier than ~ M0), the WDMS colors are too close to the main sequence to be selected (lower end of the red line).

2.2.1 Expected WDMS *ugriz* colors

To understand possible biases of the SDSS sample of WDMS and to develop efficient color selection criteria, we calculate *ugriz* colors for WDMS binaries. Using Pickles (1998) we determine the Johnson *UBVRI* magnitudes of K- and M dwarfs. Combining this with *UBVRI* colors for white dwarfs (Bergeron, private communication) and using the empirical color transformation provided by Jordi et al. (2006), we derive *ugriz* colors for WDMS binaries for a broad range of white dwarf temperatures ($T_{\rm eff,WD} = 6000 - 60\,000$ K) and secondary spectral types (K0-M6).

Figure 2.1 shows the loci of the calculated WDMS colors in three different color-color diagrams. We used the entire range of secondary spectral types and five different effective temperatures of the white dwarf ($T_{\rm eff,WD}$ = 40 000 K (blue) , 30 000 K (cyan), 20 000 K (green), 15 000 K (magenta), and 10 000 K (red)). For late M-dwarfs the WDMS systems are located near the white dwarf region (located at the top and to the left in all the three color-color diagrams) while they are close to the main sequence for early K stars. For hot white dwarfs the binary colors are similar to those of a main sequence star only for the earliest secondary stars (K0) we considered (blue line). Conversely, if the white dwarf is rather cold, the binary colors may be hardly distinguishable from those of main sequence stars even for early M-dwarf secondary stars (red line).

2.2.2 The bias of the SDSSI sample

The top panel of Fig. 2.1 also shows the selection criteria presented in (Raymond et al. 2003) and (Silvestri et al. 2006). In each plot, the selected regions are shaded. The selection criteria are apparently based on the idea that a WDMS system has to be red (MS) and blue (WD) at the same time. Consequently, they selected a "blue" region in the $u-g$ versus $g-r$ plot (left panel) and a "red" region in the $r-i$ versus $i-z$ diagram (right panel). A combination of the "blue" and "red" cuts is shown in the $g-r$ versus $r-i$ plot (middle panel). Comparing the color-cuts with our theoretical WDMS colors it becomes obvious that these selection criteria cover only a small fraction of possible WDMS colors. In $u-g$ versus $g-r$ (left) they select mainly systems with hot white dwarfs and/or late type secondaries. While most of the blue and cyan lines are inside the "blue" criterion, large parts of the other lines are outside the cut. This means that most WDMS containing white dwarfs colder than $\sim$ 20000 K are not selected. In addition, systems with moderately hot white dwarfs ($\sim$ 20000 – 30000 K) and early M-dwarf secondary stars are also not "blue" enough. In contrast, the "red" cuts applied by Silvestri et al. (2006) (shown in the $r-i$ versus $i-z$ plot, right panel of Fig. 2.1) select most of the WDMS containing white dwarfs colder than $\sim$ 40 000 K. Significant parts of the blue and cyan lines are outside the "red" condition. Finally, as the "red" and "blue" criteria have been combined with a logical AND, the target selection used by Silvestri et al. (2006) leads to a sample of WDMS heavily biased towards hot white dwarfs ($T_{\rm eff,WD} \gtrsim$ 15 000 K) and late type secondary stars (later than ~M3).

In reality, the SDSS sample of the 749 WDMS systems presented by Silvestri et al. (2006) is somewhat less biased than one would expect according to the color selection. The reason for this is obvious: as stated by Silvestri et al. (2006) many WDMS systems have been targeted as quasar (QSO) candidates. Hence, the part of the WDMS bridge overlapping with the QSO region (yellow in Fig. 2.1) is well covered by SDSSI. However, the SDSSI QSO selection algorithm explicitly excludes the color-color space of WDMS containing cold white dwarfs (see Richards et al. 2002, Fig. 7) and hence the strong bias towards hot white dwarfs and late type secondaries remains. Fortunately, Silvestri et al. (2006) finally revised their selection algorithm during 2005 and future SDSS samples of WDMS as that one from Rebassa-Mansergas et al. (2009) are less biased towards hot WDs.

2.2.3 WDMS color selection within SEGUE

The Sloan Extension for Galactic Understanding and Exploration (SEGUE) is the part of SDSS II which specifically targets stars in the Milky Way to map the structure and stellar makeup of the Milky Way Galaxy. The main science goal of SEGUE is to constrain how Milky Way formed and evolved. Therefore SEGUE is scanning the sky outside of the North Galactic Cap in a pattern that includes scans that pass through the Galactic plane to uniformly probe the Milky Way at all accessible longitudes and latitudes.

As partners of SEGUE we run a sub-project identifying the missing WDMS population, i.e. those containing cold white dwarfs. We developed special *ugriz* color-cuts to select those systems on each SEGUE plate-pair ($\sim$ 7deg^2). The bottom panel of Fig. 2.1 shows the SEGUE-WDMS selection criteria as black lines. We use:

$$
\begin{array}{rclll}
u-g & < & 2.25 & & g-r > -19.78(r-i)+11.13 \\
g-r & > & -0.2 & & g-r < 0.95(r-i)+0.5 \\
g-r & < & 1.2 & & i-z > 0.5 \ \text{for} \ r-i > 1.0 \\
r-i & > & 0.5 & & i-z > 0.68(r-i)-0.18 \ \text{for} \ r-i <= 1.0 \\
r-i & < & 2.0 & & 15 < g < 20.
\end{array}
$$

The main cuts are in $g-r$ and $r-i$. Clearly, we will only select few systems with hot white dwarfs as significant parts of the blue line are outside our criteria. In addition, WDMS consisting of both cold white dwarfs ($T_{\rm eff,WD} \lesssim 10.000$ K) and early type secondaries (earlier than ~M0) will not be detected, as they are too close to the main sequence (lower part of the red line). However, according to the calculated WDMS colors one clearly expects to identify substantially more WDMS containing cold white dwarfs and early type secondaries, i.e. exactly those systems that are extremely underrepresented in the SDSS I sample.

Our criteria have been optimized by performing extensive tests with data release 4 (DR4). Combining our final color-criteria with the standard clean-photometry flag-setting and requesting the psf-errors to be below 0.2 we find 3713 candidates in DR4. With the footprint area of DR4 (6670 deg^2) this gives an average 3.9 candidates per plate pair (covering 7 deg^2). Among these 293 systems were observed spectroscopically and we identify 187 WDMS and 21 WDMS candidate systems which gives an expected success rate of~ 64%. The DR4 candidates and targets are shown in Fig. 2.2. Apparently, while the candidates (green) cover the total area we selected in color-color space, those systems with SDSS I spectrum (red) cluster close to the QSO region. This has been expected, as most of them have been selected for spectroscopy as QSO candidates.

Somewhat surprising, 10 of the 187 WDMS we identified during our target selection tests (see Sect.2.2.3) with DR4 have not been published in the corresponding DR4 or DR5 WDMS or white dwarf catalogues (Silvestri et al. 2006, 2007; Eisenstein et al. 2006). This incompleteness inspired us to apply our color-selection to DR5 without any flag restrictions to determine the definite number of WDMS inside our criteria using DR5. We find 437 systems that have been

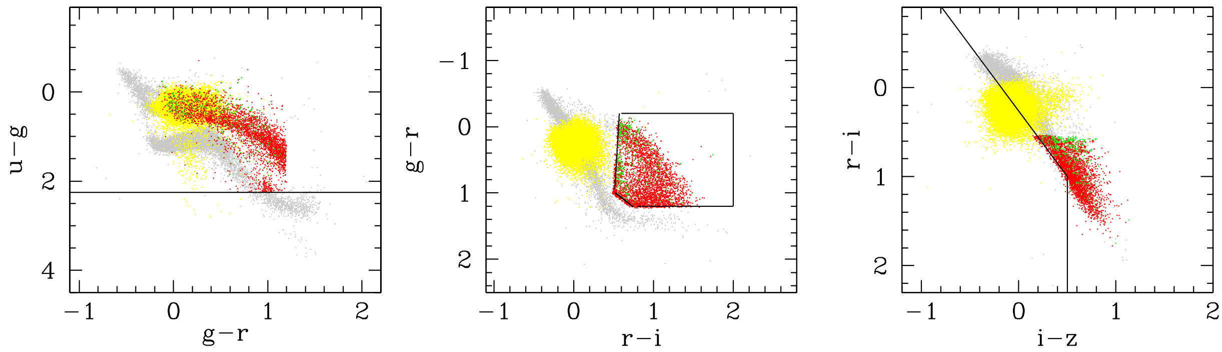

Figure 2.2: WDMS target selection tests with data release 4 (DR4). As in Fig. 2.1 stars and quasars are in grey and yellow respectively. Applying our color selection to DR4 we get 3247 candidates (red) that cover the cold white dwarf region of the WDMS bridge. 283 of these systems have been selected for spectroscopy (green) among these we find 201 WDMS. Most of the spectroscopic targets (green) are close to the QSO region because they were selected as QSO candidates. This further demonstrates the bias of the SDSS I sample.

observed spectroscopically. Among these are 276 WDMS and 36 WDMS candidates. Of the 276 WDMS 45 have not been published so far. In Table 2.1 we provide the *ugriz* colors, plate and fiber numbers as well as times of observations of these 45 WDMS. Apparently, the published SDSS catalogues of WDMS are not complete and probably about ~ 20% WDMS are missing. Obviously, a separate analysis of the WDMS content of DR6 (Adelman-McCarthy et al. 2007) and DR7 (Abazajian et al. 2009) seems to be a worthwhile exercise and part has been presented in Rebassa-Mansergas et al. (2009) (Rebassa-Mansergas et al 2010, in preparation).

2.2.4 Comparison of selection criteria

We have applied our selection criterium to the expected *ugriz* colors of WDMS binaries for spectral types in the range K6 – M6 and for effective temperatures of the white dwarf in the range $10^3 - 10^5$ K to see what area of the effective temperature-spectral type plane we expect to cover. We have also applied the selection criterium defined by Silvestri et al. (2006), and also their revised version, in the same ranges of spectral type and effective temperatures. In Fig. 2.3 we show the coverage in the effective temperature-spectral type plane of our selection criterium (left panel), that one from Silvestri et al. (2006) (middle) and their revised criterium (right).

We cover a broad range in the effective temperature of the white dwarf, 6 000 – 10^5 K and in the spectral type of the secondary star, M0 to M6. While we cover earlier spectral types than M2, this are not covered by Silvestri et al. (2006) in either criteria. We expect to detect cold white dwarfs (< 15 000 K), while they would only be detected by Silvestri et al. (2006) in case they contain later spectral type secondaries than M6. Although in their revised criterium they do cover cold white dwarf temperatures for earlier spectral types than M6, the spectral type is still limited to later spectral types than M2.

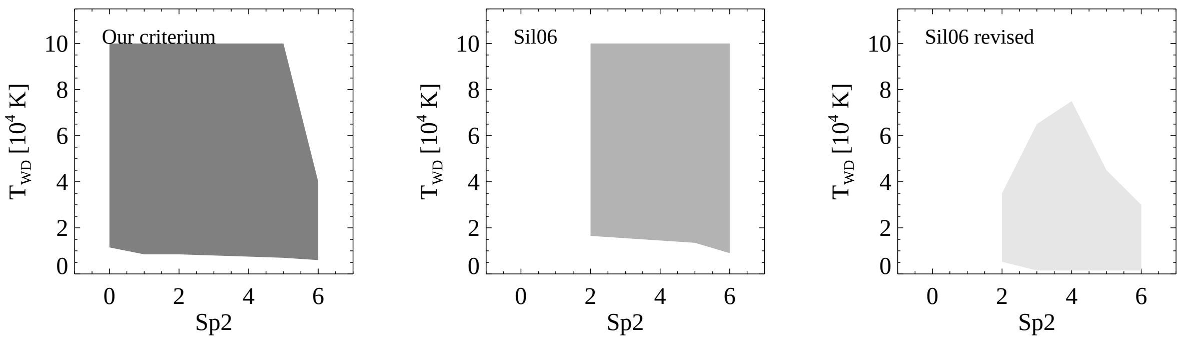

Figure 2.3: Coverage in the effective temperature-spectral type plane of our selection criterium (left), that one from Silvestri et al. (2006) (middle) and their revised criterium (right).

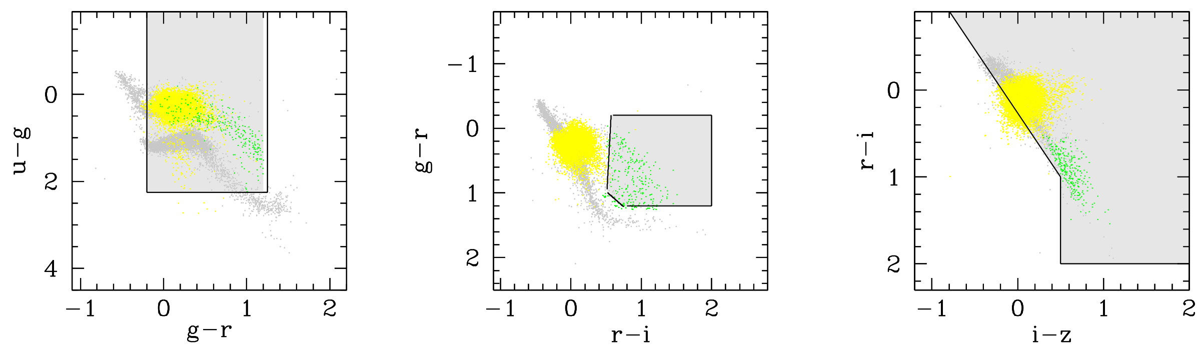

Figure 2.4: The position of the SEGUE WDMS binaries in *ugriz* color-space. Apparently, in contrast to the spectroscopic DR4 sample shown as green dots in in Fig. 2.2, the SEGUE WDMS sample includes significantly more WDMS binaries close to the main sequence, i.e. systems containing cold white dwarfs.

2.3 The SEGUE white dwarf/main sequence binary sample

In October 2005 SEGUE incorporated the color selection given in Sect. 2.2.3 with the goal of targeting on average 5 WDMS candidates and up to 10 WDMS per plate-pair. Until the end of SEGUE in mid-2008 116 plate-pairs and 8 single SEGUE-plates with WDMS target selection according to our criteria have been observed. In addition to the color criteria we requested clean photometry [2] for the selection of our targets. According to DR7 9531 systems fulfilled the target selection criteria. However, one should note that 7619 of these candidates are on 12 plates that have been oriented towards the galactic plane[3], where reddening is very high, and the success rate of our selection criterium should be low, since we did not correct for reddening. Of the

[2] http://www.sdss.org/dr7/tutorials/flags/index.html#clean

[3] Plate pairs oriented towards the GP: 2555/2565, 2556/2566, 2678/2696, 2680/2698, 2812/2833, 2887/2912

9531 available candidates 431 stars have been observed spectroscopically and among these we identify 277 WDMS and 24 WDMS candidates. Two WDMS (SDSSJ135643.56-085808.9 and SDSSJ135930.96-101029.7) have been found on plate 2716, spectroscopic plate that has not been published via DR7. Although the spectra of these two systems is not available via DR7 we had access to it and we made use of them for the completeness analisys [4]. The WDMS 'candidate' category refers mostly to spectra containing a main sequence star with a strong blue excess which cannot clearly be identified as originating from a white dwarf. Dividing the number of spectra taken by the number of identified WDMS and WDMS candidates results in a overall success rate of 64%. Table 2.2 lists the number of candidates, the spectra taken according to our selection criteria, teh number of identified WDMS binaries, and the number of systems for which spectra were taken but are outside the selection criteria, the success rate, and galactic coordinates of the center of the plate, the space density, the reddening and the error on the density, for the 116 plate-pairs and the 8 single plates with WDMS target selection that have been observed in SEGUE. Table 2.3 lists on our WDMS and candidates systems, the corresponding plate numbers, date of the observation, their *ugriz* magnitudes and their errors. An excerpt of Tables 2.3 and 2.2 are now given while the full tables are available in the appendix.

Fig. 2.4 shows the positions of our SEGUE WDMS in color-color space. The background in the three panels are again single stars (grey) and quasars (yellow) from DR4. Our selection criteria have been designed for the measured *ugriz* magnitudes, i.e. not reddening corrected. However, 14 SEGUE plate pairs and 2 single plates i.e. those with plate numbers < 2377 that belong to target selection version 3.3, accidently used reddening corrected magnitudes for the selection of WDMS candidates. Therefore 31 WDMS of the 301 identified WDMS or WDMS candidate systems are located slightly outside our criteria.

Fig. 2.5 shows the positions of our WDMS candidates in galactic and equatorial coordinates. One of the big advantages of SEGUE is that it covers a wide range of galactic latitudes and, as we will see later, this gives an idea of the spatial distribution of the galactic population of WDMS. Table 2.3 lists the 301 WDMS and WDMS candidate systems, the corresponding plate as well as fiber numbers, the dates of observation (MJD) and the measured ugriz magnitudes.

2.4 Stellar parameters

We use the same method, templates, and spectral models as Rebassa-Mansergas et al. (2007) to determine the stellar parameters of the SEGUE-WDMS binaries. In brief, the method can be described as follows: we fit the WDMS spectrum using grids of observed M-dwarf and white dwarf template spectra. Our white dwarf library consists of 488 high S/N DA from DR6 (Adelman-McCarthy et al. 2007) covering the entire parameter space of the effective temperature and the gravity and 222 DB spectra taken from Eisenstein et al. (2006). The M-dwarf templates are based on several hundred M-dwarf spectra also taken from DR6. These spectra have been

[4]http://www.sdss.org/dr7/start/aboutdr7.html

Table 2.1: During our target selection tests we identified 45 so far unpublished WDMS binaries that are in DR5 and fullfill our target selection criteria.

System	Ra	Dec	u	g	r	i	z	MJD	Plate	Fiber
SDSSJ075325.93+164132.7	07 53 25.93	+16 41 32.7	20.186	19.076	17.997	17.308	16.935	53317	1921	177
SDSSJ080524.40+232411.6	08 05 24.40	+23 24 11.6	18.955	18.181	17.225	16.614	16.207	52705	1265	117
SDSSJ082903.53+231651.0	08 29 03.53	+23 16 51.0	20.085	19.141	18.084	16.874	16.193	53327	1928	220
SDSSJ093236.83+053026.6	09 32 36.83	+05 30 26.6	19.822	18.320	17.199	16.414	15.973	52644	992	175
SDSSJ095250.11+324328.8	09 52 50.11	+32 43 28.8	20.810	19.492	18.630	17.541	16.926	53387	1945	20
SDSSJ095250.98+055636.9	09 52 50.98	+05 56 36.9	20.339	18.948	17.771	17.064	16.663	52725	994	117
SDSSJ100255.48+424320.9	10 02 55.48	+42 43 20.9	20.068	19.516	18.848	17.570	16.755	52672	1217	538
SDSSJ103152.46+362832.8	10 31 52.46	+36 28 32.8	19.648	18.974	18.118	17.039	16.355	53432	1973	165
SDSSJ104142.56+391900.2	10 41 42.56	+39 19 00.2	20.121	19.758	19.231	18.396	17.854	53433	1998	413
SDSSJ104459.32+360554.7	10 44 59.32	+36 05 54.7	18.616	17.870	17.160	15.824	14.999	53463	2090	273
SDSSJ105853.18+390018.2	10 58 53.18	+39 00 18.2	20.265	19.484	18.612	17.519	16.873	53469	1988	380
SDSSJ110736.88+612232.8	11 07 36.88	+61 22 32.8	20.091	18.738	17.669	16.936	16.506	52286	774	555
SDSSJ113833.13+351825.8	11 38 33.13	+35 18 25.8	20.315	19.468	18.669	17.714	17.139	53493	2012	162
SDSSJ114046.44+331843.0	11 40 46.44	+33 18 43.0	20.019	18.988	18.012	16.746	16.013	53491	2097	310
SDSSJ114509.77+381329.2	11 45 09.77	+38 13 29.2	17.641	16.994	16.284	15.068	14.256	53442	1997	491
SDSSJ115031.25+365416.1	11 50 31.25	+36 54 16.1	18.454	18.301	17.887	17.079	16.553	53436	2035	419
SDSSJ120455.42+133715.7	12 04 55.42	+13 37 15.7	19.959	19.540	19.248	18.268	17.523	53467	1764	139
SDSSJ121010.13+334722.9	12 10 10.13	+33 47 22.9	18.424	17.268	16.478	15.251	14.366	53498	2089	102
SDSSJ121356.86+363531.0	12 13 56.86	+36 35 31.0	18.145	17.786	17.085	16.376	15.982	53472	2105	546
SDSSJ121928.05+161158.7	12 19 28.05	+16 11 58.7	18.784	18.123	17.723	16.736	15.845	53468	1766	569
SDSSJ122544.63+381605.3	12 25 44.63	+38 16 05.3	20.734	19.824	19.172	18.133	17.500	53466	1992	277
SDSSJ122604.78+375827.5	12 26 04.78	+37 58 27.5	19.542	18.372	17.315	15.875	14.982	53466	1992	231
SDSSJ122634.97+322020.8	12 26 34.97	+32 20 20.8	20.111	19.483	19.064	18.009	17.225	53472	1971	315
SDSSJ123223.80+380858.6	12 32 23.80	+38 08 58.6	18.085	18.087	18.010	17.193	16.566	53466	1992	76
SDSSJ130403.64+144955.5	13 04 03.64	+14 49 55.5	20.566	20.184	20.069	19.372	19.009	53498	1771	632
SDSSJ134624.89+021734.2	13 46 24.89	+02 17 34.2	19.596	18.364	17.423	16.153	15.838	52026	530	279
SDSSJ134901.85+020136.5	13 49 01.85	+02 01 36.5	20.402	18.587	17.573	16.921	16.538	52026	530	200
SDSSJ140816.84+331448.4	14 08 16.84	+33 14 48.4	20.247	19.378	18.541	17.188	16.338	53471	1839	253
SDSSJ140949.55+433911.4	14 09 49.55	+43 39 11.4	20.289	19.149	18.198	17.089	16.404	53115	1467	20
SDSSJ143649.61+323734.1	14 36 49.61	+32 37 34.1	17.489	17.060	16.256	15.608	15.224	53491	1841	78
SDSSJ151714.96+423924.7	15 17 14.96	+42 39 24.7	17.859	17.477	16.843	15.904	15.304	53433	1678	440
SDSSJ152116.97+420159.2	15 21 16.97	+42 01 59.2	19.284	19.210	18.863	18.264	17.829	53433	1678	163
SDSSJ152341.27+430528.9	15 23 41.27	+43 05 28.9	20.114	19.352	18.529	17.310	16.586	53433	1678	616
SDSSJ152517.89+362945.2	15 25 17.89	+36 29 45.2	18.956	18.007	17.204	16.065	15.361	53470	1400	135
SDSSJ154605.27+370854.3	15 46 05.27	+37 08 54.3	20.487	19.095	18.064	17.002	16.381	52875	1416	458
SDSSJ155022.11+323548.5	15 50 22.11	+32 35 48.5	18.776	17.790	16.747	15.525	14.804	52825	1404	318
SDSSJ160136.70+050527.9	16 01 36.70	+05 05 27.9	18.246	18.301	17.896	17.382	16.993	53494	1837	431
SDSSJ160645.02+284725.9	16 06 45.02	+28 47 25.9	19.206	18.845	18.724	18.033	17.417	53496	1578	104
SDSSJ160824.57+285524.9	16 08 24.57	+28 55 24.9	20.395	19.753	19.352	18.400	17.730	53496	1578	72
SDSSJ160915.97+273559.4	16 09 15.97	+27 35 59.4	18.466	18.023	17.643	16.695	16.023	53495	1577	252
SDSSJ161505.51+235746.3	16 15 05.51	+23 57 46.3	19.356	18.569	18.010	17.079	16.456	53520	1657	515
SDSSJ162051.70+343815.3	16 20 51.70	+34 38 15.3	19.964	18.491	17.457	16.410	15.840	52522	1057	195
SDSSJ163020.19+305254.5	16 30 20.19	+30 52 54.5	20.634	19.384	18.227	17.021	16.345	53463	1685	496
SDSSJ164131.77+212727.2	16 41 31.77	+21 27 27.2	20.419	18.862	17.681	16.614	15.977	53149	1570	178
SDSSJ204117.49-062847.0	20 41 17.49	-06 28 47.0	19.325	19.059	18.477	17.850	17.452	52164	634	47

Table 2.2: Number of candidate, spectra taken according to our selection criteria, number of identified WDMS binaries, number of systems for which spectra were taken but are outside the selection criteria, success rate, galactic coordinates, space density, reddening and error on the density, for the 116 plate-pairs and 8 single plates with WDMS target selection that have been observed in SEGUE. See appendix for a complete version of the table.

plate	$N_{\rm cand}$	$N_{\rm spec}$	$N_{\rm WDMS}$	$N_{\rm out}$	$\frac{(N_{\rm WDMS}-N_{\rm out})}{N_{\rm spec}}$	$\frac{(N_{\rm WDMS}-N_{\rm out})}{N_{\rm spec}} * N_{\rm cand}$	l	$\lvert b\rvert$	ρ	$E(B-V)$	$\sigma\rho$
2303/2318	31	3	0	0	0	0	21.999	31.001	0	0.113	0
2304/2319	3	1	1	0	1	3	41.947	206.641	2.13127e-05	0.038	2.13127e-05
2305/2320	9	1	0	0	0	0	36.654	44.839	0	0.227	0
2306/2321	1	1	1	0	1	1	50.928	156.158	7.10422e-06	0.07	7.10422e-06
2307/2322	2	2	1	0	0.5	1	44.606	171.393	7.10422e-06	0.105	7.10422e-06
2308/2323	6	2	1	1	0	0	38.777	67.763	0	0.101	0
2310/2325	2	1	2	2	0	0	46.371	80.426	0	0.07	0
2312/2327	2	1	1	0	1	2	55.193	116.279	1.42084e-05	0.038	1.42084e-05
2313/2328	4	4	2	1	0.25	1	62.582	131.954	7.10422e-06	0.029	7.10422e-06
2315/2330	3	1	2	1	1	3	31.957	199.78	2.13127e-05	0.033	2.13127e-05
2316/2331	3	3	4	1	1	3	37.195	164.26	2.13127e-05	0.033	1.23049e-05
2317/2332	4	3	5	2	1	4	29.168	221.468	2.84169e-05	0.055	1.64065e-05
2334/2339	4	4	1	0	0.25	1	40.799	177.708	7.10422e-06	0.132	7.10422e-06
2335/2340	3	1	0	0	0	0	42.745	174.648	0	0.201	0
2378/2398	9	5	3	0	0.6	5.4	22	150.001	3.83628e-05	0.118	2.21488e-05
2379/2399	2	2	1	1	0	0	32	150.001	0	0.114	0
2380/2400	4	3	2	0	0.666667	2.66667	40.307	185.88	1.89446e-05	0.043	1.33959e-05
2381/2401	7	4	4	0	1	7	43.491	195.57	4.97296e-05	0.023	2.48648e-05
2382/2402	1	1	0	0	0	0	37.581	225.304	0	0.052	0
2383/2403	2	2	2	0	1	2	43.624	150.918	1.42084e-05	0.029	1.00469e-05
2384/2404	3	3	3	0	1	3	46.196	163.484	2.13127e-05	0.014	1.23049e-05
2386/2406	5	5	4	0	0.8	4	53.919	205.391	2.84169e-05	0.029	1.42084e-05
2387/2407	4	4	3	0	0.75	3	54.796	189.365	2.13127e-05	0.013	1.23049e-05
2389/2409	2	1	1	0	1	2	49.817	250.281	1.42084e-05	0.039	1.42084e-05
2390/2410	6	5	5	0	1	6	59.243	162.384	4.26253e-05	0.016	1.90626e-05
2393/2413	4	3	2	0	0.666667	2.66667	61.303	245.98	1.89446e-05	0.023	1.33959e-05
2394/2414	6	3	3	0	1	6	54.158	143.487	4.26253e-05	0.009	2.46098e-05

Table 2.3: Plate number, Fiber number, MJD of the observation, and *ugriz* colors of the 301 WDMS and WDMS candidate systems identified with SEGUE.

System	Plate	Fiber	MJD	u	σ_u	g	σ_g	r	σ_r	i	σ_i	z	σ_z
SDSSJ000250.64-045041.6	2630	439	54327	19.846	0.042	19.728	0.021	19.464	0.018	18.569	0.014	17.903	0.022
SDSSJ013000.74+385205.4	2336	7	53712	20.128	0.039	19.030	0.017	17.935	0.011	17.203	0.012	16.762	0.016
SDSSJ014143.68-093811.7	2865	170	54497	19.663	0.037	19.377	0.022	18.931	0.015	18.072	0.019	17.435	0.022
SDSSJ023438.48+244535.6	2399	75	53764	21.155	0.108	20.012	0.021	18.851	0.016	18.040	0.014	17.524	0.017
SDSSJ025555.87+352830.2	2378	538	53759	18.370	0.023	17.559	0.014	16.519	0.009	15.550	0.007	14.992	0.013
SDSSJ030247.65+372125.9	2443	185	54082	20.634	0.071	19.589	0.014	18.444	0.012	17.749	0.012	17.367	0.018
SDSSJ030716.44+384822.8	2441	564	54065	20.642	0.075	19.039	0.126	17.861	0.316	16.698	0.201	16.056	0.122
SDSSJ030956.31+411049.2	2397	255	53763	24.598	1.009	18.405	0.030	16.976	0.014	15.777	0.011	14.979	0.009
SDSSJ032140.00+415307.5	2417	633	53766	21.078	0.135	20.582	0.076	19.490	0.024	18.345	0.012	17.674	0.018
SDSSJ042053.72+064922.4	2826	526	54389	20.922	0.071	19.755	0.019	18.655	0.012	17.165	0.011	16.231	0.013
SDSSJ070322.17+664908.0	2337	419	53740	19.973	0.044	18.642	0.019	17.512	0.011	16.366	0.015	15.712	0.020
SDSSJ070628.57+383650.2	2943	204	54502	20.217	0.049	19.412	0.016	18.507	0.011	17.554	0.015	16.984	0.016

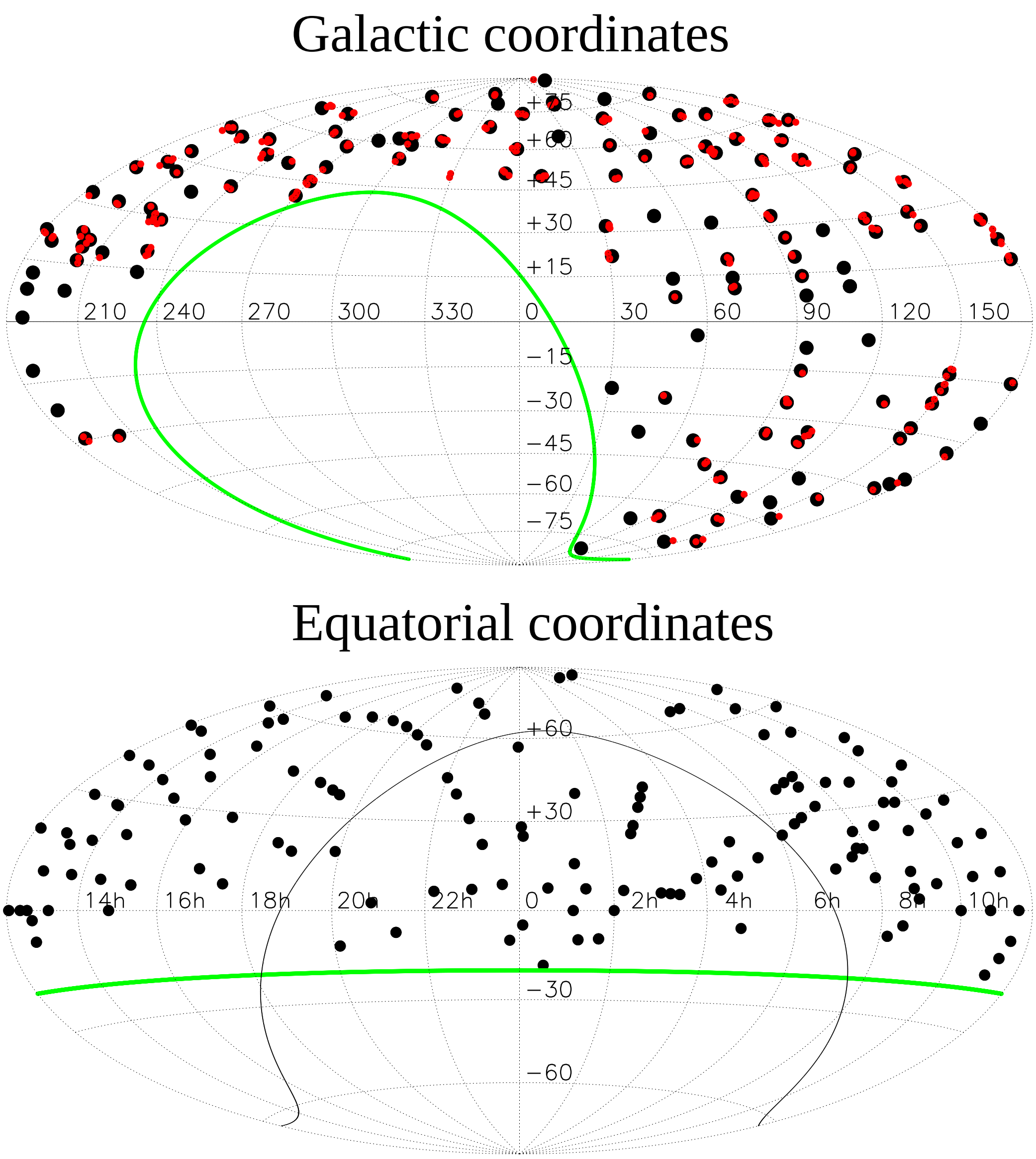

Figure 2.5: Position of the plate-centers (black) and identified WDMS binaries (red) in galactic and equatorial coordinates. In contrast to SDSS I and the Legacy survey, SEGUE observed a large number of plates at low galactic latitudes.

classified using the templates of Beuermann et al. (1998). For each spectral subtype the best 10 – 20 spectra have been averaged and scaled in flux to match the surface brightness at 7500 Å.

In a first step the best match of the SDSS WDMS spectrum to a WD and MS combination of the just described templates is determined. We used an evolutionary strategy based on a weighted χ^2 to find the best solution. This allows to determine the spectral type of the secondary and using the spectral type-radius relation from Rebassa-Mansergas et al. (2007) and the apparent magnitude of the scaled template we derive a first estimate of the distance to the M star, $d_{\rm sec}$. We subtract the best-fitted M-dwarf template spectrum, and determine the parameters of the white dwarf via χ^2 minimization in a $\log g - T_{\rm eff}$ grid of DA model spectra from Koester (2008), based on the atmosphere code described in Finley et al. (1997), to the Balmer lines of the remaining WD. We use $H\beta - H\epsilon$, and avoid using $H\alpha$ since it might contain some residual emission from the red dwarf (see left panel of Fig. 2.6). As we have seen in chapter 1 the solution is bi-valued, giving two solutions, a 'hot' and a 'cold' solution, shown in the right upper panel of Fig. 2.6. In order to discern between these two solutions, we fit template DA to the continuum from 3850 – 7150 Å, avoiding the reddest part of the white dwarf since it might contain some residual flux from the M star. With the $\log g - T_{\rm eff}$ combination and using an updated version of Bergeron et al. (1995) we estimated the mass and the radius of the white dwarf. Combining with the flux scaling factor this gives us a second estimate of the distance, $d_{\rm wd}$, through the relation between the observed flux (F_{obs}) and the astrophysical flux at the surface of the WD as given by the model (F_{em}), $F_{obs} = F_{em}(R_{\rm wd}/d_{\rm wd})^2$.

In some cases it is not possible to distinguish between the 'hot' and the 'cold' solution using the spectrum plus lines. However, as the hot solution predicts significantly more UV flux than the cold solution, we can identify the correct fit by comparing the predicted UV flux with NUV and FUV magnitudes measured by GALEX[5]. An example is given in Fig. 2.6 and 2.7. While the decomposition of the spectrum of SDSSJ134008.04+082248.4 does not provide a unique solution, comparing the predicted UV fluxes with GALEX data clearly favors the cold solution. Among the 301 systems identified as WDMS or candidates we find that 230 systems have GALEX counterparts withing a 0.05 arc minutes radius search.

We found 277 clear WDMS and 24 candidates that have a dM star and some excess in the blue. Among the WDMS 193 contain DAs, there are 14 systems where the DA nature is a bit dobious and we labelled as DA:/dM and for which we decided not to give stellar parameters for the white dwarf, 15 DB/dM, 20 DC/dM, and 35 WD/dM. Table 2.4 lists the obtained stellar parameters of the 193 SEGUE WDMS binaries containing DA white dwarfs and the secondary star spectral type for all the 277 clear WDMS binaries and 24 candidates (abridged version is shown in Table 2.4 a full table is available in the appendix). We also identified 2 new CVs (Szkody et al. 2009) and one low accretion rate magnetic binary (Schwope et al. 2009). The most likely scenario for the later systems is that accrete they accrete matter from the stellar wind of the secondary star. These type of binaries are thought to be precursors of magnetic CVs (Webbink & Wickramasinghe 2005; Schmidt et al. 2005; Vogel et al. 2007).

2.5 Distributions

In this section we briefly discuss the distributions of the obtained parameters and compare our results with those obtained by Silvestri et al. (2006), and Eisenstein et al. (2006). While our decomposition method has shown to work quite well in most cases, in some cases the obtained

[5]http://www.galex.caltech.edu/

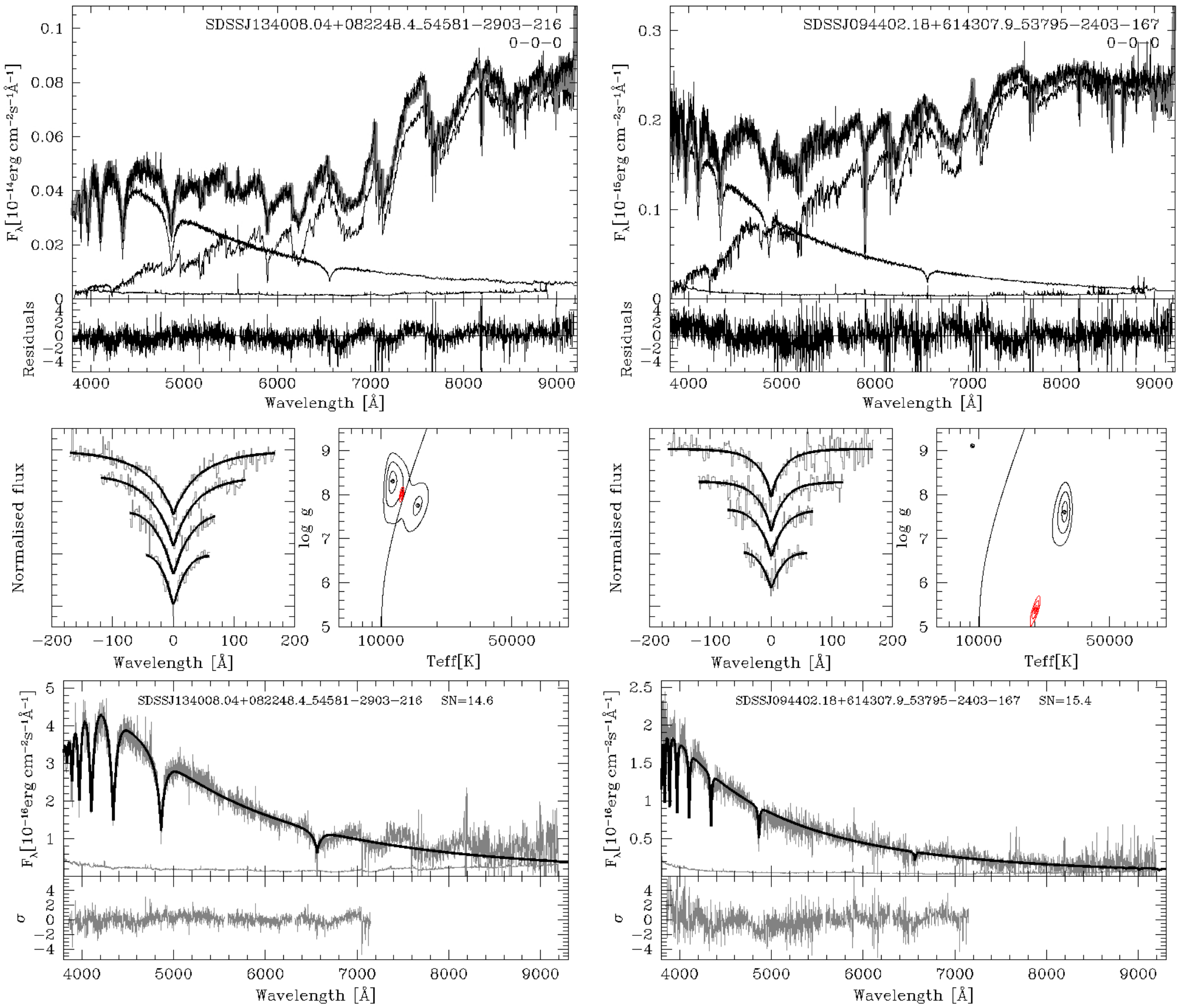

Figure 2.6: Top panel: two component fit to SDSSJ134008.04+082248.4 and to SDSSJ094402.18+614307.9. The top panel shows the WDMS spectrum (black line) and the white dwarf and the M-dwarf templates (dotted lines), while the lower panel shows the residuals to the fit. Bottom panels: spectral fit to the white dwarf in SDSSJ134008.04+082248.4 and in SDSSJ094402.18+614307.9 obtained by subtracting the best-fit M-dwarf template from the SDSS spectrum. Top left panels: normalized Hβ to Hϵ line profiles (top to bottom, gray lines) along with the best-fit white dwarf model (black lines). Top right panels: 3, 5, and 10σ χ^2 contour plots in the $T_{\rm eff} - \log g$ plane. The black contours refer to the best line profile fit, the red contours to the fit of the whole spectrum. The solid line indicates the location of maximum Hβ equivalent width in the $T_{\rm eff} - \log g$ plane, dividing it into "hot" and "cold" solutions. The best-fit parameters of the "hot" and "cold" normalized line profile solutions and of the fit to the 3850 − 7150 Å range are indicated by red and black dots, respectively. Bottom panels: the white dwarf spectrum and associated flux errors (gray lines) along with the best-fit white dwarf model (black lines) to the 3850–7150 Å wavelength range (top) and the residuals of the fit (gray line, bottom). Apparently, the fit to the continuum for SDSSJ134008.04+082248.4 does not indicate whether the "hot" or the "cold" solution should be prefered. In such cases GALEX data was helpful identifying the best fit (see text and Fig. 2.7).

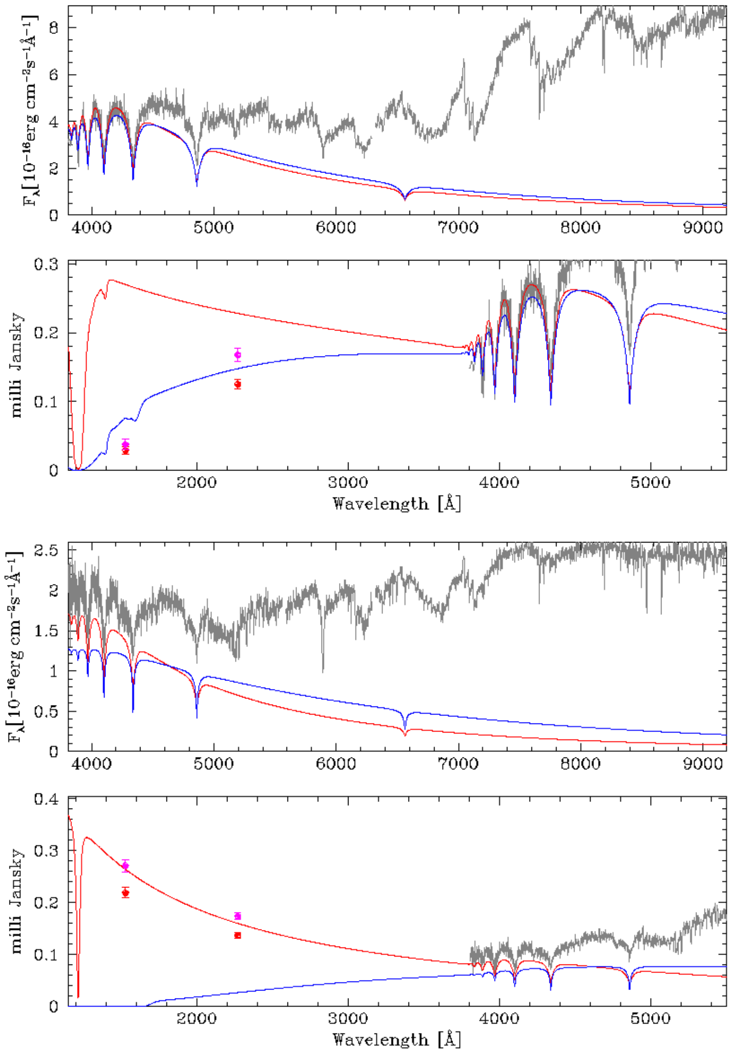

Figure 2.7: Predicted flux of the "hot" (red) and "cold" (blue) solution for SDSSJ134008.04+082248.4 and SDSSJ094402.18+614307.9 at optial and UV wavelengths. NUV and FUV fluxes provided by GALEX clearly show that the "cold" solution is the correct one.

parameters are relatively uncertain. To avoid incorporating large numbers of uncertain values we not only show distributions of all systems but also those including only systems having uncertainties less than 25%. Fig. 2.8 shows the distributions of white dwarf temperatures, masses, and secondary spectral types for the whole sample (solid lines) and for systems with uncertainties lower than 25% and effective temperature higher then 12 000 K (dashed lines).

Table 2.4: Stellar parameters of the 277 WDMS systems identified with SEGUE and for the 24 candidates. For the 84 binaries containing a DB, DC, or unclear white dwarf spectral type, only some parameters obtained for the secondary star are given, this is also true for the candidates.

System	Type	$T_{\rm eff}$	$\sigma_{T_{\rm eff}}$	$\log g$	$\sigma_{\log g}$	$M_{\rm wd}$	$\sigma_{M_{\rm wd}}$	$d_{\rm wd}$	$\sigma_{d_{\rm wd}}$	Sp2	$d_{\rm sec}$	$\sigma_{d_{\rm sec}}$
SDSSJ000250.64-045041.6	DB/dM									3	797	157
SDSSJ000356.93-050332.7	DA/dM	17106	438	8.07	0.10	0.66	0.06	285	19	4	386	114
SDSSJ000453.93+265420.4	DA/dM	18974	1594	7.97	0.33	0.60	0.20	683	142	3	1037	204
SDSSJ000504.91+243409.6	DA/dM	13127	2160	8.16	0.34	0.71	0.22	304	70	4	350	103
SDSSJ000531.09-054343.2	DA/dM	13127	657	7.91	0.14	0.56	0.08	129	11	4	167	49
SDSSJ000559.87-054416.0	DA/dM	31128	921	7.89	0.21	0.59	0.12	692	99	2	553	132
SDSSJ000651.91+284647.1	DA/dM	12976	688	7.83	0.21	0.51	0.12	343	44	3	420	83
SDSSJ000829.92+273340.5	DA/dM	15782	1481	7.73	0.37	0.47	0.20	615	131	2	656	156
SDSSJ000935.50+243251.2	DA/dM	14393	4221	8.58	0.68	0.98	0.32	347	162	2	479	114
SDSSJ003804.41+083416.9	DA/dM	8673	255	7.73	0.59	0.45	0.35	216	69	3	223	44
SDSSJ010341.59+003132.6	DA/dM	21535	1234	7.76	0.21	0.50	0.11	849	113	2	1159	276
SDSSJ010448.50-010516.7	cand									3	339	67
SDSSJ010704.58+005907.9	cand									1	1063	208
SDSSJ011123.90+000935.2	DA/dM	15071	547	7.72	0.13	0.47	0.06	458	36	2	654	156
SDSSJ011932.38-090219.1	DA/dM	15601	1500	8.44	0.35	0.89	0.20	497	126	2	629	150
SDSSJ013000.74+385205.4	DA:/dM									1	805	158
SDSSJ014143.68-093811.7	DC/dM									3	642	126
SDSSJ014147.33-094200.3	cand									3	490	96
SDSSJ014232.59-083528.4	DA/dM	9187	148	8.77	0.18	1.08	0.10	113	17	3	428	84
SDSSJ020351.29+004025.0	DA/dM	10918	589	7.98	0.45	0.59	0.28	420	115	3	501	99
SDSSJ021145.57+071831.1	DA/dM	19193	1301	8.09	0.26	0.67	0.16	700	123	3	758	149
SDSSJ023438.48+244535.6	WD/dM									1	1141	223

2.5.1 White dwarf temperatures

The distribution of white dwarf effective temperature is shown in the top left panel of Fig. 2.8. The measured white dwarf temperatures are less accurate if the white dwarf is very cool. Therefore several of the oldest systems have errors exceeding the 25% criterion (dashed histogram in Fig. 2.8). As expected, our selection criteria select mostly cold white dwarfs and our distribution peaks roughly at 10 000 K while the distribution published by Silvestri et al. (2006) has a broader peak at a higher temperature, 17 500 K. The difference between the two distributions is straight forward to understand if one takes into account the different selection algorithms applied (see Sect.2.2.3).

A detailed comparison with previously published samples is shown in Fig. 2.9. The upper left panel compares the white dwarf temperature in our sample with the single DA white dwarfs listed by Eisenstein et al. (2006). We selected from their Table 11 [6] systems flagged as 1 in their autofit quality flag and removed double entries and systems with companions. Both distributions are normalized to facilitate comparison. The solid line represents the effective temperature of the WDs in our SEGUE WDMS sample while Eisenstein's distribution of single white dwarfs

[6]http://das.sdss.org/wdcat/dr4/table11_dr4.wd.dat

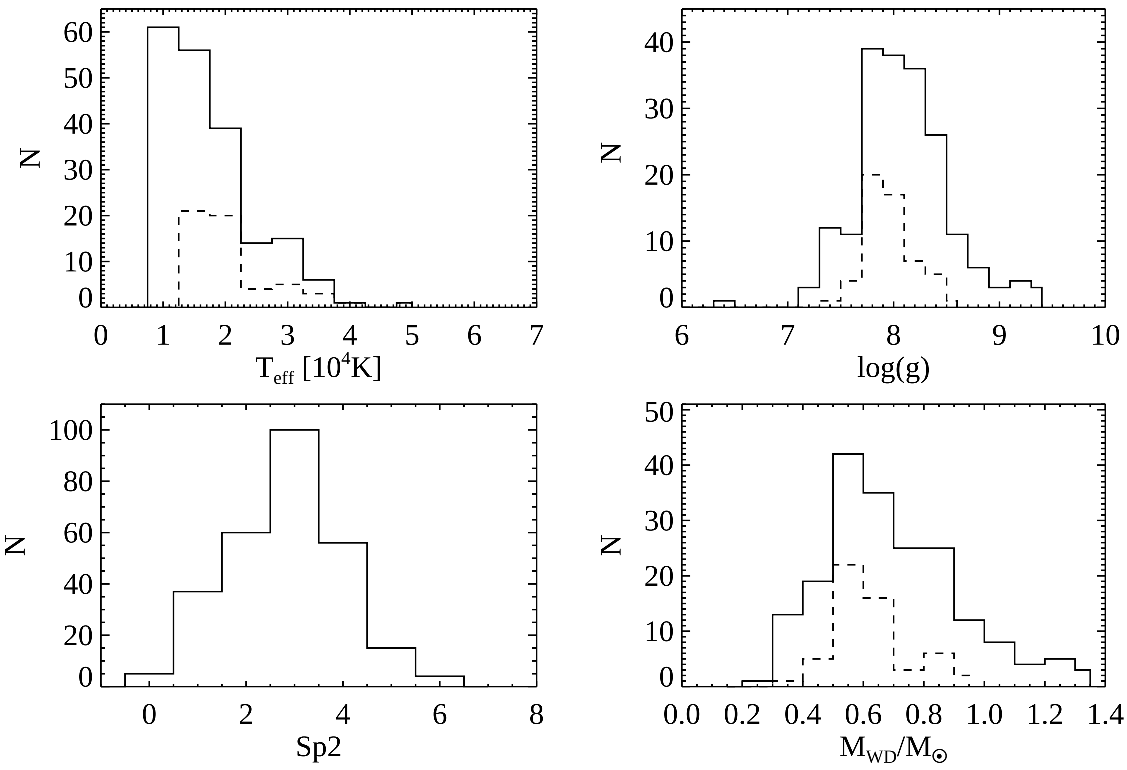

Figure 2.8: The distributions of white dwarf temperatures (upper left), $\log g$ (upper right), secondary star spectral types (lower left) and white dwarf masses (lower right). In all cases except the secondary spectral types we plot only the parameters of WDMS containing DA white dwarfs (solid lines) and the distributions of the primary's parameters for systems with $T_{\rm eff}$ < 12 000 K and with relative errors smaller than 25 % (dashed lines). In general, the white dwarf temperature distribution peaks at ~ 10 000 K i.e. at significantly lower temperatures than in previously published WDMS samples (e.g. Silvestri et al. 2006) but looks quite similar to those of single white dwarfs identified with SDSS (Eisenstein et al. 2006). The distributions of $\log g$ and the white dwarf mass are broader than those of single stars and the expected peaks at $M_{\rm wd} = 0.6 M_\odot$ and $\log g \sim 8$ are less pronounced. Finally, the distribution of spectral types in the bottom left panel is broader than the one published earlier for WDMS from SDSS I (Silvestri et al. 2006) and peaks at $M3$ instead of M4. Comparing our distribution with those of single low mass stars (West et al. 2004) we find general agreement for systems later than M3 but our sample contains less systems with M0 – M2 companions.

is drawn with a dashed line. Apparently, the two distributions are quite similar, the peak at low temperatures is only slightly less pronounced for the white dwarfs in the SEGUE binaries. The single star distribution also has a larger tail extending to very high temperatures which we don't see in the SEGUE WDMS sample as most systems containing hot white dwarfs are excluded by our color cuts (see Sect. 2.2.3).

Silvestri et al. (2006) studied a sample of 747 WDMS and estimated the temperature of the

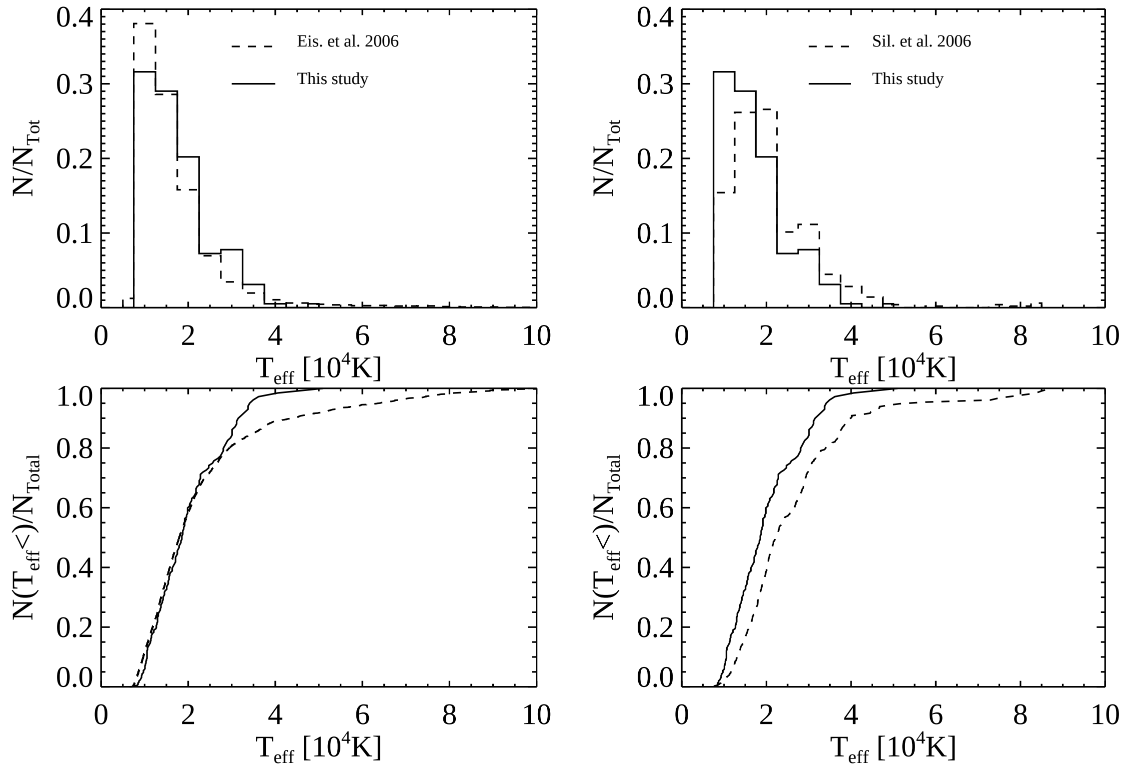

Figure 2.9: Comparison of the SEGUE-WDMS white dwarf temperatures (solid lines) with those of single SDSS white dwarfs (Eisenstein et al. 2006) (left, dashed lines) and with the sample from Silvestri et al. (2006) (right, dashed lines). The upper panels show normalized distributions to the maximum. The bottom panels show the cumulative distribution functions. While the distribution of the SEGUE WDMS white dwarf temperatures is very similar to the distribution obtained by Eisenstein et al. for single white dwarfs, the previous sample of SDSS WDMS binaries contains significantly less systems with cold white dwarfs.

DAs in their sample in a similar way (but see Rebassa-Mansergas et al. 2007, for a more detailed comparison of the applied methods). The temperature distribution of their sample peaks at 20 000 K, while ours peaks around 10 000 K (see Fig. 2.9 left panel). While different to the SEGUE and the single star sample at low temperatures ($T_{\rm eff,WD} \lesssim 20\,000$ K), the sample presented by Silvestri et al. resembles the single star distribution at higher temperatures.

Another way of representing and comparing the data is using cumulative distributions. In the bottom panels of Fig. 2.9 we show the cumulative distributions of our sample (solid line) and those from Eisenstein et al. (2006) (left panel) and from Silvestri et al. (2006) (right panel) (both plotted with dashed lines). To compare in a quantitative way the $T_{\rm eff}$ of the different datasets we made use of the Kolmogorov-Smirnov statistics (KS-test) [7]. The KS-test for systems between

[7]The KS-test compares two distributions without assuming an underlying distribution of the data and tries to

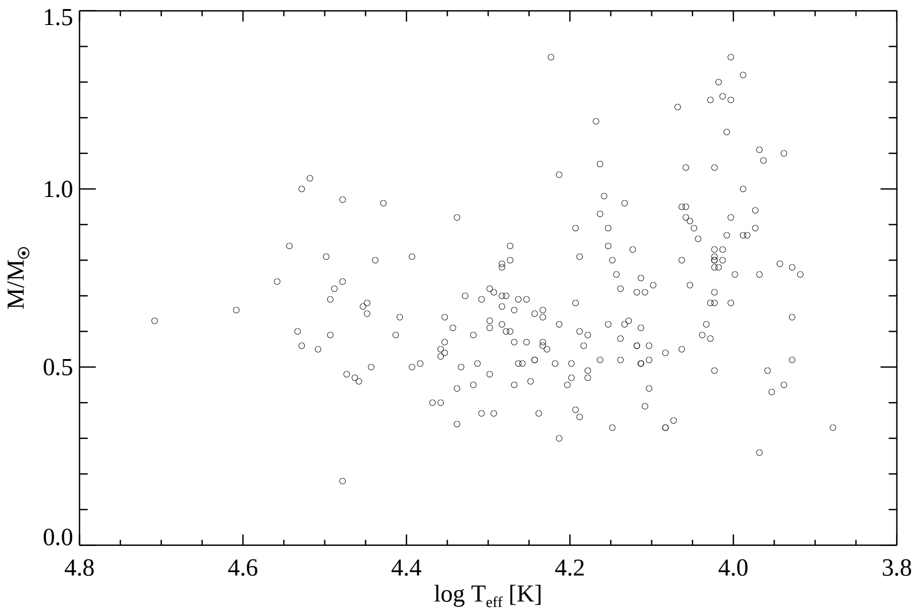

Figure 2.10: White dwarf masses versus $T_{\rm eff}$ for the sample of 193 WDMS that contain DAs.

7 500 K and 50 000 K gives a maximum deviation for the cumulative functions of 0.12 between this study and Eisenstein et al. (2006) at a significance level of 2σ and of 0.21 between our sample and the one from Silvestri et al. (2006) at a significance level of 4σ. If we select systems with higher temperatures than 10 000 K, then the KS-test gives a maximum distance of 0.07 in the cumulative distributions between this study and Eisenstein et al. (2006) and a significance of 39%. While the result between our sample and the one from Silvestri et al. (2006) is 0.19 and 3σ for the distance and for the significance level respectively.

The above result clearly shows that our selection criteria works as expected and we reached one of our main goals: the SEGUE WDMS sample is significantly less biased with respect to white dwarf temperatures (i.e. to the age of the systems) than previous samples of SDSS-WDMS.

2.5.2 White dwarf masses and $\log g$

The distribution of the masses of the 193 DA white dwarfs primaries in our sample is given in the lower right panel of Fig. 2.8. Compared to the recent analysis of single SDSS white dwarfs by De Gennaro et al. (2008) the mass distribution of the white dwarfs in the SEGUE WDMS is

determine if the datasets differ significantly and if they come from the same distribution. The parameter D gives the maximum distance between the two comulative functions, $0 < D < 1$, so that when the two datasets come from the same distributions the value of D trends to zero. The probability gives the significance level of the KS-test at which the compared distributions are different.

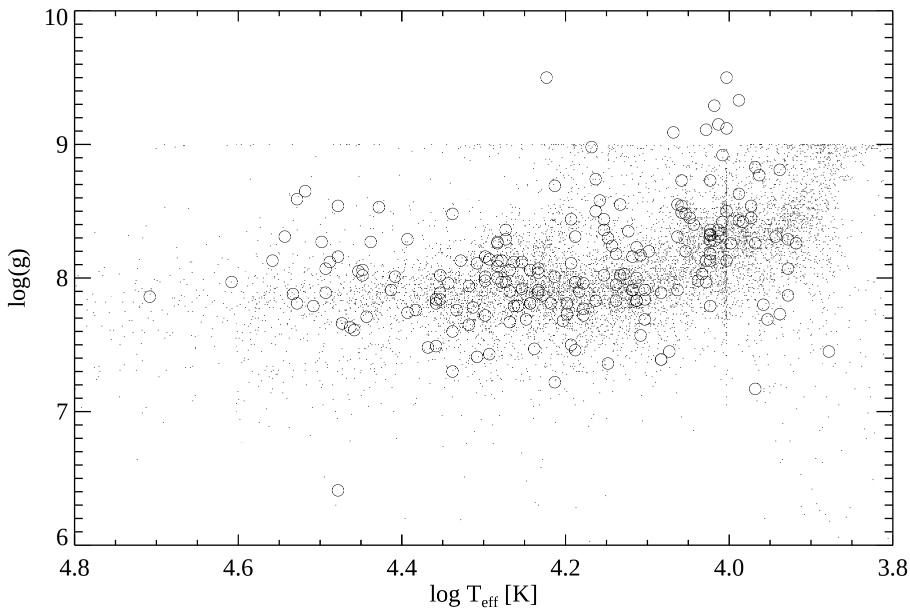

Figure 2.11: White dwarf $\log g$ versus $T_{\rm eff}$ for the sample of 193 WDMS that contain DAs (open circles) and that one of Eisenstein et al. (2006) (dots).

significantly broader, i.e. the peak at $M_{\rm wd} \sim 0.6 M_\odot$ is less pronounced. This difference is partly explained by the fainter limiting magnitude in our sample that implies a larger uncertainty of the white dwarf masses in our sample which directly transform into a broader distribution.

The mean mass of the entire sample is $M_{\rm wd}$= 0.69 and has a standard deviation of 0.23 $M_\odot$, while the peak is at a significantly lower mass, 0.59 $M_\odot$ with a FWHM of 0.47 $M_\odot$(see Fig. 2.12). Liebert et al. (2005) draw the $M_{\rm wd}$ distribution for a sample of 348 white dwarfs, covering a temperature range from 100 000 K to 7 000 K. They find a mean of 0.603 ± 0.134 $M_\odot$ and a peak at 0.572 $M_\odot$, with a FWHM of 0.188 $M_\odot$. Our values differ significantly from these, being in all cases superior. The high mass tail of our $M_{\rm wd}$ distribution is dominated by WD with low temperatures (see Fig. 2.10). If we select systems with $T_{\rm eff}$ larger than 12 000 K the mean of the 135 left systems is 0.62 ± 0.19 $M_\odot$, the peak shifts to 0.54 $M_\odot$ and the FWHM is then 0.35 $M_\odot$(see Fig. 2.12), a bit narrower but still broader than for single white dwarfs. The tail towards massive white dwarfs is then less significant. And if we also restrict to systems with uncertainties in the white dwarf parameters of less than 25% (see Fig. 2.8) then the mean based on 55 systems is 0.61 and it's standard deviation is 0.12 $M_\odot$, value closer to that found by Liebert et al. (2005).

In Fig. 2.11 we compare the $\log g$ versus effective temperature distribution with that one of field white dwards from Eisenstein et al. (2006). Eisenstein et al. (2006) cut their distribution at $\log g = 9$ so for higher gravities we can not compare our results. Still we can see that for lower effective temperatures of teh white dwarf the gravity seems to be correlated with it. For white dwarfs with effective temperature higher than around 12 500 K the gravity becomes independent

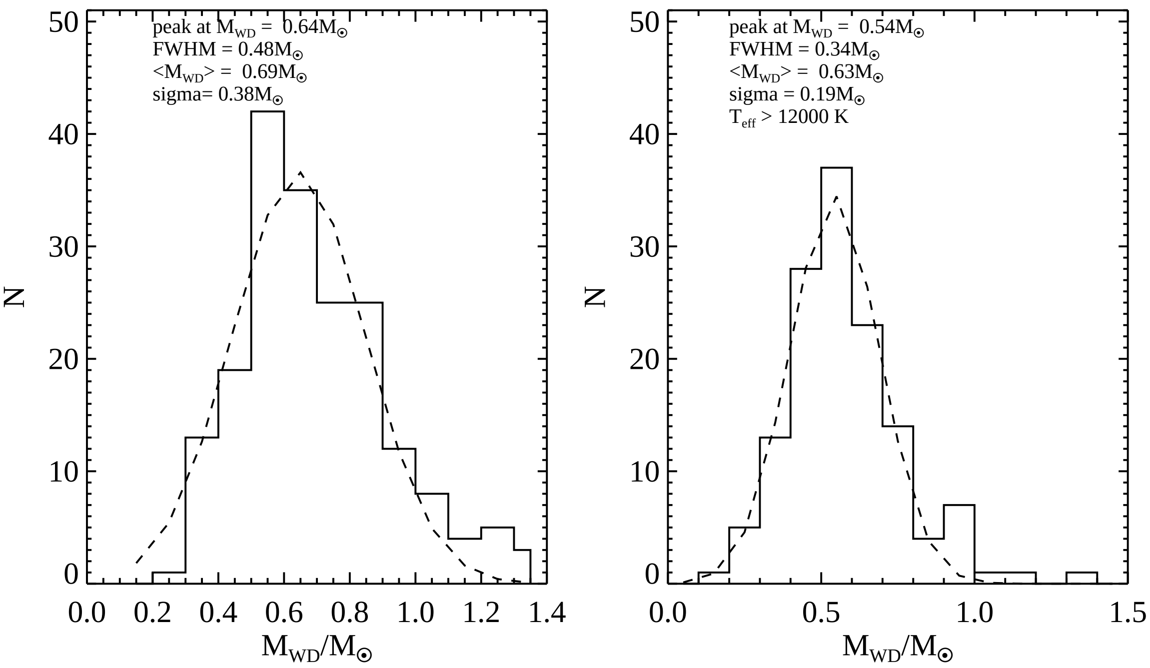

Figure 2.12: White dwarf masses for the entire sample (left) and for systems with $T_{\rm eff}$< 12 000 K. Gaussian fits are over-plotted with dashed lines and each plot contains information about the position of the peak, the FWHM, the mean mass and the standard deviation.

as expected. White dwarfs with temperatures between 25 000 K and 12 500 K in our sample are distributed as field white dwarfs. Hotter systems than 25 500 K seem to have high masses again. This might be a bias introdued by our selection criteria and further investigation should be carried out.

In Fig. 2.13 we compare the obtained values of $\log g$ of the SEGUE WDMS white dwarfs with the single white dwarf distribution of Eisenstein et al. (2006), shown in the left panels, and the WDMS sample of Silvestri et al. (2006) in the right panels. In the upper panels we show the distributions normalized to the maximum and in the bottom panels the cumulative distributions. We draw our distributions with solid lines and with dashed lines the other two samples. In general, the three distributions are quite similar the only significant difference being the tail towards high values of $\log g$ that we find but which is missing in the other two distributions.

The KS statistics between our distribution and the one of Eisenstein et al. (2006) gives 0.1 for the maximum distance between the cumulative distributions and a significance level of 2%. Between ours and the one from Silvestri et al. (2006) the KS statistics gives 0.3 and almost 0 % for the significance level. We computed the KS statistic again using only those systems with $T_{\rm eff}$> 12 000 K and with $7 < \log g < 9$. It gives a maximum distance between both cumulative distribution functions of 0.08 and a 27 % significance level when comparing with Eisenstein et al.

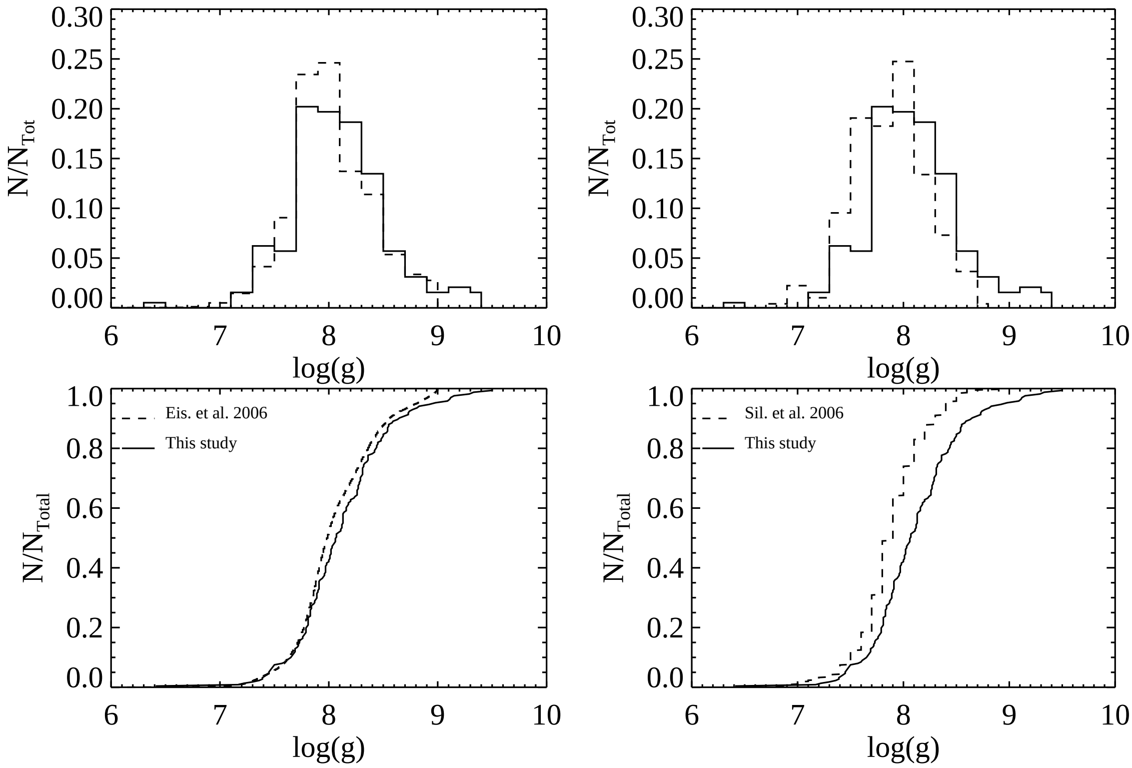

Figure 2.13: Comparing $\log g$ of the SEGUE-WDMS white dwarfs with those of single SDSS white dwarfs (Eisenstein et al. 2006) and previous WDMS samples (Silvestri et al. 2006). The SEGUE WDMS distribution looks similar to both distribution but is slightly broader and contains more high gravity white dwarfs.

(2006), and 0.54 and almost 0 % significance level when comparing with Silvestri et al. (2006). We conclude that the observed long tail at high masses is due to systems with WDs with low temperatures, and according to Kepler et al. (2007) one should not trust the inferred masses for those systems.

2.5.3 Secondary star spectral types

The spectral type distribution of the secondary stars of our WDMS binary sample is shown in the lower right panel of Fig. 2.8. The spectral type distribution covers the range from M0 to M6. The number of systems at a given spectral type increases until spectral type M3, where it reaches a maximum, and then declines towards later spectral types, being rather symmetric. There are no WDMS binaries containing secondaries with earlier spectral type than M0 nor later than M6 as a natural consequence of our selection criterium (see Sect. 2.2).

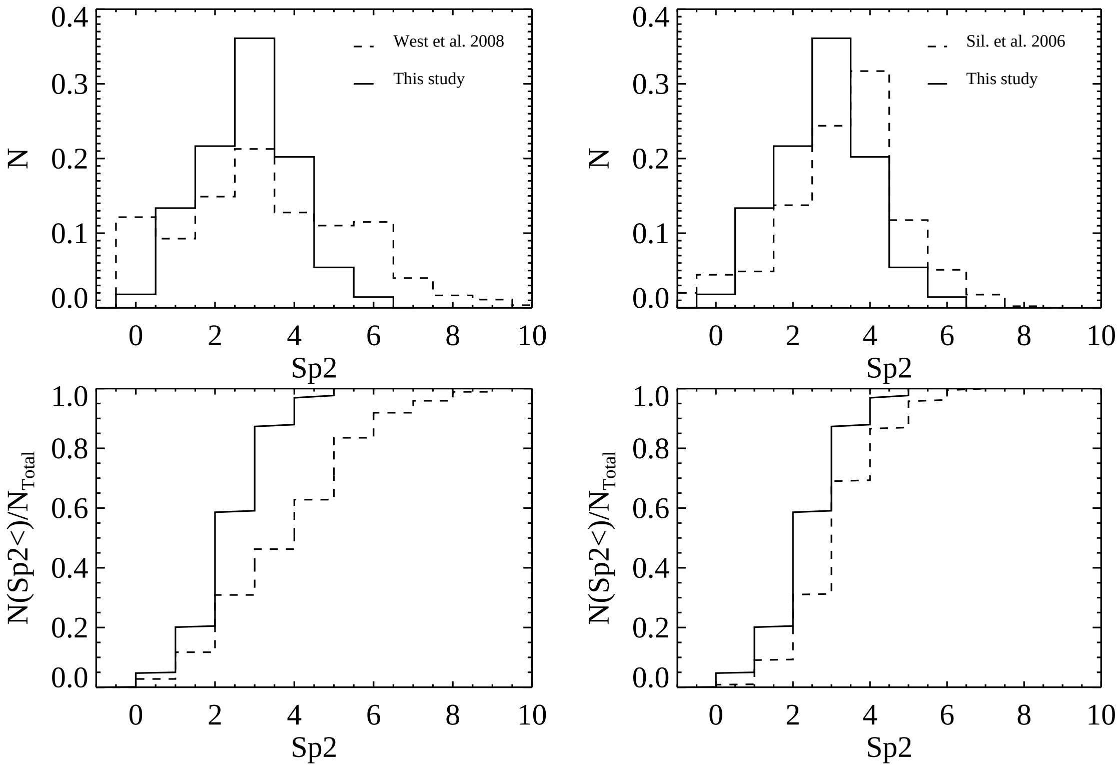

Figure 2.14: Comparing the spectral type of the secondary stars of the SEGUE-WDMS with those of single SDSS (West et al. 2008) and previous WDMS samples (Silvestri et al. 2006). The SEGUE WDMS distribution looks similar to the distribution of Silvestri et al. (2006) but with more early type secondaries.

We compared the spectral type distribution with single dM stars from West et al. (2008) and with the WDMS binaries from Silvestri et al. (2006), see Fig. 2.14. We find that the secondary spectral type distribution of our sample of WDMS binaries is narrower than for single dM stars (see left panel of Fig. 2.14), but broader than the distribution drawn for a sample of WDMS binaries by Silvestri et al. (2006). The peak at M3 is also present in field dM stars, while for the previous sample from Silvestri et al. (2006) it shifts to M4. Our sample compared with that of single low mass stars contains less systems with M0 – M2 and late type companions. This indicates that our sample is still biased towards low mass secondaries. But we find more early type secondaries than in previous WDMS binary samples, hence, the goal of our target selection algorithm to establish a WDMS sample less biased towards late type secondary stars has been reached.

To compare the distributions in a quantitative manner we performed χ^2-tests. We obtained a value of 101.47 when comparing with the distribution from West et al. (2008), and 97.10 when comparing with Silvestri et al. (2006). So it seems that our distribution is very likely to be different from that one of field M stars and from that one from the sample from Silvestri et al. (2006). Biases in our distribution are still present, and their influence is discussed in detail in Sect. 2.6,

2.5.4 Distances

We compare the two distances derived from our deconvolution process, $d_{\rm sec}$ and $d_{\rm wd}$. It seems that there are two trends, systems with $d_{\rm wd} > 500$ pc seem to have systematically $d_{\rm wd} > d_{\rm sec}$, while the opposite is true for systems with $d_{\rm wd} < 500$ pc. A significant fraction of the systems has $d_{\rm sec} > d_{\rm wd}$ by more than 1.5σ (red dots in Fig.2.15, similar results have been obtained previously by Rebassa-Mansergas et al. (2007) and Schreiber et al. (2008). Activity faking a too early a spectral type which leads to a too large distance estimate has been suggested as the cause of this trend by (Rebassa-Mansergas et al. 2007).

To explain the opposite trend at larger distances, we first did take into account the effect of reddening in our estimates of the distances. We used Schlegel dust maps (Schlegel et al. 1998) [8] to derive the extinction for each system and applied a correction to the distance. Of course, since the extinction values in Schlegel's map only depend on the galactic latitude and longitude (and not on the distance), the distance corrections should be interpreted as an upper limit on the effect of extinction on the distance determination. As nearby stars are less affected by reddening, we applied the reddening correction only to systems with $d_{\rm wd} > 500$ pc. Inspecting the left panel of Fig.2.15 we see that the effect in some cases is far from being negligible but it can certainly not explain the observed discrepancy.

In the right panel of Fig. 2.15 we compare $d_{\rm wd}$ and $d_{\rm sec}$ for those sytems having system parameters with errors less than 25%. Here, the effect of reddening was not taken into account, since most of the remaining systems have $d_{\rm wd} < 500$ pc and correcting for the galactic reddening would probably lead to underestimating the distances. Apparently, in the right panel the discrepancy at large distances disappears thereby indicating that at very large distances the parameters from fitting the white dwarf spectrum are not reliable. In contrast, the disagreement at short distances remains. This means that the larger values of $d_{\rm sec}$ are not caused by uncertainties related to noisy spectra which is in agreement with the interpretation that magnetic activity is causing the effect (see above and Rebassa-Mansergas et al. 2007).

2.5.5 Secondary masses

As shown e.g. in Rebassa-Mansergas et al. (2008) and as just discussed in the context of our distance estimates, activity seems to make a significant fraction of late type secondary stars appearing as an earlier spectral type than secondaries with the same mass but without magnetic activity. In these cases the empirical mass-spectral type relation by (Rebassa-Mansergas et al.

[8] http://www.astro.princeton.edu/ schlegel/dust/

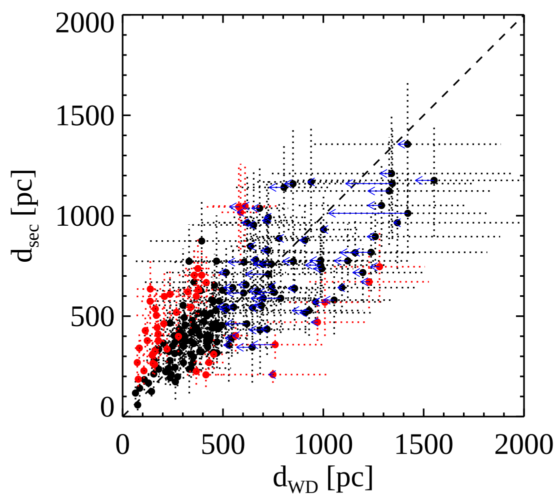

Figure 2.15: Left: distances obtained for the WDMS that contain DA white dwarfs in our sample, based on spectral fits to the white dwarf $d_{\rm wd}$, and on the spectral fit to the secondary star $d_{\rm sec}$. As noted earlier in Rebassa-Mansergas et al. (2007); Schreiber et al. (2008); Rebassa-Mansergas et al. (2008) about 30% of the d_2 distances appear to be too large when compared to $d_{\rm wd}$. This is probably caused by magnetic activity in late type M-dwarfs. For systems at larger distances we here observe another effect, i.e. $d_{\rm wd}$ appears to be larger than $d_{\rm sec}$ at distance exceeding ~ 500 pc. This is only partially caused by reddening which makes especially distant white dwarfs appearing more distant than they actually are. Correcting for this reddening effect results in slightly shorter distances as displayed by the blue arrows. Right: The distribution of distances for systems with errors smaller than 25%. Apparently, the agreement between the two distances is much better. More specifically, there is no longer a discrepancy at larger distances while the effect of having $d_{\rm sec} > d_{\rm wd}$ for about 30% of the systems at shorter distances remains.

2007) leads to systematically overestimating the secondary mass and consequently also to distance estimates that are systematically too large (see Fig. 2.15).

In Nebot Gómez-Morán et al. (2009) we have developed and applied a possible way out of this problem based on information provided in the 2MASS data base. We find entries in the 2MASS catalog (Cutri et al. 2003) with photometric quality flags set to 'AAA' for 105 systems with DA primary star. We derive the masses of the secondary stars using the empirical mass K-luminosity relation from Delfosse et al. (2000), assuming $d_{\rm wd}$ as the distance to the system and subtracting the contribution of the white dwarf to the luminosity in the infrared (see chapter 6 for a detailed description of the method). The derived masses from 2MASS are compared with the masses obtained from the empirical spectral type-mass relation from Rebassa-Mansergas et al. (2007) in Fig. 2.16, in the left panel we show all the systems while in the right panel we plot only those with relative errors lower than 25% in the white dwarfs parameters. The Sp2-mass relation seems to be overestimating the masses of the secondary stars for masses lower than $0.35M_{\odot}$, consistent with the 'activity hyphothesis', while the opposite trend is seen for masses

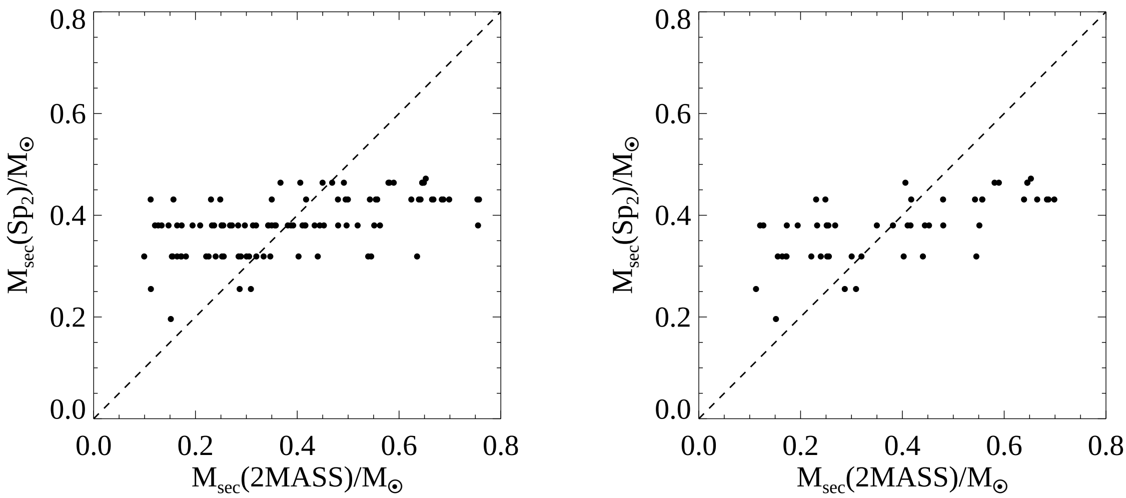

Figure 2.16: Comparison of the obtained secondary star masses from K-luminosity relation and the empirical spectral-type mass relation Rebassa-Mansergas et al. (2007). For low values $M_2(2MASS) \lesssim 0.35 M_\odot$ the masses obtained from the spectral type–mass relation are systematically larger while the opposite is true for $M_2(2MASS) \gtrsim 0.35 M_\odot$. The discrepancy at low masses could be explained by activity in late type stars and we therefor consider the $M_2(2MASS)$ values to be more reliable in this mass range.

larger than 0.35. This is probably related to the fact that more massive secondary stars are found at larger distances where the parameters for the white dwarf derived from spectral fitting become uncertain. From this study it becomes obvious the necessity of a better estimate of the masses in low mass stars. Eclipsing systems are very important in this context since we can contrain the radii and masses of the secondary stars accurately (see chapter 6).

2.6 Completeness

As described in Sect. 2.2.3 our color selection has been designed to detect WDMS containing cold white dwarfs ($\sim 10\,000 - 20\,000$ K) and these become hardly detectable in color-space for secondary stars earlier than $\sim M3 - M2$ (see also Sect. 2.5.3). As a consequence our sample is biased towards old systems containing late type secondary stars. The bias towards old systems has been a goal of the survey and the bias towards late type secondary stars is at least smaller than in previous samples. In this section we analyse how this bias relates to distances.

Our limiting g magnitues, $15 \leq g \leq 20$ imply distance limits to detect a WDMS system for a given set of stellar parameters. These distance limits mainly depend on the white dwarf temperature and the secondary star spectral type. Following our approach in Sect. 2.2 we calculate for different white dwarf temperatures and secondary spectral types the distance at which

$g = 20$ and $g = 15$. The values obtained for the mass of the white dwarf and its effective temperature can be used to calculate the age of the WDMS binary by interpolating the cooling tracks by Wood (1995). Fig. 2.17 shows the lower and upper distance limits as a function of age for different secondary star spectral types. As mentioned above, our color selection citeria preferentially select old white dwarfs with late type secondary companions. Of such binaries (lower magenta and blue lines) only very nearby ($d \lesssim 50$ pc) systems are excluded by the lower distance limit (resulting from $g \geq 15$). The upper distance limits (upper lines) are significantly decreasing with increasing age of the WDMS binary (i.e. decreasing temperature of the WD) especially if little is contributed by the secondary in the g-band, i.e. if the secondary is a late spectral type. In other words, for old white dwarfs ($\gtrsim$1 Gyr) with a M6 (M4) secondary star, the magnitude limit of $g \leq 20$ implies a distance limit of $d \lesssim 200$ pc ($d \lesssim 500$). This effect is displayed in Fig.2.18. With increasing distance earlier spectral type secondary stars are detected (top and middle panel). These systems contain systematically hotter white dwarfs than the nearby WDMS (bottom panel of Fig. 2.18).

To summarize, the combination of our color selection criteria and the SDSS magnitude limits favours the detection of rather nearby ($d \lesssim 500$ pc) WDMS that contain cold white dwarfs and late type secondary stars. However, as WDMS systems containing cold white dwarfs should represent the vast majority of all WDMS binaries, we should be able to at least derive reasonable lower limits on the space density of WDMS.

2.7 The galactic WDMS population

In this section we base our analysis on the DR7 database. Please note that this excludes two WDMS systems (SDSSJ135643.56-085808.9 and SDSSJ135930.96-101029.7) that have been found on plate 2716 which is not included in DR7 (see http://www.sdss.org/dr7/start/aboutdr7.html).

2.7.1 Space density

To estimate the space density we performed a detailed analysis of our success rates for each plate-pair based on the CAS database DR7. Table 2.2 gives the most important numbers for each plate-pair that contained SEGUE-WDMS color-selection. $N_{\rm cand}$ is the number of candidates, i.e. the number of systems with ugriz colors obeying our selection criteria and with clean photometry flags. $N_{\rm spec}$ gives the number of candidates that have been observed spectroscopically. In some rare cases we find objects that got a spectrum although their flags indicate photometric problems. This is probably caused by changes in the photometry pipeline after the target selection process. In the very few cases were this happened, the missing system is added to the list of candidates. The total number of spectroscopically identified WDMS is given by $N_{\rm WDMS}$. Please note that some early plates (plate numbers < 2377) have been accidently observed with a target selection algorithm based on reddening corrected colors. On these plates we therefore find some WDMS

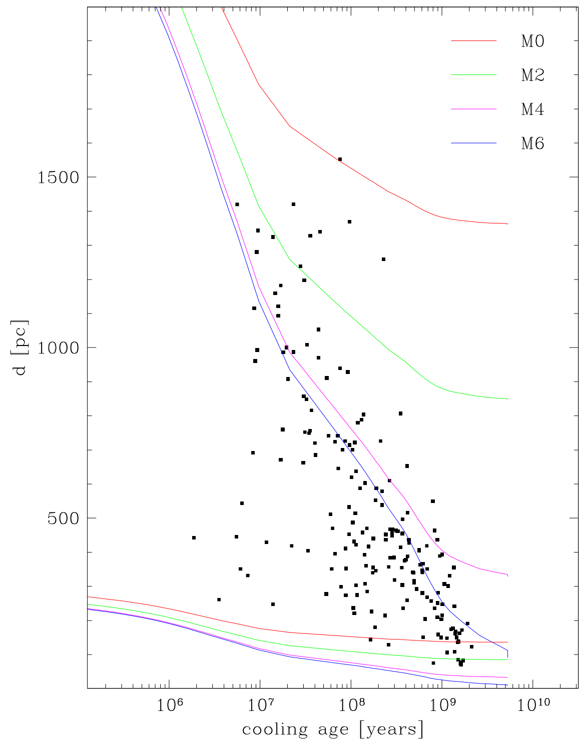

Figure 2.17: The 193 DA WDMS of our sample in the distance-age plane. Using the approach described in Sect. 2.2.3 we calculated distance limits corresponding to the magnitude limits $15 \leq g \leq 20$ for different secondary spectral types as a function of white dwarf age (i.e. decreasing white dwarf temperature). Apparently, systems older than 1 Gyr containing late type companions are only detected up to distances of $\sim$ 400 – 500 pc.

systems that are outside our color criteria. The number of these systems is given by $N_{\rm out}$. The success rate of our target selection is hence given by $(N_{\rm WDMS}-N_{\rm out})/N_{\rm spec}$ and the intrinsic number of WDMS can be estimated by multiplying the success rate with the number of candidates for each plate. Dividing this number by the volume of the spherical sector finally gives the local space density. The volume of the spherical sector V, of course, depends on the distance that actually defines the survey volume. In the previous section we have shown that our selection criteria select mostly old systems with late type secondary stars and that this implies a selection effect even at rather short distances $d \lesssim 100-200$ pc. Defining the survey volume is therefore not straight forward. If we use a very short distance, the involved selection effects decrease but our estimates are based on quite a few WDMS detections and the statistical error increases. If, on the other hand, a large distance is assumed (e.g. $d \sim 1000\,pc$) the statistical error decreases but the selection effects begin to strongly influence our results leading to very much underestimating the space density. We performed a KS-test between the effective temperature distributions drawn for systems at larger distances than 500 pc and at closer distances to see whether they are similar

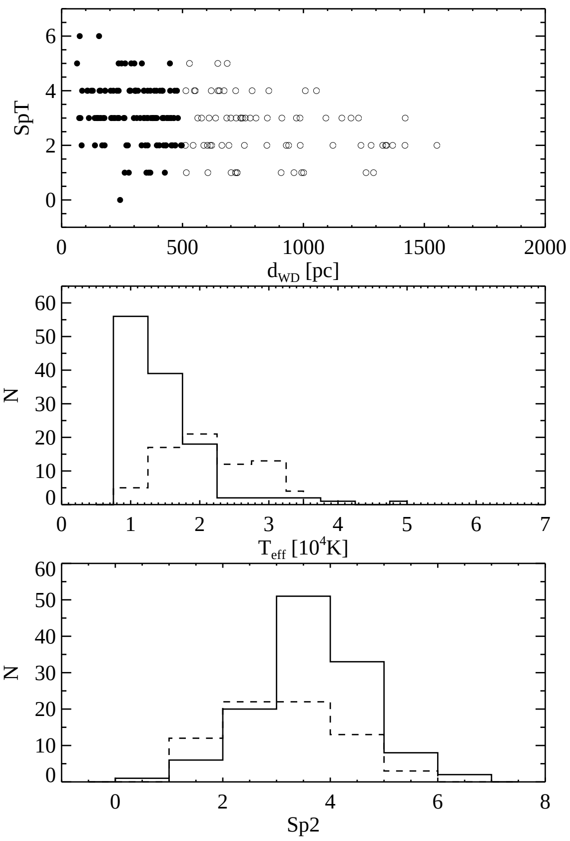

Figure 2.18: Relations between distance, secondary star spectral type and white dwarf temperature. With dashed lines are shown those systems with distance estimates exceeding 500 pc. As discussed in Sect. 2.6 the combination of our color selection and magnitude limits favours the detection of systems containing cold white dwarfs, that are nearby, and have late type secondary stars.

or not. We obtained a maximum distance in the cumulative function of 0.25 at a significance level of 0.4 %. We performed a KS test for the spectral type distributions as well and obtained a distance of 0.54 at a significance level of $\sim$ 4 % . From this analysis and inspecting Fig 2.17 and 2.18 we think that assuming $d = 500$ pc is a reasonable compromise: we detect WDMS with secondary spectral types later than M3 and 63% of the identified WDMS are closer than $d = 500$ pc. The space density is then given by

$$\rho = \frac{(N_{\mathrm{WDMS}} - N_{\mathrm{out}})N_{\mathrm{cand}}}{V\,N_{\mathrm{spec}}}. \tag{2.1}$$

Estimates of the space density can be obtained for each plate by inserting the numbers for a given plate-pair. The space density of SEGUE-SDSS, shown in Fig. 2.19, varies from $\sim 2\times10^{-4}$ at low galactic latitudes to $\sim 2\times10^{-5}$ at higher galactic latitudes. The mean space density can be derived by averaging the space densities of all plates and we obtain $\rho = 3.33\times10^{-5} \pm 6.6\times10^{-6}\,\mathrm{pc}^{-3}$. In Fig. 2.19 we show success rates and space densities for each plate pair as a function of galactic latitude and $E(B-V)$.

The obtained space densities are smaller than the values predicted by Willems & Kolb (2004) ($10^{-3}-10^{-4}\,\mathrm{pc}^{-3}$). However, one should keep in mind that the predictions of Willems & Kolb (2004) have been made for the entire WDMS population ranging from short orbital period post common envelope binaries to very wide systems and covering the whole range of possible secondary star masses. In contrast our SEGUE-WDMS sample is subject to serious biases and selection effects. First of all, based on *ugriz* colors it is impossible to detect white dwarf companions to secondary spectral types earlier than M0 but such systems certainly represent a significant fraction of the WDMS population simulated by Willems & Kolb (2004, their Fig. 10). Second, a significant fraction of wide WDMS are resolved by SDSS imaging and are hence not in our sample. Willems & Kolb (2004) give an upper limit of the PCEB fraction of 25% while Schreiber et al. (2008) obtain 35% from radial velocity studies of SDSS WDMS. This implies that only $\gtrsim$30% of the intrinsic WDMS population is resolved in the SDSS imaging data base. Taking into account the two effects just mentioned, our results are in agreement with those of binary population studies.

2.7.2 Spatial distribution

As WDMS binaries certainly form a relatively old stellar population they should be concentrated towards the Galactic plane and the space density ρ of WDMS should exponentially decrease with the height above the Galactic plane z, i.e. $\rho \propto exp(-z/h)$ where h is the typical scale height of the population. Both plots on the right hand side of Fig. 2.19 show the expected steep decrease of the space density for increasing galactic latitude. In the lower right panel the error bars for low galactic latitudes are quite large as the obtained values depend on few WDMS (N_{WDMS}) detections among large numbers of candidates (N_{cand}). The dashed lines in the bottom right panel show calculated space densities as a function of galactic latitude assuming a limiting distance of $d = 500\,\mathrm{pc}$, and three different scale heights: 100, 150, and 200 pc. Keeping in mind the large uncertainties of the measured values of the space density close to the galactic plane we conclude that the SEGUE WDMS population agrees best with scale heights of $h = 100-150\,\mathrm{pc}$. This result appears to be reasonable as similar values have been obtained for cataclysmic variables (CVs) (Patterson 1984; Ak et al. 2008) and late type stars (Vallenari et al. 2006).

2.8 Summary

The SEGUE WDMS survey differs from SDSS I WDMS surveys in the applied color-selection algorithm. The SEGUE WDMS search has been especially designed to identify WDMS systems containing cold white dwarfs. In addition, SEGUE covered a much broader range of galactic latitudes. We here present 277 new white dwarf/main sequence binaries and 24 candidates identified with SEGUE. We characterized the sample using spectral decomposition techniques, discussed

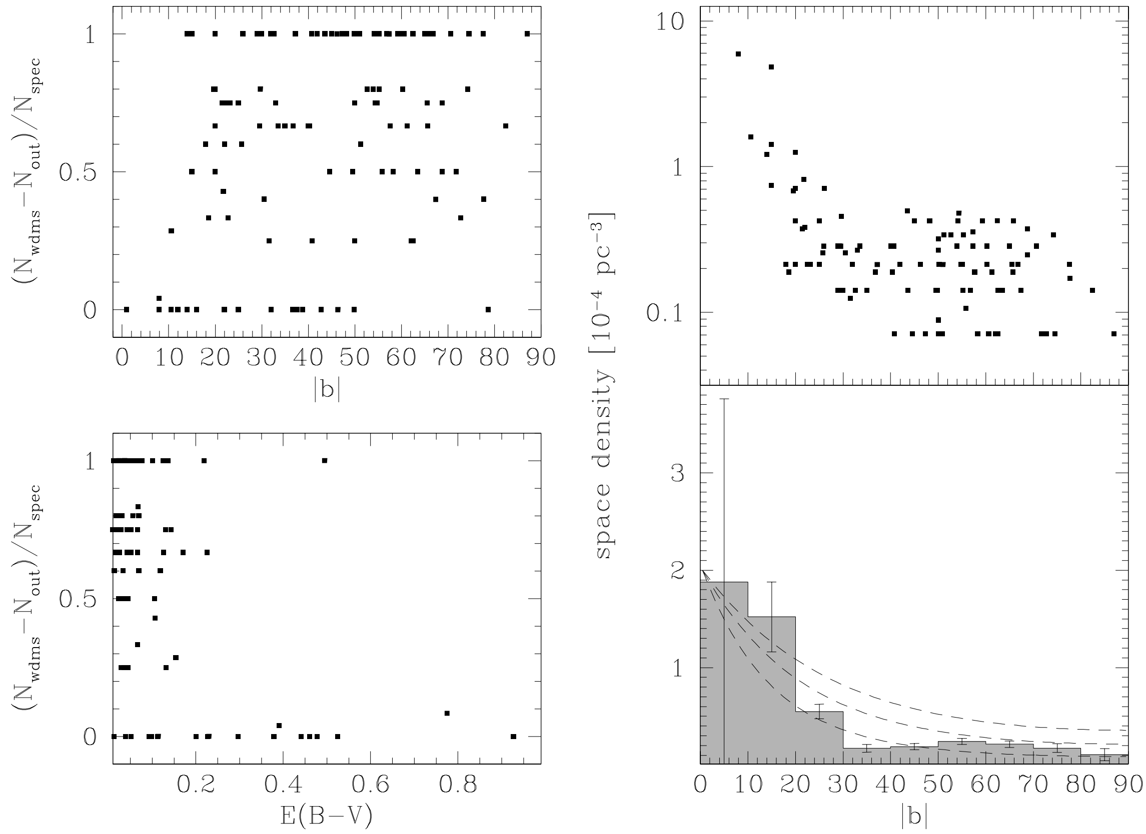

Figure 2.19: Left: success rates as a function of galactic latitude and $E(B-V)$. The squares in the top panels and the lower left panel represent values derived for single plate-pairs as given in Table 2.2. The success rate is on average slightly better for low $E(B-V)$ and high galactic latitudes. Right: Space densities as a function of galactic latitude for each plate (top) and a binned distribution (bottom). In the top panel only values that differ from zero (i.e. those with at least one WDMS detection) are shown. The histogram in the bottom panel gives space densities averaged over a given range in $|b|$. As expected, the derived space densities increase towards the galactic plane. Also shown (dashed lines) are calculated space densities assuming an exponential distribution, a limiting distance of $d = 500$ pc, and scale height of $h = 100$, 150, and 200 pc.

the obtained distributions, and derived plausible values for the space density and the scale height. The main results of this analysis can be summarized as follows.

- As expected, our sample contains significantly more old systems than SDSS I. The combination of our color selection and the magnitude limits of SDSS causes our sample to be biased towards cold white dwarfs and late type secondary stars that are relatively nearby $d \lesssim 500$ pc.

- The space density of WDMS inside our selection criteria is $\sim 2\times10^{-4}\,\mathrm{pc}^{-3}$ and decreases to $\sim 2\times10^{-5}\,\mathrm{pc}^{-3}$ at higher galactic latitudes.

- The space density of SDSS WDMS increases significantly towards the galactic plane in agreement with a scale height of the galactic population of WDMS binaries of $100-150$ pc. This value is similar to values estimated previously for the population of cataclysmic variables and late type stars.

Chapter 3

Post common envelope binaries from SEGUE

White dwarf/main sequence binaries are perfect laboratory systems for testing current theories of angular momentum loss and constrain the efficiency of the common envelope phase. Using a sample of white dwarf/main sequence binaries We test the disrupted magnetic braking law that has been questioned in the last years. From a statistical analysis of the radial velocities measured from the SDSS sub-exposures of the 277 (plus one candidate) white dwarf/main sequence binaries with stellar parameters derived in chapter 2 we select those that have gone through a common envelope phase. We derive a lower limit of $\sim$ 13 % to the post-common envelope fraction of white dwarf/main sequence binaries. The number of PCEBs decreases with increasing mass of the secondary star, and has a drop of 15% at the boundary where the secondary star becomes fully convective. This indicates that the angular momentum loss is less efficient at later spectral types, and according to predictions of binary population synthesis studies, in agreement with the disrupted magnetic braking law, firstly proposed to explain the orbital period gap between 2 and 3 hours in the orbital period distribution of cataclysmic variables.

3.1 Introduction

The orbital period distribution in cataclysmic variables (CVs) extends from $\sim$ 1 hour to $\sim$ 10 hours and presents a gap between 2-3 hours. To explain the observed orbital period distribution of CVs one needs to know which are the mechanisms involved in angular momentum loss. Above the orbital period gap the main mechanism leading to an angular momentum loss is magnetic braking (MB). The main idea of MB is that dynamo processes generate magnetic fields which are responsible of the spin-down of stars with age. Ionized material is coupled to the large scale magnetic field lines. Small amounts of mass are carried away in the magnetized stellar wind to large distances, carrying with it more angular momentum than it had at the surface, and slowing down the star (Verbunt & Zwaan 1981). Below the period gap (2 hours) gravitational radiation is responsible for bringing the systems closer ($\dot{J}_{GR} \propto \omega^{(7/3)}$). To explain the period gap (only 10% of all the CVs are inside this region) it has been proposed that, since the dynamo changes once the star becomes fully convective (around spectral type M3), for later spectral types, which have no tachocline[1] magnetic braking would be inefficient ($\dot{J}_{DMB} \propto \omega^3$ for $M > M_{conv}$, $\dot{J}_{DMB} = 0$ for $M < M_{conv}$), the so called disrupted magnetic braking (DMB) model (Rappaport et al. 1983).

Observations from field stars and open clusters seem to disagree with the DMB model. Delfosse et al. (1998) studied a sample of field M dwarfs and showed that only late spectral types have a measurable rotation, $v \sin i > 2-3$ km/s, and that young disk stars rotate faster than old disk stars. For interpreting this effect they suggested that the spin-down depends on the mass, low mass stars would need more time for decreasing their rotation, varying from few Gyr for M3-M4 to 10 Gyr for M6. They also observed that all fast rotating stars are active, and that the flux from the Hα emission increases with rotation until it saturates at a certain $v \sin i$, remaining constant for higher values. In other words, the flux in Hα is independent of the rotation for fast rotators. They see no clear change in the rotation nor the activity of the stars at the limit when they are fully convective.

Sills et al. (2000) studied a sample of 4 open clusters in the age range 30-600 Myrs and find the DMB overestimates the angular momentum loss as given by Rappaport et al. (1983) at high rotation rates. They give an empirical AML law that fits the data better in the form $\dot{J} \propto \omega^3$, when the rotation is lower than ω_{crit} and $\dot{J} \propto \omega$ for faster rotations, the lower the value the longer a fast rotation can last. This model is known as the reduced magnetic braking (RMB). They find that ω_{crit} increases for increasing mass: low mass stars can have fast rotations for a longer time, in agreement with the idea of Delfosse et al. (1998). Since no sharp break in the angular momentum loss rate when the star becomes fully convective is seen, they claim that the DMB model can not be the cause of the period gap, but give no alternative explanation.

Politano & Weiler (2006) proposed a new test for magnetic braking. They calculate the present day population of post common envelope binaries (PCEB) as a function of the secondary star mass assuming different mechanisms of angular momentum loss. Would magnetic braking get disrupted the number of PCEB be different by almost 2 orders of magnitude when the secondary becomes completely convective, around $0.3M_\odot$. They observe a decrease of 38% in the number of PCEBs at the boundary where the secondary star becomes fully convective, since magnetic braking would be more efficient for stars with a radiative core, the remaining systems would be already CVs. The influence of different efficiencies for the CE phase, the α_{CE} parameter, which can be dependent or not on the mass of the secondary star is investigated by Politano & Weiler (2007), finding that the total number of PCEBs is affected by the choice of α_{CE}, but the drop at the fully convection boundary is always present.

The current observed population of PCEBs is very small. The pre-SDSS sample has been analyzed in detail by Schreiber & Gänsicke (2003). They could discuss only 30 systems with determined orbital period and white dwarf temperature (today we know ~ 50, Morales-Rueda et al.

[1]The tachocline is the dividing zone between the radiative core and the convective envelope, where the $\alpha\omega$ dynamo is thought to have its anchor and differential rotation arises.

(2005), and also see table 1.2.2). In the past, PCEBs have been discovered as white dwarfs in the first place, with some evidence for a faint red companion found later. Schreiber & Gänsicke (2003) showed that the current sample of PCEBs is therefore not only small but also heavily biased towards hot white dwarfs and late type secondary star spectral types.

White dwarf/main sequence binaries (WDMS) represent the most numerous compact binaries in the universe. The population of WDMS binaries consists of two types of systems which differ due to their evolutionary history. According to recent binary population synthesis calculations more than 75% are wide binaries in which the stellar components evolve like single stars (Willems & Kolb 2004). Virtually all of the remaining $\lesssim 25\%$ suffered from common envelope evolution when the more massive star left the main sequence. This population of PCEBs represents the largest population of close compact binaries.

Fortunately, a large population of WDMS has been identified since the launch of the SDSS: based on SDSS imaging and some DR 1 spectra Smolčić et al. (2004) identified a new stellar locus in color-color diagrams, i.e. the WDMS binary bridge. Later, the SDSS turned out to be also very efficient in spectroscopically identifying new unresolved WDMS binaries, e.g. Silvestri et al. (2006) published a list of $\sim$ 747 new WDMS binary systems found in SDSS/DR4 and Silvestri et al. (2007) published a list of more than 1200 systems using SDSS/DR5. These WDMS are biased towards hot white dwarfs and as pointed by Politano & Weiler (2006) *their sample is neither well-defined photometrically nor statistically complete and should not be considered as representative of the secondary mass function in PCEBs*.

Recently Rebassa-Mansergas et al. (2009) published the most complete sample of WDMS binaries, with around 1600 WDMS. We have already measured the orbital period of a dozen of those systems (see Rebassa-Mansergas et al. (2008); Schreiber et al. (2008); Pyrzas et al. (2009); Nebot Gómez-Morán et al. (2009)).

In Schreiber et al. (2007) and in chapter 2 we describe a complementary survey, i.e. a dedicated search for old WDMS binaries performed with SEGUE. Using this sample of WDMS binaries we want to test the magnetic braking as suggested by Politano & Weiler (2006). We identified the PCEBs using radial velocities and calculated the fraction of PCEBs among the WDMS sample.

3.2 The data: SDSS subspectra

Since the DR6 of the SDSS (Adelman-McCarthy et al. 2008) access is given to the sub-spectra of which every spectrum is composed. Sub-exposures of up to 25 minutes are taken and coadded to achieve sufficient signal to noise in a single spectrum. We have retrieved the individual sub-exposures of the 277 WDMS systems from chapter 2. In total we have 2048 spectra, that is 7 spectra per object in mean. In Fig. 3.6 we show in the upper panel the frequency of the number of sub-spectra per object. Most of the systems got 5–7 sub-exposures, with a minimum of 2 and up to a maximum of 19 sub-exposures. In the bottom panel we show the time elapsed between the first and the last exposures for each system as a function of the number of sub-exposures. Some systems are observed only during one night, while others are reobserved months later. In general, systems with more sub-exposures are spread over a wider range in time, but there can be up to 8 sub-exposures in one night.

3.3 Post common envelope binary identification

As shown by Rebassa-Mansergas et al. (2007) it is possible to identify PCEBs among WDMS binaries from multiple SDSS spectroscopy, and as shown by Schwope et al. (2009) when the signal to noise in the individual sub-exposures that make a SDSS spectrum is high enough, radial velocities can be measured with sufficient accuracy.

We measured radial velocities by fitting a double Gaussian of fixed separation to the laboratory value of the Na absorption doublet (8183/8194 Å) originating from the atmosphere of the secondary star, plus a polynomial to the normalized continuum. We also measured the radial velocity from the Hα by fitting a polynomial, representing the underlying continuum, plus a Gaussian for the emission line.

We calculated the χ^2 of the n radial velocities with respect to the mean value:

$$\chi^2 = \sum_{k=1}^{n} \left[\frac{\mathrm{RV}_k - \overline{\mathrm{RV}}}{\sigma_{\mathrm{RV}_k}} \right]^2, \tag{3.1}$$

and the probability for a χ^2 value with $N = n - 1$ degrees of freedom, to exceed the calculated χ^2 value, which is given by

$$P(\chi; N) = \int_{\chi^2}^{\infty} \frac{2^{-N/2}}{\Gamma(N/2)} \chi'^{N-2} e^{-\chi'^2/2} d\chi'^2, \tag{3.2}$$

where $\Gamma(x)$ is the gamma function. We consider strong PCEB candidates those systems showing a probability at a significance level $\geq 99.73\%$. In Fig. 3.2 we plot the radial velocities for a subsample of systems, with PCEBs highlighted in pink [2] and the name of the particular system written above.

1. **PCEB identification from SDSS-sub-exposures** Among the 277 WDMS from chapter 2, 29 systems were identified as PCEB from the Na doublet (see Fig. A.1) and 28 systems from the Hα emission (see Fig. A.2). We considered all the systems satisfying the criterium aabove explained as PCEB, independent on the spectral line which was used for measuring the radial velocities. We identified a total of 33 PCEBs alone from the SDSS-sub-exposures. Some systems had only two-three sub-exposures and for many systems

[2]We make the reader note that the plot does not contain information on time in the x-axis, but that it is just a sequence.

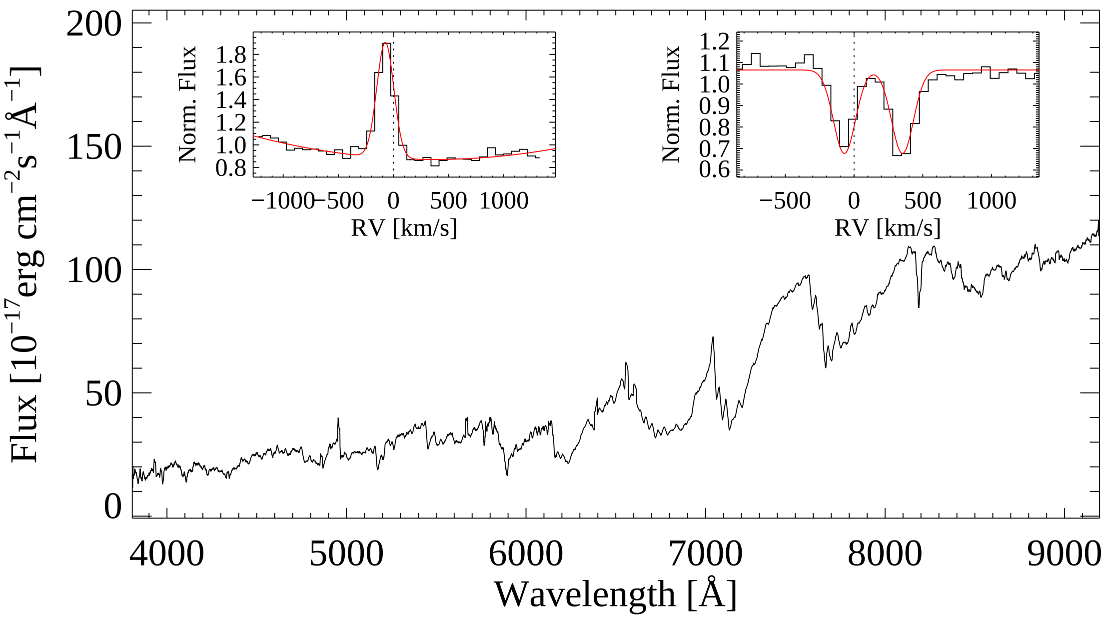

Figure 3.1: Example of a single spectral exposure (30 min) and radial velocities fits for the Hα, emission line and the Na absorption doublet shown in the boxes.

the time span between sub-exposures was very short, around 4 hours, therefore no significant radial velocity variation could be measured, perhaps faking a wide system (only short orbital period systems can be detected in such a short time span). In Fig. 3.1 we show an example of one of the sub-exposures of SDSS1055+4729, where the fits to the Hα emission line and to the Na doublet are shown in the left and the right boxes respectively.

2. **PCEB identification from spectroscopic follow-up** From own observations we have identified 19 PCEBs (see chapter 4), three of them where not classified as such when using the sub-spectra: SDSS1429+5759, SDSS1436+5741 and SDSS1437+5737.

3. **PCEB identification combining SDSS with own spectroscopic follow-up** Finally if we combine the data from own observations with the sub-exposures from the SDSS database we were able to identify one further PCEB candidate: SDSS2258+0710.

SDSS1436+5741 was classified as a candidate (dM plus a blue excess) in chapter 2, and it's binary nature is clear from the radial velocity shifts. We include this system in our study, which brings the total number of WDMS to 278 and among those we have identified 37 secure PCEBs. On the other hand 45 systems do not show any radial variation which means that either they have a low inclination or that they are wide systems (see Sect. 3.4.2). We list the radial velocities of the 37 PCEBs in table 3.2. In the following sections we will refer as 'wide' systems to all those

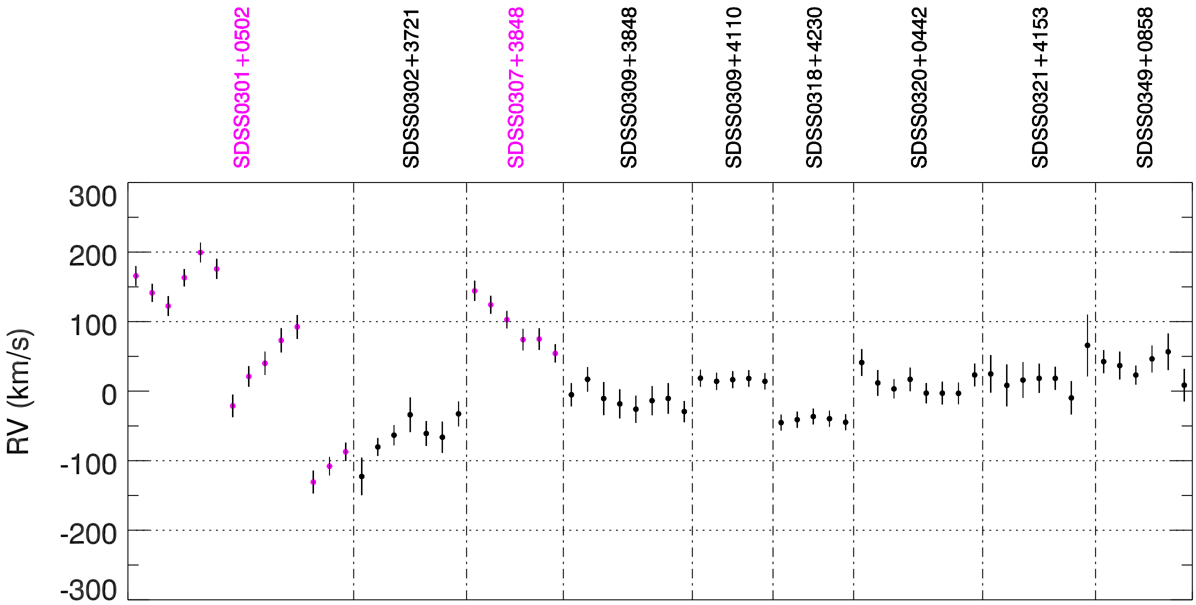

Figure 3.2: Radial velocities of the Na absorption doublet for a subsample of WDMS binaries taken around R.A. 03. PCEB candidates are plotted in pink.

Table 3.2: Radial velocities of the WDMS measured from the SDSS subexposures. Extract of the table, for a complete table see the appendix.

	Name			**Name**	
HJD	RV(Na)	RV(Hα)	HJD	RV(Na)	RV(Hα)
	SDSS0142-0835			**SDSS1114+0924**	
54469.5887	4.1 ± 13.5	-17.3 ± 11.9	54169.7317	-103.2 ± 17.6	-
54469.6080	5.8 ± 14.6	-13.8 ± 13.1	54169.7494	-45.4 ± 21.5	-
54491.5776	-18.3 ± 13.2	-23.7 ± 12.5	54169.7691	53.2 ± 24.5	-
54491.6026	-9.9 ± 14.2	-29.3 ± 13.8	54169.7883	105.4 ± 22.2	113.0 ± 17.4
54495.5732	28.4 ± 12.6	6.2 ± 15.7	54169.8095	-	130.6 ± 18.4
54495.5928	23.4 ± 15.0	17.5 ± 14.2		**SDSS1123-1155**	
54497.5811	-37.4 ± 13.9	-47.5 ± 13.9	54565.6238	-124.7 ± 11.3	-132.1 ± 10.5
54497.6022	-27.8 ± 14.3	-54.5 ± 15.7	54565.6397	-120.9 ± 11.4	-124.0 ± 10.6
54498.5811	-0.3 ± 15.5	2.1 ± 12.1	54565.6553	-111.8 ± 12.0	-124.3 ± 10.6
54498.6039	11.1 ± 16.6	8.2 ± 12.6	54568.6426	-122.9 ± 12.7	-147.2 ± 10.8
54499.5716	-3.5 ± 12.7	1.2 ± 15.5	54569.6279	15.1 ± 11.8	3.0 ± 10.9
54499.5945	8.3 ± 14.6	-26.9 ± 16.5	54569.6534	43.5 ± 11.9	35.6 ± 11.3

systems that are not PCEB candidates but we make the reader note that this might contain a small fraction of close binaries.

Table 3.3: Stellar parameters derived from the SDSS spectrum for the 37 PCEB detected through radial velocity variations measured from the Na doublet or/and the Hα emission line. Maximum orbital period are calculated and shown in the last column.

System (SDSS)	type	$T_{\rm eff}$(K)	$\log g$	$M_{\rm wd}$($M_\odot$)	$d_{\rm wd}$(pc)	Sp	$M_{\rm sec}$($M_\odot$)	$d_{\rm sec}$(pc)	$P^{max}_{orb}(d)$
0142 − 0835	DA/dM	9187 ± 148	8.77 ± 0.18	1.08 ± 0.10	113 ± 17	3	0.380	428 ± 84	121[4]
0239 + 2736	DA/dM	12681 ± 1145	7.91 ± 0.38	0.56 ± 0.23	468 ± 107	4	0.319	774 ± 228	0.784
0301 + 0502	DA/dM	11565 ± 680	8.46 ± 0.23	0.90 ± 0.14	209 ± 36	4	0.319	380 ± 112	0.982[1]
0307 + 3848	DA:/dM					3	0.380	373 ± 73	[1]
0420 + 0649	WD/dM					5	0.255	173 ± 89	[1]
0722 + 3859	DA:/dM					4	0.319	264 ± 78	[4]
0730 + 4054	WD/dM					3	0.380	295 ± 58	
0734 + 4105	DA/dM	19868 ± 353	8.01 ± 0.07	0.63 ± 0.04	299 ± 14	3	0.380	354 ± 70	13.742
0753 + 1754	DA/dM	18756 ± 1415	8.36 ± 0.30	0.84 ± 0.18	553 ± 121	4	0.319	545 ± 161	3.730
0853 + 0720	DC/dM					3	0.380	573 ± 113	[1]
1021 + 1744	DA/dM	32972 ± 2038	8.65 ± 0.36	1.03 ± 0.18	720 ± 207	4	0.319	435 ± 128	0.571
1024 + 1624	DA/dM	15422 ± 1049	8.31 ± 0.21	0.81 ± 0.13	385 ± 59	3	0.380	403 ± 79	19.400
1028 + 0931	DA/dM	18756 ± 313	8.29 ± 0.06	0.80 ± 0.04	144 ± 7	3	0.380	125 ± 25	0.891
1047 + 4835	DA/dM	12681 ± 1394	7.84 ± 0.45	0.52 ± 0.27	610 ± 161	3	0.380	1048 ± 206	31.886
1055 + 4729	DA/dM	10073 ± 579	9.50 ± 0.08	1.37 ± 0.02	73 ± 7	3	0.380	269 ± 53	24.830[2]
1105 + 3851	DA/dM	10548 ± 142	8.18 ± 0.13	0.71 ± 0.09	205 ± 19	3	0.380	462 ± 91	1.499[1]
1114 + 0924	DA/dM	10427 ± 211	8.28 ± 0.23	0.78 ± 0.15	236 ± 38	5	0.255	465 ± 238	3.762
1123 − 1155	DA/dM	10073 ± 215	9.12 ± 0.25	1.25 ± 0.08	64 ± 14	5	0.255	117 ± 60	13.974
1135 + 0103	DA/dM	30071 ± 3076	6.41 ± 0.66	0.18 ± 0.14	3523 ± 1174	4	0.319	550 ± 162	0.269
1300 + 1908	DA/dM	8673 ± 259	8.81 ± 0.41	1.10 ± 0.18	123 ± 39	4	0.319	378 ± 111	21.461[1]
1316 − 0037	DC/dM					3	0.380	394 ± 78	
1320 + 6612	DA/dM	28389 ± 1407	8.05 ± 0.27	0.67 ± 0.16	719 ± 131	1	0.464	976 ± 191	11.454[4]
1348 + 1834	DA/dM	15071 ± 355	7.96 ± 0.07	0.59 ± 0.04	180 ± 8	4	0.319	236 ± 69	0.346[1]
1429 + 5759	DA/dM	16336 ± 1781	8.69 ± 0.35	1.04 ± 0.17	378 ± 104	3	0.380	632 ± 124	[1,3]
1436 + 5741	cand					3	0.380	511 ± 101	[1,3]
1437 + 5737	DA/dM	17912 ± 846	8.12 ± 0.19	0.69 ± 0.120	392 ± 50	4	0.319	323 ± 95	[3]
1524 + 5040	DA/dM	19640 ± 587	8.14 ± 0.12	0.71 ± 0.07	221 ± 18	3	0.380	336 ± 66	1.082[1]
1558 + 2642	DA/dM	14560 ± 4069	8.74 ± 0.64	1.07 ± 0.26	281 ± 129	4	0.319	320 ± 94	2.328[1]
1623 + 6306	DA/dM	9731 ± 289	8.63 ± 0.35	1.00 ± 0.19	180 ± 48	4	0.319	335 ± 99	21.483[1]
1625 + 6400	DA/dM	8773 ± 169	8.31 ± 0.27	0.79 ± 0.17	155 ± 30	6	0.196	212 ± 98	3.270[1]
1635 + 6201	DA/dM	17505 ± 582	7.81 ± 0.13	0.52 ± 0.07	378 ± 31	3	0.380	514 ± 101	10.907
1724 + 0733	DA/dM	13588 ± 989	8.02 ± 0.24	0.62 ± 0.15	384 ± 59	4	0.319	324 ± 95	113.591[4]
1844 + 4120	DA/dM	7554 ± 28	7.45 ± 0.12	0.33 ± 0.05	75 ± 5	6	0.196	58 ± 27	6.320[1]
1919 + 6214	WD/dM					3	0.380	583 ± 115	
2243 + 3122	DC/dM					5	0.255	171 ± 87	[1]
2258 + 0710	DA/dM	8475 ± 272	8.07 ± 0.57	0.64 ± 0.37	248 ± 87	5	0.255	351 ± 180	
2311 + 2202	DA/dM	10189 ± 460	8.92 ± 0.40	1.16 ± 0.15	163 ± 52	3	0.380	536 ± 105	3.806[1]

[1] The orbital period was measured and is given in table 4.3. [2] The stellar parameters are uncertain due to poor signal to noise in the SDSS spectrum. [3] Only two subspectra were available, therefore the system was not classified as PCEB from the SDSS alone, but further spectra showed strong radial velocity variation. [4] The systems was classified as a PCEB only through variation in the Hα emission line.

3.4 Results

3.4.1 The PCEB fraction

The fraction of PCEBs among WDMS binaries and the corresponding distributions of their stellar parameter represents an important tool to constrain current theories of close binary formation and evolution. We estimate that the fraction of PCEB among WDMS is > 13%, lower than the predicted value of 25% by Willems & Kolb (2004). Nevertheless our estimated value is just a lower limit to the total number of PCEBs. Many of the subexposures were taken in one day a most of them in a time span of less than 10 days so our result is strongly biased towards fast rotating system, i.e. short orbital periods, being therefore just a lower limit of the entire population of PCEB. Also a number of systems with low orbital inclination will not be detected as PCEBs. Based on 101 WDMS binaries with multiple SDSS spectra, Rebassa-Mansergas et al. (2007) estimated a fraction of PCEBs to WDMS of ~ 15 %. Later on Schreiber et al. (2008) based on a subsample of these 101 WDMS and taking higher S/N spectra found a value of 35 ± 12 %. This result suggests that our observed fraction is a lower limit and underlines the relevance of taking further spectra with higher S/N.

The secondary spectral type distribution in the SEGUE PCEB sample

The fraction of PCEBs in the SEGUE subsample is presented in the bottom left panel Fig. 3.4 as a function of the secondary spectral type with Poissonian errors. For completeness the spectral type distribution is included in the upper panel, where WDMS are plotted with solid line and PCEBs with dashed lines. The PCEB fraction is strongly correlated with the spectral type of the secondary star, increasing towards later spectral types. The fraction of PCEB in the SEGUE subsample presents a drop of 17% around M3. This subsample has been combined with SDSS-WDMS to create a dataset representative of the entire population of WDMS binaries, which is better populated at earlier and later spectral types. In the right panels of Fig. 3.4 we show the spectral type distribution of the entire sample composed of 589 WDMS binaries (solid line), among which 193 are PCEBs (plotted with dashed line). The fraction of PCEBs, shown in the bottom panel, is around 20% for early spectral types, M0 – M3, increasing towards later spectral types until it reaches ~ 50% at M5, where it seems to be flat until it drops again to 20% at M8. The decrease in the fraction of PCEBs around the spectral type where the secondary stars are fully convective, M3 is of the order of 80%. Politano & Weiler (2006) predict a pronounced drop in the relative number of PCEBs around this range in spectral type, 38 – 73% for disrupted magnetic braking, where the relative fraction depends on the efficiency of the CE phase. When assuming any other prescription for AML, only GR, GR plus IMB or GR plus RMB this feature would not be present (see Fig. 3.3). We have therefore confirmed DMB (Schreiber et al.submitted).

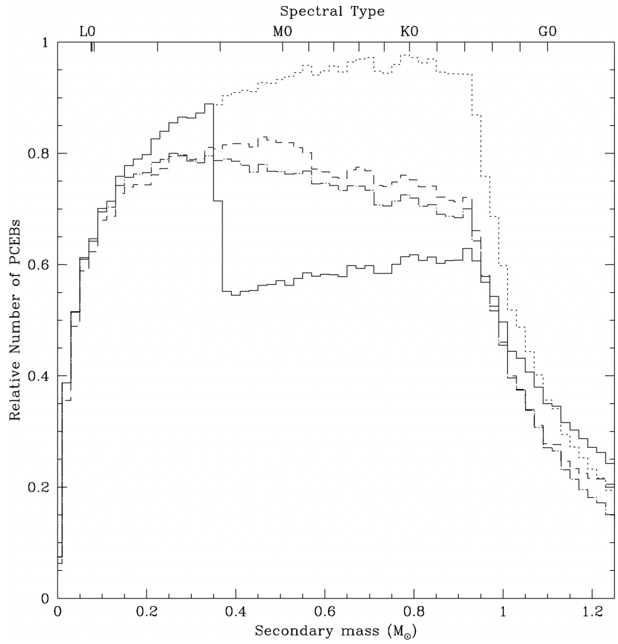

Figure 3.3: Fraction of PCEBs as a function of the secondary spectral mass when assuming different prescriptions for the angular momentum loss: only GR, GR+DMB, GR+IMB and GR+RMB. Figure was taken from Politano & Weiler (2006).

The white dwarf mass distributions

The $M_{\rm wd}$ distribution of the WDMS containing a DA as primary star and with $T_{\rm eff} > 12000$ K and with relative errors lower than 25%, so that it's spectroscopic mass is reliable (Kepler et al. 2007), is shown in Fig. 3.5. This distribution is explained in chapter 2, so we just mention here that it resambles the distribution of single white dwarfs, peaking around 0.6 $M_\odot$ and decreasing towards higher masses. With dashed lines the distribution of PCEB is overplotted. After the strong filtering of having a relative error lower than 25% and an $T_{\rm eff} > 12000$ K we end up with only 11 PCEB, which is not enough to draw any significant result. Nevertheless we comment that the $M_{\rm wd}$ distribution in the PCEB SEGUE subsample spreads from 0.5 to 0.9 $M_\odot$ and that it is wider, with a mean value of $M_{\rm wd} = 0.607 M_\odot$, differing from that one of single white dwarfs. All WDMS which have a primary star with lower mass than ~ 0.48 $M_\odot$, that is He core WDs, are thought to be PCEBs (Liebert et al. 2005) (see chapter 1). We have 6 WDMS with $M_{\rm wd} < 0.48$ which show no significant radial velocity variation, even though their spectra are spread over several days. In Chapter 4 we discuss in detail the $M_{\rm wd}$ distribution of PCEBs.

3.4.2 Upper limits on the orbital period

Among the 37 PCEBs, 24 contain a white dwarf of type DA as a primary star, for which we were able to derive the mass (see 2). Using these and assuming the maximum radial velocity

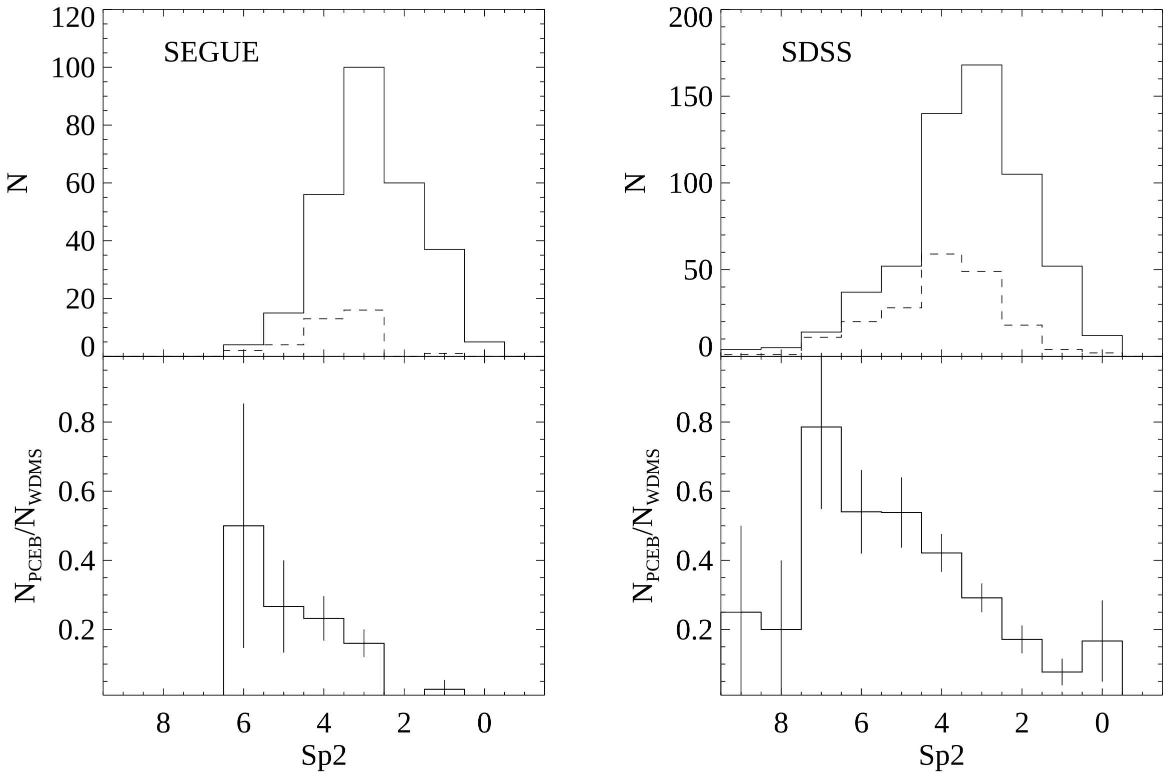

Figure 3.4: The distribution of the secondary spectral type for all the WDMS is shown in the upper panels, PCEB are overplotted with dashed lines. In the panels bellow we show the fraction of PCEB as a function of the secondary mass, with Poissonian errors. In the left panels we show the distribution and fractions from the SEGUE subsample, wich forms part of the larger sample from SDSS shown in the right panels.

difference to be equal to the radial velocity semi-amplitude and assuming an inclination of 90° we have derived upper limits on the orbital period using Kepler's third law:

$$P_{\rm orb} = 2\pi G \frac{(M_{\rm wd} \sin i)^3}{(M_{\rm wd} + M_{\rm sec})^2} \frac{1}{K_{sec}^3} \simeq 2\pi G \frac{{M_{\rm wd}}^3}{(M_{\rm wd} + M_{\rm sec})^2} \frac{1}{\Delta V^3} \quad (3.3)$$

We include the estimated upper orbital period in Table 3.3.

3.5 Discussion

To understand our detection biases we have to investigate how the spectra are spread in time. In Fig. 3.6 we show the frequency in the number of sub-spectra per object (upper panel), where we can see that most of the systems have around 5-7 sub-exposures. The maximum time elapsed between the exposures ranges from $\sim$ 1 hour to several hundreds of days (lower panel). Systems

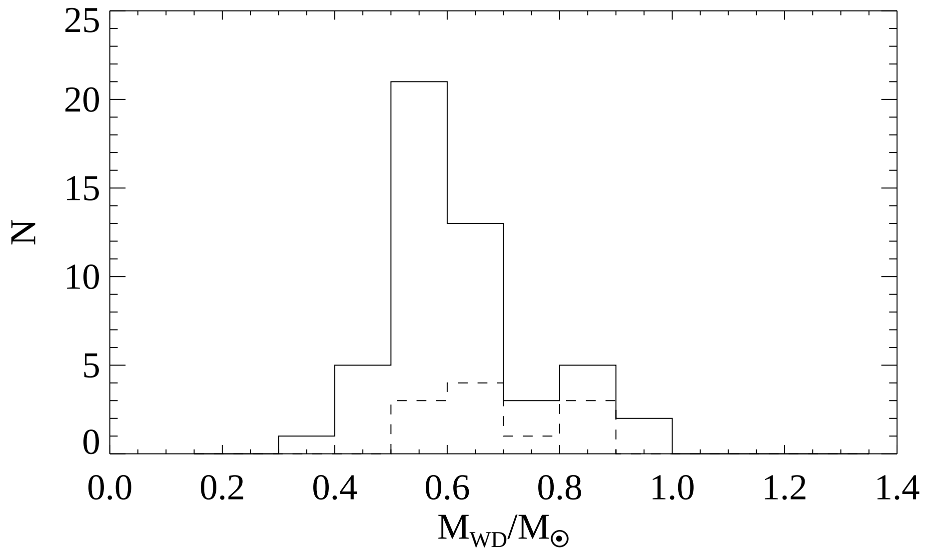

Figure 3.5: White dwarf mass distribution of all the WDMS containing a DA as a primary and with $T_{\rm eff}$ > 12000 K and a relative error lower than 25%, with overplotted values for the PCEB with dashed line.

with more spectra cover in general a broader range in time. On the one hand where the sampling covers just few hours we are only sensible to shorter orbital period systems ($P_{\rm orb}$< 1 day). On the other hand many spectra were taken covering several days and we should then be able to detect the long orbital periods as well. We separate PCEBs from wide systems, with open circles we show those systems where no high radial velocity variation was found, while we show those systems above the $3 - \sigma$ detection with crosses.

Apparently there is no preference in the diagram for one or another type. There are 114 systems for which the sub-spectra were taken during the same night, among these, only 9 were detected as being PCEB candidates. That represents less than 8% of the systems. This low fraction of PCEBs indicates that, for systems with such a sampling, we are biased towards detection of short orbital periods, missing all the long orbital periods in this area. Among these systems we have measured the orbital period of 4 systems and all of them have periods shorter than ~ 10 hours. At this point, it is worth mentioning that the three systems which are confirmed as PCEBs from own spectroscopic observations (SDSS1429+5759, SDSSS1436+5741 and SDSS1437+5737) had only 2 sub-exposures spread in less than 1 hour, and could therefore not be detected as PCEBs alone from the SDSS-sub-spectra. We have measured the orbital period for two of those systems and they do have a period longer than 12 hours in agreement with the statement made before.

We find 24 PCEB candidates among systems with a sampling spread over more than a day, representing a fraction of ~ 15%. Among these 24 PCEB candidates we have measured the orbital period of 9 systems, and just 1 has an orbital period longer than a day. For these systems, in principle we are not biased towards short orbital periods due to the sampling. But we might still be biased because long orbital periods have lower radial velocity amplitude and that might cause the system to fall outside our criteria although it is a PCEB. We now investigate this possible bias.

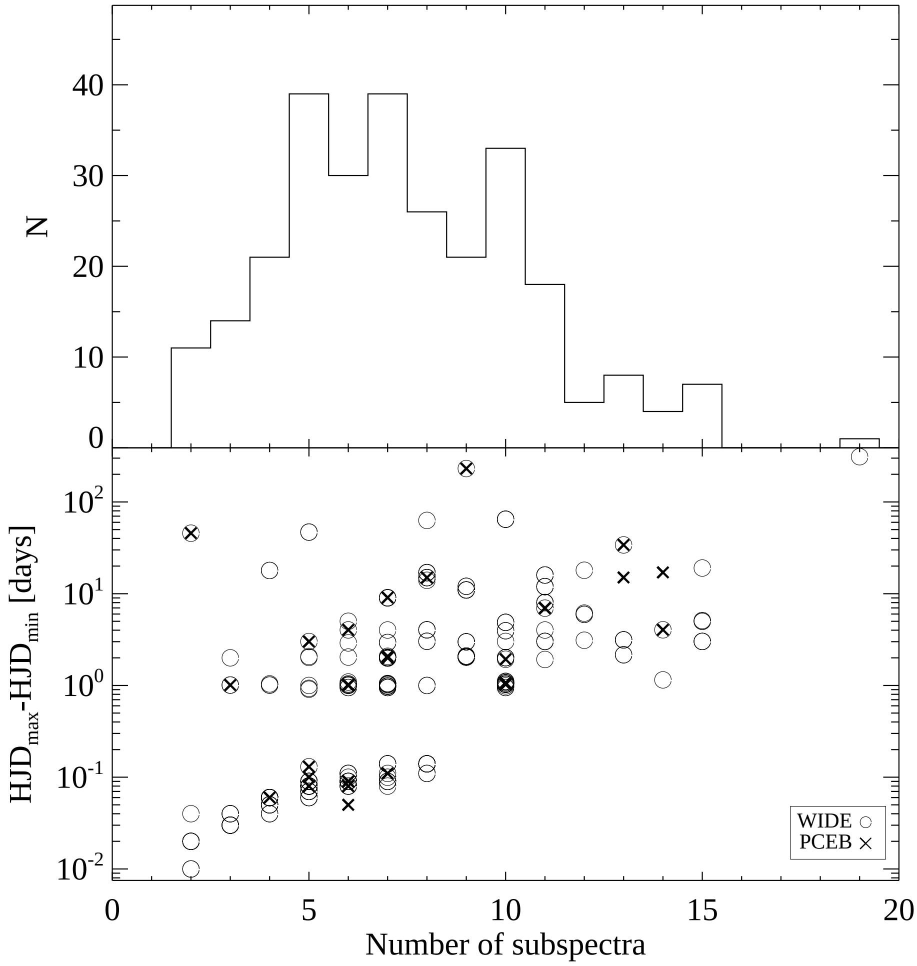

Figure 3.6: Frequency of number of sub-spectra per system (upper panel). Maximum difference in time versus number of sub-spectra per system. Confirmed PCEBs are plotted with crosses while the rest of the systems are plotted with open circles.

Using the mass function we have derived the possible radial velocity amplitudes for the secondary star as a function of the inclination, the mass of the white dwarf, the mass of the secondary and the orbital period. In Fig. 3.7 we plot K_{sec} for M_{wd}=0.3,0.6,0.9 $M_\odot$ plotted with solid, dotted and dashed lines respectively, for inclinations of 30° (black), 60° (red) and 90° (blue) and for a typical spectral type M3, $M_{sec}\sim$ 0.35 $M_\odot$.

From the SDSS-sub-exposures we have a typical error of 15 km/s in the radial velocity, with this relatively large error the minimum ΔRV that we have been able to detect is around 45 km/s.

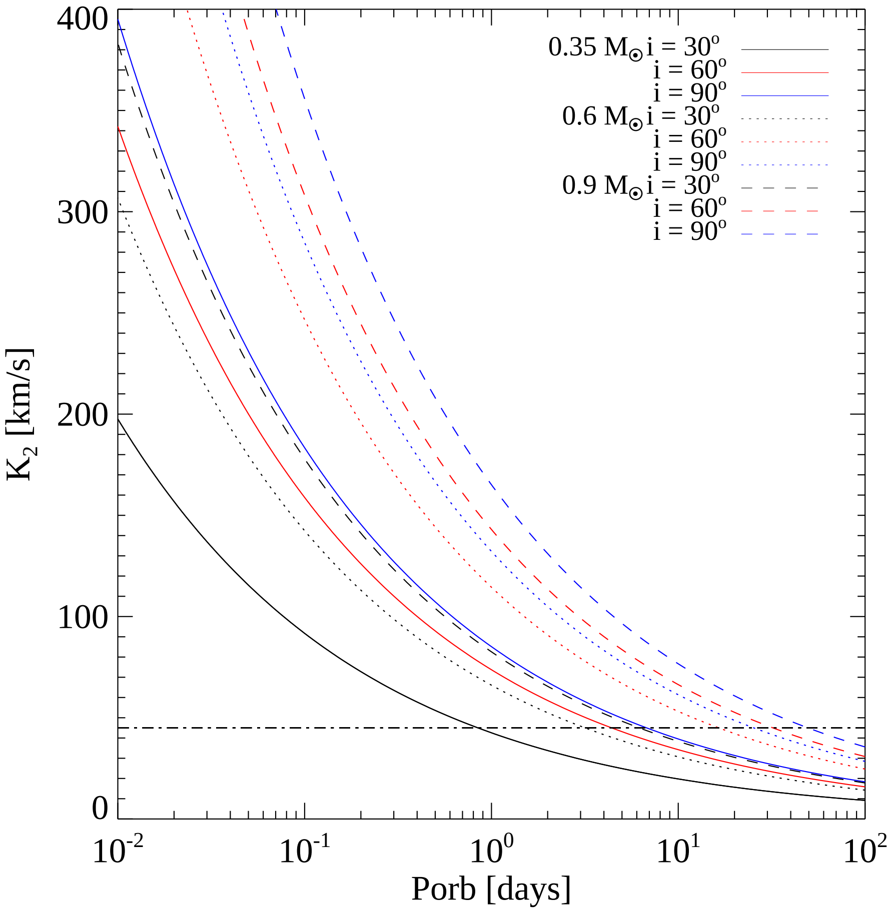

Figure 3.7: Radial velocity amplitude of the secondary star as a function of the orbital period. K_2 is calculated for different primary masses, $M_{\rm wd}$=0.3, 0.6, 0.9 M$_\odot$from left to right, and for orbital inclinations 30, 60 and 90 degrees. A detection limit of 45 km/s is over-plotted with a dotted-dashed line.

This limit defines the minimum orbital inclination at a given orbital period that a system can have to be detectable with out sensitivity and is presented in Fig. 3.8. In other words, at a certain orbital period we should be able to detect all systems above this critical inclination. As we can see, for a given secondary star, which in this example was fixed to a spectral type M3 ($M_{\rm sec}\sim$ 0.35 M$_\odot$), the higher the primary's mass the longer the orbital period we will be able to detect, since lower masses will have smaller values of K$_{\rm sec}$. Now we may ask ourselves how many systems have a higher inclination and how many systems will have a lower inclination and will therefore be outside of our detection limit. The probability of an orbit to have a inclination, i, larger than a certain value is given by cos(i). In Fig. 3.9 we show the detection probability, assuming there is no preference for a certain inclination, of a system having an orbit with an inclination higher than the critical inclination as a function of the orbital period.

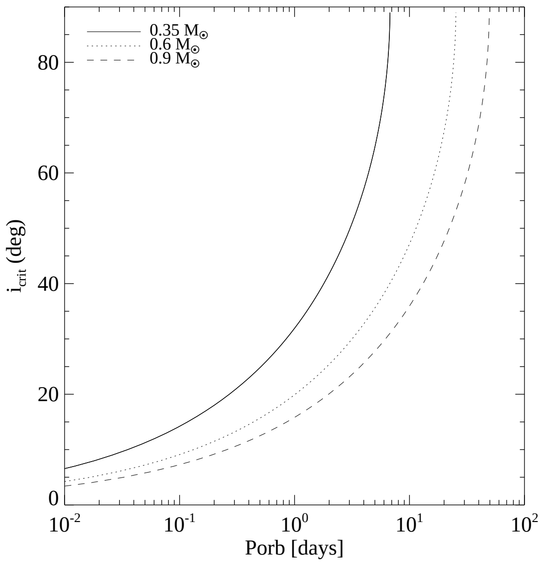

Figure 3.8: Minimum orbital inclination that can be detected as a function of orbital period for the same masses as in the Fig. 3.7.

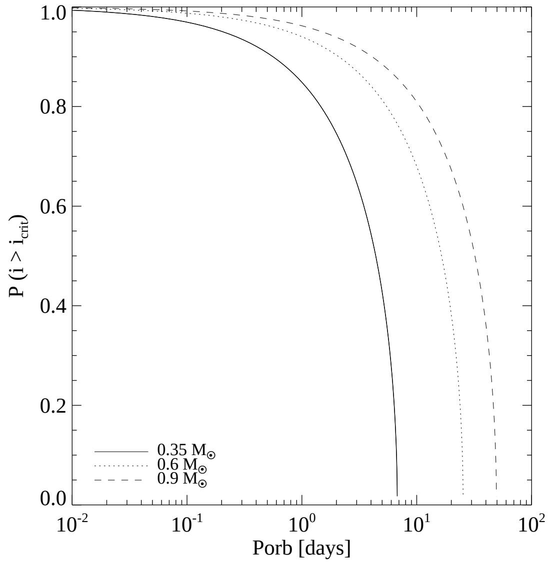

Figure 3.9: Probability of detecting a larger inclination than the critical detection inclination as a function of the orbital period, again for the same masses as for the plot above.

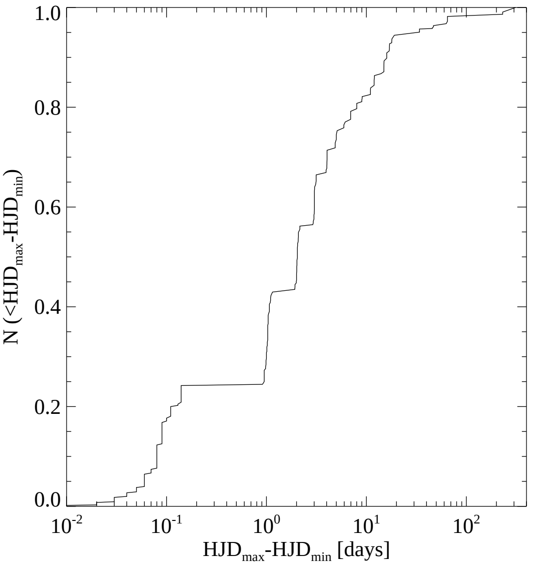

Figure 3.10: Cumulative sampling distribution.

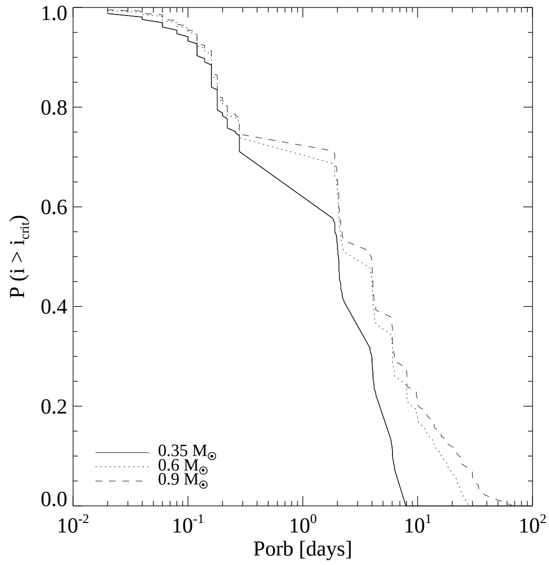

Figure 3.11: Probability of detection as a function of the orbital period, where the sampling has been taken into account.

But we would like to include our sampling into the detection probability. In Fig. 3.10 we show the cumulative sampling distribution, using the maximum difference in time between the sub-exposures as the sampling time. Under the conservative assumption that in order to detect variability for a system with a given period we need to cover at least half of an orbit (ΔHJD $\simeq \frac{1}{2}P_{\rm orb}$) we have calculated the detection probability by multiplying the previously calculated detection probability (see Fig. 3.9) with the inverse of the CDF (Fig. 3.10), see Fig. 3.11.

For a typical white dwarf mass of 0.6 $M_\odot$ and a typical M3 ($\sim$ 0.35 $M_\odot$), represented with dotted lines in Fig. 3.7,3.8,3.9 and 3.11, this implies that it is possible to detect higher inclination systems than e. g. 40 degrees up to orbital periods of 6 days, which translates into a probability detection of $\sim$ 50%.

From this analysis we learn two important things: on the one hand we will always be able to detect short orbital periods (<1 day) since the minimum inclination that we are able to detect is lower and the detection probability at higher inclinations than the critical inclination is very high (> 80%); and on the other hand we should be able to detect long orbital periods up to several days even for the less favored case, corresponding to low $M_{\rm wd}$.

3.6 Summary

Using the SDSS sub-exposures that are coadded to create a single SDSS spectrum, based on a statistical approach we have discovered 33 new PCEBs. Combining with own spectroscopic follow-up we have increased that number to 37. The PCEB fraction is $\sim$ 13 %, number below the theoretical value predicted by Willems & Kolb (2004). Nevertheless our result is just a lower limit to the total number of PCEB in the sample, in order to have the complete number further spectroscopy is required. The fraction of PCEBs increases towards later spectral type secondary stars, presenting an increase between M2-M3, where the secondary becomes fully convective, which according to Politano & Weiler (2006) indicates that magnetic braking gets disrupted once the secondary becomes fully convective (at around 0.35 $M_\odot$). We have studied our detection probability finding that even though we are biased towards systems with short orbital periods (< 1 day) we should be able to detect as well longer orbital periods. Given our sampling rate and radial velocity accuracy we reach a 50% detection probability at an orbital period of 2 days, and we are completely insensitive for objects with periods longer than $\sim$ 10 days. To test the exintance of longer orbital period systems we need a better sampling and better spectral resolution.

Chapter 4

Orbital period distribution of PCEBs

The number of PCEB with orbital period known and well determined stellar parameters was only $\sim$ 30 in 2003. From spectroscopic and photometric follow-up observations we measured the orbital period of 15 new systems, in the range $2.8h < P_{\rm orb} < 2d$. This sample provides the largest sample of post common envelope binaries until the date to be used to proof the CE efficiency. We analyze the orbital period and the white dwarf mass distributions. We analyze the remaining PCEBs in detail and constrain their orbital period limit, finding 7 long orbital period candidates and 15 short orbital period candidates.

4.1 Observations and reduction

4.1.1 Spectroscopic follow-up observations

We made spectroscopic follow-up observations of 65 WDMS binaries at different telescopes. The SEGUE WDMS project is part of a large multinational campaign, where several observers have been involved. We describe in detail the spectroscopic observations and reduction that took place in Calar Alto, where the writer was the responsible and list in Table 4.1 the telescopes, period, number of nights, observed time, and name of the observers during that period.

TWIN at the 3.5m Telescope

Observations at the 3.5 meter telescope in Calar Alto (Spain) were carried out during 19–24 July 2007, 09–13 and 26–30 June, 23–27 July, 17–21 October 2008, between the 30 April and 4 May 2009, and between the 09-13 and the 23–27 September 2009. Observations were carried out for a total of 31 nights, 3% of the time was lost due to technical problems and 40% due to bad weather conditions, leaving 57% of the time for observations. A total of 430 spectra were taken during

Table 4.1: Observations carried out at the 3.5m telescope in Calar Alto with the period over which the obervations took place, the name of the observers, the number of nights and the observed time.

Telescope	Period	Observers	N° Nights	Observed (%)
CAHA3.5	2007	Ada Nebot	6	83
	2008A1	Ada Nebot, Alberto Rebassa-Mansergas	5	60
	2008A2	Ada Nebot, Stelios Pyrzas, Matthias Müller	5	100
	2008B1	Ada Nebot, Stelios Pyrzas	5	80
	2008B2	Robert Schwarz, Matthias Müller	5	22
	2009A1	Ada Nebot, Daniele Faccino	5	0
	2009A2	Ada Nebot, Justus Vogel	5	65
	2009B1	Ada Nebot, Robert Schwarz	5	55
	2009B2	Ada Nebot, Andreas Rabitz	5	37

that time, and among these spectra, 309 were for SEGUE systems and are thus presented in the present work.

The TWIN spectrograph was equipped with the grating T05 in the blue arm and T06 in the red (1200 lines/mm) and all observations were done through a 1.5″ width slit, giving a reciprocal dispersion of 0.54 Å per pixel. The coverage was $\sim 4500 - 5500$ in the blue, covering $H\beta$, and $\sim 7500 - 8500$ Å in the red, to cover the Na doublet coming from the secondary star. The mean resolution estimated from the FWHM of sky emission lines in the spectra was approximately 1.6 Å around 8200 Å. All exposures were done in synchronous mode and the exposure time was selected to optimize the signal in the red arm. Images were reduced using MIDAS and the spectra were extracted using the optimal algorithm (Horne 1986). We observed the standard stars BD332642, BD+254655 and Feige66 for flux calibration. HeAr arc lamps were used to calibrate in wavelength and to optimize the observations we cross-correlated the telluric lines to correct for wavelength shifts due to telescope flexures. We corrected the spectra from sky lines, for creating a sky spectrum template we used the standard stars.

IMACS/Baade–Magellan, LDSS3/Clay–Magellan, EMMI/NTT, FORS/VLT, ISIS/WHT

Long slit spectroscopy was also carried out at the Baade and the Clay Magellan telescopes in Las Campanas, using LDSS3 and IMACS respectively; at the NTT in La Silla using EMMI. FORS2/VLT observations were carried out in service mode. Reduction and calibration were carried out in the same way as described in Rebassa-Mansergas et al. (2008). Since the observations were carried out in the same periods as the observations by Schreiber et al. (2008) and Rebassa-Mansergas et al. (2008) we refer the reader to those papers to see details. A total of 163 spectra were obtained for the SEGUE subsample.

A complete log of the observations is presented in Table 4.2, listing the 65 objects that were observed spectroscopically, the date of observation, the telescopes, the instrument and setup, the integration time, the number of spectra taken and finally there is a column that indicates whether the system is a clear PCEB or not (see Chapter 3).

4.1.2 Photometric follow-up observations

DuPont and IAC80 telescopes

Observations were carried out during 18-21 May 2007 at the DuPont telescope at Las Campanas (Chile). The telescope was equipped with the CCD camera, with a resolution of 0.259″per pixel over a field of 8.85 arcmin square. 337 frames were taken for SDSS0853+0720 in filter r and with a 40 seconds exposure time. Observations were carried out with the CCD camera CAMELOT installed at the IAC80 telescope in Observatorio del Teide (Spain) for SDSS2243+3122 in the sloan *i* filter between the 15th and the 19th of August 2009. A total of 397 frames were taken with exposure time of 240 seconds. A binning of 2 was applied in both spatial directions and only a small window was read in order to decrease the readout time. The area covered by each frame was around 3′ at a resolution of ∼ 0.6″/pixel. Reduction was performed using standard packages in IRAF[1]. An observation log including all observations and details about exposure times, number of frames, filters and setup is given in Table 4.2.

4.2 Results

4.2.1 Orbital periods from spectroscopic observations

From the spectroscopic observations described in Sect. 4.1 we measured the RV velocities from the Na doublet for the 65 WDMS binaries and applied the same analysis described in Chapter 3 to identify the PCEBs. We identified 19 clear PCEBs and the rest did not show any high radial velocity variation. In Table 4.2 we include a column with this information. When only one spectrum was available from own observations we have combined the RVs with those from the SDSS-sub-spectra from Chapter 3 to discern whether the system is a PCEB or not.

A period search was performed by computing periodograms using the Multi-harmonic Fourier spectrum by orthogonal projections as implemented in MIDAS (Schwarzenberg-Czerny 1996). Trial periods were selected from the highest peaks and sine curves of the form:

$$v_r = \gamma_{\rm sec} + K_{\rm sec}\sin\left[\frac{2\pi(t-t_0)}{P_i}\right], \tag{4.1}$$

[1]IRAF is distributed by the National Optical Astronomy Observatory, which is operated by the Association of Universities for Research in Astronomy, Inc., under contract with the National Science Foundation, http://iraf.noao.edu

Table 4.2: Log of observations. Object name, date, telescope, instrument, and number of frames taken for each system. A last column indicating whether the system is a PCEB candidate is included.

Name (SDSS)	Date	Tel	Inst	$N_{\rm frames}$	PCEB?	Name (SDSS)	Date	Tel	Inst	$N_{\rm frames}$	PCEB?
0005+2434	27/07/08-22/10/08	CAHA3.5	TWIN	3	no	1429+5759	20/07/07-01/07/08	CAHA3.5	TWIN	16	yes
0006+2846	09/09/09	CAHA3.5	TWIN	1	no		06/07/08-11/08/08	WHT	ISIS	5	
0009+2432	26/07/08-16/10/08	CAHA3.5	TWIN	9	no	1436+5719	26/07/08-27/07/08	WHT	ISIS	2	no
0038+0834	03/09/06	VLT (sm)	FORS2	2	no	1436+5741	19/07/07-01/07/08	CAHA3.5	TWIN	19	yes
0103+0031	04/11/08-19/11/08	VLT (sm)	FORS2	2	no		07/07/08-10/07/08	WHT	ISIS	4	
0111+0009	25/08/06-05/09/06	VLT (sm)	FORS2	3	no	1437+5737	19/07/07-23/07/07	CAHA3.5	TWIN	4	no
	05/10/07	NTT	EMMI	1		1439+5739	20/07/07-22/07/07	CAHA3.5	TWIN	2	yes
	05/09/07	WHT	ISIS	1		1439+5741	20/07/07-22/07/07	CAHA3.5	TWIN	4	no
0249+3350	11/09/09	CAHA3.5	TWIN	1	no	1504+3214	28/07/08-29/07/08	WHT	ISIS	2	no
0253+3352	11/09/09	CAHA3.5	TWIN	1	no	1524+5047	24/07/08-25/07/08	CAHA3.5	TWIN	6	no
0255+3528	09/09/09	CAHA3.5	TWIN	1	no	1558+2642	11/06/08-01/07/08	CAHA3.5	TWIN	29	yes
0301+0502	19/09/06-22/10/06	VLT (sm)	FORS2	3	yes	1623+6306	20/07/07-01/07/08	CAHA3.5	TWIN	25	yes
	05/10/07-08/10/07	NTT	EMMI	18			08/07/08-10/07/08	WHT	ISIS	4	
0302+3721	24/09/09-25/09/09	CAHA3.5	TWIN	3	no	1625+6400	21/07/07-22/07/07	CAHA3.5	TWIN	2	yes
0307+3848	13/09/09-25/09/09	CAHA3.5	TWIN	24	yes		07/07/08-10/07/08	WHT	ISIS	10	
0309+4110	10/09/09	CAHA3.5	TWIN	1	no	1635+6201	20/07/07-24/07/07	CAHA3.5	TWIN	6	yes
0318+4230	10/09/09	CAHA3.5	TWIN	1	no	1654+1310	24/07/08-25/07/08	CAHA3.5	TWIN	4	no
0320+0442	22/10/06-24/10/06	VLT (sm)	FORS2	2	no	1725+6329	12/09/09	CAHA3.5	TWIN	1	no
0420+0649	19/10/08-22/10/08	CAHA3.5	TWIN	17	yes	1731+0703	24/07/08-25/07/08	CAHA3.5	TWIN	6	no
0830-0536	03/12/08-04/12/08	M-Clay	LDSS3	5	no	1833+6431	25/07/08-26/07/08	CAHA3.5	TWIN	4	no
	06/12/08-07/12/08	M-Baade	IMACS	5		1834+4137	09/09/09	CAHA3.5	TWIN	1	no
0848+0501	24/10/07-26/10/07	VLT (sm)	FORS2	2	no	1844+4108	09/09/09-12/09/09	CAHA3.5	TWIN	3	no
0852+1154	03/12/08	M-Clay	LDSS3	1	no	1844+4120	14/06/08-01/07/08	CAHA3.5	TWIN	14	yes
0852+0713	12/11/07-13/11/07	VLT (sm)	FORS2	2	no		06/07/08-10/07/08	WHT	ISIS	7	
0853+0720	12/11/07-13/11/07	VLT (sm)	FORS2	2	yes	1919+3703	24/07/08-25/07/08	CAHA3.5	TWIN	4	no
	03/12/08-04/12/08	M-Clay	LDSS3	8		1923+6203	10/09/09	CAHA3.5	TWIN	1	no
	06/12/08	M-Baade	IMACS	4		2012+6017	09/09/09	CAHA3.5	TWIN	1	no
1055+4729	01/05/09-05/05/09	CAHA3.5	TWIN	6	yes	2046+0218	27/07/08	CAHA3.5	TWIN	3	no
1105+2824	23/03/09-25/03/09	NTT	EMMI	2	no	2213+0722	09/09/09	CAHA3.5	TWIN	1	no
1105+3851	02/05/09-05/05/09	CAHA3.5	TWIN	16	yes	2228+3912	25/07/08-27/07/08	CAHA3.5	TWIN	7	no
1114+0838	25/12/07-26/12/07	VLT (sm)	FORS2	2	no	2243+3122	22/10/08	CAHA3.5	TWIN	3	yes
1114+0924	15/04/07-17/04/07	VLT (sm)	FORS2	2	yes		09/09/09/10/09/09	CAHA3.5	TWIN	12	
	25/12/07-26/12/07	VLT (sm)	FORS2	2		2257+0745	21/07/07-23/07/07	CAHA3.5	TWIN	4	no
1138-0011	15/04/07-17/04/07	VLT (sm)	FORS2	2	no		14/10/07-17/10/07	VLT (sm)	FORS2	2	
	17/05/07-19/05/07	M-Clay	LDSS3	6			09/08/08-10/08/08	GEMINI-S	GMOS	2	
	19/06/07	WHT	ISIS	1		2258+0710	21/07/07-23/07/07	CAHA3.5	TWIN	4	yes
1239+0055	08/04/07-10/04/07	VLT (sm)	FORS2	2	no		17/10/07-18/10/07	VLT (sm)	FORS2	2	
1242-0853	06/01/08-08/01/08	VLT (sm)	FORS2	2	no		09/08/08-06/11/08	GEMINI-S	GMOS	2	
1243-0647	06/01/08-09/01/08	VLT (sm)	FORS2	2	no	2308+2240	20/07/07-23/07/07	CAHA3.5	TWIN	3	no
1300+1908	01/05/09-05/05/09	CAHA3.5	TWIN	16	yes	2311+2202	21/07/07-28/07/08	CAHA3.5	TWIN	29	yes
1347+2707	18/03/09-19/03/09	NTT	EMMI	2	no	2338+0744	09/09/09	CAHA3.5	TWIN	1	no
1348+1834	12/06/08-30/06/08	CAHA3.5	TWIN	24	yes	2339+0744	13/09/09	CAHA3.5	TWIN	1	no
Photometry Name (SDSS)	Date	Tel	Filter	$t_{\rm int}$	$N_{\rm frames}$	Name (SDSS)	Date	Tel	Filter	$t_{\rm int}$	$N_{\rm frames}$
0853+0720	18/05/07-21/05/07	DuPont	r	40	337	2243+3122	15/08/09-19/08/09	IAC80	i	240	397

were fitted to the phase folded radial velocity curves. Where $\gamma_{\rm sec}$ is the systemic velocity of the secondary star, t_0 corresponds to the zero point defined by the inferior conjunction of the secondary star and with $v_r = \gamma_{\rm sec}$, $K_{\rm sec}$ the radial velocity amplitude of the secondary star and P_i ($i = 1, 2, ...$) are the trial periods picked from the periodogram. In Fig. 4.4 we show two examples of the periodograms with the highest peak marked and with the associated sine fits to the RVs. We accept the orbital period from the best fit solution, corresponding to a minimum chi-square value, which was always coinciding with the highest peak in the periodogram. Radial velocity curves are presented in Fig. 4.2. We derived the orbital period of 15 PCEBs, their spectra are shown in Fig. 4.2.1 and their stellar parameters given in Table 3.3. The orbital periods were always below the upper limits estimated in Chapter 3. The orbital periods of the 15 systems

Table 4.3: Orbital period, amplitude of the secondary's radial velocity, systemic velocity with errors included in parenthesis, estimated primary's radial velocity amplitude, limits for the orbital inclination, orbital separation and minimum filling factor of the secondary star ($f_{\rm min}$). For those systems where no mass of the white dwarf is known we assumed an 0.6 $M_\odot$ white dwarf.

Name	$P_{\rm orb}$ (days)	$K_{\rm sec}$ (km/s)	$\gamma_{\rm sec}$ (km/s)	$K_{\rm WD}$ (km/s)	i (deg)	a ($R_\odot$)	$f_{\rm min}$ $\left(\frac{R_{\rm sec}}{R_{\rm lob}}\right)$
SDSS0301+0502	0.540 (9)	175 (3)	13 (2)	62	52 - 68	3.0 ± 0.2	0.32
SDSS0307+3848	0.430 (8)	147 (2)	-9 (1)	93	51 - 74	2.4 ± 0.2	0.36
SDSS0420+0649	0.203 (1)	156 (3)	47 (2)	66	36 - 46	1.4 ± 0.1	0.45
SDSS0853+0720	0.150 (1)	221 (7)	-8 (6)	139	56 - 90	1.2 ± 0.1	0.70
SDSS1105+3851	0.344 (4)	152 (2)	-9 (2)	81	44 - 54	2.1 ± 0.1	0.46
SDSS1300+1908	0.308 (3)	142 (3)	-14 (2)	41	28 - 35	2.2 ± 0.2	0.50
SDSS1348+1834	0.2483 (4)	222 (3)	-21 (2)	120	~ 90	1.6 ± 0.1	0.50
SDSS1429+5759	0.545 (1)	147 (8)	-12 (5)	53	39 - 49	3.2 ± 0.2	0.38
SDSS1436+5741	0.864 (3)	119 (2)	-16 (2)	75	53 - 78	3.8 ± 0.3	0.23
SDSS1558+2642	0.661 (2)	145 (3)	-10 (2)	43	38 - 53	3.6 ± 0.3	0.27
SDSS1623+6306	2.23 (3)	70 (4)	-9 (3)	22	28 - 36	7.9 ± 0.6	0.13
SDSS1625+6400	0.218 (2)	106 (5)	-10 (4)	26	20 - 25	1.5 ± 0.2	0.36
SDSS1844+4120	0.2255 (3)	148 (4)	-80 (3)	87	50 - 68	1.3 ± 0.2	0.27
SDSS2243+3122	0.11954 (3)	183 (4)	-21 (3)	77	35 - 45	1.0 ± 0.1	0.65
SDSS2311+2202	0.580 (2)	116 (3)	-1 (2)	38	29 - 35	3.4 ± 0.2	0.39

range from 2.86 to 53.52 hours, values are given in Table 4.3 together with $K_{\rm sec}$ and $\gamma_{\rm sec}$. Their orbital period distribution is discussed in Sect. 4.3.1. The number of spectra needed to determine the orbital period varied from 15 to 36, and in general the longer the orbital period the more spectra are required.

Orbital inclinations

From the masses of the white dwarfs, including their errors we calculated the range of possible orbital inclinations, combining the mass function and Kepler's third law:

$$\sin i = (M_{\rm wd} + M_{\rm sec})^{2/3} \frac{K_{\rm sec}}{M_{\rm wd}} \left(\frac{P_{\rm orb}}{2\pi G}\right)^{1/3} \tag{4.2}$$

For those systems for which we do not have the mass of the primary star we assumed a white dwarf of mass of 0.6 $M_\odot$. We give these values in Table 4.3 together with the radial velocity amplitude of the secondary stars and the systemic velocities. Note that system SDSS1348+1834 is a strong candidate for being an eclipsing binary and photometry should be done to confirm.

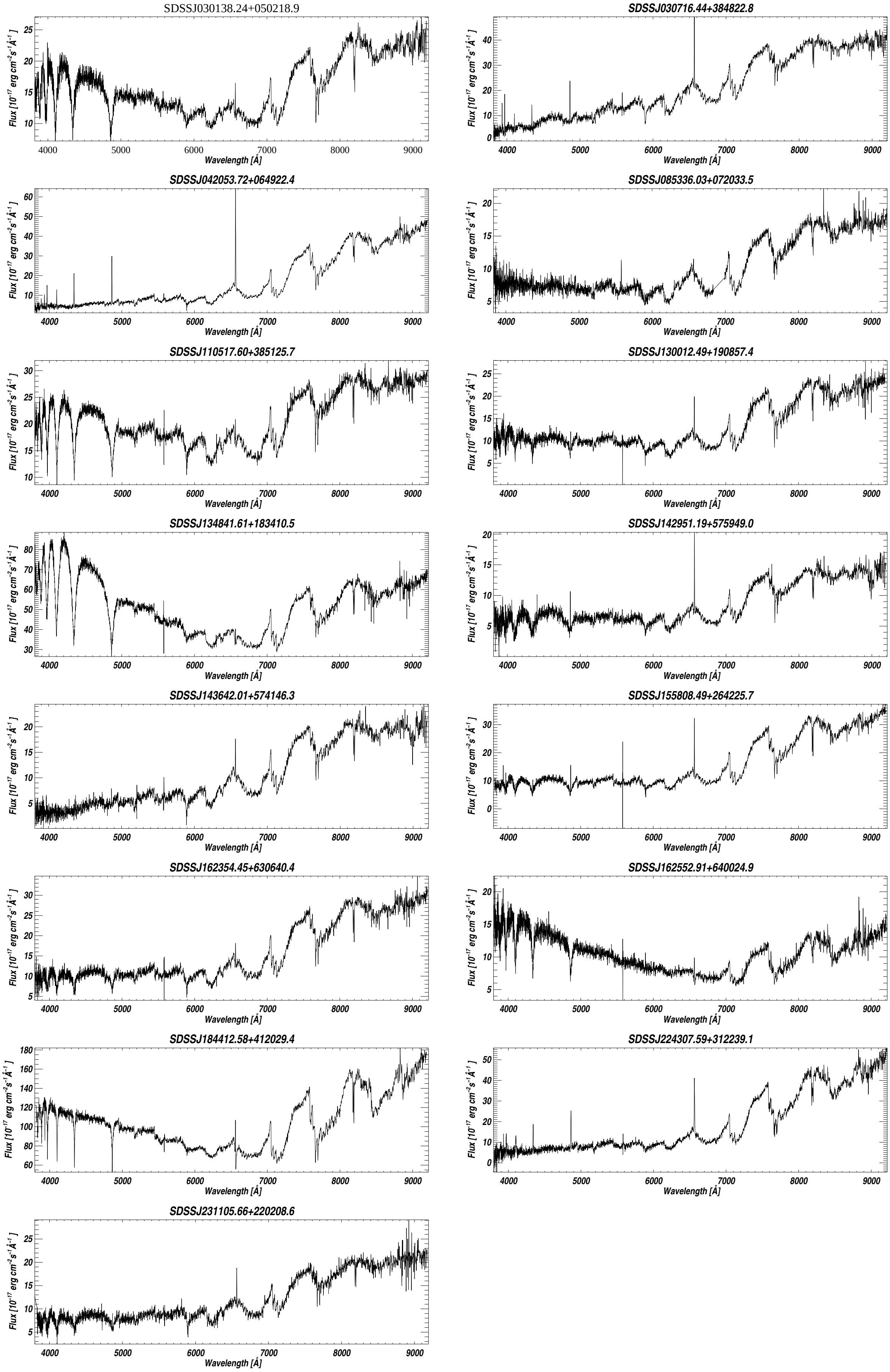

Figure 4.1: SDSS spectra of the 15 systems with orbital period measurement.

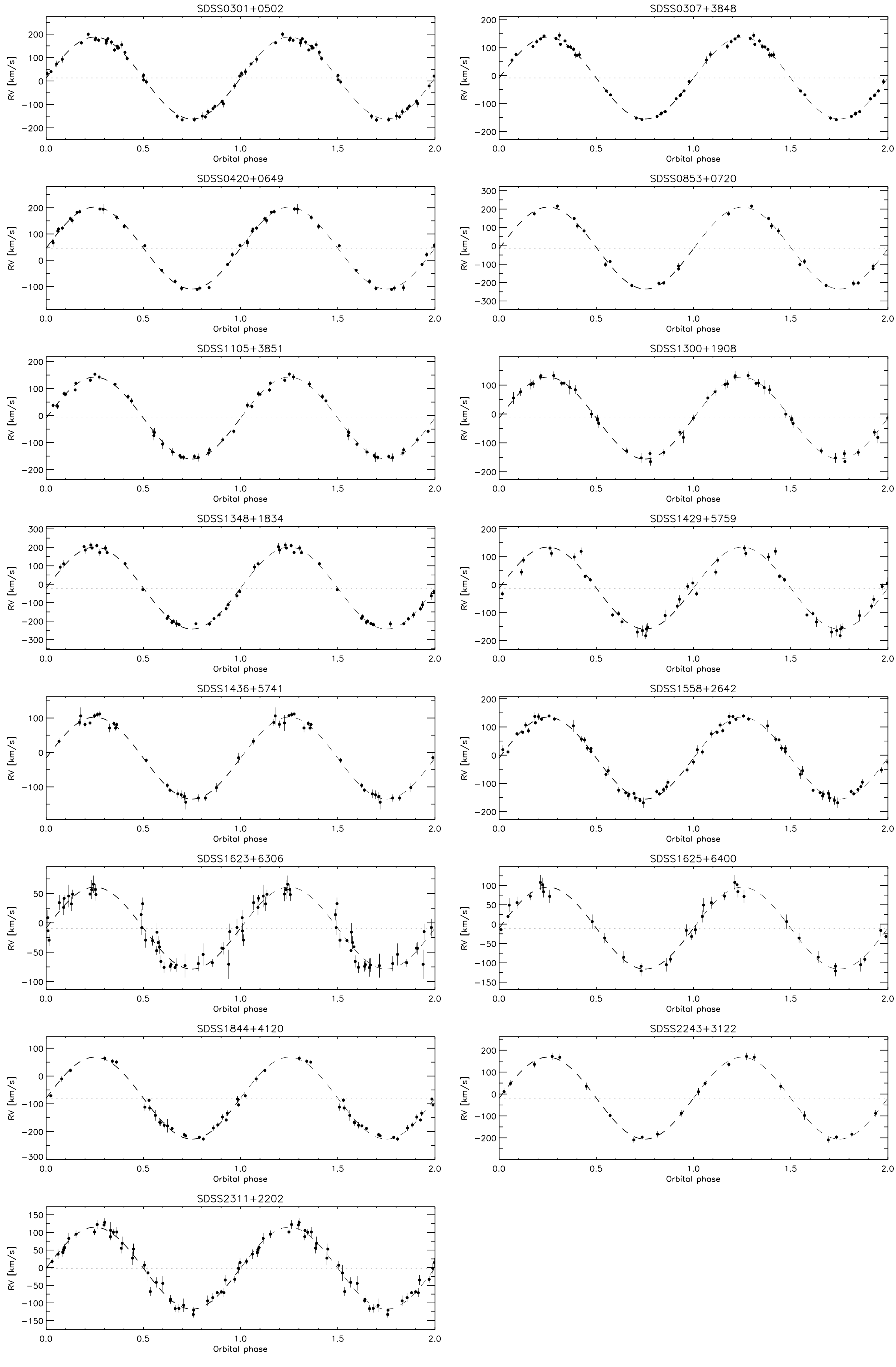

Figure 4.2: Phase folded radial velocities curves and sine fits to the data (dotted lines).

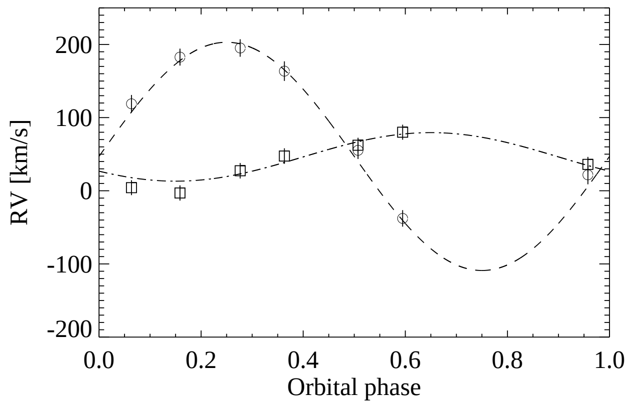

Figure 4.3: Radial velocity curve for SDSS0420+0649 as measured from the Hα emission line (squares) and from the Na absorption doublet in the SDSS-sub-spectra.

Estimates of orbital separation, K_{WD} and R_{lob}

Using Eggleton's equation (Eggleton 1983) for the radius of the Roche lobe, given in equation 4.3 we derived the minimum filling factors of the secondary star for those systems. We estimated the radius of the secondary star using the empirical radius-spectral type relation given by Rebassa-Mansergas et al. (2007). An error of spectral type of one subclass would imply in mean an error on the radius of $\sim 0.05 R_{\odot}$, so we assumed an error of 0.05 $R_{\odot}$for estimating the minimum filling factor.

$$R_{\mathrm{lob}} = \frac{a \cdot 0.49 \cdot q^{2/3}}{0.6 \cdot q^{2/3} + \log(1 + q^{1/3})} \tag{4.3}$$

Using Kepler's third law we derived the orbital separation and, finally we estimated the amplitude of the radial velocity for the primary star using: $K_{\mathrm{WD}} = K_{\mathrm{sec}} \frac{M_{\mathrm{sec}}}{M_{\mathrm{wd}}}$. For those cases where we have no estimate of the mass of the white dwarf we used the standard value of 0.6 $M_{\odot}$. We give these values in Table 4.3.

On the nature of SDSS0420+0649

For SDSS0420+0649 we could measure the RVs from the Na doublet and of the Hα emission line. In Fig. 4.3 we show the measured RVs from the SDSS-sub-spectra, where we plot RV(Na) with circles and RV(Hα) with squares. SDSS0420+0649 has on one hand the velocity coming from the Hα line anti-correlated with the one from the Na doublet. The anti-correlation is not perfect, but has a shift of round 0.1 in orbital phase. The amplitude of the RV(Na) curve is 156 km/s, while for RV(Hα) it is 33 km/s. On the other hand the Hα EW > 20 Å suggesting a CV nature of the system. If the binary has a disk this behavior would be explained (Thorstensen et al. 2009).

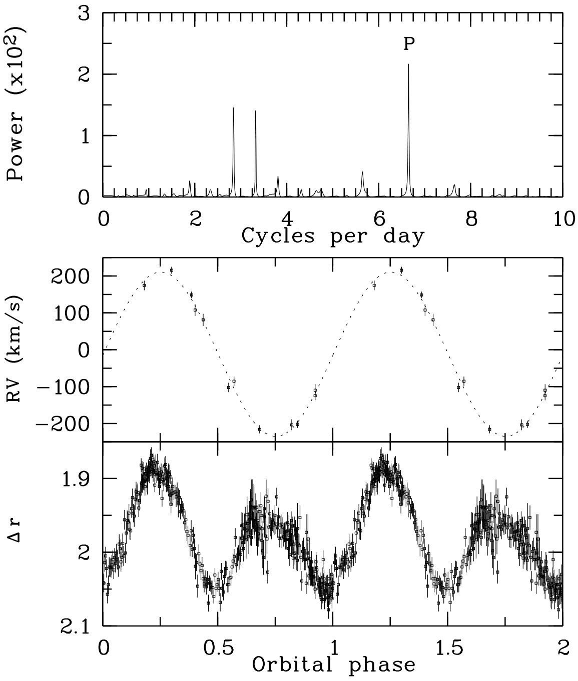

Figure 4.4: Calculated periodogram from using the spectroscopic data, radial velocity and photometric light curves for SDSS0853+0720 phase folded with the orbital period corresponding to the highest peak in the periodogram, $P_{\rm orb}$=0.1503 days.

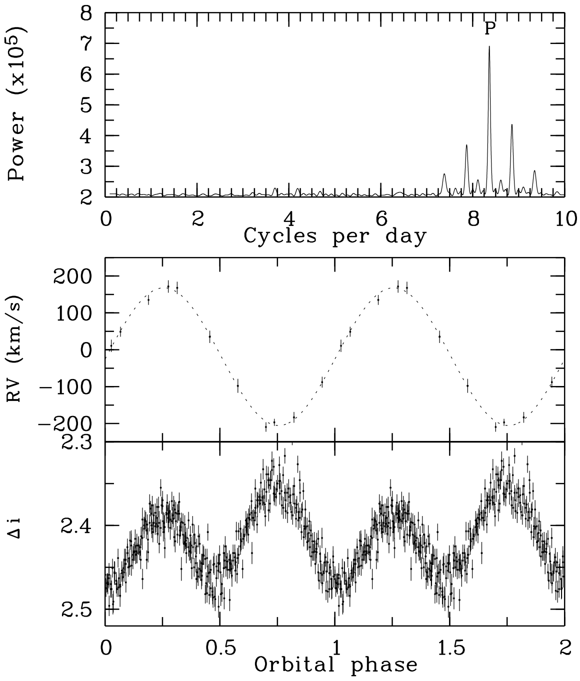

Figure 4.5: Periodogram calculated using the photometric data, radial velocity and photometric light curves for SDSS2243+3122 phase folded with the orbital period corresponding to the highest peak in the periodogram, $P_{\rm orb}$=0.11954 days.

4.2.2 Orbital periods from photometric observations

SDSS0853+0720 was observed with the Du Pont telescope for three consecutive nights (see details in Sec. 4.1) in the r band. We estimated the orbital period computing a periodogram (see section). A phase folded light curve using the photometric period, $P_{\rm orb}$=3.6 hours, is presented in Fig. 4.4, together with the ort periodogram (upper panel) and the radial velocity curve phase folded over the same orbital period (middle panel). The light curve shows two uneven maxima at phases 0.25 and 0.75, being the first maximum, $\phi = 0.25$, brighter than the second one, and equal minima at phases 0 and 0.5. The maximum variation is almost 0.2 magnitudes in the r band. Ellipsoidal modulation might be the cause of such a variability, although one would expect to have equal maxima, spots in one of the hemispheres of the secondary star could explain the uneven maxima (O'Connell effect, see Liu & Yang 2003). We explored the activity on the secondary star by measuring the equivalent width of the Hα line. The obtained value, EW = 1.3 Å, is at the lower end of the activity scale, which might contradict the hypothesis just mentioned.

Photometry in the *i* band was obtained for SDSS2243+3122 for four nights. We estimated the orbital period, by computing a periodogram, to be $P_{\rm orb}$= 2.86 hours (upper panel of Fig. 4.5). The

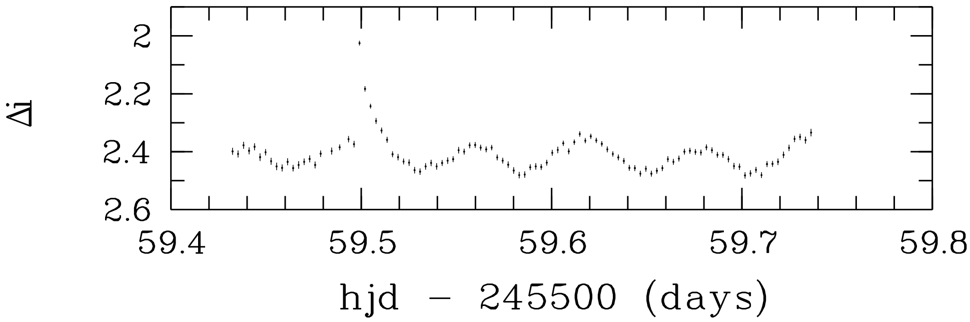

Figure 4.6: Differential photometry in the *i* band obtained for SDSS2243+2122 the 15th August 2009. A flare of ~ 25 minutes length with a relative enhancement of ~ 0.4 magnitudes was observed.

radial velocity curve phase folded with the photometric orbital period is shown in the upper panel of Fig. 4.5. Using the photometric period we could put the spectroscopic observations in phase obtained 25 days (208 binary cycles) later without cycle count ambiguity. We combined the epochs of the spectrocopic phase zero and the photometric minimum to obtain a final estimate of the orbital period of $P_{\rm orb} = 0.11954 \pm 0.00003$ days. In the bottom panel we show the light curve. As for SDSS0853+0720 uneven consecutive maxima and two equal minima are observed, but in this case the brightest maximum is observed at $\phi = 0.75$ (see Fig. 4.5). The variability in the light curve presents a maximum difference of 0.2 mag in the *i* band and it's nature might be due to ellipsoidal modulation. The night of the 15th of August 2009 a flare with ~ 25 minutes length in the decay, and rising Δr by 0.35 mag., was observed (see Fig. 4.6), which would strengthen the argument of magnetic activity being the cause of the disparity in the maxima. Although, the origin of the O'Connell effect might be a mix of different phenomena, such as spots and capture of circumstellar material (Liu & Yang 2003). With its $P_{\rm orb}$= 2.86 hours the system in located in the CV orbital period gap. The probability of this system to be a detached CV, that has relaxed to it's equilibrium, instead of being a detached system in which the secondary star has never filled it's Roche lobe is between 4–13 to 1 according to Davis et al. (2008), where the assumed prescription for MB is as given by Hurley et al. (2002) and the efficiency of the CE phase is taken from the numerical calculations from Iben & Livio (1993), $\alpha_{CE} = 0.13 - 0.6$. There are just two other systems with similar properties, HS2237+8154 (Gänsicke et al. 2004) and SDSS0052–0053 (Rebassa-Mansergas et al. 2008), but this is the only one in which a flare has been detected so far.

The minimum filling factors calculated in Sect. 4.2.2 are 0.6 and 0.49 for SDSS0853+0720 and SDSS2243+3122 respectively. It is worth mentioning that both systems have the largest minimum filling factors among the 15 systems.

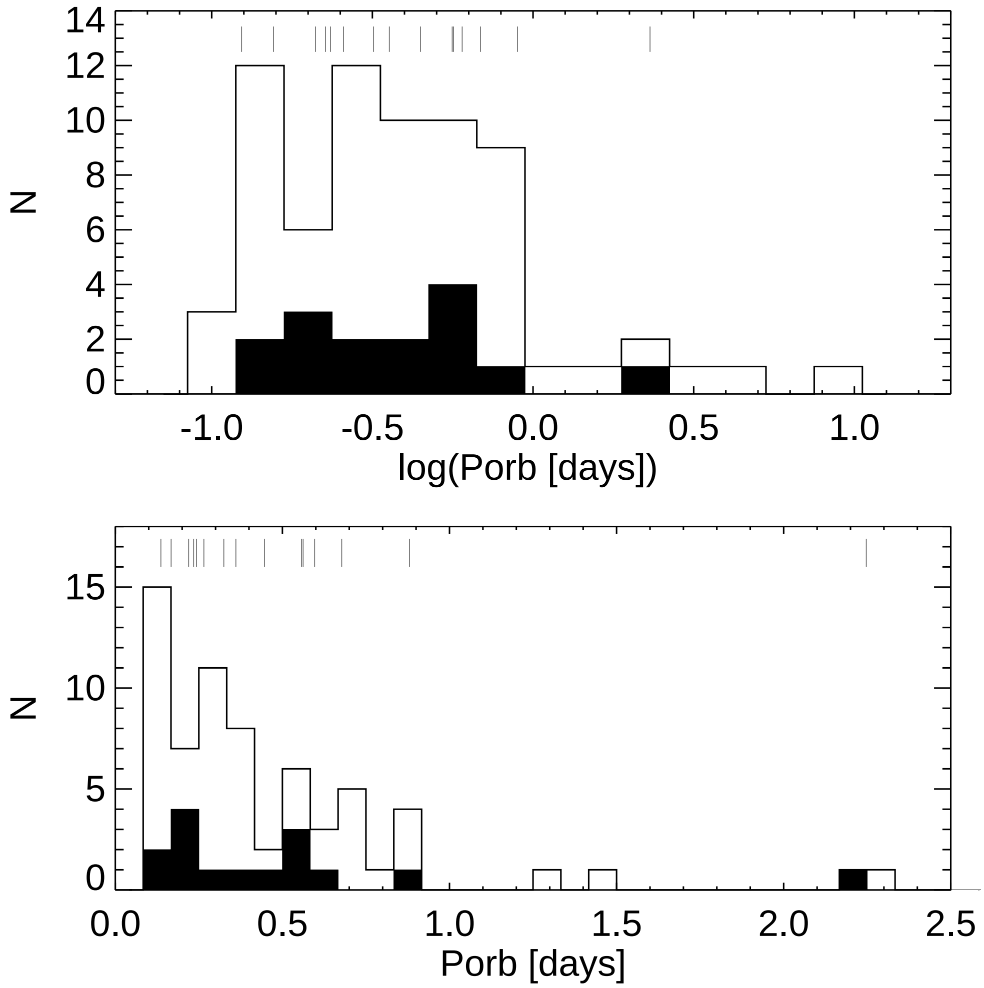

Figure 4.7: Orbital period distribution in days (the upper panel is in logarithmic scale to highlight the absence of systems with longer orbital periods than one day. The plot includes all the known PCEBs listed in Ritter & Kolb (2003) (version v7.12 from 2009) that containing a white dwarf plus a main sequence and the 15 new systems (69 PCEBs in total) for which we give the orbital period in this study marked in the plots and over-plotted in black.

4.3 Discussion

4.3.1 The PCEB orbital period distribution

In Fig. 4.7 we show the orbital period distribution of all the known PCEB from (Ritter & Kolb 2003) containing a white dwarf plus a main sequence and include the 15 new systems (69 PCEBs in total). We show the distribution on a linear and a logarithmic scale. The former to show the continously decreasing number of systems towards longer periods and the latter to be able to compare with past representations. The upper panel shows that the orbital period distribution is flat, dropping dramatically around 1 day. A long tail towards longer orbital periods which extends up to 100 days is predicted by Willems & Kolb (2004), which might indicate that the amount of angular momentum extracted from the orbit during the CE phase is higher than predicted, bringing the systems closer. Nevertheless care must be taken with possible biases. This orbital period distribution contains all the systems known until the date and investigating the biases on the detection of these becomes an almost impossible task. In Chapter 3 we investigated the limits of our criterium to detect systems at long orbital periods and we saw that we should be able to detect longer orbital periods than a day (see discussion in the previous chapter). But, one thing is being able to detect a system and another is to measure it's orbital period. As can be seen in the lower panel of Fig. 4.7, the number of systems decreases with the orbital period in a continuous way, reflecting on one hand the fact that it is easier to measure short orbital periods since they are less time demanding and on the other hand also an accumulation of systems at short orbital periods due to their high $K_{\rm sec}$. The positions of the orbital period of our 15 systems is marked in the figure and plotted in black, we see there that among them only 1 system has a period longer than 1 day. We now investigate the remaining PCEBs presented in Chapter 3 for which we haven't measured the orbital periods to see whether there are long orbital period systems.

4.3.2 Long orbital period candidates

In Chapter 3 we identified 37 systems as PCEB. We measured the orbital period of 15 of these systems. Among the remaining 22 systems without $P_{\rm orb}$ measured we calculated upper limits for 16 of them (Chapter 3, Sect. 3.4.2). We found that 5 have $P_{\rm orb}$<1 day: SDSS0239+2736, SDSS1021+1744, SDSS1028+0931, SDSS1135+0103 and SDSS15245040. We investigated the long orbital period candidates as well as those for which we did not give upper limits on the $P_{\rm orb}$in more detail since they are of most interest for our purpose. We inspected in a case by case the radial velocity variations for these systems (see Fig. 4.8).

- SDSS0734+4105 varies ~ 110 km/s, SDSS0753+1754 varies ~ 190 km/s and SDSS1114+0924 varies ~ 220 km/s, in less than 2 hours, SDSS1047+4835 varies ~ 80 km/s, in less than 30 minutes, implying that these systems must have an orbital period shorter than 1 day.

- SDSS1024+1624 was observed two consecutive nights. The first day the maxima of the radial velocity was covered, and the second day, ~ 25 hours later, almost the same phase was re-observed, implying a maximum of two cycles per day.

- SDSS1055+4729 was observed two consecutive nights, covering the minima in the first night and somewhere close to the maxima in the second night, making the system a good candidate for having a longer orbital period than a day, close to 2 days.

- SDSS1123-1155 was observed three different nights. The first night it almost did not vary, but the time span between the first spectrum and the last in night 1 was 45 minutes, and it looks like being around the minimum, where variations in the radial velocity are slower. The second night, three days later, one spectrum was taken and the same phase was covered, so the maxima of the orbital period is 3 days. Nevertheless two more spectra were taken a day later and they vary around 30 km/s in less than 30 minutes, so it could be that the period is rather short.

- SDSS1635+6201 was observed 6 nights. There are 11 spectra and they all show rather small velocity, so it is a candidate for having a long orbital period.

There are 3 systems for which we derived upper limits on the orbital period based on the RV from the Hα emission line. We look into their RV with more detail, and show the RVs in Fig. 4.8.

- SDSS0142–0835 was observed 7 different nights, spread over 34 days. Radial velocities variation are rather small, making it a good candidate for having long $P_{\rm orb}$.
- SDSS1320+6612 varied $\sim$ 100 km/s in less than 1 hour during the second night that it was observed, so once more this system might have a short orbital period.
- SDSS1724+0733 observed 2 different nights, varied only $\sim$ 40 km/s in $\sim$ 1.5 hours. It is difficult to draw any strong conclusion on this specific system.

We finally inspect the radial velocities of the remaining 6 systems, for which we have no mass estimate of the primary star.

- SDSS0722+3859 was observed in 2 consecutive nights. We could measure the radial velocities only from the Hα emission line and it varies $\sim$ 250 km/s, covering what could be the minimum and the maximum, over $\sim$ 4.5 hours in the first night, so it has a short orbital period.
- SDSS0730+4054 and SDSS1919+6214 vary both $\sim$ 160 km/s in $\sim$ 2 and $\sim$ 3 hours respectively, so they must have a rather short orbital period. RVs of SDSS0730+4054 show a clearly sinusoidal trend, of what could be, if the systemic velocity of the secondary star is close to 0 km/s, a fourth of a cycle, implying a $P_{\rm orb}$close to 9 hours.
- SDSS1316–0037 was observed three consecutive nights, the first and the third night approximately the same radial velocity was observed, hence the system has $P_{\rm orb}$<2 day. During 1 hour it varied 100 km/s so it has rather short orbital period.
- For SDSS1437+5737 there are two spectra taken during the same night and spread over less than 30 minutes, so we cannot learn much from the sub-exposures of the SDSS. We confirmed its PCEB nature from own observations and they point that it might be long orbital period systems. SDSS2258+0710 was also identified from own observations as a PCEB, and since the time spread between them is very long it is difficult to learn more than saying that it might be a long orbital period as well. We don't show the RVs from the sub-spectra for these two systems.

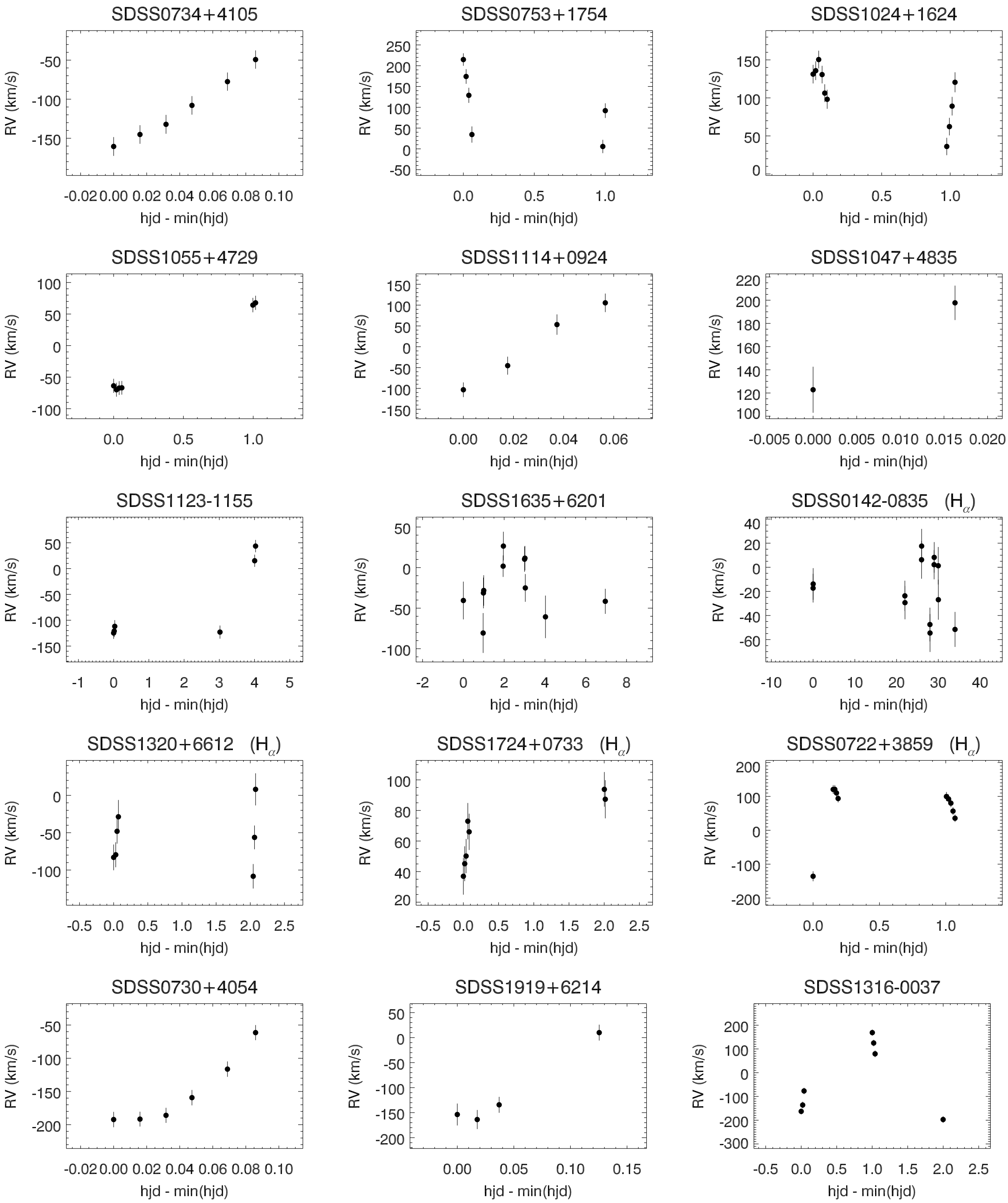

Figure 4.8: From left to right and from top to bottom: 1) Radial velocities from the SDSS sub-spectra for 8 long orbital period candidates. Inspecting their radial velocity variation in time we see that only 3 systems, SDSS1055+4729, SDSS 1123–1155 and SDSS1635+6201 can have $P_{\rm orb} > 1$ day; 2) Radial velocities from the Hα emission line of the SDSS sub-spectra for 4 systems, among which only SDSS1724+0733 can have a long orbital period; 3) Radial velocities from the SDSS sub-spectra for 3 systems for which we have no estimate of the mass of the primary star and no maximum $P_{\rm orb}$ was given. Their RV variation indicates they have short orbital period.

Table 4.4: Maximum orbital period.

System (SDSS)	$P_{orb}{}^{max}$ (days)	System (SDSS)	$P_{orb}{}^{max}$ (days)
SDSS0142–0835	121	SDSS1114+0924	1
SDSS0239+2736	0.784	SDSS1123-1155	3
SDSS0722+3859	1	SDSS1135+0103	0.269
SDSS0730+4054	1	SDSS1316-0037	1
SDSS0734+4105	1	SDSS1320+6612	1
SDSS0753+1754	1	SDSS1437+5737	$P_{orb}>1$
SDSS1021+1744	0.571	SDSS1524+5040	1.082
SDSS1024+1624	1	SDSS1635+6201	11
SDSS1028+0931	0.891	SDSS1724+0733	114
SDSS1047+4835	1	SDSS1919+6214	1
SDSS1055+4729	2	SDSS2258+0710	$P_{orb}>1$

To sum up, we have that among 37 PCEBs, 29 systems have $P_{orb}<1$ day, and 8 systems could have $P_{orb}>1$ day (only 1 confirmed). We list the maximum periods of the 22 systems without P_{orb} measure in Table 4.4. To constrain the CE efficiency it is necessary to observe these systems and measure their true orbital period. If the CE phase is very efficient (small values of α_{CE}) extracting energy and angular momentum from the orbit then we would expect less systems at short orbital periods (Politano & Weiler 2007). The orbital period distribution of WDMS binaries predicted from Willems & Kolb (2004) consists of two different kind of populations: a large fraction of the systems, $\sim$ 75%, which have very long orbital periods and have never gone through a CE phase; and a smaller fraction, $\sim$ 25%, of systems which have gone through a CE phase. The later distribute peaking around 1 day and with a long tail towards up to 100 days.

Davis et al. (2009) calculated the present day population of PCEBs for different values of the CE efficiency parameter α_{CE} and compared their orbital period distribution with that one of known PCEBs until 2009 for a range of secondary masses (see Fig. 4.9). They find that the best solution that fits the data has a distribution with an initial mass ratio on the form $n(q_i) = q_i^{-0.99}$. They predict a smooth decline of systems towards longer orbital periods (red lines) in contrast with the sharp observed cut at 1 day (gray histograms). Systems with later spectral types secondaries have shorter orbital periods. Since the discovery of WDMS binaries has been biased towards systems with late spectral types secondaries this implies that the orbital period distribution is biased towards short orbital periods. Davis et al. (2009) corrected for the detection biases (green lines), and even though the observed and the predicted distributions are in a better agreement, a KS test over the CDF gives a better result, 0.35 versus 0.11 (see right panels of the same figure), the predicted tail towards long orbital periods is still present. We contribute with new 15 PCEBs spread from M3 to M6 in the secondary spectral type, corresponding to a mass range of 0.196-0.380 $M_\odot$ according to the spectral type-mass relation from Rebassa-Mansergas et al. (2007). All but one have shorter orbital period than a day, so that we can not reconcile observations and predictions yet. This highlights the relevance of measuring the P_{orb} of the 7 new long orbital period candidates.

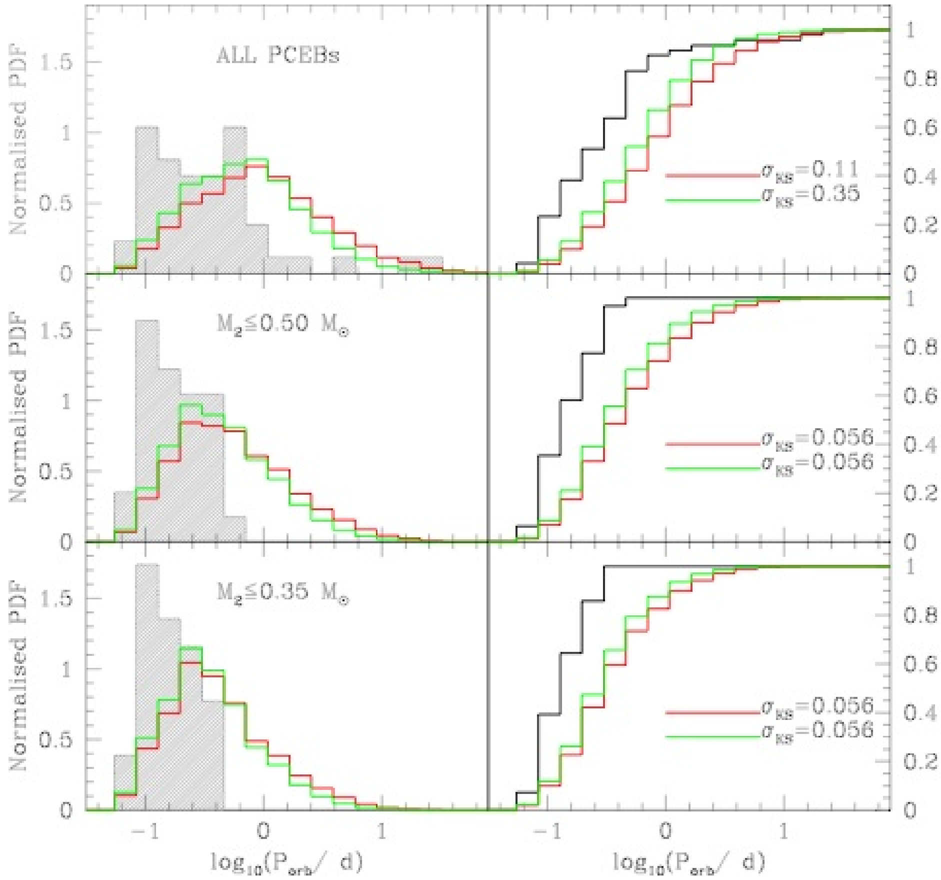

Figure 4.9: Orbital period distribution of PCEBs from Davis et al. (2009). The gray histograms show the known PCEBs until 2009, for 3 different ranges in the secondary mass. The red line shows the calculated distribution of the intrinsic population ($n(q_i) = q_i^{-0.99}$, model A where $\alpha_{CE} = 1.0$) and the green is the same but taking into account the detection probability. The right panels show the CDF with the KS significance level (σ_{KS}) indicated. Figure was taken from Davis et al. (2009).

4.3.3 The white dwarf mass distribution of PCEBs

In order to investigate the white dwarf masses of PCEBs we select systems which have $T_{\rm eff}>$ 12000 K and relative error lower than 25%, so that its spectroscopic masses are reliable Kepler et al. (2007). After this strong filtering we end up with only 11 PCEBs from our initial sample of 37. We investigated the white dwarf masses of other systems and include 45 systems given in the cataloge from Ritter & Kolb (2003) (see Table 1.2.2).

The $M_{\rm wd}$ distribution (see Fig. 4.10) has a mean mass of 0.617 ± 0.165, and presents two peaks. Although the number of PCEB is very small in order to contrain their positions with enough accuracy one is located around 0.58 $M_\odot$ and the second at 0.85 $M_\odot$. Both peaks are present in field WDs being the later weaker in single WDs (Liebert et al. 2005). The distribution has a more pronounced tail towards lower masses than the found for our wide WDMS sample. It is thought that all WDs with $M_{\rm wd} < 0.47$ M$_\odot$ are product of binary evolution Marsh et al. (1995) (see Chapter 1). Single stars would need more time than the age of the Galaxy to achieve this stage, while if being member of a close binary, a common envelope phase achieved during the red giant branch would allow the star to loose it's envelope, becoming a white dwarf with He in it's core. We have 6 systems with $M_{\rm wd}$<0.47 M$_\odot$ which did not show any significant radial velocity in our analysis, SDSS0111+0009, SDSS0852+1154, SDSS0944+6143, SDSS1235+0030, SDSS1239+0055 and SDSS1241+6007, but as shown in Fig. 3.9 the lower the mass of the primary star the less sensitive we are with our detection criterium, so it could be that they are indeed close binaries and these systems should be reobserved.

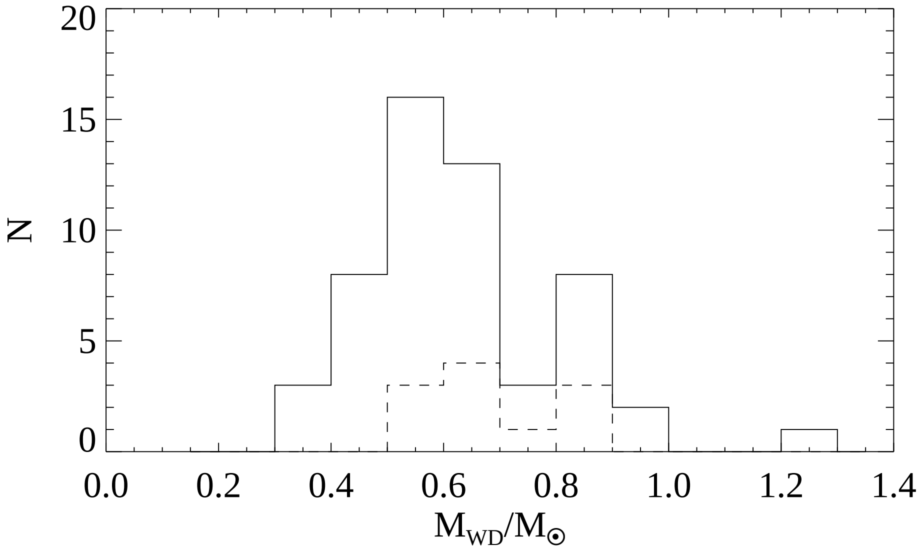

Figure 4.10: Distribution of white dwarf's mass for all the known PCEB binaries that contain a DA as primary from Ritter & Kolb (2003) and the PCEBs from this work.

4.4 Summary

We have determined the orbital periods of 15 sytems, and only one of them has an orbital period longer than one day. The orbital period distribution of all the known PCEBs apparently presents a sharp cut at around one day. This seems to contradict the distribution predicted by Willems & Kolb (2004) and Davis et al. (2009), which contains an extended tail of systems with orbital period up to 100 days. This could imply that the CE phase might extract more energy and angular momentum than previously thought. But one must notice that the actual period distribution is biased towards short orbital periods, since their measurement is less time demanding than for those with longer orbital periods and since the secondaries are also biased towards late spectral types. Investigating in more detail the remaining 22 PCEBs that were identified in Chapter 3 for which we don't have a measurement of the orbital period we have identified 7 long orbital period (> 1 day) candidates and 15 short orbital period (<1 day) candidates. To learn about the efficiency of the CE phase it is very important to measure their true orbital period. The white dwarf mass distibution of PCEBs is similar to that of field white dwards, presenting two peaks, one around 0.58 $M_{\odot}$ and the other around 0.84 $M_{\odot}$. It has an extended tail towards low masses, in agreement with the idea of all He core white dwarfs ($M_{\rm wd}$<0.47 $M_{\odot}$) being product of a common envelope phase. We have 6 WDMS with lower mass than this limit, making them good candidates for being close binary systems, this systems should be reobserved to proof their close binary nature.

Chapter 5

Activity binarity relation

We study the influence of binarity in the stellar activity of the secondary stars, measuring the equivalent width of the Hα emission line originating from the chromosphere of the red dwarf. We would like to know if the fast rotating secondaries in PCEBs harbor stronger magnetic fields than their slow-rotating counterparts and if so, whether we can make use of magnetic activity to single out the PCEBs among a sample of WDMS binaries. We find that the fraction of active stars increases with the spectral type, a result found for single field red dwarfs as well, though we find a higher fraction at earlier spectral types. This result can be explained by the age of the systems. We find that the majority of the PCEBs contain active secondaries, and at a given spectral type the EW(Hα) is higher than for wide WDMS binaries. We also investigate the relation between the estimated distances, $d_{\rm sec}$ and $d_{\rm wd}$, and the activity as a possible cause for the previously found mismatch.

5.1 Introduction

Chromospheric magnetic activity, can be measured from CaII H and K for spectral types G and K. Since M stars have very little flux in the blue, their spectral energy distribution dominates at longer wavelengths than 6500 Å, it becomes more difficult to analyze activity from these lines. In active G stars there is a correlation between the fluxes from CaII H and K lines and the emission which fills in the Hα absorption line (Stauffer & Hartmann 1986), making Hα a better activity indicator for later spectral types. Early models of M stars have shown that the photospheric Hα absorption line is very weak due to their low temperatures, but the chromosphere can produce a prominent Hα line, which can be in absorption or in emission (Cram & Mullan 1979, 1985). Stauffer & Hartmann (1986) studied a sample of M stars, they measured Hα EW and used broad band photometry to separate between different activity levels. They find that redder objects have higher EW and claim that the stronger the absorption the weaker the activity. Recently, Walkowicz & Hawley (2009) studied a sample of 81 close dM3 stars. They took intermediate and high resolution spectra covering simultaneously the CaII H and K lines and the Hα line to allow comparison of both elements at the same time. They restricted their sample to M3 stars to remove a dependence with the spectral type and choose M3 since it is at the boundary of being total convective ($\sim$ 0.35 $M_{\odot}$). From spectra of intermediate resolution (R $\sim$ 2000) they found that for weak and intermediate activity (EW(CaII K) < 2 Å), there is no correlation between CaII K line (CaII H is normally not used since it is blended with Hϵ) and the emission of Hα while for stars with strong activity one observes a positive correlation, a monotonic increase with the CaII K EW. They find that weak active stars can have Hα in absorption and that to distinguish between inactive and weak active stars high resolution spectroscopy is needed. When using Hα emission as an activity indicator one has to be cautious and keep in mind that it will only give a lower limit to the total number of dM active stars.

The fraction of field M stars with Hα in emission increases with the spectral type (Hawley et al. 1996). Based on a study on 7840 single M stars, West et al. (2004) found that the fraction of active stars is very small for early stars, has a steep increase in the range M3-M5 and, reaches a maximum around M7. They also find a correlation between activity and distance to the Galactic plane: stars closer to the plane would be younger and therefore they would be active. From a later study, based on a very large sample of dM spectra from the SDSS-DR5, West et al. (2008) found similar results, but with a more pronounced enhancement at Sp2=M5, where $\sim$ 60% of the systems are active. As before they find that for a given spectral type the activity fraction decreases with the distance to the Galactic plane and by comparison with 1D dynamical models conclude that this effect can be explained with a dynamically heated disk and a dependence of the activity lifetime with the spectral type. They conclude that the activity lifetime is longer for later spectral types, varying from 1.8 Gyr for M0 to 8.0 Gyr for M7 and with a very steep increase at the boundary where stars become completely convective, between M3-M5, which they interpret as a different physical mechanism responsible for the magnetic field.

Activity is expected to be enhanced in stars when being members of a close binary system. Due to tidal forces, they would be forced to rotate faster than single stars of the same age, enhancing activity. Several studies have been carried out in this direction. Basri (1987) found that the activity does not change when a star is a member of a binary system. Strassmeier et al. (1990) found that while activity in main sequence binary stars show higher levels of activity than single stars (rotation is faster due to tidal forces), evolved systems show no obvious difference. The components of wide binary systems have never interacted, therefore the secondary stars should be comparable with single stars. We investigate the activity and compare the results between wide binaries and PCEBs.

5.2 Analysis

We have studied the activity in our WDMS binaries by measuring the EW of the Hα line. To get a true continuum for the red dwarf we subtracted the contribution of the white dwarf from the SDSS spectrum. We used the white dwarf that best fitted the SDSS WDMS spectrum (see chapter 2). We measured the equivalent width of Hα selecting interactively the emission region. For systems

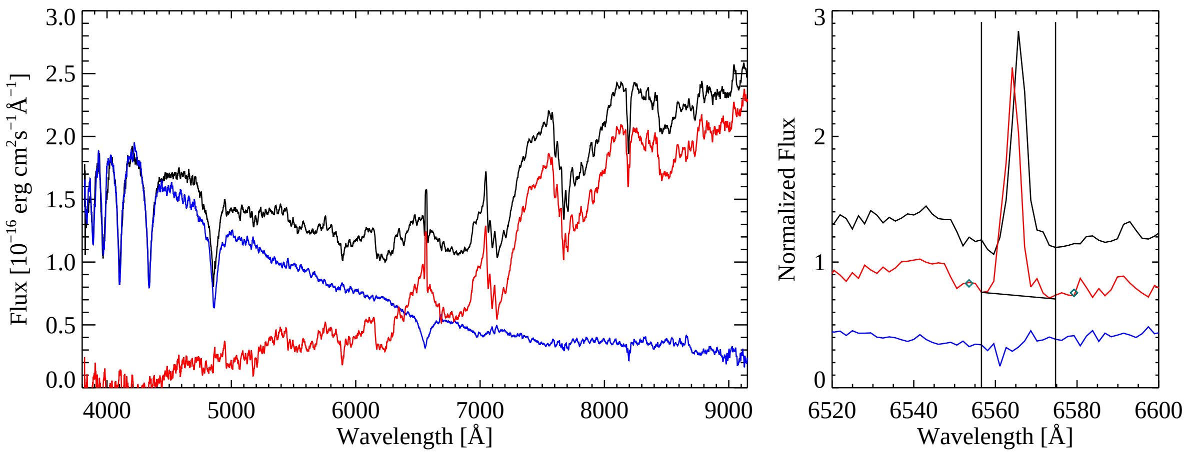

Figure 5.1: The spectrum of SDSSJ030138.24+050218.9 (black) with the best fitted white dwarf (blue) and the residual rew dwarf (red). A zoom into the Hα emission line is plotted in the right panel, with the selected region for measuring the EW plotted with vertical lines, and the underlying continuum is also shown.

with no obvious emission we chose the range 6556-6570 Å. We assumed a continuum level of constant slope defined by the median flux in two neighboring regions around Hα of 11 Å in size (see Fig. 5.1). We consider active those stars with EW > 1 Å for comparison with previous studies.

5.3 Fraction of active stars

The fraction of active stars for wide and for close binaries is shown in the two upper panels in Fig. 5.2. We find that among 278 WDMS (277 wdms + 1 candidate), 144 are active. The fraction of active stars in PCEBs is $\sim$ 90 %, significantly higher than the fraction of active stars in wide binaries, which is $\sim$ 45 %.

In the upper left panel of Fig. 5.2 we plot the fraction of active stars for the wide WDMS, and plot the values obtained for field stars from West et al. (2008) with squares. The fraction of active stars is higher at earlier spectral types. For wide systems we find that the fraction of active stars is smaller at early spectral types, increases with the spectral type and reaches a maximum at M5 and M6. Although the general trend is consistent with results in field M stars (West et al. 2008), the fraction of dMe in the range M0 – M3 is much higher, 40 % versus 10 %. Our wide systems can be contaminated with PCEB by up to $\sim$ 12 % (Willems & Kolb 2004). Assuming this 12 % of PCEB are distributed in spectral type according to our previous result (see 3.4.1), we don't expect to see more than $\sim$ 50 % of them in that spectral type range. We have 185 wide WDMS with spectral type between M0 – M3, so we would have less than 13 PCEB in our sample, being

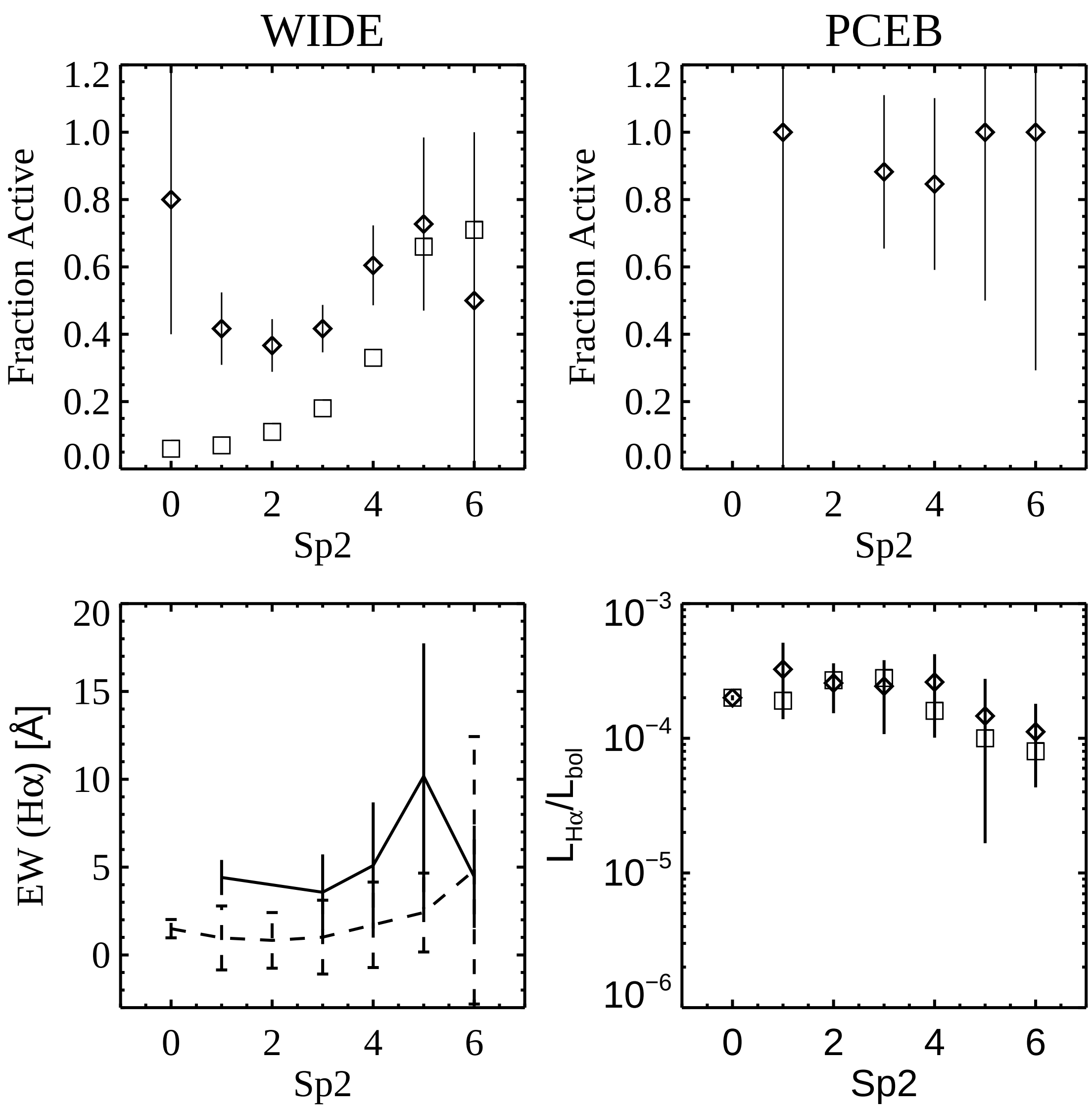

Figure 5.2: Upper panels: fraction of active stars as a function of the secondary spectral type for WIDE (left) and for PCEB (right). On the upper left panels the fraction of active stars from field M stars from West et al. (2008) is plotted with squares for comparison. Lower left panel: mean Hα EW as a function of spectral type (Sp2) for wide systems (dashed-dotted line) and for PCEBs (solid line). Right panel: Strength of magnetic activity (diamonds) for all the WDMS compared with dMe field stars from West et al. (2008).

the majority M3. To match the fraction of active stars with the one given by West et al. (2008), we would need a PCEB fraction of ~ 57%. In other words the "missing" PCEBs are not enough to explain the higher fraction of dMe. In Sect. 5.5 we investigated the age as a possible reason of such enhancement, finding that dMe in this spectral type range, are young systems, younger than the activity lifetime. Silvestri et al. (2005) studied the activity in a sample of wide WD+dM binaries. They found that ~ 16 % of the systems where active. The fraction, although higher

Table 5.1: Mean EW(Hα) for wide and close dMe, with the number of stars in each spectral type bin given in parenthesys.

$Sp2$	EW_{WIDE}	EW_{PCEB}
M0	1.50 (5)	-
M1	0.97 (36)	4.41(1)
M2	0.83 (60)	-
M3	1.01 (84)	3.57 (17)
M4	1.72 (43)	5.10 (13)
M5	2.41 (11)	10.13 (3)
M6	4.81 (2)	4.45 (2)

than for field M stars is still lower than our result. This discrepancy could be due to two reasons. They measure the equivalent width for the M stars without subtracting the white dwarf, deriving lower values since the continuum of the red dwarfs would be enhanced by the white dwarf's and in some cases the Hα could be even masked. On the other hand a large fraction of the systems they studied are older than 4 Gyr, and less active systems are expected.

In the left bottom panel of Fig. 5.2 we plot the mean EW as a function of spectral type for wide (dashed-dotted line) systems and for PCEBs (continuous line) (SDSS0420+0649 has been excluded since it might be a CV, see Sect. 4.2.1 for details). We see that in both cases it increases towards later spectral type. That is due to decreasing photospheric luminosity with spectral type and not to an increase in the chromospheric activity (Stauffer & Hartmann 1986). The lower the temperature the redder the object and the lower the contribution of the photosphere around Hα therefore, the higher the contrast with an emission in Hα, which means an increase of the EW. At each spectral type there is a scatter in the EW which seems to increase with the spectral type. This spread can reflect different rotation levels at each spectral type, which can be an age effect (young objects rotate faster) or be associated with the orbital period of the PCEBs. In Sect. 5.5 we study the ages and their relation with the activity in detail.

We give the mean EW(Hα) for PCEBs and wide systems in table 5.1. We include the number of systems used to compute the mean at each spectral bin in parenthesis. Although the number of objects is small in order to draw any strong conclusion, the mean EW(Hα) is higher for PCEBs than for wide binaries at every spectral type in agreement with the idea exposed at the beginning of the section.

5.4 Activity strength

The strength of magnetic activity can be quantified using the ratio between the luminosity in Hα and the bolometric luminosity, $\chi_{H\alpha} = L_{H\alpha}/L_{bol}$. This value can be inferred by multiplying the EW of Hα by the ratio of the flux in the continuum around Hα to the bolometric flux,

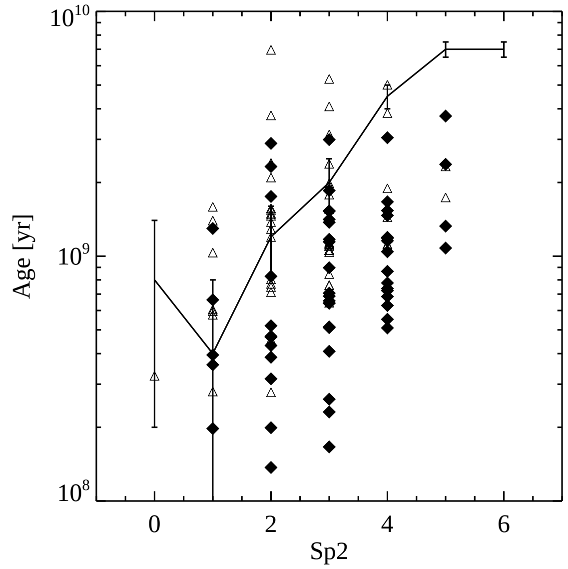

Figure 5.3: Age of the systems as a function of the spectral type of the secondary star. Active systems are plotted with filled diamonds, while inactive systems are plotted with open triangles. The line indicates the activity lifetime given by West et al. (2008).

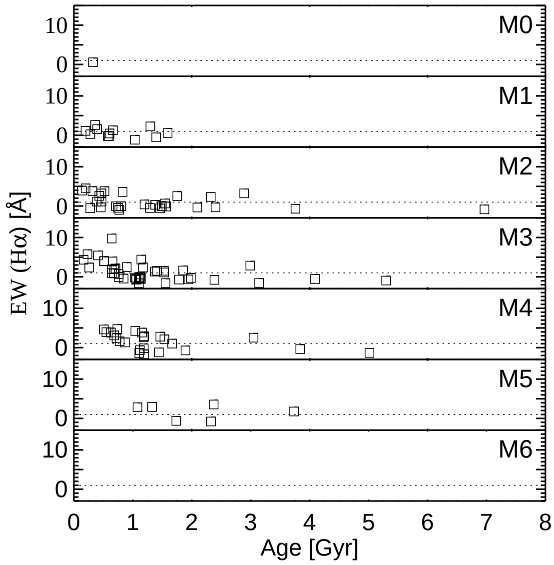

Figure 5.4: Hα EW and age of the systems for different spectral types of the secondary star. All systems above the dotted line (EW $>$ 1 Å) are active.

$\chi = f_{\mathrm{H}\alpha}/f_{bol}$ (Walkowicz et al. 2004; West et al. 2004, 2008). Based on a sample of M stars covering the spectral range M0-L0, Walkowicz et al. (2004) tabulated χ as a function of spectral type and we make use of their values. In the bottom right panel of Fig. 5.2 we plot the calculated $\chi_{\mathrm{H}\alpha}$ as a function of the spectral type (diamonds) together with values from the fit given by West et al. (2008) for field dM stars (squares). The strength of magnetic activity is more or less constant for earlier spectral types than M4 and a decrease towards later spectral types. Although the results are similar to those from field stars, there is a systematic trend to higher values, effect which is related to higher EW for the PCEBs.

5.5 Binary age

For wide binaries the age of the system can be estimated from the age of the white dwarf, which is the sum of the cooling age of the white dwarf (time passed since the planetary nebulae phase, t_{cool}) and the time it took to evolve a star from the main sequence to a white dwarf of mass M_{wd} (t_{evol}), that is $t = t_{cool} + t_{evol}$. For all the systems with reliable stellar parameters we calculated the cooling age of the white dwarfs by interpolating the cooling tracks provided by Wood et al. (1995) for CO white dwarfs and Althaus & Benvenuto (1996) for He core white dwarfs, i.e. for

WDs with masses below 0.47 $M_{\odot}$. We asumed the initial to final mass empirical relation from Catalán et al. (2008) given by:

$$M_f = (0.096 \pm 0.005)M_i + (0.429 \pm 0.015), \quad (5.1)$$

for M_i <2.7 $M_{\odot}$ and:

$$M_f = (0.137 \pm 0.007)M_i + (0.318 \pm 0.018), \quad (5.2)$$

for larger masses. We calculated the nuclear time scale for the progenitor mass, t_{evol}, using the relation from Iben & Laughlin (1989):

$$\log t_{nucl} = 9.921 - 3.6648 \log M + 1.9697(\log M)^2 - 0.9369(\log M)^3, \quad (5.3)$$

We added the calculated nuclear time to the cooling ages. Please note that the total age derived in this way represents a reliable estimate for wide WDMS only, i.e. for systems that did not interact in the past. The total age of PCEBs has to be calculated by reconstructing common envelope evolution and significantly depends on the common envelope efficiency (Nelemans & Tout 2005) (Zorotovic et al. 2009, in prep.). As there are probably some PCEBs even among those systems that did not show radial velocity variations, the given total ages can be significantly wrong for individual systems. However, the majority of the WDMS without radial velocity variations are wide WDMS and the derived ages can therefore be used for describing the typical age of wide WDMS binaries.

In Fig. 5.3 we plot the age of the system as a function of spectral type, active systems are plotted with filled diamonds and inactive with black triangles, the line indicates the mean activity lifetime given by West et al. (2008). Most of the active systems are younger than the activity lifetime explaining the higher fraction of active stars with respect to field stars obtained in Sect. 5.3. For comparison of our results with the results from Silvestri et al. (2005) we plot the EW versus the age for different spectral types as in their Fig. 4 and show it in Fig. 5.4. Our systems are in general younger than the sample from Silvestri et al. (2005) which can then explain why we obtain a higher fraction of active systems at each spectral type (see Sect. 5.3).

5.6 Activity and distance

We estimated the distances to our subsample of 193 WDMS binaries with DAs as primary stars in chapter 2. We have two estimates, one coming from the fit to the WD, $d_{\rm wd}$, and another coming from the fit to the secondary spectral type, $d_{\rm sec}$. We obtained a disagreement of more than 1.5σ for about 30% of the systems. Rebassa-Mansergas et al. (2007) suggested that activity could be the cause of such discrepancy. Active M stars show larger radii (López-Morales & Shaw 2007) and lower effective temperatures at constant luminosities (Morales et al. 2008) than their inactive counterparts, resembling earlier spectral types and leading to a larger distance estimate. We have distinguished between active and inactive systems so we investigate this possibility in detail.

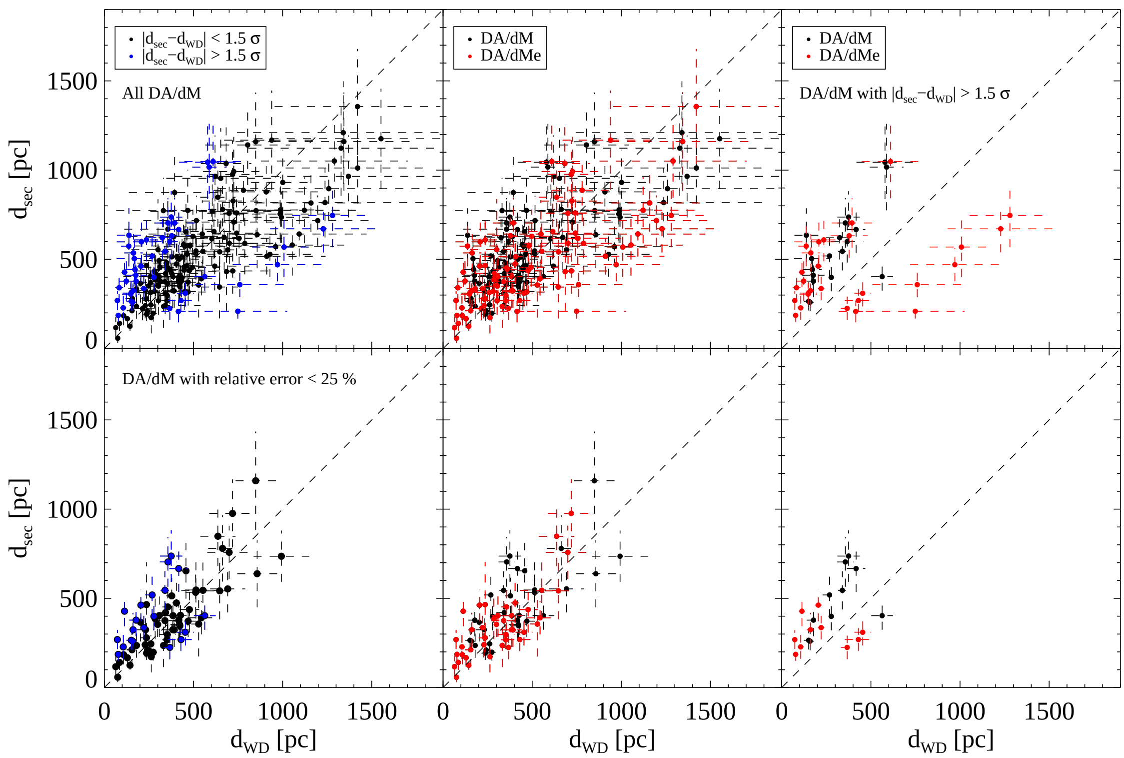

Figure 5.5: Distances estimated to the WDMS with DA as primary in chapter 2. In the upper panels all the systems are included, independent on their errors, while in the bottom panels only those with relative error smaller than 25% are included. In the left panels we plot systems differing in more than $1-\sigma$ with blue filled circles. In the middle panels we plot systems with active secondaries with red filled circles. In the left panels we show only systems that differ more than $1-\sigma$ and plot systems with active secondaries with red filled circles.

In the left panels of Fig. 5.5 we plot the two estimated distances, $d_{\rm sec}$ against $d_{\rm wd}$, for all the systems (upper panel) and for those that have stellar parameters of the DA with relative errors smaller than 25% (bottom panel), plotting in blue the systems for which the difference between $d_{\rm sec}$ and $d_{\rm wd}$ is larger than 1.5σ. Among the 193 DA/dM binaries, 98 contain active secondary stars (middle panels, red filled circles). In the right panels we plot only those systems for which we obtained a difference between the two estimated distances larger than 1.5σ, with systems with active secondaries plotted in red. While around 50% of all the DA/dM contain active secondaries, if we only select the systems for which we obtained a difference between the two estimated distances larger than $1.5-\sigma$, more than 60% of them contain active secondaries (plotted in red in the right panel). We expected to have the active systems located at the left side of the right panels, but as we can see they are distributed over $d_{\rm wd} > d_{\rm sec}$ too. In fact, we found the opposite: the majority of the systems with longer $d_{\rm wd}$ are active. We can only conclude that for around 50% of the systems activity might be the cause of the discrepancy between the distances derived from the dM and the WD, but this is still work in progress.

5.7 Summary

We have measured the activity of the secondary stars, finding that wide binaries have a similar trend as field stars, that is an increase in the number of active stars with spectral type. Although, at earlier spectral types than M4 the fraction of active stars is higher than for field stars, and also higher than found before in WDMS wide systems by Silvestri et al. (2005). To explain such effect we investigated the possibility of PCEB contamination at this spectral types and also calculated the age of the systems. We conclude that since the systems with secondaries in this spectral type range are younger than the activity lifetime it reflects an age effect. At least 90% of the PCEB are active, since we have just used the Hα emission as an activity indicator, this value is just a lower limit, and it might well be that all the PCEB are active, pointing to an enhancement of activity due to the fact of having a companion star. The EW of the Hα line is higher for close systems at each spectral type, but on the one hand the number of close binaries at earlier spectral types is rather small. And on the other hand as we have seen in chapter 4 most of the close binary stars have a rather short orbital period, which when having a hot white dwarf as a primary would cause the secondary's surface to be heated, enhancing the Hα emission line. We investigated whether the difference in the two estimated distances from chapter 2 could be explained by the activity of the secondary star, finding a positive result for $\sim 50\%$ of the systems. A more detail analysis based on a larger database is in progress and will give more light into the activity-binarity relation.

Chapter 6

The eclipsing system SDSS1212-0123

From optical photometry we show that SDSSJ121258.25–012310.1 is a new eclipsing, post common–envelope binary with an orbital period of 8.06 hours and an eclipse length of 23 minutes. We observed the object over 11 nights in different bands and determined the ephemeris of the eclipse to $\mathrm{HJD_{mid}} = 2454104.7086(2) + 0.3358706(5) \times \mathrm{E}$, where numbers in parenthesis indicate the uncertainties in the last digit. The depth of the eclipse is 2.85 ± 0.17 mag in the V band, 1.82 ± 0.08 mag in the R band and 0.52 ± 0.02 mag in the I band. From spectroscopic observations we measured the semi-amplitude of the radial velocity $K_2 = 181 \pm 3$ km/s for the secondary star. The stellar and binary parameters of the system were constrained from a) fitting the SDSS composite spectrum of the binary, b) using a K-band luminosity-mass relation for the secondary star, and c) from detailed analyses of the eclipse light curve. The white dwarf has an effective temperature of 17700 ± 300 K, and its surface gravity is $\log g = 7.53 \pm 0.2$. We estimate that the spectral type of the red dwarf is M4 ± 1 and the distance to the system is 230 ± 20 parsec. The mass of the secondary star is estimated to be in the range $M_{\mathrm{sec}} = 0.26 - 0.29\ \mathrm{M}_\odot$, while the mass of the white dwarf is most likely $M_{\mathrm{wd}} = 0.46 - 0.48\ \mathrm{M}_\odot$. From an empirical mass-radius relation we estimate the radius of the red dwarf to be in the range $0.28 - 0.31\ \mathrm{R}_\odot$, whereas we get $R_{\mathrm{wd}} = 0.016 - 0.018\ \mathrm{R}_\odot$ from a theoretical mass-radius relation. Finally we discuss the spectral energy distribution and the likely evolutionary state of SDSS1212–0123.

6.1 Introduction

In this chapter we report the discovery of a new eclipsing PCEB. In our ongoing search for PCEBs among white-dwarf/main-sequence binaries (Schreiber et al. 2008; Rebassa-Mansergas et al. 2007, 2008, 2009), SDSSJ121258.25–012310.1 (Adelman-McCarthy et al. 2008) (henceforth SDSS1212–0123) was included in our target list for photometric monitoring of candidate objects. The serendipitous discovery of a binary eclipse from time-resolved differential photometry triggered a photometric and spectroscopic follow-up. Only seven eclipsing binaries containing a white dwarf and a low mass main sequence star were known until 2007. Since then another three eclipsing systems have been published (Steinfadt et al. 2008; Drake et al. 2009), and a further three systems have been discovered by us (Pyrzas et al. 2009). Eclipsing binaries are of great interest since they offer the possibility of deriving fundamental properties of stars with a high accuracy. SDSS1212–0123 was firstly listed as a quasar candidate by Richards et al. (2004) and later classified as a DA + dMe by Silvestri et al. (2006). It contains a relatively hot white dwarf (from now on primary) and an active mid-type dM star (from now on secondary).

We summarize our current knowledge about this source from own observations and archival work. It is organized as follows. In Sect. 6.2 we describe the observations and reductions. In Sect. 6.3 we present the results, we study the evolution of the system in Sect. 6.4 and conclude in Sect. 6.6.

6.2 Observations and reductions

6.2.1 IAC80 and AIP70 photometry

Optical photometric observations were obtained using two different telescopes over 11 nights. The 80 cm telescope IAC80 in Observatorio del Teide, Spain, was equipped with the standard CCD camera and the 70 cm telescope of the Astrophysical Institute Potsdam at Babelsberg was used with a cryogenically cooled 1x1 k TEK-CCD. A log of observations is presented in Table 6.1. A field of ~ 3 arc minutes was read with the IAC80 CCD camera, and we used a binning factor of 2 in both spatial directions (scale of 0.6”), while we used a binning factor of 3 for the 70 cm telescope (scale of 1.41”), in order to decrease the readout time and improve the signal to noise. Reduction was performed using standard packages in IRAF[1] and MIDAS. Differential magnitudes were obtained with respect to the comparison star SDSS J121302.39–012343.5 (see Fig.6.1), with magnitudes *ugriz*=17.40, 16.00, 15.51, 15.36, 15.30. SDSS magnitudes were transformed into Johnson’s using equations taken from the Sloan pages[2]. Neglecting the color term, we calculated absolute magnitudes of SDSS1212–0123. The estimated error of the absolute calibration is 0.05 mag.

6.2.2 Spectroscopy

Spectroscopic follow up observations were obtained during the period 16-19 May 2007 with the LDSS3 imaging spectrophotograph at the Magellan Clay telescope. Ten spectra were taken for SDSS1212–0123. Exposure times varied from 300 to 600 seconds. Seeing and transparency were highly variable. The VPH_Red grism and an OG590 blocking filter were used. The detector

[1]IRAF is distributed by the National Optical Astronomy Observatory, which is operated by the Association of Universities for Research in Astronomy, Inc., under contract with the National Science Foundation, http://iraf.noao.edu

[2]http://www.sdss.org/dr7/algorithms/sdssUBVRITransform.html

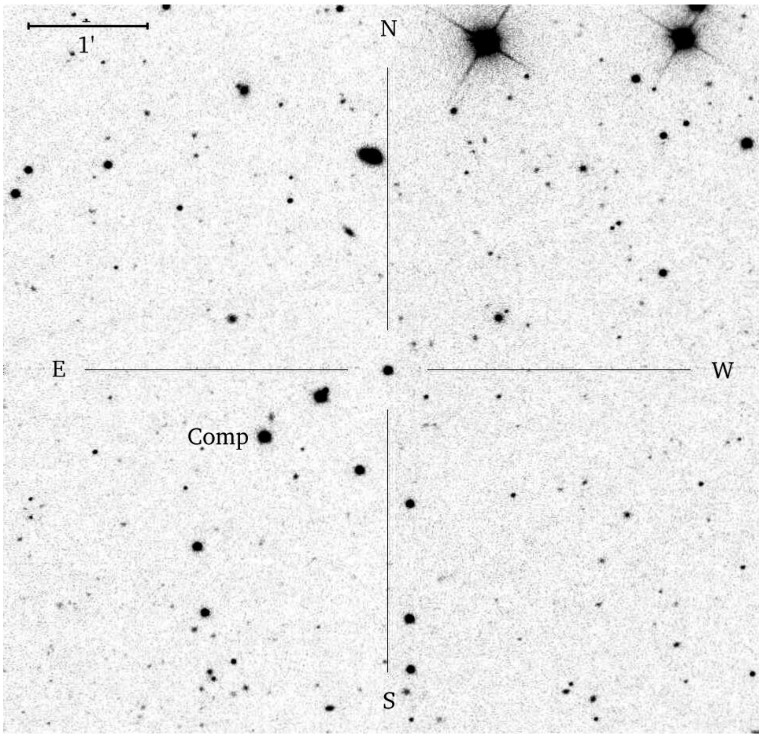

Figure 6.1: SDSS image of SDSS1212–0123 (in the cross-hair) and the comparison star (RA = 12:13:02.39, DEC = −01:23:43.5).

Table 6.1: Log of photometric observations for SDSS1212–0123.

Date	Tel	Filter	$t_{\rm int}$	$N_{\rm obs}$	$\phi_{\rm ini}$	$\phi_{\rm fin}$
04 Jan 2007	IAC80	I	180	74	0.805	1.278
26 Jan 2007	AIP70	V	180	19	0.041	0.156
13 Feb 2007	IAC80	V	70	191	0.607	1.202
14 Feb 2007	IAC80	V	70	221	0.525	1.292
12 Mar 2007	AIP70	I	120	181	0.031	0.946
13 Mar 2007	AIP70	I	120	153	0.377	1.343
14 Mar 2007	AIP70	I	120	49	0.786	1.040
15 Mar 2007	AIP70	R	120	73	0.683	1.023
26 Mar 2007	AIP70	I	120	45	0.994	1.179
21 May 2007	AIP70	I	90	59	0.907	1.097
06 May 2008	IAC80	R	120	32	0.913	1.049

was a STA 4k×4k pixel CCD with two read out amplifiers. We used a slit width of 0.75 arcsec, that together with the spectral resolution R = 1810, gave a coverage of 5800 – 9980 Å at a reciprocal dispersion of 1.2 Åpix^{-1}. Four of the spectra taken at quadrature were obtained through a narrow slit of 0.5 arcsec resulting in a FWHM spectral resolution of 4.8 Å, with the purpose of measuring the radial velocity amplitude with a higher accuracy. Flat-field images were taken at the position of the target to allow effective fringe removal in the red part of the spectra. The spectral images were reduced using STARLINK packages FIGARO and KAPPA, and the spectra were optimally extracted (Horne 1986) using the PAMELA package (Marsh 1989). Wavelength calibration was done using sky lines. Wavelengths of good sky lines were obtained from the atlas of Osterbrock et al. (1996, 1997). A fifth-order polynomial was fitted to 36 sky lines. Spectra were flux calibrated and corrected for telluric lines using spectra of the standard star LTT3218 taken during the same observing run.

6.3 Results

6.3.1 The light curve

The optical light curve of SDSS1212–0123 displays a total eclipse of the primary with length of approximately 23 minutes. The depth of the eclipse is 0.52 ± 0.02 mag in the I band, 1.82 ± 0.08 mag in the R band and 2.85 ± 0.17 mag in the V band (see Fig. 6.2). Eclipse magnitudes are $m_I = 16\overset{\mathrm{m}}{.}56 \pm 0\overset{\mathrm{m}}{.}02$, $m_R = 18\overset{\mathrm{m}}{.}58 \pm 0\overset{\mathrm{m}}{.}08$ and $m_V = 19\overset{\mathrm{m}}{.}68 \pm 0\overset{\mathrm{m}}{.}17$. The much deeper eclipse in the V band is due to the fact that the primary emits most of the light in the blue, while the secondary dominates in the I band. Photometric variability outside of the eclipse, e.g. from an irradiated secondary or from ellipsoidal modulation of the secondary, was found to be less than $0\overset{\mathrm{m}}{.}01$.

At the given time resolution of our photometry, the WD ingress and egress phases are not resolved. Five eclipses were completely covered and the eclipse length was determined in these light curves measuring their full width at half maximum of the flux level. The weighted mean of those five measurements gives an eclipse length of 23 ± 1 min.

6.3.2 Ephemeris

In addition to the five eclipses which were covered completely one further eclipse was covered partially. Using the measured eclipse length from the previous section we thus determined six eclipse epochs (Table 6.2). The eclipses of March 12, 14 and 26, respectively, were not covered due to bad weather conditions. Using a phase-dispersion minimization technique a tentative period was determined, $P_{\mathrm{orb}} = 0.3359 \pm 0.0006$ hours, which was sufficiently accurate to connect all follow-up observations without a cycle count alias.

We then used the six mid eclipse epochs to calculate a linear ephemeris by fitting a line to the cycle number and eclipse epoch:

$$\mathrm{HJD}_{\mathrm{mid}} = 2454104.7086(2) + 0.3358706(5) \times \mathrm{E}, \tag{6.1}$$

where numbers in parenthesis indicate the 1σ uncertainty in the last digits. The observed minus calculated values are tabulated in Table 6.2.

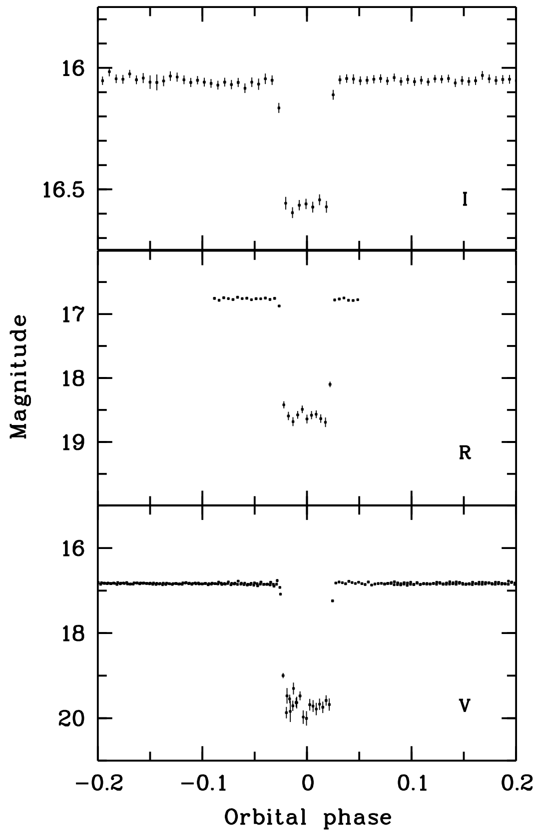

Figure 6.2: Optical photometry from the IAC80 telescope in the V, R and I band (from bottom to top) phase folded over the orbital period, $P_{\rm orb}$ = 8.06 hours. The eclipse has $\sim$ 23 minutes length. Note the different scales for each panel.

Table 6.2: Date, times of mid eclipses, cycle number obtained from the photometric observations and residuals from the linear ephemeris.

Date	HJD (Mid-eclipse)	Cycle	$O-C$ (s)
04 Jan 2007^c	2454104.7085(21)	0	-9.9
13 Feb 2007^c	2454145.6847(8)	122	-11.0
14 Feb 2007^p	2454146.6922(8)	125	-19.0
13 Mar 2007^c	2454173.5621(10)	205	-0.3
21 May 2007^c	2454242.4163(21)	410	66.9
06 May 2008^c	2454593.4000(14)	1455	-25.9

^{c} Eclipse completely covered.

^{p} Eclipse partially covered.

6.3.3 Stellar parameters

Decomposition of the SDSS spectrum

We determined the stellar parameters of SDSS1212–0123 from the SDSS spectrum following the procedure described in Rebassa-Mansergas et al. (2007).

In a first step the best match of the SDSS composite spectrum is determined with an optimization strategy on a grid of observed white dwarf and M-dwarf template spectra created from the SDSS DR6 database. The main result of this first step is the determination of the spectral type of the secondary. Using the spectral type-radius relation from Rebassa-Mansergas et al. (2007) and the apparent magnitude of the scaled template results in a first distance estimate $d_{\rm sec}$. After subtracting the best-fitting M-star template, white-dwarf parameters are determined via χ^2 minimization in a $\log g$ – $T_{\rm eff}$ grid of model atmospheres (Koester et al. 2005). Since this analysis step is performed on spectra normalized to a continuum intensity, the results are bi-valued yielding a 'hot' and a 'cold' solution (see Fig. 6.4). The degeneracy can typically be broken by an additional fit to the overall spectrum (continuum plus lines in the wavelength range 3850 – 7150 Å). In the present case of SDSS1212–0123 the GALEX detection (see below) provides an additional constraint excluding the 'cold' solution. The results of the spectral decomposition and the white dwarf fit for SDSS1212–0123 are shown in Fig. 6.4.

Mass and radius of the white dwarf are calculated with the best-fitting $\log g$ – $T_{\rm eff}$ combination using updated versions of the tables by Bergeron et al. (1995). The flux scaling factor together with the derived radius of the white dwarf results in a second distance estimate of the binary, $d_{\rm wd}$.

The spectral type of the secondary was determined to be M4 ± 1 implying a distance $d_{\rm sec}$ = 320 ± 95 pc, mass range of the secondary $M_{\rm sec} = 0.255 – 0.380\ {\rm M}_\odot$ and radius range $R_{\rm sec}$ = 0.258 – 0.391 $R_\odot$, using Rebassa-Mansergas et al. (2007) spectral type-mass and spectral type-radius empirical relations respectively. The derived temperature and $\log g$ of the primary were found to be only weakly dependent on the chosen spectral type and spectral template of the secondary, because we use Hβ – Hϵ for the white dwarf line fit, where the secondary star contribution is small. It is also weakly dependent on the accuracy of the spectral flux calibration and also the small radial velocity line displacements. The best fit was found for $T_{\rm eff}$ = 17700 ± 300 K and $\log g$ = 7.53 ± 0.05 (implying a white dwarf mass $M_{\rm wd}$ = 0.39 ± 0.02 ${\rm M}_\odot$, and $R_{\rm wd}$ = 0.018 ± 0.001 $R_\odot$). The obtained values are in agreement with those published by Silvestri et al. (2006). However, one should be aware of the fact that all the quoted errors are purely statistical. The true uncertainty of the white dwarf spectral parameters is clearly higher than suggested by the derived numbers. We estimate the systematic uncertainty of our $\log g$ determination to be on the order of 0.2 dex, which results in rather wide ranges of possible values for the mass and the radius of the primary, i.e. $M_{\rm wd}$ = 0.33 – 0.48 ${\rm M}_\odot$ and $R_{\rm wd}$ = 0.015 – 0.021 $R_\odot$.

The derived distance to the white dwarf is $d_{\rm wd}$ = 226 ± 8 pc (assuming the statistical error only). The two distance estimates differ, $d_{\rm sec}$ being longer than $d_{\rm wd}$, but in agreement within the errors. A similar trend was found by Rebassa-Mansergas et al. (2007) for 101 WDMS binaries in

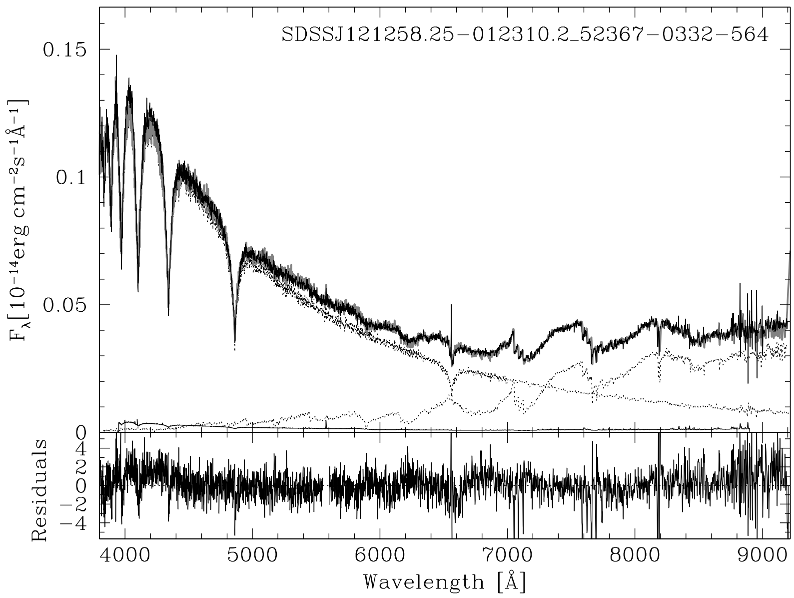

Figure 6.3: Two component fit to SDSS1212–0123. The top panel shows the WDMS spectrum (black line) and the white dwarf and the M4 M-dwarf templates (dotted lines), while the lower panel shows the residuals to the fit.

their study. They argue that such difference could be due to stellar activity of the secondary star, and that the spectral type determined from the optical SDSS spectrum is too early for the mass of the secondary star, which would lead to a larger radius and consequently a larger distance to the system. Since the secondary in SDSS1212–0123 was found to be active too, we regard the distance estimate for the white dwarf being more reliable. Taking into account systematic errors we obtain $d_{\rm wd} = 230 \pm 20$ pc as the distance to the system.

Constraining the secondary mass using 2MASS

In the previous section we derived the mass and the radius of the secondary star using empirical relations from Rebassa-Mansergas et al. (2007) and obtained $M_{\rm sec} = 0.255 - 0.380\,{\rm M}_\odot$ and $R_{\rm sec} = 0.258 - 0.391\,{\rm R}_\odot$, respectively. However, as clearly shown in Fig. 7 of Rebassa-Mansergas et al. (2007), the masses and radii derived from observations largely scatter around the empirical relations. In addition, according to Rebassa-Mansergas et al. (2007) increased activity of the rapidly rotating secondary stars in close binaries can cause the stars to appear as earlier spectral types when compared to non-active stars of the same mass. To sum up, the secondary masses derived from empirical relations can obviously only considered to reasonable but rough estimates.

An alternative method to determine the mass of secondary star is to use luminosity-spectral type relations. To that end, we explored the Two Micron All Sky Survey Point Source Catalog (Cutri et al. 2003), finding magnitudes $J = 14.90 \pm 0.03$, $H = 14.39 \pm 0.05$ and $K_{\rm s} = 13.96 \pm 0.05$ for SDSS1212–0123. Subtracting the extrapolated contribution of the primary star ($\log g = 7.5$

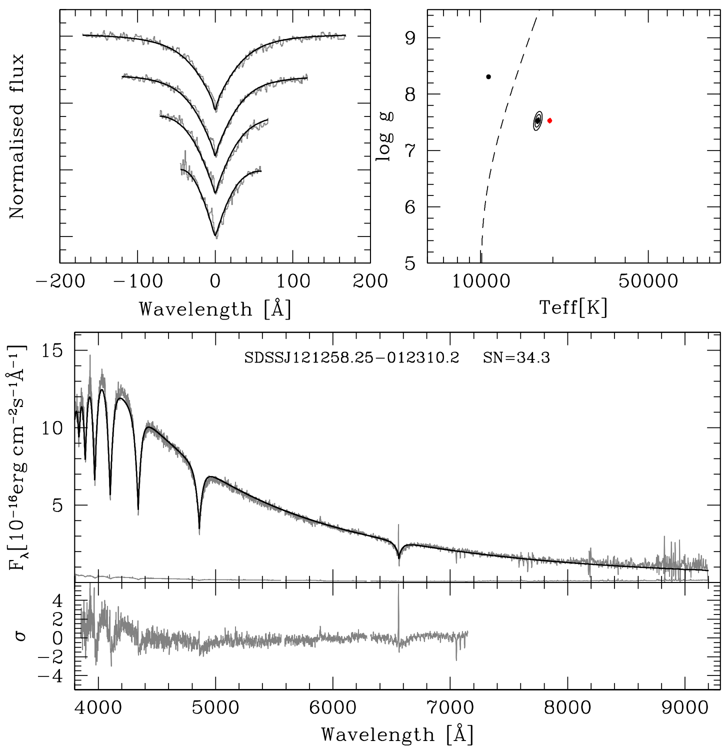

Figure 6.4: Spectral model fit to the white dwarf component of SDSS1212–0123, obtained after subtracting the best-fit M-dwarf template from its SDSS spectra. Top left panel: best fit (black lines) to the normalized Hβ to Hϵ line profiles (gray lines, top to bottom). Top right panel: 1, 2 and 3σ χ^2 contour plots in the $T_{\rm eff}$ − *log*g plane. The black contours refer to the best line profile fit, the red contours to the fit of the whole spectrum. The dashed line indicates where the maxima of the Hβ equivalent width occurs in the $T_{\rm eff}$–$\log g$ plane, dividing it into two different solutions, a cold and a hot one. The best-fit parameters of the hot and the cold normalized line profile solutions and of the fit to the 3850 – 7150 Å range are indicated by the black and the red dots, respectively. Bottom panel: the white dwarf spectrum and associated flux errors (gray lines) along with the best-fit white dwarf model (black lines) to the 3850 – 7150 Å wavelength range (top) and the residuals of the fit (gray line, bottom).

and $d_{\rm wd}$ = 230 pc) yields infra-red colors of $J-H = 0.51\pm0.06, H-K_s = 0.43\pm0.07$, respectively. Using the empirical mass-luminosity relation from Delfosse et al. (2000), we derive the mass of the secondary star to be 0.26 ± 0.03. Using again the mass-radius relation from Rebassa-Mansergas et al. (2007) this implies a spectral type M5, i.e. later by one spectral type than estimated from the deconvolution of the SDSS spectrum. This supports the idea of activity significantly affecting the determination the secondary star spectral types and the corresponding distances.

Radial velocity

In each of our observed spectra we measured the radial velocities of the NaI absorption doublet (8183.27Å, 8194.81Å), which originates from the secondary star. A double Gaussian with a fixed separation of 11.54 Å was fitted to the line profiles using the FIT/TABLE command provided by ESO/MIDAS.

Hα was deconvolved into an absorption and an emission line component using two Gaussians. While the emission line showed pronounced wavelength shifts, the centroids of the absorption lines thus measured did not constrain the curve of the white dwarf significantly.

Assuming a circular orbit a sine-function was fitted to the measured radial velocity curves to obtain the radial velocity semi-amplitude K_2 of the secondary star:

$$v_r = \gamma_2 + K_2 \sin\left[\frac{2\pi(t - t_0)}{P}\right], \tag{6.2}$$

The orbital period P and the epoch of mid eclipse t_0 were determined photometrically and were kept fixed for the radial velocity fit. For the NaI doublet we find the systemic velocity $\gamma_2 = 17 \pm 3\,\mathrm{km\,s^{-1}}$ and $K_2 = 181 \pm 3\,\mathrm{km\,s^{-1}}$, while we find for the Hα line $\gamma_2 = 21 \pm 2\,\mathrm{km\,s^{-1}}$and $K_2 = 161 \pm 3\,\mathrm{km\,s^{-1}}$. The fit to the NaI lines is shown if Fig. 6.5 together with the residuals.

The semi-amplitudes of the two radial velocity curves are different and these differences seem to be significant. The semi-amplitude derived from Hα is lower, indicating that its emission is displaced towards the inner hemisphere of the secondary star with respect to the NaI doublet. As neither of the two line features shows significant photometric variability, which would indicate a biased origin of one of the line species (e.g. towards the non-irradiated side of the secondary), we exclude irradiation as the explanation for the observed difference in K_2. A detailed comparison of radial velocities derived from the NaI doublet and Hα lines has been performed by Rebassa-Mansergas et al. (2007). They find that both velocities often significantly differ but that there seems to be no systematic shift of Hα radial velocities towards smaller values. As discussed in detail in Rebassa-Mansergas et al. (2008), this is probably explained by the Hα emission being related to activity and not uniformly distributed over the surface of the secondary. Kafka et al. (2005) studied in detail the origin of different line species, however SDSS1212–0123 shows no evidence of accretion nor irradiation. We therefore assume that in SDSS1212–0123 the NaI doublet much better traces the center of mass of the secondary and we use its semi-amplitude for the mass estimate.

We write the mass function of the binary assuming a circular orbit in the form

$$M_{\mathrm{sec}} = \left(\sqrt{\frac{2\pi G \sin^3 i}{PK_2^3} M_{\mathrm{wd}}} - 1\right) M_{\mathrm{wd}}, \tag{6.3}$$

and derive an upper limit for M_{sec} for a given white-dwarf mass M_{wd} assuming $i = 90°$ (see bottom panel of Fig. 6.6).

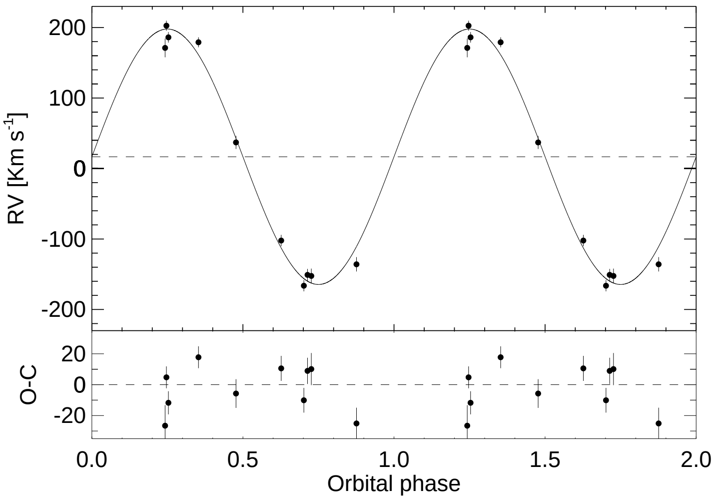

Figure 6.5: Radial velocities measured from the NaI doublet 8183, 8194 Å originating from the secondary star of SDSS1212–0123 folded over the orbital period obtained from the photometry. Sine fit and residuals (lower panel) are shown.

Using the empirical mass-radius relation for main sequence stars derived by Bayless & Orosz (2006) we estimate the radius of the secondary (middle panel of Fig. 6.6). The top panel of the same figure illustrates the maximum possible eclipse length ($i = 90°$, black line) for the given stellar radius, the orbital period P and the orbital separation a according to

$$t_{\mathrm{ecl}} = \frac{R_{\mathrm{sec}} P}{\pi a}. \tag{6.4}$$

The measured values of the eclipse length and the range of the white-dwarf mass from Sec. 6.3.3 are shown in the figure with horizontal and vertical lines, respectively, their intersection is shaded in grey in the top panel. It is also plotted the solution for $i = 75°$ for comparison. From the eclipse length the range of possible values for the mass of the WD is $M_{\mathrm{wd}} = 0.46 - 0.52$, and for the dM $M_{\mathrm{sec}} = 0.21 - 0.32\ \mathrm{M}_{\odot}$, and $R_{\mathrm{sec}} = 0.23 - 0.34\ \mathrm{R}_{\odot}$.

Light curve modeling

A determination of most of the physical parameters of an eclipsing system can be achieved by fitting model light curves to the actual data. We made use of a newly developed light curve fitting code, written by T.R. Marsh, for the general case of binaries containing a white dwarf. The code is described in detail in Pyrzas et al. (2009). Briefly, a model light curve is computed based on user-supplied initial system parameters. These are the two radii, scaled by the binary separation, R_{wd}/a and R_{sec}/a, the orbital inclination, i, the un-irradiated stellar temperatures of the white dwarf and the secondary star $T_{\mathrm{eff,WD}}$ and $T_{\mathrm{eff,sec}}$ respectively, the mass ratio $q = M_{\mathrm{sec}}/M_{\mathrm{wd}}$ and t_0 the time of mid-eclipse of the white dwarf.

Starting from this parameter set, the model light curve is then fitted to the data using Levenberg-Marquardt minimization. Every parameter can either be allowed to vary or remain fixed, during

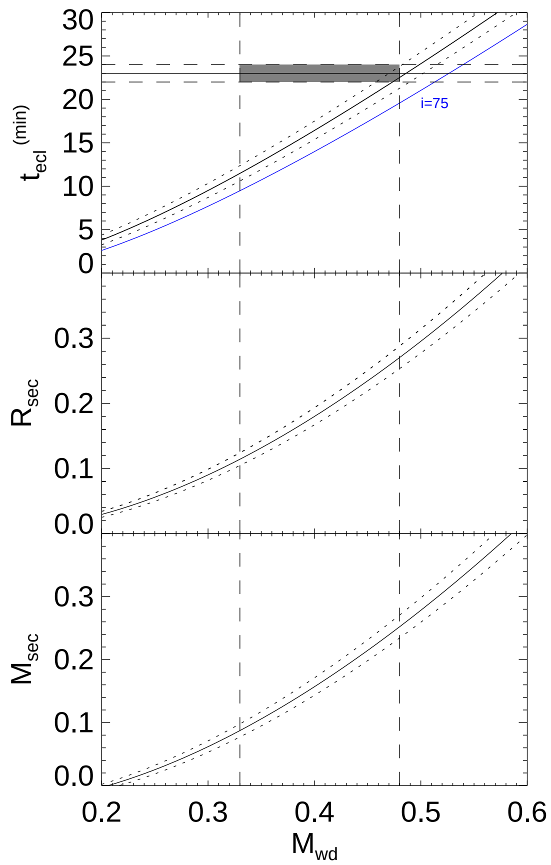

Figure 6.6: Solution of the mass function for $K_2 = 181 \pm 3$ km/s as a function of $M_{\rm wd}$ (bottom panel); radius from the mass-radius empirical relation from Bayless & Orosz (2006) (mid panel); eclipse duration (top panel), assuming circular orbit and an inclination angle of 90°. Vertical lines indicate the mass of the primary star, $M_{\rm wd}$ = (0.33 – 0.48) $M_\odot$, as determined from the deconvolution of the SDSS spectrum. The eclipse length, $t_{\rm ecl} = 23 \pm 1$ min, is marked with horizontal lines, and the intersection in shaded in grey. The errors in K_2 are shown with the small dashed lines in the three panels. In the top panel the solution for an inclination of 75° is plotted with a blue line to show it's influence. See text for a more detailed description.

the fitting process.

Our approach for modeling the I band photometry of SDSS1212–0123 was the following. A large and dense grid of points in the $M_{\rm wd} - M_{\rm sec}$ plane was first calculated, generously bracketing the estimates for the mass of the two components (see Sec. 6.3.3). Each point defines a mass ratio q, and through $P_{\rm orb}$, a binary separation a. Furthermore, from the mass function equation (Eq. 6.3), using the value of K_2 (derived in Sec. 6.3.3) and $P_{\rm orb}$, one can calculate the inclination angle i. Points for which (formally) $\sin i > 1$ were discarded from the grid, for all other points the corresponding light curve model was computed, leading to the computation of some 9000 models.

As an initial estimate for the radii of the binary components, we adopted values from the theoretical M – R relations of Bergeron et al (1995) for the white dwarf, and Baraffe et al. (1998) - the 5 Gyr model - for the secondary. Regarding the two temperatures, $T_{\rm eff,WD}$ and $T_{\rm eff,sec}$, the value from our spectral decomposition (Sec. 6.3.3) was used for the white dwarf, while the Sp(2) – T relation from Rebassa-Mansergas et al. (2007), together with our result for the spectral type of the secondary, were used to obtain an initial value for $T_{\rm eff,sec}$.

For the fitting process q, i, $R_{\rm wd}$ and $T_{\rm eff,WD}$ were fixed, leaving only $R_{\rm sec}$, $T_{\rm eff,sec}$ and t_0 free to vary. $R_{\rm wd}$ was fixed mainly because of the poor temporal resolution of our data set, which does not resolve the white dwarf ingress and egress. Consequently, if allowed to vary, the white dwarf radius would only be loosely constrained and it would introduce large uncertainties in the determination of $R_{\rm sec}$. $T_{\rm eff,WD}$ was also fixed, because allowing both temperatures to vary simultaneously would lead to a degenerate situation, as they are strongly correlated. Our spectral decomposition results are sufficiently accurate, so as to allow us to fix $T_{\rm eff,WD}$ without affecting the fitting result. The parameter t_0 on the other hand, was left free during the fitting, to account for the $O-C$ errors in the mid-eclipse times, which in some cases were significant (see Table 6.2 again).

The results of the light curve fitting process were analyzed as follows. We first applied a cut in the quality of the fits. This was done by selecting the minimum χ^2 value of all fits and then culling all model fits at $> 1\sigma$ above the best fit. Afterwards, we selected from the remaining, equally good light curve fits, those which where physically plausible. We defined a δR parameter, as $\delta R = (R_{\rm fit} - R_{\rm th})/R_{\rm th}$, i.e. how much the fitted radius value deviates from the theoretical radius value, obtained from a M-R relation, for a given model. Thus, we selected only those models that had $\delta R \leq 0.15$, to allow for an oversized secondary.

The results are illustrated in Fig. 6.7. Black dots designate those light curve fits making the 1σ cut, red dots those that satisfy both the 1σ and $\delta R = 15\%$ cuts. The resulting ranges in white dwarf masses and secondary star masses (indicated with dashed, vertical, red lines) are $M_{\rm wd} = 0.46 - 0.6\ {\rm M}_\odot$ and $M_{\rm sec} = 0.23 - 0.4\ {\rm M}_\odot$, respectively, corresponding to a white dwarf radius of $R_{\rm wd} = 0.013 - 0.016\ {\rm R}_\odot$ and a secondary radius of $R_{\rm sec} = 0.27 - 0.41\ {\rm R}_\odot$. The range for the inclination angle is $i = 82^\circ - 90^\circ$. Also indicated, with dotted, horizontal, gray lines are the radii of M-dwarfs with spectral types Sp(2) = M3 – M5 in steps of 0.5, based on the spectral type-mass relation given by Rebassa-Mansergas et al. (2007).

Fig. 6.8 shows one example of the light curve fits within the components masses range for the model parameters: $M_{\rm wd} = 0.49\ {\rm M}_\odot$, $M_{\rm sec} = 0.26\ {\rm M}_\odot$ and $i = 89.2^\circ$. The detailed models do not predict any variation in the light curve caused by irradiation of the secondary star by the white dwarf. The predicted variations due to ellipsoidal modulation are expected to be quite small, i.e. ~ 0.005 mag, consistent with our observational non-detection of any variability outside the eclipse.

Spectral energy distribution

We cross-identified SDSS1212–0123 with the database from the Galaxy Evolution Explorer (GALEX (Martin et al. 2005; Morrissey et al. 2005)), and found a detection in the far and near ultraviolet (FUV and NUV). The magnitudes are $m_{\rm FUV} = 16.79\pm0.03$ mag and $m_{\rm NUV} = 16.81\pm0.02$ mag, exposure times were 150 sec. FUV and NUV fluxes can provide an estimate of the effective temperature of the white dwarf for a certain $\log g$, assuming that all the flux in the UV is emitted by the primary. White dwarf models for $\log g = 7.5$ and $\log g = 8.0$ and effective temperature in the range 6000 – 100000 K, were folded over the FUV and NUV filters. The calculated

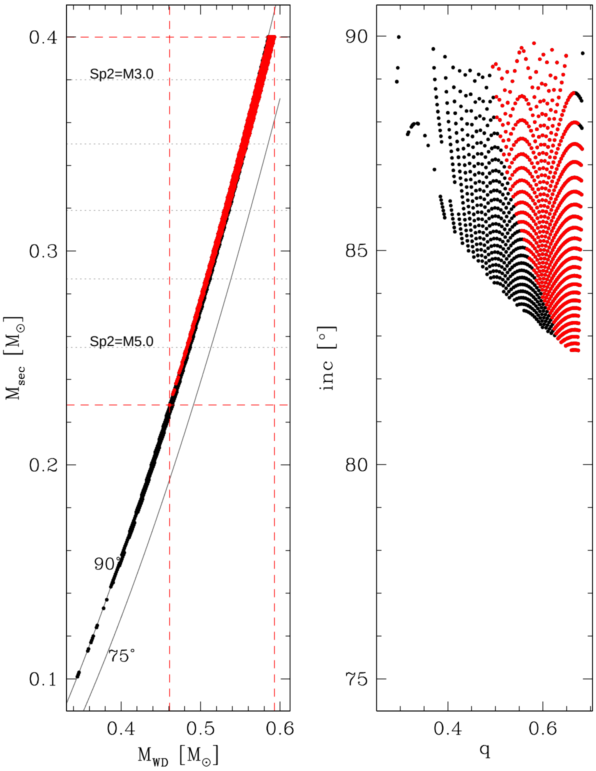

Figure 6.7: Light curve model fitting results for SDSS 1212-0123. Left panel: $M_{\rm wd}$ and $M_{\rm sec}$ values corresponding to fits with χ^2 values within 1σ of the minimum value (black points) and, simultaneously, with $\delta R \leq 0.05$ (red points). Right panel: the same, only in the $q-i$ plane. Also depicted in the left panel are curves corresponding to the mass function (solid black lines, $i = 90°$ and $75°$) which (by definition) bracket the possible solutions, Sp(2) – M relations (dotted, horizontal, gray lines) and the range of possible ($M_{\rm wd}, M_{\rm sec}$) values (dashed, horizontal and vertical, red lines)

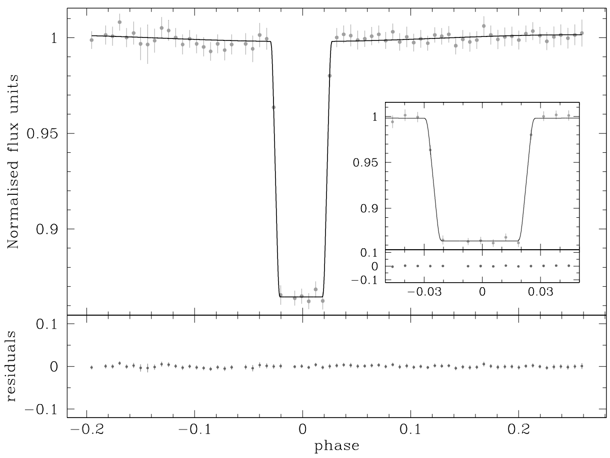

Figure 6.8: Model fit to the I band light curve of SDSS1212–0123, for $M_{\rm wd} = 0.49\,{\rm M}_\odot$ and $M_{\rm sec} = 0.26\,{\rm M}_\odot$. The model meets both the χ^2 (within 1σ) and the δR (within 15%) cut-offs. The residuals from the fit are shown at the bottom of the panel. Inset panel: data points and model fit focused around the eclipse phase.

flux ratio FUV/NUV was compared with the observed for SDSS1212–0123 (see Fig. 6.9) . The GALEX flux ratio implies $T_{\rm eff} \sim 13000$ K, significantly colder than what we obtain from the optical spectrum in Sec. 6.3.3. However, discrepant temperatures from GALEX UV and optical photometry were noticed earlier from an analysis for a large number of white dwarfs (~ 250) by Kawka & Vennes (2007). We searched for standard stars with well determined temperatures and gravities that had been observed with GALEX and retrieved their fluxes. In table 6.3 we list their

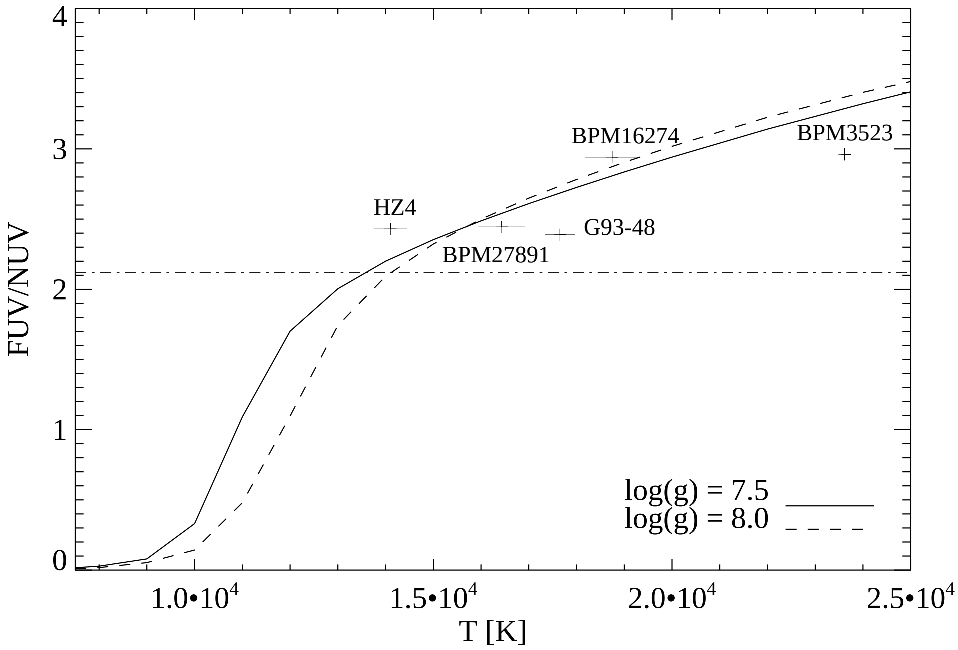

Figure 6.9: Calculated FUV/NUV ratio for white dwarf models for $\log g = 7.5$ and $\log g = 8.0$ (solid and dashed lines) and effective temperature in the range 6000 – 100000 K, observed FUV/NUV for 5 standard stars with well determined temperatures and gravities (indicated with their name) and for SDSS1212–0123 (horizontal line).

Table 6.3: Temperatures, gravities and GALEX fluxes for a number of standard stars in the same $\log g$range as SDSS1212–0123.

Name	$T_{\rm eff}$	log(g)	NUV	FUV
BPM16274	18745 ± 564	7.80 ± 0.5	6.16864e+15	1.81443e+16
BPM3523	23614 ± 78	7.82 ± 0.04	1.09845e+16	3.25284e+16
G93-48	17653 ± 319	7.99 ± 0.06	1.82277e+16	4.35370e+16
BPM27891	16435 ± 488	7.93 ± 0.36	2.39285e+15	6.82102e+15
HZ4	14100 ± 350		2.96225e-14	7.19828e-14

temperatures, gravities (Bragaglia et al. 1995) and GALEX fluxes and we show their FUV/NUV ratios in Fig. 6.9.

This shows that one cannot expect the same UV and optical temperatures in a case-by-case basis, but at best on a statistical average. For the time being we accept the temperature from our fit to the SDSS spectrum, which grossly reflects the UV to optical SED.

The spectral energy distribution is shown in Fig. 6.10, including ultraviolet, optical and infrared fluxes from 2MASS. A model spectrum for a white dwarf of pure Hydrogen (Koester et al.

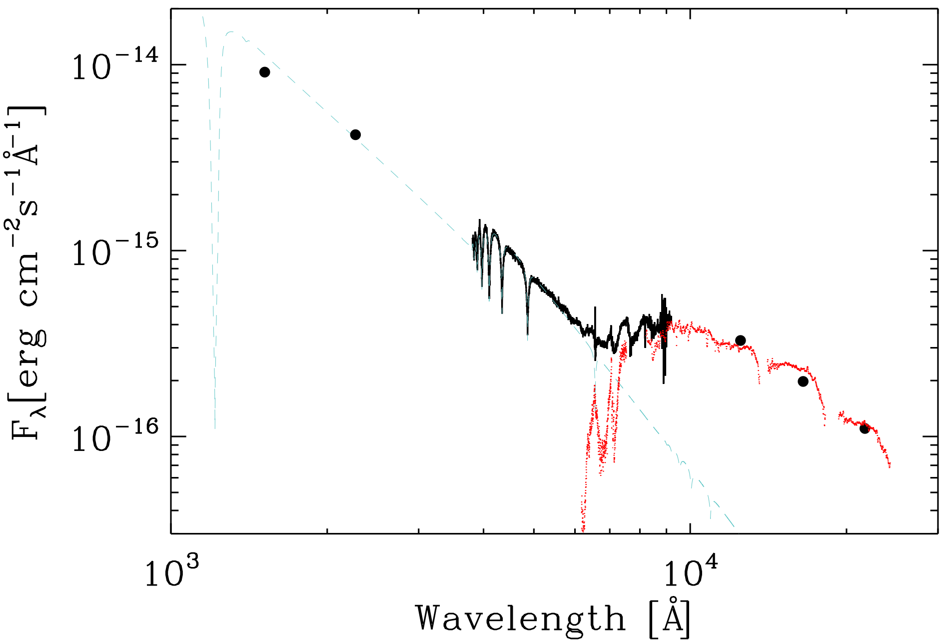

Figure 6.10: Spectral energy distribution of SDSS1212–0123. GALEX near and far ultraviolet and 2MASS infrared fluxes (black circles), optical SDSS spectrum (black line). A white dwarf model of $T_{\rm eff}$ = 17500 K and $\log g$ = 7.5 (blue dashed line) and the spectrum of LHS1504 with spectral type M5 from Legget's library (red dots) are shown for comparison .

2005) with effective temperature of 17500 K and $\log g$ = 7.5 and a spectrum of the M5 star LHS1504 from Legget's library [3] are shown for comparison (Leggett et al. 2000).

Binary parameters summary

Fig. 6.11 shows the different ranges for the masses of the primary and the secondary from the spectral decomposition fit (Sect. 6.3.3), the K-band luminosity-mass relation (Sect. 6.3.3), the radial velocity amplitude and eclipse length (Sect. 6.3.3) and the detailed light curve fitting (Sect. 6.3.3). Of course, the different methods are not entirely independent, e.g. the constraints from the eclipse length/radial velocities studies and the detail light curve fitting basically use the same information with the only difference being that we could derive a clear lower limit from the latter. The dark shaded region in Fig. 6.11 represents the ranges of stellar masses in agreement with all the derived constraints i.e., $M_{\rm wd}$ = 0.46 – 0.48 $M_\odot$, $M_{\rm sec}$ = 0.26 – 0.29 $M_\odot$, implying a radius of the secondary star in the range $R_{\rm sec}$ = 0.28 – 0.31 $R_\odot$ using the empirical M–R relation from Bayless & Orosz (2006) and $R_{\rm wd}$ = 0.016 – 0.018 $R_\odot$ ($\log g$ = 7.5 – 7.7). We adopt these values as the most probable ones and all finally accepted stellar and binary parameters based on Sloan-data, other catalogues and our own follow-up observations are collected in Table 6.4.

[3]http://ftp.jach.hawaii.edu/ukirt/skl/dM.spectra/

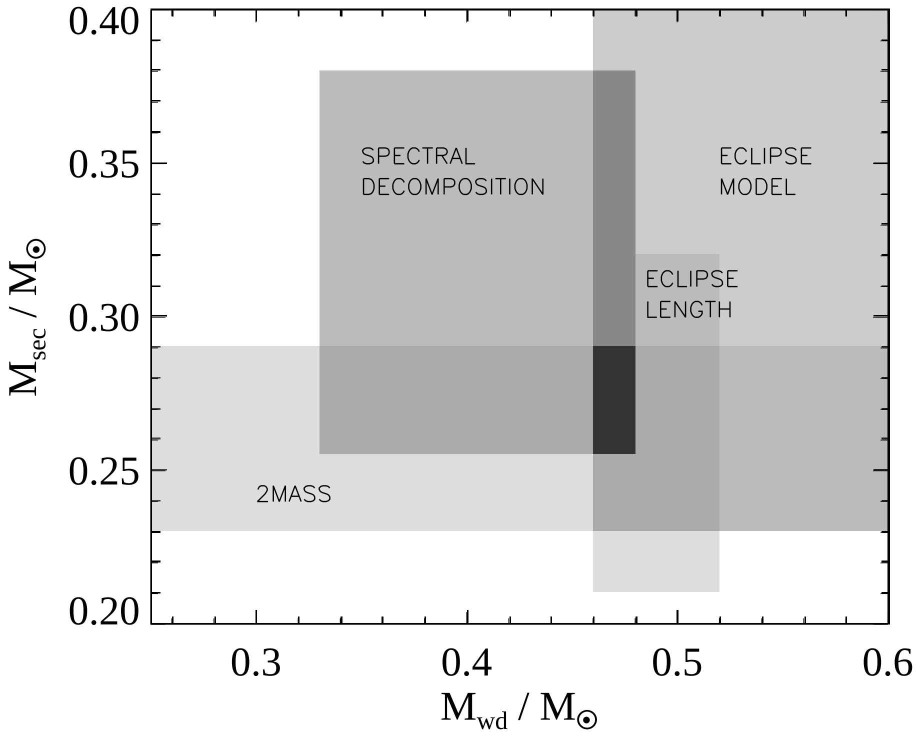

Figure 6.11: The ranges of masses of the white dwarf and the red dwarf coming from: the decomposition of the SDSS spectrum; the infrared brightness; the eclipse length for an inclination of 90°, and, the detailed light curve modeling. Each of the areas is labeled correspondingly, the intersection of the four different methods occurs for $M_{\rm sec} = 0.26 - 0.29\ \mathrm{M}_{\odot}$ and $M_{\rm wd} = 0.44 - 0.46\ \mathrm{M}_{\odot}$.

6.4 Evolutionary state

The post CE evolution of compact binaries is driven by angular momentum loss due to gravitational radiation and – perhaps much stronger – magnetic wind braking. Unfortunately, the latter mechanism is currently far from being well constrained, and predicting and reconstructing the post CE evolution sensitively depends on the assumed prescription for magnetic braking.

However, the disrupted magnetic braking scenario proposed by Rappaport et al. (1983) can still be considered the standard model for magnetic braking in close compact binaries. In this scenario it is assumed that magnetic braking ceases when the secondary star becomes fully convective at $M_{\rm sec} \sim 0.3\mathrm{M}_{\odot}$ (which corresponds to $P_{\rm orb} \sim 3$ hrs). Although observations of the spin down rates of single stars do drastically disagree with the predictions of disrupted magnetic braking (Sills et al. 2000), it remains the only consistent theory explaining the orbital period gap i.e. the observed deficit of CVs in the range of $P_{\rm orb} \sim 2 - 3$hrs. Moreover, first results of our radial velocity survey of PCEBs seem to support the idea of disrupted magnetic braking

Table 6.4: Stellar and binary parameters of SDSS1212–0123.

Parameter	Value	Parameter	Value
$R.A.\,(J2000.0)$	12 12 58.25	T_{eff} (K)	17700 ± 300
$Dec.\,(J2000.0)$	-01 23 10.1	$\log g$ (dex)	7.5 – 7.7
u	17.045 ± 0.020	Sp(2)	M4 ± 1
g	16.769 ± 0.013	R_{wd} ($R_{\odot}$)	0.016 – 0.018
r	16.936 ± 0.013	R_{sec} ($R_{\odot}$)	0.28 – 0.31
i	16.627 ± 0.015	M_{wd} ($M_{\odot}$)	0.46 – 0.48
z	16.136 ± 0.018	M_{sec} ($M_{\odot}$)	0.26 – 0.29
J	14.83 ± 0.03	P_{orb} (days)	0.3358706(5)
H	14.35 ± 0.05	K_2 (km s^{-1})	181 ± 3
K_s	13.93 ± 0.05	γ_2 (km s^{-1})	17 ± 3
m_{FUV}	16.79 ± 0.03	a ($R_{\odot}$)	1.8 ± 0.1
m_{NUV}	16.81 ± 0.02	i_{min}	82°
d (pc)	230 ± 20		

(Schreiber et al. 2008). To predict and reconstruct the post CE evolution of SDSS1212–0123 according to Schreiber & Gänsicke (2003), we therefore assume disrupted magnetic braking.

First, we interpolate the cooling tracks of Wood et al. (1995) and estimate that the cooling age of SDSS1212–0123 is 6.8×10^7 yrs (see top panel of Fig. 6.12). Second, according to the mass derived for the secondary star ($M_{\mathrm{sec}} \sim 0.27 M_{\odot}$) we assume that, since SDSS1212–0123 left the CE phase, the only mechanism driving the evolution of SDSS1212–0123 towards shorter orbital periods is (and has been) gravitational radiation. As shown in Fig. 6.12 (bottom panel), SDSS1212–0123 left the CE phase with an orbital period of $P_{\mathrm{CE}} \sim 8.07$ hrs, very similar to the present value. Significant changes in the orbital period are predicted to occur on timescales longer than the current cooling age of the white dwarf. In $\sim 1.8 \times 10^{10}$ years SDSS1212–0123 will eventually become a CV within the orbital period gap, however, giving that it's calculated PCEB lifetime exceeds the age of the Galaxy it is not representative of the progenitors of todays CV population.

The mass of the primary star, makes SDSS1212–0123 more interesting since, as Shen et al. (2009) realized, it will become a CVs with a He core. Up to know there no CVs and only 8 WDMS with a He core.

6.5 Mass-radius relation for dM stars

Empirical mass-radius relations of low mass stars around 0.3 $M_{\odot}$, are up to 15 % larger than predicted by models (López-Morales & Shaw 2007). Observations of eclipsing systems are of utmost relevance, since we can get accurate parameters from them, for improving this relation.

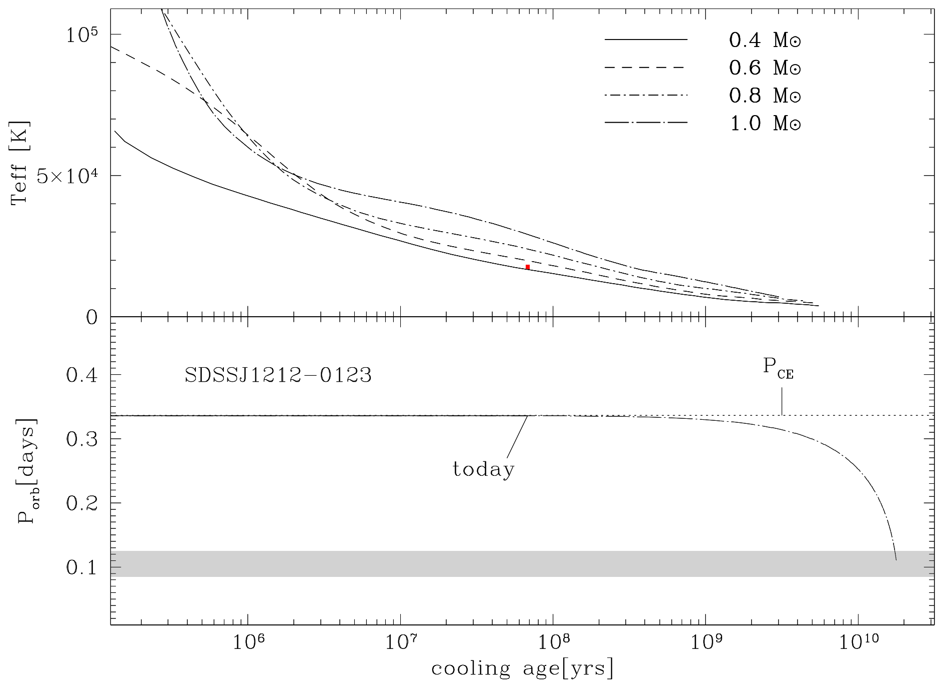

Figure 6.12: Top panel: Interpolating the cooling tracks from Wood (1995) and according to the current temperature of the white dwarf ($T_{\rm eff}$ = 17700 K) we derive for SDSS1212–0123 a cooling age of ~ 7 × 10^7 years. Bottom panel: Assuming gravitational radiation as the only angular momentum loss mechanism we reconstructed the post-CE evolution of SDSS1212–0123 and find that it left the CE phase with an orbital period of $P_{\rm CE}$ ~ 8.07 hrs. Apparently, SDSS1212–0123 has passed only a small fraction of its PCEB lifetime and it will take ~ 1.8 × 10^{10} years until SDSS1212–0123 will become a CV. At that moment the white dwarf temperature will be $T_{\rm eff}$ ~ 4000 K and the system will be inside the period gap (grey bar).

Masses and radius of the secondary star for all close WDMS are given in table 1.2.2 and presented in Fig. 6.13. The empirical mass-radius relations from Rebassa-Mansergas et al. (2007) and Bayless & Orosz (2006) are also shown. All the known eclipsing systems (Pyrzas et al. 2009) with a white dwarf as a primary and a low mass secondary star are plotted with squares and the position of SDSS1212–0123 is highlighted with a black filled square. We show the theoretical mass-radius relation from Baraffe et al. (1998) for 1 Gyr, Z=0.02, and mixing length $\alpha = 1$. We can see that models and observations are in agreement at the bottom of the mass-radius relation, but that as soon as we go to masses higher than 0.3 $M_\odot$ the differences increase. This behavior is seen in dM binaries as well and it has been suggested that this could be a result of stellar rotation linked to magnetic activity (López-Morales 2007). Nevertheless our systems with smaller mass than 0.3 $M_\odot$ have short orbital periods, that is they are fast rotators and they are in agreement with the theoretical values.

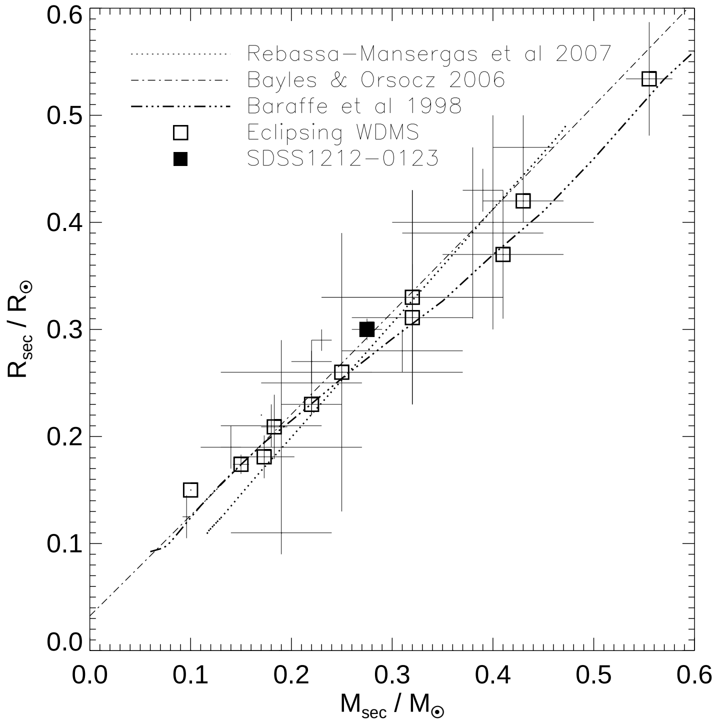

Figure 6.13: Masses and radius for all the close WDMS. Eclipsing systems are shown in squares, the position of SDSS1212–0123 is highlighted with a black filled square. The empirical mass-radius relations from Rebassa-Mansergas et al. (2007) and Bayless & Orosz (2006) and the theoretical predicted values from Baraffe et al. (1998) are also shown.

6.6 Summary

From optical photometry we conclude SDSS1212–0123 is a eclipsing PCEB with an orbital period of 0.336 days and an eclipse length of 23 min. From spectroscopic follow-up observations we have derived a systemic velocity of 17 ± 3 km/s and a semi-amplitude of the radial velocity of 181 ± 3 km/s. From the SDSS spectrum we derived $T_{\rm eff}$ = 17700 ± 300 K, $\log g$ = 7.53 ± 0.2 implying a mass in the range 0.33 – 0.48 $M_\odot$ and a secondary spectral type M4 ± 1, and a distance to the system of 230 ± 20 parsecs. From infrared photometry, using a mass–luminosity empirical relation we derived $M_{\rm sec}$ = 0.26 ± 0.03 $M_\odot$. We have calculated the radius of the secondary star using an empirical mass–radius relation. The mass function, combined with the eclipse length, points towards the high end of the allowed mass range of the primary, i.e. $M_{\rm wd} \sim 0.46 - 0.48$, indicating it has a He core, one of the few know until the date. We have modeled the I band light curve and find the inclination of the orbit to be $i > 82°$, and the masses to be consistent with previously determined values. The different methods applied are all consistent with $M_{\rm wd}$ = 0.46 – 0.48 $M_\odot$, implying $R_{\rm wd}$ = 0.016 – 0.018 $R_\odot$ ($\log g$ = 7.5 – 7.7) for the primary and $M_{\rm sec}$ = 0.26 – 0.29 $M_\odot$, $R_{\rm sec}$ = 0.28 – 0.31 $R_\odot$ for the secondary. We have reconstructed and predicted the post CE evolution of SDSS1212–0123, finding that SDSS1212–0123 at the end of the CE phase had a very similar orbital period. The only mechanism involved in shrinking the orbital period is and has been gravitational radiation. As the PCEB lifetime of SDSS1212–0123 exceeds the Hubble time we conclude that it is not representative of the progenitors of the current CV population. We collected data from other WDMS binaries with known masses and radii and see that for low masses the mass-radius relation is in agreement with the models, but for higher masses than 0.3 $M_{\odot}$ models and observations differ up to 15%. The number of eclipsing systems, which give the most accurate parameters, is increasing, and with them we will be able to give a better empirical mass-radius relation.

Chapter 7

Conclusion and outlook

Before the era of the Sloan Digital Sky Survey only a few white dwarf/main sequence binaries were known. Due to the way these systems were discovered this sample was biased towards hot white dwarfs. Since then the number of WDMS binaries has been continuously increasing and has already reached more than 1600, where only a fraction of them have gone through a common envelope phase. Unfortunately these systems have also been biased towards systems containing hot white dwarfs. In this case the cause is that they were not one of the main targets of the SDSS but they were the byproduct of one of the main targets, quasars, and their colors resemble those of WDMS binaries with hot white dwarfs. As members of SEGUE, the Sloan Extension for Galactic Understanding and Exploration, a survey has been especially designed to identify WDMS binaries containing cold white dwarfs and covering a much broader range of galactic latitudes than SDSS I. In this work we present 277 new WDMS binaries and 24 candidates identified with SEGUE. We characterized the sample using spectral decomposition techniques, discussed the obtained distributions, and derived plausible values for the space density and the scale height. As expected, our sample contains significantly more cold systems than SDSS I. The combination of our color selection and the magnitude limits of SDSS causes our sample to be biased towards cold white dwarfs and late type secondary stars that are relatively nearby ($d \lesssim 500$ pc). The space density of WDMS binaries inside our selection criteria is $\sim 2 \times 10^{-4}\,\mathrm{pc}^{-3}$ and decreases to $\sim 2 \times 10^{-5}\,\mathrm{pc}^{-3}$ at higher galactic latitudes. The space density of SDSS WDMS binaries increases significantly towards the galactic plane in agreement with a scale height of the galactic population of WDMS binaries of $100 - 150$ pc, value that is similar to values estimated for the population of cataclysmic variables and late type stars.

Until 2003 only $\sim$ 30 post common envelope binaries containing a white dwarf and a main sequence star with well determined parameters were known. Using the SDSS sub-exposures that are coadded to create a single SDSS spectrum, based on a statistical approach we discovered 33 new PCEBs. From own spectrocopic follow-up observations of 65 WDMS binaries we have independently confirmed 19 close binaries and combining with the mentioned SDSS sub-exposures we find a total number to 37 PCEBs. Willems & Kolb (2004) predicted a fraction of PCEB to WDMS binaries of $\sim$ 25 %, while we found a value of $\sim$ 13 %. Nevertheless our result is just a lower limit to the total number of PCEB in the sample which is not in contradiction with the theoretical predicted value. This becomes obvious when thinking that some systems will have a low orbital inclination so that no radial velocity variation can be measured within our detection limit.

One of the big questions of close binary evolution is whether a magnetized stellar wind is efficient extracting angular momentum for fully convective secondary stars, as it is for stars with a radiative core, or if this changes with the structure of the star. Politano & Weiler (2006) proposed a test to answer this question. If magnetic braking gets disrupted the relative number of PCEBs should increase at the boundary where the star is fully convective, at around 0.35 $M_{\odot}$, which corresponds to spectral type around M3, and towards later spectral types, i. e. lower masses. The SEGUE WMDS has been combined with a larger sample of WDMS-SDSS binaries to answer this question. We have found that the fraction of PCEBs to WDMS binaries is very low at early spectral type secondary stars, presents an steep increase to $\sim$ 50 % at M3-M4, where the secondary becomes fully convective, and peaks at around M7, where 75 % of the systems are PCEBs. This is the first test of magnetic braking and indicates that magnetic braking gets disrupted once the secondary star becomes fully convective.

The orbital period distribution of WDMS binaries predicted by Willems & Kolb (2004) contains two groups. One formed by very long orbital period WDMS binaries where the components never interacted and evolved as single stars, and another, representing $\sim$ 25 % of the total WDMS binaries, formed by PCEBs. The latter extends from very short orbital periods up to 100 days, peaking at around 1 day. From own spectroscopic and photometric follow-up observations we have determined the orbital period of 15 systems among the 37 new PCEBs. Only one of them has an orbital period longer than 1 day. We studied our detection probability and found that even though we are biased towards systems with shorter orbital periods than 1 day we should be able to detect longer orbital periods as well. We made a compilation of all the known PCEBs until the date and realized that their orbital period distribution also presents a sharp cut at around 1 day. This seems to contradict the distribution predicted by Willems & Kolb (2004) and Davis et al. (2009), which contains an extended tail of systems with orbital periods up to 100 days. This could imply that the CE phase might extract from the orbit more energy and angular momentum than previously thought. But one must not forget that the actual period distribution is biased towards short orbital periods, since their measurement is less time demanding than for those with longer orbital periods. Investigating in more detail the remaining 22 new SEGUE-PCEBs for which we don't have a measurement of the orbital period, we have identified 7 systems as long orbital period (> 1 day) candidates and 15 as short orbital period (<1 day) candidates. To learn about the efficiency of the CE phase it is very important to measure their true orbital period.

All low mass white dwarf stars ($M_{\rm wd}$<0.47 $M_{\odot}$) are thought to be a product of close binary evolution (Marsh et al. 1995). In a single star wind mass loss wouldn't be strong enough so as to get rid of all the giant's envelope before the ignition of the He, while the existance of He-WDs can be explained with the ejection of the common envelope of a binary system. We investigated the white dwarf mass distribution of PCEBs and found that it is similar to that of single white dwarfs, presenting two peaks, one around 0.58 $M_{\odot}$ and the other around 0.84 $M_{\odot}$, but it has an extended tail towards low masses. This is in agreement with the idea of all He core white dwarfs being product of a common envelope phase. Among the SEGUE sample there are 6 WDMS binaries for which the white dwarf mass is below the He-WD mass limit and that did not show any strong radial velocity variation. This seems to contradict the most likely evolutionary scenario for He-WD stars.

The empirical mass-radius relation of low mass stars is in agreement with predicted values from models up to 0.3 $M_{\odot}$, but for higher masses models and observations seem to differ up to 15%. Eclipsing systems give the most accurate parameters and can be used to give a better empirical mass-radius relation. We discovered 5 new eclipsing systems (Pyrzas et al. 2009; Nebot Gómez-Morán et al. 2009), and analyzed SDSS1212–0123 in detail. We estimated the masses and radii of the components with a 5% accuracy. The estimated value of the white dwarf mass of SDSS1212–0123 suggests that it contains a He-core WD, which brings us back to the evolutionary scenario mentioned above. The number of eclipsing systems is still rather small and should be increased to improve the empirical radius-mass relation for low mass stars. Among the SEGUE sample we have found another new candidate for being eclipser and this should be observed photometrically to better constrain its stellar parameters and populate better the mass-radius diagram.

The activity-binarity relation is a field that has not been very much investigated among WDMS binaries. We have used our SEGUE-WDMS binaries, studying wide and close binaries separately in order to learn about possible connections. From the Hα emission line we have measured the stellar activity of the secondary stars. Wide binaries present an increase in the fraction of active secondary stars with spectral type, similar trend as found for field stars (West et al. 2008). At spectral types earlier than M4 the fraction of active stars is significantly higher than for field stars, and also higher than found before in WDMS wide binaries by Silvestri et al. (2005). To explain such effect we investigated the possibility of PCEB contamination in our wide binary sample at these spectral types and also calculated the age of the systems. We conclude that since most of the systems with secondaries in this spectral type range are younger than the activity lifetime it reflects an age effect. At least 90% of the PCEB are active pointing to an enhancement of activity due to the fact of having a companion star. The EW of the Hα line is higher for close systems at each spectral type for later spectral types than M2. But most of the close binary stars have a rather short orbital period, which when having a hot white dwarf as a primary could cause the secondary's surface to be heated, enhancing the Hα emission line. This needs to be investigated and a more detailed analysis based on a larger database is in progress and will give more light into the activity-binarity relation.

Bibliography

Abazajian, K. N., Adelman-McCarthy, J. K., Agüeros, M. A., et al. 2009, ApJS, 182, 543 17

Abt, H. A. 1983, ARA&A, 21, 343 1

Adelman-McCarthy, J. K., Agüeros, M. A., Allam, S. S., et al. 2008, ApJS, 175, 297 45, 85

Adelman-McCarthy, J. K., Agüeros, M. A., Allam, S. S., et al. 2007, ApJS, 172, 634 17, 19

Ak, T., Bilir, S., Ak, S., & Eker, Z. 2008, New Astronomy, 13, 133 40

Althaus, L. G. & Benvenuto, O. G. 1996, MNRAS, 278, 981 81

Aungwerojwit, A., Gänsicke, B. T., Rodríguez-Gil, P., et al. 2007, 469, 297 10

Baraffe, I., Chabrier, G., Allard, F., & Hauschildt, P. H. 1998, A&A, 337, 403 2, 95, 102, 103

Basri, G. 1987, ApJ, 316, 377 77

Bayless, A. J. & Orosz, J. A. 2006, ApJ, 651, 1155 94, 95, 99, 102, 103

Bergeron, P., Saumon, D., & Wesemael, F. 1995, 443, 764 23, 90

Beuermann, K., Baraffe, I., Kolb, U., & Weichhold, M. 1998, 339, 518 22

Bragaglia, A., Renzini, A., & Bergeron, P. 1995, 443, 735 98

Catalán, S., Isern, J., García-Berro, E., & Ribas, I. 2008, MNRAS, 387, 1693 82

Cram, L. E. & Mullan, D. J. 1979, ApJ, 234, 579 76

Cram, L. E. & Mullan, D. J. 1985, ApJ, 294, 626 76

Cruz, K. L. & Reid, I. N. 2002, AJ, 123, 2828 2

Cutri, R. M., Skrutskie, M. F., van Dyk, S., et al. 2003, 2MASS All Sky Catalog of point sources. 35, 91

Davis, P. J., Kolb, U., & Willems, B. 2009, ArXiv e-prints VI, 8, 13, 72, 73, 74, 106

Davis, P. J., Kolb, U., Willems, B., & Gänsicke, B. T. 2008, ArXiv e-prints, 805 13, 67

De Gennaro, S., von Hippel, T., Winget, D. E., et al. 2008, AJ, 135, 1 29

de Marco, O. 2009, PASP, 121, 316 7

Delfosse, X., Forveille, T., Perrier, C., & Mayor, M. 1998, 331, 581 44

Delfosse, X., Forveille, T., Ségransan, D., et al. 2000, A&A, 364, 217 35, 92

Drake, A. J., Djorgovski, S. G., Mahabal, A., et al. 2009, ApJ, 696, 870 10, 86

Eggleton, P. P. 1983, 268, 368 65

Eisenstein, D. J., Liebert, J., Harris, H. C., et al. 2006, ApJS, 167, 40 V, 4, 5, 16, 19, 23, 26, 27, 28, 29, 30, 31, 32

Finley, D. S., Koester, D., & Basri, G. 1997, 488, 375 23

Fontaine, G., Brassard, P., & Bergeron, P. 2001, 113, 409 3, 6

Fuhrmeister, B. & Schmitt, J. H. M. M. 2003, 403, 247 10

Fulbright, M. S., Liebert, J., Bergeron, P., & Green, R. 1993, 406, 240 10

Gänsicke, B. T., Jordan, S., Beuermann, K., et al. 2004, 613, L141 10, 67

Gänsicke, B. T., Dillon, M., Southworth, J., et al. 2009, MNRAS, 397, 2170 11

Haefner, R., Fiedler, A., Butler, K., & Barwig, H. 2004, A&A, 428, 181 10

Hawley, S. L., Gizis, J. E., & Reid, I. N. 1996, AJ, 112, 2799 77

Heller, R., Homeier, D., Dreizler, S., & Østensen, R. 2009, Journal of Physics Conference Series, 172, 012023 8

Hillwig, T. C., Gale, A. A., Honeycutt, R. K., & Rengstorf, A. W. 2002, 114, 756 10

Hjellming, M. S. & Taam, R. E. 1991, 370, 709 7

Horne, K. 1986, 98, 609 59, 88

Hurley, J. R., Tout, C. A., & Pols, O. R. 2002, 329, 897 67

Iben, I. J. & Laughlin, G. 1989, ApJ, 341, 312 82

Iben, I. J. & Livio, M. 1993, 105, 1373 8, 67

Jordi, K., Grebel, E. K., & Ammon, K. 2006, 460, 339 14

Kafka, S., Honeycutt, R. K., Howell, S. B., & Harrison, T. E. 2005, AJ, 130, 2852 93

Kawaler, S. D., O'Brien, M. S., Clemens, J. C., et al. 1995, ApJ, 450, 350 10

Kawka, A. & Vennes, S. 2007, ArXiv Astrophysics e-prints 97

Kawka, A., Vennes, S. ., Koch, R., & Williams, A. 2002, 124, 2853 10

Kawka, A., Vennes, S., Dupuis, J., Chayer, P., & Lanz, T. 2008, ApJ, 675, 1518 10

Kepler, S. O., Kleinman, S. J., Nitta, A., et al. 2007, MNRAS, 375, 1315 32, 51, 73

Kirkpatrick, J. D., Henry, T. J., & McCarthy, D. W., J. 1991, 77, 417 2

Koester, D. 2008, ArXiv e-prints 23

Koester, D., Napiwotzki, R., Voss, B., Homeier, D., & Reimers, D. 2005, 439, 317 5, 90, 98

Leggett, S. K., Allard, F., Dahn, C., et al. 2000, ApJ, 535, 965 99

Liebert, J., Wickramsinghe, D. T., Schmidt, G. D., et al. 2005, 129, 2376 30, 51, 74

Liu, Q. & Yang, Y. 2003, Chinese Journal of Astronomy and Astrophysics, 3, 142 66, 67

López-Morales, M. 2007, 660, 732 102

López-Morales, M. & Shaw, J. S. 2007, in Astronomical Society of the Pacific Conference Series, Vol. 362, The Seventh Pacific Rim Conference on Stellar Astrophysics, ed. Y. W. Kang, H.-W. Lee, K.-C. Leung, & K.-S. Cheng, 26–+ 82, 101

Marsh, T. R. 1989, 101, 1032 88

Marsh, T. R., Dhillon, V. S., & Duck, S. R. 1995, 275, 828 4, 74, 106

Martin, D. C., Fanson, J., Schiminovich, D., et al. 2005, ApJ, 619, L1 96

Martín, E. L., Delfosse, X., Basri, G., et al. 1999, 118, 2466 2

Maxted, P. F. L., Gänsicke, B. T., Burleigh, M. R., et al. 2009, MNRAS, 1464 10

Maxted, P. F. L., Marsh, T. R., Morales-Rueda, L., et al. 2004, 355, 1143 10

Maxted, P. F. L., Marsh, T. R., Moran, C., Dhillon, V. S., & Hilditch, R. W. 1998, 300, 1225 10

Maxted, P. F. L., Napiwotzki, R., Dobbie, P. D., & Burleigh, M. R. 2006, 442, 543 10

Maxted, P. F. L., Napiwotzki, R., Marsh, T. R., et al. 2007, in Astronomical Society of the Pacific Conference Series, Vol. 372, 15th European Workshop on White Dwarfs, ed. R. Napiwotzki & M. R. Burleigh, 471–+ 10

Morales, J. C., Ribas, I., & Jordi, C. 2008, A&A, 478, 507 82

Morales-Rueda, L., Marsh, T. R., Maxted, P. F. L., et al. 2005, 359, 648 10, 44

Morrissey, P., Schiminovich, D., Barlow, T. A., et al. 2005, ApJ, 619, L7 96

Nagel, T., Schuh, S., Kusterer, D., et al. 2006, A&A, 448, L25 10

Nebot Gómez-Morán, A., Schwope, A. D., Schreiber, M. R., et al. 2009, A&A, 495, 561 10, 13, 35, 45, 107

Nelemans, G. & Tout, C. A. 2005, 356, 753 13, 82

O'Brien, M. S., Bond, H. E., & Sion, E. M. 2001, 563, 971 10

O'Donoghue, D., Koen, C., Kilkenny, D., et al. 2003, MNRAS, 345, 506 10

Osterbrock, D. E., Fulbright, J. P., & Bida, T. A. 1997, 109, 614 88

Osterbrock, D. E., Fulbright, J. P., Martel, A. R., et al. 1996, PASP, 108, 277 88

Paczyński, B. 1976, in IAU Symp. 73: Structure and Evolution of Close Binary Systems, 75 7, 8

Patterson, J. 1984, 54, 443 40

Pickles, A. J. 1998, PASP, 110, 863 14

Pinsonneault, M. H., Andronov, N., & Sills, A. 2002, in The Physics of Cataclysmic Variables and Related Objects, ed. B. T. Gänsicke, K. Beuermann, & K. Reinsch (ASP Conf. Ser. 261), 208–216 11

Politano, M. & Weiler, K. P. 2006, 641, L137 VI, 13, 44, 45, 50, 51, 57, 106

Politano, M. & Weiler, K. P. 2007, 665, 663 44, 72

Pyrzas, S., Gänsicke, B. T., Marsh, T. R., et al. 2009, MNRAS, 394, 978 10, 13, 45, 86, 94, 102, 107

Rappaport, S., Joss, P. C., & Verbunt, F. 1983, 275, 713 44, 100

Raymond, S. N., Szkody, P., Hawley, S. L., et al. 2003, 125, 2621 14, 15

Rebassa-Mansergas, A., Gaensicke, B. T., Rodriguez-Gil, P., Schreiber, M. R., & Koester, D. 2007, ArXiv e-prints, 707 8, 13, 19, 22, 28, 34, 35, 36, 46, 50, 65, 72, 82, 85, 90, 91, 92, 93, 95, 96, 102, 103

Rebassa-Mansergas, A., Gaensicke, B. T., Schreiber, M. R., Koester, D., & Rodriguez-Gil, P. 2009, ArXiv e-prints 11, 13, 15, 17, 45, 85

Rebassa-Mansergas, A., Gaensicke, B. T., Schreiber, M. R., et al. 2008, ArXiv e-prints, 808 10, 13, 34, 35, 45, 59, 67, 85, 93

Richards, G. T., Fan, X., Newberg, H. J., et al. 2002, 123, 2945 15

Richards, G. T., Nichol, R. C., Gray, A. G., et al. 2004, ApJS, 155, 257 86

Ritter, H. & Kolb, U. 2003, 404, 301 68, 73, 74

Saffer, R. A., Wade, R. A., Liebert, J., et al. 1993, 105, 1945 10

Salasnich, B., Girardi, L., Weiss, A., & Chiosi, C. 2000, A&A, 361, 1023 3

Sandquist, E. L., Taam, R. E., Chen, X., Bodenheimer, P., & Burkert, A. 1998, ApJ, 500, 909 7

Schlegel, D. J., Finkbeiner, D. P., & Davis, M. 1998, ApJ, 500, 525 34

Schmidt, G. D., Szkody, P., Vanlandingham, K. M., et al. 2005, ApJ, 630, 1037 23

Schreiber, M. R. & Gänsicke, B. T. 2003, 406, 304 8, 13, 44, 45, 101

Schreiber, M. R., Gänsicke, B. T., Southworth, J., Schwope, A. D., & Koester, D. 2008, 484, 441 10, 13, 34, 35, 40, 45, 50, 59, 85, 101

Schreiber, M. R., Nebot Gomez-Moran, A., & Schwope, A. D. 2007, in Astronomical Society of the Pacific Conference Series, Vol. 372, Astronomical Society of the Pacific Conference Series, ed. A. Napiwotzki & M. R. Burleigh, 459–+ 45

Schwarzenberg-Czerny, A. 1996, 460, L107 60

Schwope, A. D., Nebot Gomez-Moran, A., Schreiber, M. R., & Gänsicke, B. T. 2009, A&A, 500, 867 23, 46

Shen, K. J., Idan, I., & Bildsten, L. 2009, ApJ, 705, 693 101

Shimanskii, V. V. & Borisov, N. V. 2002, Astronomy Reports, 46, 406 10

Shimanskii, V. V., Borisov, N. V., Pozdnyakova, S. A., et al. 2008, Astronomy Reports, 52, 558 10

Shimansky, V. V., Borisov, N. V., & Shimanskaya, N. N. 2003, Astronomy Reports, 47, 763 10

Sills, A., Pinsonneault, M. H., & Terndrup, D. M. 2000, 534, 335 44, 100

Silvestri, N. M., Hawley, S. L., & Oswalt, T. D. 2005, AJ, 129, 2428 79, 82, 84, 107

Silvestri, N. M., Hawley, S. L., West, A. A., et al. 2006, 131, 1674 8, 13, 14, 15, 16, 17, 18, 23, 26, 27, 28, 29, 31, 32, 33, 34, 45, 86, 90

Silvestri, N. M., Lemagie, M. P., Hawley, S. L., et al. 2007, ArXiv e-prints, 704 13, 16, 45

Sing, D. K., Holberg, J. B., Howell, S., et al. 2005, in Astronomical Society of the Pacific Conference Series, Vol. 334, 14th European Workshop on White Dwarfs, ed. D. Koester & S. Moehler, 393–+ 10

Sion, E. M., Greenstein, J. L., Landstreet, J. D., et al. 1983, ApJ, 269, 253 4

Smolčić, V., Ivezić, Ž., Knapp, G. R., et al. 2004, 615, L141 13, 45

Stauffer, J. R. 1987, 94, 996 10

Stauffer, J. R. & Hartmann, L. W. 1986, ApJS, 61, 531 76, 80

Steinfadt, J. D. R., Bildsten, L., & Howell, S. B. 2008, ApJ, 677, L113 86

Strassmeier, K. G., Fekel, F. C., Bopp, B. W., Dempsey, R. C., & Henry, G. W. 1990, ApJS, 72, 191 77

Szkody, P., Anderson, S. F., Hayden, M., et al. 2009, AJ, 137, 4011 23

Tappert, C., Gänsicke, B. T., Schmidtobreick, L., et al. 2007, 474, 205 10

Tappert, C., Gänsicke, B. T., Zorotovic, M., et al. 2009, A&A, 504, 491 10

Tauris, T. M. & Dewi, J. D. M. 2001, A&A, 369, 170 8

Thorstensen, J. R., Schwarz, R., Schwope, A. D., et al. 2009, PASP, 121, 465 65

Vallenari, A., Pasetto, S., Bertelli, G., et al. 2006, A&A, 451, 125 40

van den Besselaar, E. J. M., Greimel, R., Morales-Rueda, L., et al. 2007, 466, 1031 10

Vennes, S., Ferrario, L., & Wickramasinghe, D. T. 1999, 302, L49 10

Verbunt, F. & Zwaan, C. 1981, 100, L7 11, 43

Vogel, J., Schwope, A. D., & Gänsicke, B. T. 2007, 464, 647 23

Walkowicz, L. M. & Hawley, S. L. 2009, AJ, 137, 3297 76

Walkowicz, L. M., Hawley, S. L., & West, A. A. 2004, PASP, 116, 1105 81

Webbink, R. F. 1984, 277, 355 7

Webbink, R. F. & Wickramasinghe, D. T. 2005, in Astronomical Society of the Pacific Conference Series, Vol. 330, The Astrophysics of Cataclysmic Variables and Related Objects, ed. J.-M. Hameury & J.-P. Lasota, 137–+ 23

West, A. A., Hawley, S. L., Bochanski, J. J., et al. 2008, AJ, 135, 785 33, 77, 78, 79, 81, 82, 107

West, A. A., Hawley, S. L., Walkowicz, L. M., et al. 2004, AJ, 128, 426 27, 77, 81

Willems, B. & Kolb, U. 2004, 419, 1057 7, 8, 13, 40, 45, 50, 57, 69, 72, 74, 78, 105, 106

Wood, J. H., Naylor, T., & Marsh, T. R. 1995, 274, 31 81, 101

Wood, M. A. 1995, in White Dwarfs, ed. D. Koester & K. Werner, LNP No. 443 (Heidelberg: Springer), 41–45 4, 5, 6, 37, 102

Yanny, B., Rockosi, C., Newberg, H. J., et al. 2009, AJ, 137, 4377 13

Appendix A

Tables

Table A.1: Number of candidate, spectra taken according to our selection criteria, number of identified WDMS binaries, number of systems for which spectra were taken but are outside the selection criteria, success rate, galactic coordinates, space density, reddening and error on the density, for the 116 plate-pairs and 8 single plates with WDMS target selection that have been observed in SEGUE.

Plate	$N_{\rm cand}$	$N_{\rm spec}$	$N_{\rm WDMS}$	$N_{\rm out}$	$\frac{(N_{\rm WDMS}-N_{\rm out})}{N_{\rm spec}}$	$\frac{(N_{\rm WDMS}-N_{\rm out})}{N_{\rm spec}} * N_{\rm cand}$	l	$\|b\|$	ρ	$E(B-V)$	$\sigma\rho$
2303/2318	31	3	0	0	0	0	21.999	31.00	0	0.113	0
2304/2319	3	1	1	0	1	3	41.947	206.64	2.13e-05	0.038	2.13e-05
2305/2320	9	1	0	0	0	0	36.654	44.84	0	0.227	0
2306/2321	1	1	1	0	1	1	50.928	156.16	7.10e-06	0.07	7.10e-06
2307/2322	2	2	1	0	0.5	1	44.606	171.39	7.10e-06	0.105	7.10e-06
2308/2323	6	2	1	1	0	0	38.777	67.76	0	0.101	0
2310/2325	2	1	2	2	0	0	46.371	80.43	0	0.07	0
2312/2327	2	1	1	0	1	2	55.193	116.28	1.42e-05	0.038	1.42e-05
2313/2328	4	4	2	1	0.25	1	62.582	131.95	7.10e-06	0.029	7.10e-06
2315/2330	3	1	2	1	1	3	31.957	199.78	2.13e-05	0.033	2.13e-05
2316/2331	3	3	4	1	1	3	37.195	164.26	2.13e-05	0.033	1.23e-05
2317/2332	4	3	5	2	1	4	29.168	221.47	2.84e-05	0.055	1.64e-05
2334/2339	4	4	1	0	0.25	1	40.799	177.71	7.10e-06	0.132	7.10e-06
2335/2340	3	1	0	0	0	0	42.745	174.65	0	0.201	0
2378/2398	9	5	3	0	0.6	5.4	22	150.00	3.84e-05	0.118	2.21e-05
2379/2399	2	2	1	1	0	0	32	150.00	0	0.114	0
2380/2400	4	3	2	0	0.66	2.66	40.307	185.88	1.89e-05	0.043	1.33e-05
2381/2401	7	4	4	0	1	7	43.491	195.57	4.97e-05	0.023	2.49e-05
2382/2402	1	1	0	0	0	0	37.581	225.30	0	0.052	0
2383/2403	2	2	2	0	1	2	43.624	150.92	1.42e-05	0.029	1.00e-05
2384/2404	3	3	3	0	1	3	46.196	163.48	2.13e-05	0.014	1.23e-05
2386/2406	5	5	4	0	0.8	4	53.919	205.39	2.84e-05	0.029	1.42e-05
2387/2407	4	4	3	0	0.75	3	54.796	189.36	2.13e-05	0.013	1.23e-05
2389/2409	2	1	1	0	1	2	49.817	250.28	1.42e-05	0.039	1.42e-05
2390/2410	6	5	5	0	1	6	59.243	162.38	4.26e-05	0.016	1.91e-05
2393/2413	4	3	2	0	0.66	2.66	61.303	245.98	1.89e-05	0.023	1.34e-05
2394/2414	6	3	3	0	1	6	54.158	143.49	4.26e-05	0.009	2.46e-05
2397/2417	11	3	3	3	0	0	14.001	150.00	0	0.127	0
2441/2443	5	5	3	0	0.6	3	18	150.00	2.13e-05	0.119	1.23e-05
2442/2444	2	2	2	0	1	2	29	150.00	1.42e-05	0.136	1.00e-05
2445/2460	3	3	4	1	1	3	50.16	116.77	2.13e-05	0.02	1.23e-05
2446/2461	4	3	3	0	1	4	57.369	122.84	2.84e-05	0.012	1.64e-05
2447/2462	2	2	2	0	1	2	56.812	100.68	1.42e-05	0.015	1.00e-05

Table A.1: continued.

plate	N_{cand}	N_{spec}	N_{WDMS}	N_{out}	$\frac{(N_{\text{WDMS}}-N_{\text{out}})}{N_{\text{spec}}}$	$\frac{(N_{\text{WDMS}}-N_{\text{out}})}{N_{\text{spec}}} * N_{\text{cand}}$	l	$\lvert b\rvert$	ρ	$E(B-V)$	$\sigma\rho$
2449/2464	6	5	4	0	0.8	4.8	52.657	81.08	3.41e-05	0.018	1.70e-05
2452/2467	1	1	1	0	1	1	74.5	154.34	7.10e-06	0.028	7.10e-06
2457/2472	1	1	1	0	1	1	87.02	147.00	7.10e-06	0.016	7.10e-06
2459/2474	4	4	2	0	0.5	2	49.491	42.88	1.42e-05	0.041	1.00e-05
2537/2545	366	1	0	0	0	0	10.5	110.00	0	0.478	0
2538/2546	429	21	0	0	0	0	16	110.00	0	0.525	0
2539/2547	9	8	6	0	0.75	6.75	54.362	100.60	4.79e-05	0.012	1.96e-05
2540/2548	6	5	3	0	0.6	3.6	25.711	130.00	2.56e-05	0.056	1.48e-05
2541/2549	8	5	4	0	0.8	6.4	29.71	130.00	4.55e-05	0.031	2.27e-05
2551/2561	5	4	3	0	0.75	3.75	33	94.00	2.66e-05	0.025	1.54e-05
2553/2563	6	4	2	0	0.5	3	20	94.00	2.13e-05	0.045	1.51e-05
2554/2564	17	1	1	0	1	17	14	94.00	1.21e-04	0.219	1.20e-04
2555/2565	914	16	0	0	0	0	8	94.00	0	0.927	0
2556/2566	272	3	0	0	0	0	8	94.00	0	0.297	0
2557/2567	4	3	2	0	0.66	2.66	57.629	171.74	1.89e-05	0.017	1.34e-05
2558/2568	4	4	1	0	0.25	1	62.082	288.15	7.10e-06	0.029	7.10e-06
2559/2569	2	1	0	0	0	0	49.817	250.28	0	0.039	0
2621/2627	4	4	3	0	0.75	3	25	94.00	2.13e-05	0.053	1.23e-05
2622/2628	6	4	3	0	0.75	4.5	50	94.00	3.20e-05	0.131	1.85e-05
2623/2629	3	3	2	0	0.66	2	35	94.00	1.42e-05	0.171	1.00e-05
2624/2630	4	4	4	0	1	4	65	94.00	2.84e-05	0.034	1.42e-05
2667/2671	7	4	1	0	0.25	1.75	31.529	216.61	1.24e-05	0.045	1.24e-05
2668/2672	15	1	0	0	0	0	12	187.00	0	0.46	0
2669/2673	29	4	0	0	0	0	22	187.00	0	0.379	0
2670/2674	2	1	1	0	1	2	32.64	183.37	1.42e-05	0.04	1.42e-05
2676/2694	21	3	0	0	0	0	12	187.00	0	0.093	0
2677/2695	9	3	2	0	0.66	6	20	187.00	4.26e-05	0.076	3.01e-05
2678/2696	59	1	0	0	0	0	8	187.00	0	0.23	0
2680/2698	76	7	0	0	0	0	25	178.00	0	0.441	0
2681/2699	68	1	1	0	1	68	15.001	178.00	4.83e-04	0.495	4.83e-04
2682/2700	21	4	2	0	0.5	10.5	15	178.00	7.46e-05	0.143	5.27e-05
2683/2701	8	4	3	0	0.75	6	25	178.00	4.26e-05	0.052	2.46e-05
2689/2707	3	3	3	0	1	3	55	300	2.13e-05	0.026	1.23e-05
2690/2708	6	6	4	0	0.66	4	40	270.00	2.84e-05	0.068	1.42e-05
2714/2729	7	4	3	0	0.75	5.25	21.5	203.00	3.73e-05	0.043	2.15e-05
2724/2739	5	4	3	0	0.75	3.75	50.001	9.84	2.66e-05	0.036	1.54e-05
2797/2818	27	7	3	0	0.43	11.57	21.75	31.00	8.22e-05	0.107	4.75e-05
2798/2819	22	5	4	0	0.8	17.6	20	70.00	1.25e-04	0.07	6.25e-05
2800/2821	79	7	2	0	0.28	22.57	10.618	70.00	1.60e-04	0.154	1.13e-04
2801/2822	4	3	2	0	0.66	2.66	36.73	109.77	1.89e-05	0.067	1.34e-05
2803/2824	6	3	3	1	0.66	4	33.5	110.00	2.84e-05	0.051	2.01e-05
2805/2826	6	3	2	0	0.66	4	29.5	187.00	2.84e-05	0.226	2.01e-05
2806/2827	96	7	0	0	0	0	14	229.00	0	0.099	0
2807/2828	6	4	4	0	1	6	20	229.00	4.26e-05	0.038	2.13e-05
2812/2833	2091	25	1	0	0.04	83.64	8	50.00	5.94e-04	0.391	5.94e-04
2849/2864	2	2	1	0	0.5	1	71.741	141.60	7.10e-06	0.042	7.10e-06
2852/2867	4	2	2	0	1	4	40.721	239.10	2.84e-05	0.035	2.01e-05
2853/2868	6	5	4	0	0.8	4.8	55.272	220.87	3.41e-05	0.026	1.70e-05
2854/2869	8	5	3	0	0.6	4.8	51.204	234.18	3.41e-05	0.033	1.97e-05
2855/2870	6	5	5	0	1	6	65.867	203.12	4.26e-05	0.032	1.91e-05
2856/2871	4	4	3	0	0.75	3	65.54	178.45	2.13e-05	0.021	1.23e-05
2857/2872	3	3	3	0	1	3	66.835	227.63	2.13e-05	0.02	1.23e-05
2858/2873	6	5	5	0	1	6	48.173	134.92	4.26e-05	0.008	1.91e-05
2859/2874	6	5	5	0	1	6	45	270.00	4.26e-05	0.065	1.91e-05
2861/2876	1	1	1	0	1	1	50	270.00	7.10e-06	0.038	7.10e-06
2862/2877	5	2	3	1	1	5	57.374	266.09	3.55e-05	0.024	2.51e-05
2887/2912	4207	12	0	0	0	0	0.999	187.00	0	0.775	0
2888/2913	4	3	3	0	1	4	29.011	225.20	2.84e-05	0.037	1.64e-05

Table A.1: continued.

plate	$N_{\rm cand}$	$N_{\rm spec}$	$N_{\rm WDMS}$	$N_{\rm out}$	$\frac{(N_{\rm WDMS}-N_{\rm out})}{N_{\rm spec}}$	$\frac{(N_{\rm WDMS}-N_{\rm out})}{N_{\rm spec}} * N_{\rm cand}$	l	$\|b\|$	ρ	$E(B-V)$	$\sigma\rho$
2889/2914	1	1	1	0	1	1	47.321	197.01	7.10e-06	0.017	7.10e-06
2890/2915	12	5	4	0	0.8	9.6	19.589	201.85	6.82e-05	0.032	3.41e-05
2891/2916	4	4	3	0	0.75	3	23.159	197.73	2.13e-05	0.067	1.23e-05
2893/2918	3	2	2	0	1	3	77.606	245.85	2.13e-05	0.027	1.51e-05
2894/2919	4	3	2	0	0.66	2.66	65.671	140.22	1.89e-05	0.025	1.34e-05
2895/2920	2	2	2	0	1	2	62.619	294.52	1.42e-05	0.019	1.00e-05
2897/2922	3	1	1	0	1	3	60.318	299.18	2.13e-05	0.032	2.13e-05
2898/2923	5	5	2	0	0.4	2	67.387	123.12	1.42e-05	0.013	1.00e-05
2899/2924	3	3	2	0	0.66	2	82.452	315.26	1.42e-05	0.022	1.00e-05
2901/2926	6	4	4	0	1	6	62.426	314.09	4.26e-05	0.037	2.13e-05
2902/2927	5	4	1	0	0.25	1.25	50.001	9.84	8.88e-06	0.036	8.88e-06
2903/2928	7	4	3	0	0.75	5.25	68.734	338.75	3.73e-05	0.026	2.15e-05
2904/2929	6	5	2	0	0.4	2.4	77.716	41.12	1.70e-05	0.014	1.21e-05
2905/2930	6	5	4	0	0.8	4.8	74.29	3.16	3.41e-05	0.024	1.70e-05
2906/2931	4	4	4	0	1	4	70.654	67.14	2.84e-05	0.009	1.42e-05
2907/2932	4	4	2	0	0.5	2	63.494	82.47	1.42e-05	0.01	1.00e-05
2908/2933	5	5	4	0	0.8	4	60.221	358.72	2.84e-05	0.023	1.42e-05
2909/2934	3	3	3	0	1	3	51.018	353.65	2.13e-05	0.043	1.23e-05
2910/2935	1	1	1	0	1	1	60.569	51.02	7.10e-06	0.022	7.10e-06
2911/2936	3	2	1	0	0.5	1.5	55.839	63.98	1.06e-05	0.023	1.07e-05
2938/2943	10	3	3	0	1	10	19.999	178.00	7.10e-05	0.066	4.10e-05
2939/2944	2	2	2	0	1	2	30	150.00	1.42e-05	0.04	1.00e-05
2940/2945	8	3	1	0	0.33	2.66	18.619	211.61	1.89e-05	0.019	1.89e-05
2941/2946	4	4	4	1	0.75	3	22.441	180.89	2.13e-05	0.052	1.23e-05
2963/2965	3	3	2	1	0.33	1	72.77	303.81	7.10e-06	0.023	7.10e-06
2336	9	3	1	0	0.33	3	22.786	130.00	2.13e-05	0.067	2.13e-05
2337	4	1	1	0	1	4	25.938	150.00	2.84e-05	0.035	2.84e-05
2475	5	1	0	0	0	0	78.701	42.31	0	0.013	0
2552	10	1	1	0	1	10	26	94.00	7.10e-05	0.044	7.10e-05
2620	20	1	1	0	1	20	15	94.00	1.42e-04	0.125	1.42e-04
2865	7	4	2	0	0.5	3.5	68.734	158.75	2.49e-05	0.028	1.76e-05
2866	2	2	1	0	0.5	1	58.262	157.01	7.10e-06	0.03	7.10e-06
2942	9	5	2	0	0.4	3.6	30.485	203	2.55e-05	0.07	1.81e-05

Table A.2: Plate number, Fiber number, MJD of the observation, and *ugriz* colors of the 301 WDMS and WDMS candidate systems identified with SEGUE.

System	Plate	Fiber	MJD	u	σ_u	g	σ_g	r	σ_r	i	σ_i	z	σ_z
000250.64–045041.6	2630	439	54327	19.846	0.042	19.728	0.021	19.464	0.018	18.569	0.015	17.903	0.022
000356.93–050332.7	2630	173	54327	18.522	0.022	18.203	0.027	18.152	0.013	17.503	0.013	16.883	0.018
000453.93+265420.4	2824	78	54452	19.935	0.046	19.596	0.025	19.436	0.017	18.846	0.023	18.345	0.043
000504.91+243409.6	2822	180	54389	19.513	0.035	18.895	0.014	18.486	0.013	17.503	0.014	16.766	0.018
000531.09–054343.2	2624	82	54380	17.282	0.016	16.727	0.013	16.599	0.013	15.807	0.013	15.098	0.012
000559.87-054416.0	2624	60	54380	18.561	0.024	18.321	0.012	17.756	0.013	17.070	0.014	16.619	0.017
000651.91+284647.1	2824	601	54452	19.271	0.033	18.665	0.020	18.247	0.015	17.146	0.016	16.470	0.014
000829.92+273340.5	2824	1	54452	19.599	0.045	18.943	0.020	18.223	0.016	17.301	0.018	16.763	0.038
000935.50+243251.2	2822	62	54389	20.293	0.051	18.966	0.017	17.776	0.012	16.856	0.018	16.337	0.016
003804.41+083416.9	2312	576	53709	19.373	0.033	18.053	0.020	16.951	0.013	15.872	0.016	15.272	0.018
010341.59+003132.6	2328	385	53728	19.354	0.032	19.114	0.025	18.822	0.024	18.130	0.017	17.628	0.032
010448.50–010516.7	2313	241	53726	20.167	0.060	18.656	0.021	17.458	0.014	16.207	0.012	15.554	0.010
010704.58+005907.9	2328	416	53728	21.780	0.220	19.851	0.030	18.626	0.013	17.748	0.011	17.264	0.020
011123.90+000935.2	2328	594	53728	19.022	0.029	18.475	0.030	17.890	0.023	17.068	0.018	16.512	0.017
011932.38–090219.1	2864	615	54467	19.909	0.046	19.280	0.019	18.421	0.016	17.582	0.011	17.088	0.017
013000.74+385205.4	2336	7	53712	20.128	0.039	19.030	0.017	17.935	0.011	17.203	0.013	16.762	0.016
014143.68–093811.7	2865	170	54497	19.663	0.037	19.377	0.022	18.931	0.015	18.072	0.019	17.435	0.022
014147.33–094200.3	2865	165	54497	21.690	0.176	19.990	0.025	18.795	0.014	17.581	0.018	16.914	0.018

Table A.2: continued.

System (SDSSJ)	Plate	Fiber	MJD	u	σ_u	g	σ_g	r	σ_r	i	σ_i	z	σ_z
014232.59–083528.4	2865	525	54497	19.501	0.037	18.819	0.024	18.082	0.013	17.040	0.013	16.348	0.016
020351.29+004025.0	2866	636	54478	20.343	0.050	19.430	0.023	18.682	0.017	17.625	0.019	16.990	0.017
021145.57+071831.1	2321	460	53711	19.816	0.035	19.468	0.025	19.081	0.023	18.161	0.022	17.457	0.014
023438.48+244535.6	2399	75	53764	21.155	0.108	20.012	0.021	18.851	0.016	18.040	0.015	17.524	0.017
023526.43+280026.6	2444	222	54082	19.963	0.044	19.689	0.152	19.110	0.308	18.365	0.386	17.875	0.307
023938.04+273654.0	2444	149	54082	20.013	0.051	19.312	0.016	19.214	0.015	18.638	0.022	17.961	0.021
024942.92+335032.5	2398	256	53768	20.400	0.054	19.459	0.018	18.277	0.012	17.504	0.010	17.028	0.015
025347.51+335221.0	2378	172	53759	19.802	0.040	18.947	0.013	17.972	0.009	17.099	0.008	16.518	0.016
025555.87+352830.2	2378	538	53759	18.370	0.023	17.559	0.014	16.519	0.009	15.550	0.008	14.992	0.013
030138.24+050218.9	2307	140	53710	19.111	0.026	18.388	0.023	18.048	0.013	17.272	0.017	16.606	0.016
030247.65+372125.9	2443	185	54082	20.634	0.071	19.589	0.014	18.444	0.012	17.749	0.012	17.367	0.018
030716.44+384822.8	2441	564	54065	20.642	0.075	19.039	0.126	17.861	0.316	16.698	0.201	16.056	0.122
030900.89+384835.2	2443	604	54082	20.318	0.049	19.873	0.016	19.424	0.014	18.339	0.013	17.551	0.018
030956.31+411049.2	2397	255	53763	24.598	1.009	18.405	0.030	16.976	0.014	15.777	0.012	14.979	0.009
031200.17+401336.9	2417	259	53766	21.550	0.134	20.016	0.018	19.102	0.013	18.401	0.015	17.937	0.021
031657.47+395931.9	2397	69	53763	20.682	0.064	18.898	0.013	17.871	0.011	17.135	0.009	16.633	0.012
031803.98+423034.4	2397	582	53763	18.409	0.025	17.199	0.013	16.252	0.008	15.185	0.011	14.507	0.012
032030.52+044243.5	2334	261	53730	18.450	0.026	18.213	0.017	17.918	0.012	16.988	0.015	16.257	0.014
032140.00+415307.5	2417	633	53766	21.078	0.135	20.582	0.076	19.490	0.024	18.345	0.013	17.674	0.018
034913.69+085810.8	2697	95	54389	20.481	0.056	19.828	0.029	18.942	0.019	17.994	0.018	17.345	0.022
041716.58+055522.4	2826	225	54389	20.108	0.043	19.913	0.017	19.585	0.016	18.846	0.016	18.253	0.026
042053.72+064922.4	2826	526	54389	20.922	0.071	19.755	0.019	18.655	0.012	17.165	0.012	16.231	0.013
044046.91–050413.0	2942	333	54521	19.703	0.044	19.348	0.014	19.144	0.017	18.267	0.017	17.548	0.018
044218.26–044820.2	2942	323	54521	19.958	0.051	19.141	0.016	18.420	0.013	17.398	0.013	16.787	0.015
044547.53–044559.1	2942	460	54521	20.975	0.097	19.265	0.015	18.295	0.018	17.776	0.017	17.486	0.019
044831.02+214909.8	2681	552	54397	19.342	0.030	18.546	0.013	17.652	0.007	16.625	0.009	15.916	0.013
054544.63+822205.9	2540	249	54110	19.615	0.037	17.431	0.013	16.438	0.013	15.764	0.016	15.385	0.015
055956.76+224704.6	2887	270	54521	20.923	0.089	18.873	0.012	17.880	0.007	17.338	0.012	16.970	0.019
063139.13+822827.8	2548	1	54152	19.286	0.031	19.084	0.020	18.819	0.018	17.956	0.018	17.333	0.026
063805.21+835526.9	2548	582	54152	19.537	0.044	19.321	0.021	19.475	0.021	18.896	0.020	18.220	0.038
064147.70+364058.9	2682	201	54401	20.483	0.049	18.816	0.010	17.874	0.009	17.171	0.012	16.665	0.013
064212.72+381638.4	2700	372	54417	19.895	0.041	19.096	0.011	18.670	0.011	17.703	0.011	17.041	0.018
064723.99+840724.1	2548	611	54152	19.981	0.050	19.424	0.021	19.175	0.017	18.499	0.020	17.942	0.030
064812.76+381005.9	2682	574	54401	19.733	0.033	18.988	0.010	17.964	0.012	17.220	0.010	16.803	0.015
070322.17+664908.0	2337	419	53740	19.973	0.044	18.642	0.019	17.512	0.011	16.366	0.016	15.712	0.020
070336.89+385142.2	2943	263	54502	20.845	0.056	19.940	0.013	19.009	0.010	17.965	0.012	17.369	0.016
070628.57+383650.2	2943	204	54502	20.217	0.049	19.412	0.016	18.507	0.011	17.554	0.015	16.984	0.016
071309.72+401249.4	2943	615	54502	19.897	0.040	19.082	0.013	18.342	0.011	17.401	0.012	16.825	0.015
072016.98+303824.6	2677	260	54180	20.789	0.067	18.810	0.011	17.672	0.011	16.441	0.016	15.820	0.013
072130.60+374228.3	2946	439	54506	20.467	0.054	19.791	0.020	19.455	0.017	18.363	0.015	17.697	0.023
072156.68+364048.5	2946	247	54506	19.526	0.033	17.865	0.010	16.697	0.007	15.959	0.018	15.557	0.020
072222.66+385702.9	2946	322	54506	19.223	0.031	17.533	0.018	16.269	0.011	15.521	0.017	15.101	0.014
072251.06+385944.6	2946	376	54506	19.997	0.048	19.068	0.021	18.269	0.013	17.002	0.010	16.231	0.014
072434.72+321609.4	2677	535	54180	18.815	0.023	18.066	0.012	17.434	0.009	16.259	0.011	15.558	0.016
072635.37+322554.3	2695	568	54409	19.701	0.031	19.212	0.015	18.677	0.011	17.811	0.013	17.276	0.015
073003.87+405450.1	2683	224	54153	19.633	0.032	18.495	0.014	17.399	0.018	16.198	0.013	15.475	0.019
073059.83+144052.0	2713	203	54397	19.035	0.021	18.155	0.013	17.289	0.007	16.070	0.009	15.349	0.016
073445.66+155448.9	2713	598	54397	18.226	0.017	17.432	0.009	16.667	0.007	15.544	0.013	14.867	0.015
073455.91+410537.4	2683	507	54153	17.698	0.017	17.403	0.010	17.220	0.019	16.423	0.019	15.796	0.018
073534.33+650648.8	2944	287	54523	20.067	0.037	19.499	0.015	19.087	0.013	18.058	0.012	17.343	0.017
073717.69+412620.1	2683	557	54153	17.891	0.020	17.590	0.018	17.104	0.012	16.495	0.012	15.877	0.014
073948.55+181813.9	2915	392	54497	20.424	0.051	19.584	0.019	18.515	0.014	17.833	0.013	17.354	0.019
074027.89+184819.8	2915	384	54497	20.163	0.045	19.556	0.016	18.745	0.010	17.885	0.010	17.413	0.018
074211.87+182227.6	2915	475	54497	19.419	0.026	18.998	0.013	18.961	0.014	18.199	0.012	17.570	0.018
074521.86+171520.6	2915	43	54497	20.852	0.097	19.462	0.013	18.602	0.009	17.821	0.011	17.192	0.017
074758.75+222942.3	2916	267	54507	19.748	0.040	19.120	0.015	18.682	0.017	17.667	0.017	17.038	0.018
074845.71+180240.4	2890	35	54495	16.741	0.017	16.337	0.026	15.616	0.069	14.965	0.042	14.518	0.029
075051.85+085020.1	2945	314	54505	19.101	0.027	18.085	0.010	17.219	0.009	16.177	0.012	15.604	0.013
075153.17+653104.6	2944	107	54523	20.955	0.077	19.975	0.017	18.871	0.014	18.014	0.016	17.442	0.018

Table A.2: continued.

System (SDSSJ)	Plate	Fiber	MJD	u	σ_u	g	σ_g	r	σ_r	i	σ_i	z	σ_z
075314.67+190926.0	2729	459	54419	20.164	0.056	19.508	0.017	18.647	0.017	17.804	0.012	17.286	0.020
075356.37+233118.9	2891	516	54507	18.535	0.021	18.019	0.015	17.436	0.010	16.442	0.011	15.829	0.019
075359.48+175445.5	2729	158	54419	20.194	0.058	19.701	0.018	19.450	0.016	18.505	0.014	17.699	0.019
075426.29+240721.3	2916	568	54507	20.417	0.052	19.921	0.017	19.192	0.021	17.999	0.017	17.275	0.019
080134.24+093643.0	2940	610	54508	18.716	0.095	17.457	0.075	16.894	0.062	15.404	0.019	14.783	0.018
081009.49+832816.5	2549	438	54523	20.271	0.077	19.699	0.023	18.796	0.015	17.852	0.017	17.295	0.021
081327.92+373245.6	2670	275	54115	18.919	0.024	18.073	0.015	16.925	0.016	16.118	0.014	15.625	0.017
081523.77+832651.2	2549	436	54523	20.096	0.063	19.576	0.018	18.751	0.015	18.001	0.019	17.525	0.026
082807.91–052045.5	2828	294	54438	20.292	0.055	19.571	0.015	18.620	0.014	17.721	0.013	17.179	0.016
082835.00+241547.6	2330	191	53738	20.503	0.066	20.050	0.021	19.378	0.020	18.448	0.024	17.959	0.023
082903.53+231651.0	2315	214	53741	19.780	0.038	18.825	0.021	17.759	0.017	16.547	0.013	15.830	0.018
083025.47–053638.7	2828	203	54438	20.034	0.046	19.411	0.017	18.834	0.012	17.883	0.013	17.259	0.017
083255.20–043046.2	2807	153	54433	19.567	0.326	17.762	0.064	16.909	0.020	15.644	0.010	14.968	0.016
083348.00+531632.1	2331	258	53742	20.725	0.069	19.959	0.030	19.353	0.021	18.493	0.019	17.868	0.033
083630.34–041018.9	2828	597	54438	19.884	0.043	19.247	0.014	18.505	0.013	17.404	0.011	16.750	0.018
083807.99+530254.3	2331	88	53742	19.366	0.038	19.397	0.023	18.922	0.018	18.330	0.020	17.807	0.029
084221.35+544834.5	2331	562	53742	20.702	0.072	20.089	0.023	19.909	0.023	19.167	0.023	18.451	0.040
084514.23+540311.6	2316	596	53757	19.754	0.036	18.720	0.018	17.736	0.018	16.821	0.015	16.273	0.014
084518.66+055911.7	2317	318	54152	19.529	0.035	18.042	0.016	16.88	0.013	15.930	0.017	15.373	0.015
084852.36+050135.6	2332	210	54149	20.022	0.035	19.480	0.016	19.297	0.020	18.726	0.018	18.221	0.024
084854.42+823437.2	2541	60	54481	19.678	0.041	18.748	0.014	17.791	0.013	16.613	0.014	15.944	0.017
085024.05+054757.8	2317	161	54152	18.070	0.023	16.323	0.016	15.071	0.011	14.270	0.015	13.848	0.014
085110.25+024731.8	2913	310	54526	20.592	0.059	19.689	0.017	18.647	0.014	17.464	0.011	16.751	0.021
085202.07+115400.1	2667	535	54142	18.760	0.023	18.093	0.024	17.424	0.011	16.693	0.008	16.214	0.014
085223.75+071326.0	2332	579	54149	21.011	0.103	20.197	0.023	19.602	0.023	18.510	0.016	17.737	0.034
085336.03+072033.5	2332	569	54149	19.985	0.050	19.213	0.023	18.525	0.018	17.469	0.013	16.701	0.019
085548.16+022341.6	2913	133	54526	20.494	0.069	19.906	0.021	19.366	0.019	18.066	0.013	17.174	0.017
085558.37+832841.5	2541	558	54481	18.790	0.024	17.911	0.029	16.926	0.019	16.141	0.016	15.702	0.020
085631.57+030554.7	2913	151	54526	19.372	0.028	19.101	0.016	19.137	0.018	18.465	0.018	17.769	0.022
085634.83+373913.4	2400	492	53765	19.929	0.044	19.441	0.030	19.024	0.021	18.095	0.018	17.394	0.019
090212.72+373757.3	2380	581	53759	17.728	0.013	16.718	0.018	15.723	0.020	14.743	0.011	14.199	0.013
091132.23+303605.3	2401	341	53768	19.602	0.031	19.023	0.018	18.676	0.019	17.919	0.014	17.352	0.031
091844.46+313743.5	2401	524	53768	19.423	0.034	18.897	0.020	18.000	0.018	17.305	0.022	16.877	0.021
091930.11+211904.7	2319	127	53763	20.664	0.068	19.332	0.017	18.371	0.014	16.831	0.019	15.755	0.018
092030.33+301831.2	2401	142	53768	20.921	0.082	19.705	0.022	18.572	0.016	17.555	0.018	16.955	0.017
092215.71+303954.5	2381	590	53762	17.733	0.017	17.113	0.017	16.340	0.016	15.190	0.014	14.504	0.020
093441.29+305026.0	2914	413	54533	20.030	0.049	19.389	0.020	18.911	0.024	17.832	0.016	17.073	0.019
094029.39+523324.7	2384	143	53763	18.653	0.035	17.814	0.031	16.843	0.013	15.954	0.017	15.399	0.017
094035.24+520007.6	2404	50	53764	19.771	0.050	19.211	0.038	18.563	0.024	17.717	0.019	17.155	0.030
094103.00+523257.4	2404	141	53764	19.574	0.036	19.256	0.020	18.934	0.054	18.259	0.015	17.729	0.021
094402.18+614307.9	2403	167	53795	19.166	0.026	18.746	0.020	17.918	0.012	17.288	0.013	16.901	0.022
094637.33+631228.1	2403	448	53795	20.044	0.053	19.885	0.033	19.478	0.024	18.655	0.023	18.098	0.033
095632.22-003341.4	2867	278	54479	20.010	0.040	19.127	0.029	18.232	0.023	16.917	0.027	16.047	0.030
095953.52-011504.4	2867	203	54479	20.318	0.052	19.695	0.020	19.575	0.022	18.741	0.016	18.073	0.028
100347.63+352958.2	2407	332	53771	20.108	0.049	19.665	0.025	19.353	0.019	18.423	0.018	17.816	0.025
100533.84+250149.4	2406	292	54084	20.080	0.044	19.425	0.025	18.627	0.024	17.684	0.017	17.065	0.020
100732.50+254334.6	2406	223	54084	20.185	0.041	19.403	0.020	18.639	0.020	17.443	0.026	16.676	0.017
100821.19+260213.9	2406	495	54084	20.182	0.046	19.964	0.020	19.374	0.016	18.507	0.017	17.994	0.030
100828.18+263732.5	2386	416	54064	19.131	0.021	17.249	0.019	16.114	0.022	15.432	0.016	15.033	0.025
100900.48+360457.6	2407	436	53771	20.039	0.042	19.510	0.015	18.537	0.014	17.749	0.017	17.269	0.019
101032.62+344527.9	2407	149	53771	20.132	0.050	19.662	0.021	19.089	0.017	18.352	0.025	17.861	0.028
102102.25+174439.9	2868	311	54451	20.350	0.059	19.512	0.017	19.013	0.019	17.972	0.021	17.223	0.021
102205.96+080246.6	2869	289	54454	19.045	0.030	18.922	0.017	18.540	0.016	17.878	0.015	17.366	0.025
102256.25+095418.5	2869	327	54454	19.887	0.049	19.147	0.025	18.334	0.020	17.037	0.012	16.238	0.020
102438.46+162458.2	2868	202	54451	19.887	0.046	19.041	0.018	18.341	0.019	17.230	0.016	16.523	0.016
102515.38+174937.6	2868	478	54451	19.935	0.041	19.704	0.025	19.746	0.023	18.870	0.034	18.157	0.029
102623.21+162938.5	2868	86	54451	20.349	0.065	19.747	0.031	19.238	0.021	18.366	0.015	17.791	0.024
102843.97+443252.6	2557	399	54178	19.254	0.036	17.781	0.015	16.652	0.016	15.640	0.019	15.100	0.020
102857.78+093129.8	2854	573	54480	17.181	0.021	16.400	0.023	15.581	0.027	14.596	0.021	13.994	0.021

Table A.2: continued.

System (SDSSJ)	Plate	Fiber	MJD	u	σ_u	g	σ_g	r	σ_r	i	σ_i	z	σ_z
103432.27+442956.6	2567	485	54179	20.691	0.071	19.584	0.025	18.601	0.016	17.255	0.016	16.385	0.019
104751.79+483503.7	2410	357	54087	20.211	0.064	19.591	0.033	19.412	0.029	18.590	0.024	18.099	0.033
105008.93+473748.0	2390	270	54094	19.933	0.035	18.718	0.011	17.634	0.019	16.731	0.018	16.229	0.018
105042.59+470628.7	2410	250	54087	20.718	0.118	19.758	0.027	18.805	0.018	17.392	0.018	16.598	0.020
105051.70–001207.7	2409	121	54210	20.051	0.035	18.952	0.017	18.017	0.024	16.941	0.018	16.313	0.012
105526.23+472923.0	2390	169	54094	19.537	0.031	18.286	0.011	17.256	0.019	16.043	0.012	15.334	0.017
105730.98+474614.3	2410	112	54087	20.886	0.087	19.922	0.036	19.016	0.025	18.049	0.020	17.528	0.029
110442.27–153936.2	2690	335	54211	20.065	0.052	17.909	0.014	16.919	0.018	16.386	0.013	16.047	0.018
110517.60+385125.7	2871	467	54536	19.054	0.022	18.443	0.019	18.083	0.016	17.320	0.014	16.736	0.016
110520.63+282408.7	2870	118	54534	20.865	0.067	19.475	0.018	18.634	0.018	17.255	0.036	16.198	0.017
110529.78–164719.3	2708	233	54561	19.513	0.045	19.407	0.020	19.186	0.017	18.440	0.018	17.900	0.029
110652.91+284245.4	2870	631	54534	20.349	0.050	19.212	0.020	18.225	0.017	17.112	0.018	16.494	0.056
110734.09-162414.4	2690	195	54211	17.747	0.020	17.614	0.028	16.916	0.012	16.273	0.011	15.823	0.019
110738.05+380051.3	2871	169	54536	20.376	0.052	19.952	0.024	19.538	0.019	18.484	0.023	17.669	0.024
110741.47+283003.1	2870	29	54534	19.525	0.031	18.197	0.028	17.083	0.015	16.150	0.013	15.628	0.012
110749.80+290939.9	2870	607	54534	21.331	0.117	19.931	0.032	18.760	0.028	17.924	0.018	17.428	0.025
110758.94+275346.2	2870	6	54534	20.211	0.053	19.318	0.031	18.247	0.029	17.375	0.023	16.866	0.047
110834.66–154847.3	2708	501	54561	19.95	0.062	19.265	0.017	18.821	0.017	17.868	0.016	17.203	0.021
110854.22–145147.0	2708	447	54561	20.165	0.061	19.817	0.022	19.232	0.018	18.556	0.018	18.081	0.026
111210.25+392453.1	2871	610	54536	19.661	0.031	18.223	0.022	17.139	0.018	16.292	0.010	15.811	0.013
111251.20+190700.3	2872	232	54533	19.996	0.035	19.462	0.020	19.062	0.018	18.341	0.019	17.811	0.025
111419.27+083829.0	2413	136	54169	18.922	0.039	18.432	0.027	18.319	0.020	17.539	0.025	16.796	0.029
111428.51+590209.1	2414	461	54526	20.116	0.047	19.649	0.049	19.164	0.019	17.945	0.019	17.012	0.025
111459.92+092411.1	2413	172	54169	19.679	0.034	19.054	0.020	18.977	0.057	18.383	0.041	17.843	0.025
111501.51–120321.9	2874	265	54561	20.198	0.049	19.664	0.020	19.522	0.018	18.763	0.018	18.103	0.020
111615.73+590509.3	2414	465	54526	19.504	0.038	18.770	0.030	17.854	0.019	16.998	0.018	16.503	0.027
111710.54–125540.9	2874	205	54561	20.270	0.048	19.668	0.019	19.239	0.015	18.456	0.017	17.915	0.022
111722.07–104556.1	2859	408	54570	17.926	0.023	17.842	0.017	17.403	0.011	16.502	0.012	15.887	0.015
111920.11–104810.6	2874	448	54561	19.827	0.044	18.867	0.016	17.793	0.012	16.857	0.011	16.339	0.011
111950.69+185351.0	2872	70	54533	19.727	0.037	18.710	0.023	17.676	0.013	16.792	0.010	16.295	0.020
112012.71+190126.8	2872	71	54533	19.085	0.030	18.353	0.020	17.688	0.026	16.663	0.022	16.022	0.035
112016.08+675750.6	2873	379	54505	20.559	0.073	19.389	0.026	18.433	0.020	17.242	0.012	16.595	0.021
112308.40–115559.3	2859	72	54570	18.585	0.024	17.991	0.022	17.480	0.016	16.322	0.015	15.510	0.021
112409.43+590935.8	2414	596	54526	20.397	0.046	19.358	0.015	18.525	0.018	17.297	0.013	16.553	0.018
112651.03–081640.1	2876	255	54581	20.041	0.059	18.960	0.020	17.922	0.013	17.048	0.011	16.503	0.017
112812.63+671738.3	2873	513	54505	19.647	0.033	18.940	0.021	18.082	0.021	17.018	0.021	16.439	0.017
113457.72+655408.7	2873	55	54505	18.231	0.023	18.138	0.015	18.124	0.019	17.416	0.024	16.672	0.024
113546.87+675832.3	2873	561	54505	20.889	0.079	19.718	0.025	18.643	0.020	17.332	0.017	16.581	0.016
113557.51+010310.4	2877	521	54523	20.455	0.046	19.754	0.024	19.446	0.018	18.437	0.018	17.601	0.017
113600.68+001212.2	2877	499	54523	20.048	0.057	20.028	0.022	19.704	0.021	19.050	0.016	18.571	0.038
113800.35–001144.4	2877	111	54523	19.135	0.025	18.849	0.020	18.868	0.021	18.162	0.023	17.535	0.027
114316.55+665813.1	2873	36	54505	20.272	0.047	19.778	0.025	19.112	0.020	18.181	0.023	17.574	0.022
120953.67+185815.7	2918	44	54554	20.376	0.046	18.866	0.022	17.740	0.014	16.946	0.017	16.460	0.022
121033.60+185346.2	2918	56	54554	20.410	0.054	19.903	0.033	19.471	0.021	18.600	0.018	18.057	0.024
121318.14+510247.4	2919	609	54537	18.867	0.030	18.468	0.017	18.317	0.020	17.586	0.021	17.059	0.018
121412.67+410132.8	2467	601	54176	20.222	0.061	19.303	0.020	18.431	0.012	17.688	0.015	17.218	0.025
122644.16+010302.5	2568	569	54153	20.433	0.049	19.083	0.018	18.039	0.015	16.710	0.013	15.941	0.015
123528.65+003042.2	2895	498	54567	18.407	0.029	17.807	0.022	17.397	0.020	16.409	0.017	15.622	0.019
123847.53–021900.8	2922	339	54612	20.460	0.054	19.083	0.016	18.001	0.015	16.904	0.014	16.257	0.014
123922.33+005548.8	2920	603	54562	19.569	0.033	19.274	0.026	19.207	0.021	18.398	0.017	17.789	0.023
124140.76+600711.4	2446	345	54571	18.056	0.018	17.726	0.037	17.522	0.027	16.763	0.033	16.212	0.027
124232.45–064607.7	2689	370	54149	18.506	0.024	17.464	0.018	16.336	0.018	15.413	0.015	14.879	0.020
124250.39–085332.0	2707	245	54144	20.171	0.057	19.973	0.026	19.475	0.017	18.593	0.013	17.985	0.025
124356.79-064758.4	2707	444	54144	18.492	0.029	18.098	0.024	18.003	0.013	17.227	0.017	16.577	0.025
124511.47+584551.8	2461	283	54570	20.811	0.065	19.327	0.018	18.210	0.018	17.422	0.028	16.971	0.022
124731.83+585158.1	2461	251	54570	20.541	0.071	19.276	0.025	18.177	0.016	17.157	0.029	16.603	0.015
124752.00+483835.3	2923	242	54563	19.544	0.027	17.310	0.024	16.305	0.021	15.759	0.037	15.460	0.022
124910.54+284333.7	2472	55	54175	20.600	0.073	19.572	0.028	18.606	0.022	17.442	0.022	16.769	0.022
124945.14+495752.7	2923	464	54563	19.007	0.027	18.176	0.015	17.300	0.020	16.187	0.018	15.473	0.018

Table A.2: continued.

System (SDSSJ)	Plate	Fiber	MJD	u	σ_u	g	σ_g	r	σ_r	i	σ_i	z	σ_z
125039.65+091634.6	2965	230	54594	21.339	0.114	19.461	0.031	18.255	0.018	17.187	0.026	16.660	0.021
125105.17+502727.5	2923	459	54563	20.171	0.039	19.665	0.017	19.125	0.028	18.101	0.015	17.540	0.021
125316.24+100744.1	2965	514	54594	19.752	0.047	18.506	0.024	17.343	0.013	16.139	0.016	15.512	0.013
125341.54+103413.9	2965	573	54594	18.274	0.034	17.843	0.017	17.788	0.021	16.974	0.019	16.347	0.020
125903.39+193145.7	2924	180	54582	20.787	0.077	19.663	0.020	18.596	0.015	17.921	0.019	17.591	0.019
130012.49+190857.4	2924	114	54582	19.850	0.040	19.220	0.024	18.679	0.021	17.663	0.020	16.887	0.018
130804.66–004031.6	2926	289	54625	20.101	0.044	19.172	0.016	18.067	0.025	17.259	0.020	16.818	0.022
131208.10+002057.9	2926	483	54625	18.746	0.030	18.485	0.015	18.347	0.014	17.561	0.014	16.924	0.025
131247.93–003427.5	2926	150	54625	20.980	0.082	19.886	0.020	18.852	0.019	17.934	0.021	17.416	0.020
131632.04–003758.0	2926	17	54625	20.607	0.058	19.355	0.019	18.230	0.016	16.967	0.022	16.263	0.027
132040.28+661214.8	2460	315	54616	18.808	0.023	18.726	0.015	18.376	0.026	17.792	0.019	17.392	0.023
132142.39+664612.7	2445	391	54573	18.429	0.021	18.097	0.050	17.262	0.016	16.401	0.016	15.854	0.022
132942.56+665539.8	2460	500	54616	20.658	0.064	19.493	0.029	18.339	0.025	17.421	0.016	16.917	0.023
133732.33+082815.5	2928	286	54614	20.802	0.080	19.922	0.027	19.130	0.019	18.020	0.017	17.313	0.021
133830.06+102034.6	2928	368	54614	20.359	0.057	19.738	0.016	19.211	0.018	18.338	0.019	17.782	0.024
133907.55+673333.9	2445	620	54573	17.938	0.026	17.144	0.023	16.241	0.010	15.706	0.018	15.394	0.011
134008.04+082248.4	2903	216	54581	18.418	0.023	17.796	0.020	17.362	0.016	16.121	0.017	15.389	0.020
134207.24+285707.9	2929	377	54616	20.471	0.061	19.406	0.021	18.216	0.015	17.099	0.018	16.512	0.019
134520.62+174805.3	2930	298	54589	19.439	0.033	18.874	0.025	18.276	0.014	17.207	0.021	16.588	0.023
134641.59+174357.4	2930	244	54589	21.070	0.080	19.836	0.036	18.698	0.021	17.682	0.021	17.036	0.020
134721.80+270724.9	2929	63	54616	17.645	0.016	17.299	0.021	16.648	0.017	15.996	0.017	15.592	0.012
134841.61+183410.5	2905	488	54580	17.702	0.013	17.310	0.017	17.194	0.013	16.470	0.019	15.879	0.014
135207.77+185033.8	2930	583	54589	20.632	0.064	19.469	0.016	18.438	0.013	17.254	0.024	16.628	0.016
135232.45+284333.8	2929	623	54616	21.426	0.110	19.943	0.025	18.788	0.015	17.825	0.011	17.324	0.018
135643.56–085808.9	2716	399	54629										
135930.96–101029.7	2716	211	54628										
140923.26+371048.5	2906	469	54577	16.598	0.013	15.859	0.013	14.879	0.013	14.323	0.013	13.962	0.023
141052.79+375435.6	2931	526	54590	19.803	0.043	19.286	0.030	18.373	0.019	17.652	0.018	17.243	0.022
141635.70+360006.5	2931	61	54590	18.983	0.023	18.156	0.025	17.201	0.021	16.240	0.024	15.763	0.021
141759.16+361542.8	2931	32	54590	19.955	0.040	18.788	0.027	17.684	0.017	16.879	0.020	16.383	0.022
142105.31+572457.1	2447	540	54498	16.879	0.044	16.851	0.034	16.280	0.021	15.602	0.021	15.155	0.021
142405.07+553008.0	2462	59	54561	20.190	0.060	18.996	0.032	18.016	0.032	17.431	0.018	17.082	0.021
142444.36+443114.5	2932	244	54595	20.691	0.085	19.991	0.043	19.465	0.033	18.832	0.026	18.464	0.035
142503.62+073846.4	2933	285	54617	20.378	0.052	19.655	0.019	18.864	0.015	17.791	0.014	17.093	0.021
142541.80+442411.7	2932	205	54595	21.235	0.088	19.977	0.020	18.888	0.020	17.804	0.016	17.166	0.016
142557.28+442554.1	2932	202	54595	19.633	0.031	18.651	0.015	17.740	0.018	16.732	0.015	16.122	0.013
142631.93+091621.1	2933	340	54617	20.493	0.057	19.509	0.022	18.685	0.014	17.540	0.018	16.879	0.013
142951.19+575949.0	2547	198	53917	20.059	0.042	19.431	0.015	18.749	0.020	17.756	0.019	17.074	0.022
143026.84+073450.0	2933	85	54617	18.493	0.026	18.279	0.027	18.063	0.015	17.187	0.016	16.498	0.023
143114.35+075707.0	2933	146	54617	19.773	0.044	19.198	0.025	18.458	0.020	17.733	0.023	17.271	0.021
143143.83+565728.2	2547	122	53917	20.590	0.062	19.918	0.020	19.803	0.021	19.033	0.018	18.232	0.030
143539.80+590529.5	2539	524	53918	20.167	0.052	18.338	0.018	17.144	0.021	16.213	0.012	15.654	0.015
143604.00+571906.2	2547	56	53917	21.126	0.105	19.911	0.019	18.837	0.015	18.191	0.013	17.745	0.022
143642.01+574146.3	2547	110	53917	20.869	0.075	19.733	0.024	18.598	0.014	17.383	0.014	16.688	0.013
143746.69+573706.0	2547	69	53917	18.962	0.024	18.517	0.025	18.113	0.013	17.057	0.011	16.354	0.017
143947.78+574115.4	2547	26	53917	20.784	0.084	19.471	0.018	18.331	0.012	17.620	0.013	17.195	0.023
143957.92+573944.6	2539	8	53918	19.615	0.036	18.243	0.016	17.157	0.011	16.413	0.012	15.963	0.019
144258.47+001031.5	2934	354	54626	18.379	0.018	18.329	0.020	18.262	0.022	17.475	0.015	16.758	0.027
144600.37+000817.0	2934	473	54626	20.574	0.051	19.981	0.019	19.815	0.018	18.983	0.019	18.146	0.027
145305.77+001048.2	2934	640	54626	19.710	0.031	18.889	0.016	18.200	0.017	17.094	0.019	16.392	0.020
150438.86+321443.4	2935	187	54652	19.342	0.029	19.078	0.016	18.367	0.014	17.682	0.025	17.277	0.024
151744.70+062011.9	2927	135	54621	21.319	0.117	19.835	0.024	18.660	0.016	17.523	0.013	16.892	0.017
151852.44+074459.3	2739	525	54618	20.488	0.048	19.958	0.020	19.533	0.020	18.565	0.020	17.938	0.021
152002.84+081231.0	2739	571	54618	19.555	0.035	19.159	0.019	18.953	0.018	17.998	0.017	17.254	0.022
152033.43+063442.9	2739	61	54618	19.475	0.035	18.960	0.016	18.572	0.041	17.591	0.034	16.923	0.026
152416.97+504749.0	2449	408	54271	18.563	0.024	17.430	0.028	16.459	0.022	15.678	0.014	15.169	0.020
152425.21+504009.7	2449	420	54271	17.436	0.014	17.312	0.015	17.267	0.014	16.597	0.018	16.059	0.019
152439.79+501147.4	2449	468	54271	19.471	0.037	18.253	0.036	17.104	0.020	15.846	0.019	15.128	0.021
152852.32+492054.7	2464	149	54272	20.304	0.056	19.553	0.026	19.026	0.023	17.999	0.017	17.294	0.021

Table A.2: continued.

System (SDSSJ)	Plate	Fiber	MJD	u	σ_u	g	σ_g	r	σ_r	i	σ_i	z	σ_z
153009.49+384439.8	2936	13	54626	21.120	0.087	19.739	0.028	18.603	0.033	17.705	0.047	17.158	0.040
155808.49+264225.7	2474	594	54564	19.820	0.031	19.177	0.018	18.473	0.016	17.314	0.017	16.557	0.013
155811.24+253803.2	2474	11	54564	20.940	0.060	19.207	0.020	18.082	0.021	17.268	0.022	16.832	0.022
162354.45+630640.4	2560	474	54205	19.811	0.043	19.114	0.020	18.478	0.021	17.377	0.014	16.693	0.019
162552.91+640024.9	2560	406	54205	19.518	0.040	19.101	0.028	18.902	0.015	18.299	0.018	17.559	0.020
163022.96+632729.9	2560	507	54205	21.018	0.089	19.900	0.023	18.932	0.015	17.784	0.016	17.113	0.031
163544.74+620156.3	2560	57	54205	18.616	0.022	18.343	0.018	18.238	0.016	17.506	0.017	16.955	0.019
165240.74+134015.0	2817	450	54627	20.938	0.105	19.983	0.018	19.117	0.016	18.067	0.014	17.436	0.018
165329.97+134102.9	2817	522	54627	20.604	0.080	19.518	0.017	18.441	0.016	17.035	0.017	16.126	0.014
165447.75+131651.2	2817	568	54627	19.599	0.041	19.161	0.014	19.075	0.013	18.352	0.015	17.775	0.020
165459.27+131024.9	2817	578	54627	20.481	0.076	19.138	0.014	18.078	0.010	17.103	0.013	16.573	0.014
165717.36+131032.2	2817	615	54627	21.002	0.104	19.861	0.030	19.003	0.024	18.036	0.012	17.529	0.023
172445.28+073324.7	2818	310	54616	19.515	0.035	18.850	0.011	18.311	0.006	17.386	0.014	16.611	0.017
172552.45+632906.7	2561	202	54597	21.220	0.145	19.785	0.023	18.760	0.014	17.713	0.013	17.188	0.025
173104.52+070345.0	2797	92	54616	18.262	0.024	17.738	0.007	17.375	0.005	16.478	0.016	15.837	0.017
173153.03+065233.6	2818	98	54616	21.084	0.099	19.635	0.018	18.712	0.008	17.907	0.010	17.365	0.016
173226.13+433311.2	2820	170	54599	21.388	0.113	19.924	0.020	19.141	0.018	18.208	0.017	17.573	0.022
173338.91+634110.7	2561	159	54597	19.877	0.041	19.571	0.021	19.173	0.014	18.269	0.022	17.589	0.020
173849.76+635042.0	2561	72	54597	20.158	0.044	19.625	0.016	19.076	0.020	18.248	0.018	17.638	0.023
183329.18+643151.7	2552	481	54632	16.419	0.013	16.608	0.012	16.439	0.012	15.815	0.017	15.379	0.016
183453.07+413757.7	2798	466	54397	18.388	0.021	17.827	0.011	17.398	0.007	16.280	0.012	15.466	0.019
183809.61+415500.9	2819	484	54617	20.091	0.038	19.023	0.012	18.530	0.014	17.927	0.014	17.391	0.019
184412.58+412029.4	2798	632	54397	17.258	0.018	16.714	0.008	16.428	0.010	15.692	0.010	14.928	0.012
184436.94+410816.2	2819	35	54617	20.219	0.056	19.224	0.010	18.297	0.007	17.235	0.011	16.612	0.014
185256.00+183812.3	2833	155	54650	19.735	0.035	19.719	0.032	19.428	0.018	18.777	0.013	18.317	0.029
191910.86+375414.7	2800	437	54326	19.250	0.032	17.679	0.008	16.741	0.012	16.194	0.017	15.630	0.024
191911.33+370319.0	2800	257	54326	19.061	0.025	18.431	0.008	17.776	0.010	16.669	0.007	16.010	0.011
191916.88+621432.9	2563	268	54653	20.764	0.095	19.914	0.022	19.052	0.020	18.027	0.012	17.300	0.018
192306.01+620310.7	2563	189	54653	20.390	0.065	19.162	0.014	18.063	0.016	17.264	0.015	16.811	0.022
201239.31+601710.3	2564	499	54275	19.938	2.182	19.034	0.521	18.752	0.258	17.625	0.045	16.752	0.016
204647.27+021805.4	2815	272	54414	17.189	0.015	17.076	0.011	16.684	0.013	15.770	0.011	15.139	0.017
220838.56+050609.8	2323	247	54380	20.963	0.073	19.897	0.024	18.873	0.013	17.472	0.016	16.640	0.019
221343.64+072221.3	2308	561	54379	18.590	0.026	18.291	0.019	17.514	0.014	16.453	0.015	15.834	0.014
221453.16+055423.1	2323	76	54380	21.188	0.108	20.105	0.021	19.067	0.015	18.411	0.015	18.010	0.027
222822.73+391239.7	2620	78	54397	19.134	0.025	18.419	0.008	17.659	0.011	16.718	0.015	16.171	0.018
224307.59+312239.1	2627	388	54379	20.759	0.097	19.585	0.022	18.689	0.015	17.283	0.010	16.264	0.017
224819.40+304803.6	2627	160	54379	21.231	0.089	19.888	0.015	18.893	0.011	17.492	0.016	16.758	0.016
225117.28+310939.8	2621	597	54380	15.748	0.017	15.900	0.010	15.488	0.006	14.837	0.011	14.442	0.015
225145.03+302807.6	2627	63	54379	21.247	0.098	19.958	0.016	18.795	0.011	17.818	0.014	17.246	0.019
225716.58+074534.3	2325	379	54082	20.545	0.055	19.507	0.022	18.423	0.013	17.511	0.019	16.980	0.019
225847.57+071026.5	2325	498	54082	20.321	0.051	19.748	0.022	19.281	0.019	18.196	0.016	17.343	0.025
230248.99+081052.5	2325	601	54082	21.199	0.106	19.584	0.018	18.367	0.016	17.461	0.018	16.990	0.027
230833.71+224052.6	2629	467	54087	20.001	0.038	19.565	0.015	18.807	0.018	18.187	0.021	17.798	0.026
231105.66+220208.6	2629	177	54087	19.609	0.042	19.074	0.016	18.382	0.016	17.452	0.016	16.801	0.019
233856.89+074456.4	2628	133	54326	19.523	0.034	19.201	0.019	18.409	0.017	17.340	0.012	16.692	0.016
233922.26+074400.3	2628	88	54326	19.836	0.041	19.089	0.019	18.221	0.017	17.386	0.012	16.887	0.016
234106.82+083550.3	2628	112	54326	20.202	0.051	19.508	0.018	19.133	0.015	18.151	0.015	17.426	0.020

Table A.3: Stellar parameters of the 277 WDMS systems identified with SEGUE. For the 84 binaries containing a DB, DC, or unclear white dwarf spectral type, only some parameters obtained for the secondary star are given. Also included are the 24 candidate systems.

System	Type	$T_{\rm eff}$	$\sigma_{T_{\rm eff}}$	$\log g$	$\sigma_{\log g}$	$M_{\rm wd}$	$\sigma_{M_{\rm wd}}$	$d_{\rm wd}$	$\sigma_{d_{\rm wd}}$	Sp2	$d_{\rm sec}$	$\sigma_{d_{\rm sec}}$
SDSSJ000250.64–045041.6	DB/dM									3	797	157
SDSSJ000356.93–050332.7	DA/dM	17106	438	8.07	0.10	0.66	0.06	285	19	4	386	114
SDSSJ000453.93+265420.4	DA/dM	18974	1594	7.97	0.33	0.60	0.20	683	142	3	1037	204

Table A.3: continued.

System	Type	$T_{\rm eff}$	$\sigma_{T_{\rm eff}}$	$\log g$	$\sigma_{\log g}$	$M_{\rm wd}$	$\sigma_{M_{\rm wd}}$	$d_{\rm wd}$	$\sigma_{d_{\rm wd}}$	Sp2	$d_{\rm sec}$	$\sigma_{d_{\rm sec}}$
SDSSJ000504.91+243409.6	DA/dM	13127	2160	8.16	0.34	0.71	0.22	304	70	4	350	103
SDSSJ000531.09–054343.2	DA/dM	13127	657	7.91	0.14	0.56	0.08	129	11	4	167	49
SDSSJ000559.87–054416.0	DA/dM	31128	921	7.89	0.21	0.59	0.12	692	99	2	553	132
SDSSJ000651.91+284647.1	DA/dM	12976	688	7.83	0.21	0.51	0.12	343	44	3	420	83
SDSSJ000829.92+273340.5	DA/dM	15782	1481	7.73	0.37	0.47	0.20	615	131	2	656	156
SDSSJ000935.50+243251.2	DA/dM	14393	4221	8.58	0.68	0.98	0.32	347	162	2	479	114
SDSSJ003804.41+083416.9	DA/dM	8673	255	7.73	0.59	0.45	0.35	216	69	3	223	44
SDSSJ010341.59+003132.6	DA/dM	21535	1234	7.76	0.21	0.50	0.11	849	113	2	1159	276
SDSSJ010448.50–010516.7	cand									3	339	67
SDSSJ010704.58+005907.9	cand									1	1063	208
SDSSJ011123.90+000935.2	DA/dM	15071	547	7.72	0.13	0.47	0.06	458	36	2	654	156
SDSSJ011932.38–090219.1	DA/dM	15601	1500	8.44	0.35	0.89	0.20	497	126	2	629	150
SDSSJ013000.74+385205.4	DA:/dM									1	805	158
SDSSJ014143.68–093811.7	DC/dM									3	642	126
SDSSJ014147.33–094200.3	cand									3	490	96
SDSSJ014232.59–083528.4	DA/dM	9187	148	8.77	0.18	1.08	0.10	113	17	3	428	84
SDSSJ020351.29+004025.0	DA/dM	10918	589	7.98	0.45	0.59	0.28	420	115	3	501	99
SDSSJ021145.57+071831.1	DA/dM	19193	1301	8.09	0.26	0.67	0.16	700	123	3	758	149
SDSSJ023438.48+244535.6	WD/dM									1	1141	223
SDSSJ023526.43+280026.6	DA/dM	31128	1884	8.07	0.45	0.69	0.27	1344	401	2	1160	276
SDSSJ023938.04+273654.0	DA/dM	12681	1145	7.91	0.38	0.56	0.23	468	107	4	774	228
SDSSJ024942.92+335032.5	DA/dM	14065	3771	8.30	0.96	0.80	0.50	605	347	1	769	151
SDSSJ025347.51+335221.0	DA/dM	33740	2650	8.59	0.41	1.00	0.21	756	241	2	618	147
SDSSJ025555.87+352830.2	DB/dM									2	299	71
SDSSJ030138.24+050218.9	DA/dM	11045	275	8.40	0.17	0.86	0.10	161	20	4	324	95
SDSSJ030247.65+372125.9	WD/dM									1	1080	212
SDSSJ030716.44+384822.8	DA:/dM									3	373	73
SDSSJ030900.89+384835.2	DA/dM	18330	1516	8.12	0.33	0.69	0.21	788	175	4	589	173
SDSSJ030956.31+411049.2	DA:/dM									3	216	43
SDSSJ031200.17+401336.9	cand									1	1232	241
SDSSJ031657.47+395931.9	cand									1	761	149
SDSSJ031803.98+423034.4	DA/dM	8475	105	8.29	0.15	0.78	0.10	78	9	3	186	37
SDSSJ032030.52+044243.5	DA/dM	19193	2046	8.13	0.43	0.70	0.27	303	86	4	268	79
SDSSJ032140.00+415307.5	DB/dM									3	674	133
SDSSJ034913.69+085810.8	DA:/dM	10427	761	9.29	0.33	1.30	0.10	137	44	3	574	113
SDSSJ041716.58+055522.4	DA/dM	21785	2645	7.30	0.44	0.34	0.15	1421	404	3	1012	199
SDSSJ042053.72+064922.4	WD/dM									5	173	89
SDSSJ044046.91–050413.0	DA/dM	18120	1246	7.79	0.27	0.51	0.15	646	105	5	345	176
SDSSJ044218.26–044820.2	DA/dM	12110	2701	7.89	0.62	0.54	0.39	464	167	3	464	91
SDSSJ044547.53–044559.1	cand									0	1081	146
SDSSJ044831.02+214909.8	DA/dM	10548	639	8.73	0.41	1.06	0.19	150	47	3	311	61
SDSSJ054544.63+822205.9	cand									0	515	69
SDSSJ055956.76+224704.6	cand									3	1214	239
SDSSJ063139.13+822827.8	DA/dM	24726	3614	7.74	0.59	0.50	0.33	986	337	3	754	149
SDSSJ063805.21+835526.9	DA/dM	20566	1325	7.78	0.24	0.51	0.13	685	102	5	431	221
SDSSJ064147.70+364058.9	cand									1	675	132
SDSSJ064212.72+381638.4	DA/dM	10793	366	8.03	0.29	0.62	0.19	316	59	4	376	111
SDSSJ064723.99+840724.1	DA/dM	12681	1596	7.69	0.50	0.44	0.28	579	160	3	1044	206
SDSSJ064812.76+381005.9	DA/dM	19193	3292	8.00	0.61	0.62	0.38	726	271	1	709	139
SDSSJ070322.17+664908.0	WD/dM									3	322	63
SDSSJ070336.89+385142.2	DA:/dM	16717	12092	9.50	1.40	1.37	0.40	236	71	3	609	120
SDSSJ070628.57+383650.2	DB/dM									2	648	154
SDSSJ071309.72+401249.4	DA/dM	14228	2766	8.44	0.41	0.89	0.24	311	92	3	456	90
SDSSJ072016.98+303824.6	cand									3	340	67
SDSSJ072130.60+374228.3	DA/dM	11433	1040	8.54	0.38	0.95	0.21	307	87	4	493	145
SDSSJ072156.68+364048.5	DA:/dM									1	400	78
SDSSJ072222.66+385702.9	DA:/dM									1	306	60
SDSSJ072251.06+385944.6	DA:/dM									4	264	78
SDSSJ072434.72+321609.4	DA/dM	11699	1594	9.09	0.18	1.23	0.06	106	17	4	228	67

Table A.3: continued.

System	Type	$T_{\rm eff}$	$\sigma_{T_{\rm eff}}$	$\log g$	$\sigma_{\log g}$	$M_{\rm wd}$	$\sigma_{M_{\rm wd}}$	$d_{\rm wd}$	$\sigma_{d_{\rm wd}}$	Sp2	$d_{\rm sec}$	$\sigma_{d_{\rm sec}}$
SDSSJ072635.37+322554.3	DA/dM	14728	6198	8.98	0.87	1.19	0.28	208	138	3	598	118
SDSSJ073003.87+405450.1	WD/dM									3	295	58
SDSSJ073059.83+144052.0	DA/dM	9293	469	7.17	1.31	0.26	0.65	341	199	3	241	48
SDSSJ073445.66+155448.9	DA/dM	9401	149	8.45	0.19	0.89	0.12	85	13	4	141	42
SDSSJ073455.91+410537.4	DA/dM	19868	353	8.01	0.07	0.63	0.04	299	14	3	354	70
SDSSJ073534.33+650648.8	DA/dM	13432	1463	8.03	0.45	0.63	0.28	449	126	4	458	135
SDSSJ073717.69+412620.1	DA/dM	22550	544	7.89	0.09	0.57	0.05	404	23	2	474	113
SDSSJ073948.55+181813.9	WD/dM									1	878	172
SDSSJ074027.89+184819.8	DA/dM	28064	2918	8.06	0.40	0.68	0.24	1122	300	2	775	185
SDSSJ074211.87+182227.6	DA/dM	13127	1005	7.91	0.21	0.56	0.12	357	46	3	704	139
SDSSJ074521.86+171520.6	cand									2	713	170
SDSSJ074758.75+222942.3	DA/dM	12976	1078	7.83	0.41	0.51	0.24	436	103	3	513	101
SDSSJ074845.71+180240.4	DA/dM	34131	606	7.88	0.11	0.60	0.05	351	26	1	268	52
SDSSJ075051.85+085020.1	DA/dM	10307	162	8.31	0.17	0.80	0.11	159	20	3	260	51
SDSSJ075153.17+653104.6	DA:/dM									2	863	206
SDSSJ075314.67+190926.0	DA/dM	25595	2352	8.01	0.33	0.64	0.20	987	216	2	777	185
SDSSJ075356.37+233118.9	DA/dM	20331	1032	8.11	0.19	0.69	0.12	353	47	3	297	58
SDSSJ075359.48+175445.5	DA/dM	18756	1415	8.36	0.30	0.84	0.18	553	121	4	545	161
SDSSJ075426.29+240721.3	DC/dM									3	577	114
SDSSJ080134.24+093643.0	cand									2	194	46
SDSSJ081009.49+832816.5	DC/dM									2	745	177
SDSSJ081327.92+373245.6	DA/dM	21785	1955	8.48	0.31	0.92	0.18	427	101	1	405	79
SDSSJ081523.77+832651.2	DA/dM	30772	2268	8.12	0.48	0.72	0.29	1290	412	1	1051	206
SDSSJ082807.91–052045.5	WD/dM									2	716	171
SDSSJ082835.00+241547.6	DA/dM	22550	4173	8.02	0.74	0.64	0.44	1340	596	2	1210	288
SDSSJ082903.53+231651.0	DC/dM									3	348	69
SDSSJ083025.47–053638.7	DA/dM	13745	1127	8.18	0.30	0.72	0.19	444	91	3	582	115
SDSSJ083255.20-043046.2	DA/dM	16525	645	7.81	0.14	0.51	0.08	237	21	3	193	38
SDSSJ083348.00+531632.1	DA/dM	16336	3489	7.22	0.87	0.30	0.37	1552	710	2	1176	280
SDSSJ083630.34–041018.9	DA/dM	10548	417	8.13	0.43	0.68	0.28	369	102	3	439	87
SDSSJ083807.99+530254.3	WD/dM									1	1377	270
SDSSJ084221.35+544834.5	DA/dM	10548	778	7.79	0.87	0.49	0.53	653	306	4	954	281
SDSSJ084514.23+540311.6	DA/dM	13745	1985	7.83	0.52	0.52	0.32	494	150	2	455	108
SDSSJ084518.66+055911.7	DA/dM	24726	1893	8.29	0.26	0.81	0.16	470	91	2	372	89
SDSSJ084852.36+050135.6	DA/dM	14065	2147	7.36	0.52	0.33	0.21	804	239	3	1141	225
SDSSJ084854.42+823437.2	WD/dM									3	315	62
SDSSJ085024.05+054757.8	DA:/dM									1	205	40
SDSSJ085110.25+024731.8	WD/dM									3	453	89
SDSSJ085202.07+115400.1	DA/dM	17304	686	7.47	0.16	0.37	0.06	512	57	2	534	127
SDSSJ085223.75+071326.0	DA/dM	10548	967	8.28	0.91	0.78	0.49	549	301	4	642	189
SDSSJ085336.03+072033.5	DC/dM									3	573	113
SDSSJ085548.16+022341.6	DC/dM									5	261	134
SDSSJ085558.37+832841.5	DA/dM	19193	1584	8.26	0.33	0.78	0.20	360	83	1	444	87
SDSSJ085631.57+030554.7	DA/dM	18542	583	7.90	0.12	0.57	0.07	529	42	5	356	182
SDSSJ085634.83+373913.4	DA/dM	20804	1543	7.65	0.29	0.45	0.14	1008	179	4	569	168
SDSSJ090212.72+373757.3	DA/dM	18756	657	7.97	0.14	0.60	0.08	274	24	2	198	47
SDSSJ091132.23+303605.3	DA/dM	12828	923	8.17	0.24	0.71	0.16	375	63	3	737	145
SDSSJ091844.46+313743.5	DB/dM									1	901	176
SDSSJ091930.11+211904.7	DC/dM									6	95	44
SDSSJ092030.33+301831.2	WD/dM									2	754	180
SDSSJ092215.71+303954.5	DC/dM									3	188	37
SDSSJ093441.29+305026.0	DA/dM	13279	1904	8.35	0.28	0.83	0.18	340	70	4	375	110
SDSSJ094029.39+523324.7	DA/dM	19868	1500	8.16	0.29	0.72	0.18	432	86	2	377	90
SDSSJ094035.24+520007.6	DA/dM	19868	1403	7.98	0.28	0.61	0.17	742	133	3	647	127
SDSSJ094103.00+523257.4	DA/dM	18542	1090	8.06	0.23	0.66	0.14	637	99	3	848	167
SDSSJ094402.18+614307.9	DA/dM	28718	1025	7.61	0.23	0.46	0.10	993	156	1	736	144
SDSSJ094637.33+631228.1	DA/dM	28064	2735	8.02	0.40	0.65	0.24	1159	306	3	816	161
SDSSJ095632.22–003341.4	DA/dM	13904	1315	8.24	0.33	0.76	0.21	415	95	4	208	61
SDSSJ095953.52–011504.4	DA/dM	12110	885	7.39	0.33	0.33	0.13	672	135	4	623	184

Table A.3: continued.

System	Type	T_{eff}	$\sigma_{T_{\mathrm{eff}}}$	$\log g$	$\sigma_{\log g}$	M_{wd}	$\sigma_{M_{\mathrm{wd}}}$	d_{wd}	$\sigma_{d_{\mathrm{wd}}}$	Sp2	d_{sec}	$\sigma_{d_{\mathrm{sec}}}$
SDSSJ100347.63+352958.2	DA/dM	18974	1669	8.13	0.31	0.70	0.20	780	166	3	887	175
SDSSJ100533.84+250149.4	DC/dM									2	808	193
SDSSJ100732.50+254334.6	DC/dM									4	378	111
SDSSJ100821.19+260213.9	DB/dM									3	891	175
SDSSJ100828.18+263732.5	WD/dM									0	408	55
SDSSJ100900.48+360457.6	DB/dM									1	1071	210
SDSSJ101032.62+344527.9	DA/dM	21289	2513	8.13	0.43	0.70	0.27	939	268	2	1168	278
SDSSJ102102.25+174439.9	DA/dM	32972	2038	8.65	0.36	1.03	0.18	720	207	4	435	128
SDSSJ102205.96+080246.6	DA/dM	22811	1240	7.84	0.19	0.55	0.10	663	81	2	780	186
SDSSJ102256.25+095418.5	DA/dM	8282	165	8.26	0.36	0.76	0.23	157	39	4	280	82
SDSSJ102438.46+162458.2	DA/dM	15422	1049	8.31	0.21	0.81	0.13	385	59	3	403	79
SDSSJ102515.38+174937.6	DA/dM	22550	1290	7.84	0.21	0.54	0.11	857	112	4	638	188
SDSSJ102623.21+162938.5	DA/dM	20331	2207	7.41	0.40	0.37	0.16	1197	303	3	717	141
SDSSJ102843.97+443252.6	DA/dM	19193	1791	8.27	0.38	0.79	0.24	470	126	2	317	76
SDSSJ102857.78+093129.8	DA/dM	18756	313	8.29	0.06	0.80	0.04	144	7	3	125	25
SDSSJ103432.27+442956.6	DC/dM									4	346	102
SDSSJ104751.79+483503.7	DA/dM	12681	1394	7.84	0.45	0.52	0.27	610	161	3	1048	206
SDSSJ105008.93+473748.0	WD/dM									2	539	128
SDSSJ105042.59+470628.7	WD/dM									4	384	113
SDSSJ105051.70–001207.7	DA/dM	11433	700	8.49	0.34	0.92	0.19	260	65	3	369	73
SDSSJ105526.23+472923.0	DA:/dM	10073	579	9.50	0.08	1.37	0.02	73	7	3	269	53
SDSSJ105730.98+474614.3	DA/dM	15422	4502	7.46	1.62	0.36	0.87	1369	976	2	965	230
SDSSJ110442.27–153936.2	cand									0	560	75
SDSSJ110517.60+385125.7	DA/dM	10548	142	8.18	0.13	0.71	0.09	205	19	3	462	91
SDSSJ110520.63+282408.7	DC/dM									6	107	49
SDSSJ110529.78–164719.3	DA/dM	25891	1896	7.91	0.30	0.59	0.17	851	166	3	773	152
SDSSJ110652.91+284245.4	DA/dM	12536	1486	8.20	0.39	0.73	0.25	436	115	3	396	78
SDSSJ110734.09–162414.4	DA/dM	33740	1070	7.81	0.20	0.56	0.10	544	75	2	391	93
SDSSJ110738.05+380051.3	DA/dM	8977	361	7.69	0.88	0.43	0.53	407	186	4	515	152
SDSSJ110741.47+283003.1	DA/dM	9731	403	9.33	0.26	1.32	0.08	83	22	2	341	81
SDSSJ110749.80+290939.9	DA/dM	12110	2146	7.39	1.01	0.33	0.53	1259	622	1	896	176
SDSSJ110758.94+275346.2	DA/dM	10307	678	9.15	0.56	1.26	0.17	138	67	2	635	151
SDSSJ110834.66–154847.3	DA/dM	12976	1622	7.83	0.46	0.51	0.27	452	119	3	573	113
SDSSJ110854.22–145147.0	DA/dM	19640	3849	7.43	0.71	0.37	0.34	1328	520	2	1123	268
SDSSJ111210.25+392453.1	DA/dM	9731	246	8.43	0.29	0.87	0.18	178	38	2	378	90
SDSSJ111251.20+190700.3	DA/dM	12828	941	7.57	0.27	0.39	0.13	588	95	2	1017	242
SDSSJ111419.27+083829.0	DA/dM	15422	624	7.97	0.13	0.60	0.08	356	30	4	452	133
SDSSJ111428.51+590209.1	DC/dM									5	255	130
SDSSJ111459.92+092411.1	DA/dM	10427	211	8.28	0.23	0.78	0.15	236	38	5	465	238
SDSSJ111501.51–120321.9	DA/dM	10548	483	8.33	0.55	0.81	0.33	288	107	5	421	215
SDSSJ111615.73+590509.3	DA/dM	13588	1465	8.55	0.18	0.96	0.11	268	39	2	519	124
SDSSJ111710.54–125540.9	DA/dM	15964	1472	7.68	0.37	0.45	0.19	741	158	3	760	150
SDSSJ111722.07–104556.1	DB/dM									3	303	60
SDSSJ111920.11–104810.6	DB/dM									2	487	116
SDSSJ111950.69+185351.0	DC/dM									2	451	107
SDSSJ112012.71+190126.8	DA/dM	12976	2861	8.23	0.47	0.75	0.29	259	81	3	314	62
SDSSJ112016.08+675750.6	DA:/dM	10073	635	8.13	0.92	0.68	0.54	419	224	3	404	80
SDSSJ112308.40–115559.3	DA/dM	10073	215	9.12	0.25	1.25	0.08	64	14	5	117	60
SDSSJ112409.43+590935.8	DA/dM	9081	292	7.80	0.61	0.49	0.37	341	115	4	309	91
SDSSJ112651.03–081640.1	DA/dM	10670	620	9.11	0.49	1.25	0.26	168	99	2	504	120
SDSSJ112812.63+671738.3	DA/dM	11565	625	7.91	0.31	0.55	0.19	355	67	3	364	72
SDSSJ113457.72+655408.7	DC/dM									4	358	105
SDSSJ113546.87+675832.3	WD/dM									3	417	82
SDSSJ113557.51+010310.4	DA:/dM	30071	3076	6.41	0.66	0.18	0.14	3523	1174	4	550	162
SDSSJ113600.68+001212.2	DA:/dM	36154	3401	8.13	0.49	0.74	0.28	1420	465	2	1356	323
SDSSJ113800.35–001144.4	DA/dM	16336	834	8.01	0.19	0.62	0.12	417	52	3	667	131
SDSSJ114316.55+665813.1	DA:/dM	31488	2259	8.27	0.50	0.81	0.29	1093	378	3	642	126
SDSSJ120953.67+185815.7	DA/dM	26801	3913	8.53	0.48	0.96	0.25	701	246	1	590	116
SDSSJ121033.60+185346.2	DA/dM	17106	1701	7.89	0.40	0.56	0.24	722	175	3	827	163

Table A.3: continued.

System	Type	$T_{\rm eff}$	$\sigma_{T_{\rm eff}}$	$\log g$	$\sigma_{\log g}$	$M_{\rm wd}$	$\sigma_{M_{\rm wd}}$	$d_{\rm wd}$	$\sigma_{d_{\rm wd}}$	Sp2	$d_{\rm sec}$	$\sigma_{d_{\rm sec}}$
SDSSJ121318.14+510247.4	DA/dM	14560	772	7.83	0.12	0.52	0.06	340	24	3	545	107
SDSSJ121412.67+410132.8	DA/dM	15601	2173	8.11	0.36	0.68	0.23	726	173	1	992	194
SDSSJ122644.16+010302.5	WD/dM									4	275	81
SDSSJ123528.65+003042.2	DA/dM	18542	675	7.67	0.15	0.45	0.07	367	35	4	225	66
SDSSJ123847.53–021900.8	DA:/dM									3	365	72
SDSSJ123922.33+005548.8	DA/dM	17707	824	7.69	0.19	0.46	0.09	647	76	4	542	160
SDSSJ124140.76+600711.4	DA/dM	21785	1015	7.60	0.17	0.44	0.07	424	48	3	346	68
SDSSJ124232.45–064607.7	DC/dM									2	282	67
SDSSJ124250.39-085332.0	WD/dM									2	1226	292
SDSSJ124356.79–064758.4	DA/dM	17106	754	8.04	0.17	0.64	0.10	308	35	4	403	119
SDSSJ124511.47+584551.8	DA:/dM									1	777	152
SDSSJ124731.83+585158.1	DA:/dM	8475	423	7.87	1.14	0.52	0.68	257	151	3	403	79
SDSSJ124752.00+483835.3	cand									0	441	59
SDSSJ124910.54+284333.7	DA:/dM	10548	1015	8.32	0.87	0.80	0.47	464	248	3	529	104
SDSSJ124945.14+495752.7	DA/dM	9293	272	8.26	0.50	0.76	0.32	148	49	3	305	60
SDSSJ125039.65+091634.6	cand									2	538	128
SDSSJ125105.17+502727.5	DA/dM	10548	383	8.32	0.34	0.80	0.22	325	79	3	621	122
SDSSJ125316.24+100744.1	WD/dM									3	255	50
SDSSJ125341.54+103413.9	DA/dM	15782	203	7.81	0.05	0.51	0.03	263	8	5	173	88
SDSSJ125903.39+193145.7	WD/dM									0	1157	156
SDSSJ130012.49+190857.4	DA/dM	8673	259	8.81	0.41	1.10	0.18	123	39	4	378	111
SDSSJ130804.66–004031.6	WD/dM									1	709	139
SDSSJ131208.10+002057.9	DA/dM	17505	536	7.81	0.12	0.52	0.06	418	32	4	378	111
SDSSJ131247.93–003427.5	DA:/dM	10307	1151	8.36	1.14	0.83	0.54	394	257	2	874	208
SDSSJ131632.04–003758.0	DC/dM									3	394	78
SDSSJ132040.28+661214.8	DA/dM	28389	1407	8.05	0.27	0.67	0.16	719	131	1	976	191
SDSSJ132142.39+664612.7	DB/dM									2	394	94
SDSSJ132942.56+665539.8	DA:/dM									2	617	147
SDSSJ133732.33+082815.5	DA/dM	11302	6104	8.20	1.18	0.73	0.60	481	311	3	575	113
SDSSJ133830.06+102034.6	DA/dM	13745	1217	7.95	0.31	0.58	0.19	621	118	2	965	230
SDSSJ133907.55+673333.9	WD/dM									0	473	64
SDSSJ134008.04+082248.4	DA/dM	11565	570	8.31	0.25	0.80	0.16	151	27	3	265	52
SDSSJ134207.24+285707.9	WD/dM									3	397	78
SDSSJ134520.62+174805.3	DA/dM	18330	799	7.79	0.18	0.51	0.09	563	61	3	403	79
SDSSJ134641.59+174357.4	WD/dM									2	649	155
SDSSJ134721.80+270724.9	DA/dM	20804	471	7.94	0.09	0.59	0.05	278	16	1	399	78
SDSSJ134841.61+183410.5	DA/dM	15071	355	7.96	0.07	0.59	0.04	180	8	4	236	69
SDSSJ135207.77+185033.8	DA/dM	9293	389	8.83	0.46	1.11	0.19	177	63	3	411	81
SDSSJ135232.45+284333.8	cand									2	741	176
SDSSJ135643.56–085808.9	DA/dM	12976	2289	8.00	0.40	0.61	0.25	367	91	1	599	117
SDSSJ135930.96–101029.7	DA/dM	15246	425	7.90	0.09	0.56	0.05	229	14	4	240	71
SDSSJ140923.26+371048.5	DA/dM	30071	289	8.16	0.07	0.74	0.04	242	12	0	210	28
SDSSJ141052.79+375435.6	DA/dM	22811	1759	7.49	0.27	0.40	0.11	1001	178	1	931	182
SDSSJ141635.70+360006.5	DA/dM	17106	831	7.91	0.19	0.57	0.11	422	51	2	353	84
SDSSJ141759.16+361542.8	DA:/dM									2	494	118
SDSSJ142105.31+572457.1	DB/dM									1	346	68
SDSSJ142405.07+553008.0	WD/dM									0	951	128
SDSSJ142444.36+443114.5	cand									0	1965	265
SDSSJ142503.62+073846.4	DA/dM	30071	2474	8.54	0.49	0.97	0.25	911	330	3	517	102
SDSSJ142541.80+442411.7	WD/dM									3	542	107
SDSSJ142557.28+442554.1	DA/dM	10548	319	8.36	0.29	0.83	0.18	231	48	3	324	64
SDSSJ142631.93+091621.1	DA/dM	22037	2456	7.96	0.41	0.61	0.25	971	251	3	470	93
SDSSJ142951.19+575949.0	DA/dM	16336	1781	8.69	0.35	1.04	0.17	378	104	3	632	124
SDSSJ143026.84+073450.0	DC/dM									3	431	85
SDSSJ143114.35+075707.0	DA/dM	29050	1738	7.63	0.27	0.47	0.12	1280	226	2	746	178
SDSSJ143143.83+565728.2	DA/dM	10189	587	8.42	0.77	0.87	0.40	301	150	5	554	283
SDSSJ143539.80+590529.5	cand									2	411	98
SDSSJ143604.00+571906.2	WD/dM									1	1304	255
SDSSJ143642.01+574146.3	cand									3	511	101

Table A.3: continued.

System	Type	$T_{\rm eff}$	$\sigma_{T_{\rm eff}}$	$\log g$	$\sigma_{\log g}$	$M_{\rm wd}$	$\sigma_{M_{\rm wd}}$	$d_{\rm wd}$	$\sigma_{d_{\rm wd}}$	Sp2	$d_{\rm sec}$	$\sigma_{d_{\rm sec}}$
SDSSJ143746.69+573706.0	DA/dM	17912	846	8.12	0.19	0.69	0.12	392	50	4	323	95
SDSSJ143947.78+574115.4	DB/dM									1	1004	197
SDSSJ143957.92+573944.6	DA/dM	29727	3054	7.66	0.57	0.48	0.30	961	327	1	571	112
SDSSJ144258.47+001031.5	DB/dM									4	351	103
SDSSJ144600.37+000817.0	DA/dM	10670	425	7.97	0.39	0.58	0.25	448	108	5	440	225
SDSSJ145305.77+001048.2	DA/dM	11565	569	8.55	0.19	0.95	0.11	236	36	4	279	82
SDSSJ150438.86+321443.4	DA/dM	24163	3303	7.76	0.54	0.51	0.30	908	289	1	878	172
SDSSJ151744.70+062011.9	WD/dM									3	466	92
SDSSJ151852.44+074459.3	DA/dM	19868	2304	7.72	0.47	0.48	0.26	1054	290	4	580	171
SDSSJ152002.84+081231.0	DA/dM	17505	789	8.06	0.17	0.65	0.11	477	55	4	437	129
SDSSJ152033.43+063442.9	DA/dM	11302	480	8.48	0.25	0.91	0.15	203	38	4	366	108
SDSSJ152416.97+504749.0	DA/dM	34926	1595	8.31	0.24	0.84	0.14	430	76	2	269	64
SDSSJ152425.21+504009.7	DA/dM	19640	587	8.14	0.12	0.71	0.07	221	18	3	336	66
SDSSJ152439.79+501147.4	DA:/dM	27425	3576	8.27	0.55	0.80	0.32	749	277	3	209	41
SDSSJ152852.32+492054.7	DA/dM	9958	461	8.26	0.66	0.76	0.40	282	120	4	435	128
SDSSJ153009.49+384439.8	DA:/dM	10073	883	8.50	1.16	0.92	0.49	356	245	2	669	159
SDSSJ155808.49+264225.7	DA/dM	14560	4069	8.74	0.64	1.07	0.26	281	129	4	320	94
SDSSJ155811.24+253803.2	WD/dM									1	745	146
SDSSJ162354.45+630640.4	DA/dM	9731	289	8.63	0.35	1.00	0.19	180	48	4	335	99
SDSSJ162552.91+640024.9	DA/dM	8773	169	8.31	0.27	0.79	0.17	155	30	6	212	98
SDSSJ163022.96+632729.9	WD/dM									3	523	103
SDSSJ163544.74+620156.3	DA/dM	17505	582	7.81	0.13	0.52	0.07	378	31	3	514	101
SDSSJ165240.74+134015.0	DA:/dM	11173	5598	8.45	1.07	0.89	0.48	389	248	3	627	123
SDSSJ165329.97+134102.9	WD/dM									4	260	76
SDSSJ165447.75+131651.2	DA/dM	16910	855	7.87	0.20	0.55	0.11	514	63	4	547	161
SDSSJ165459.27+131024.9	DA/dM	15601	2019	7.50	0.51	0.38	0.24	929	268	2	528	126
SDSSJ165717.36+131032.2	DA/dM	22811	4411	7.81	0.84	0.53	0.49	1238	579	2	818	195
SDSSJ172445.28+073324.7	DA/dM	13588	989	8.02	0.24	0.62	0.15	384	59	4	324	95
SDSSJ172552.45+632906.7	DA:/dM									2	693	165
SDSSJ173104.52+070345.0	DA/dM	14228	1186	8.02	0.30	0.62	0.18	214	40	4	224	66
SDSSJ173153.03+065233.6	WD/dM									1	912	179
SDSSJ173226.13+433311.2	cand									2	866	206
SDSSJ173338.91+634110.7	DA/dM	27743	2595	7.71	0.39	0.50	0.20	1228	298	3	671	132
SDSSJ173849.76+635042.0	DA/dM	14560	2153	8.50	0.39	0.93	0.22	394	114	3	704	139
SDSSJ183329.18+643151.7	DA/dM	51068	2064	7.86	0.14	0.63	0.06	454	47	2	310	74
SDSSJ183453.07+413757.7	DA/dM	9619	147	8.42	0.17	0.87	0.11	108	14	4	184	54
SDSSJ183809.61+415500.9	WD/dM									4	493	145
SDSSJ184412.58+412029.4	DA/dM	7554	28	7.45	0.12	0.33	0.05	75	5	6	58	27
SDSSJ184436.94+410816.2	DA/dM	10670	939	8.13	0.73	0.68	0.45	378	169	3	421	83
SDSSJ185256.00+183812.3	DA:/dM									2	1403	334
SDSSJ191910.86+375414.7	WD/dM									1	414	81
SDSSJ191911.33+370319.0	DA/dM	17912	1229	7.92	0.27	0.57	0.16	453	76	3	320	63
SDSSJ191916.88+621432.9	WD/dM									3	583	115
SDSSJ192306.01+620310.7	DA:/dM	14228	3640	8.36	0.95	0.84	0.48	516	298	1	717	140
SDSSJ201239.31+601710.3	DA/dM	32222	192	7.79	0.05	0.55	0.02	332	12	5	236	121
SDSSJ204647.27+021805.4	DB/dM									3	218	43
SDSSJ220838.56+050609.8	cand									4	316	93
SDSSJ221343.64+072221.3	DB/dM									3	272	54
SDSSJ221453.16+055423.1	cand									1	1225	240
SDSSJ222822.73+391239.7	DA/dM	23343	4002	7.48	0.57	0.40	0.26	760	252	3	358	70
SDSSJ224307.59+312239.1	DC/dM									5	171	87
SDSSJ224819.40+304803.6	WD/dM									4	346	102
SDSSJ225117.28+310939.8	DA/dM	40565	1388	7.97	0.16	0.66	0.09	261	29	1	245	48
SDSSJ225145.03+302807.6	cand									2	715	170
SDSSJ225716.58+074534.3	DA:/dM	11433	8054	8.73	1.24	1.06	0.44	331	265	2	773	184
SDSSJ225847.57+071026.5	DA/dM	8475	272	8.07	0.57	0.64	0.37	248	87	5	351	180
SDSSJ230248.99+081052.5	cand									1	896	175
SDSSJ230833.71+224052.6	DC/dM									1	1365	267
SDSSJ231105.66+220208.6	DA/dM	10189	460	8.92	0.40	1.16	0.15	163	52	3	536	105

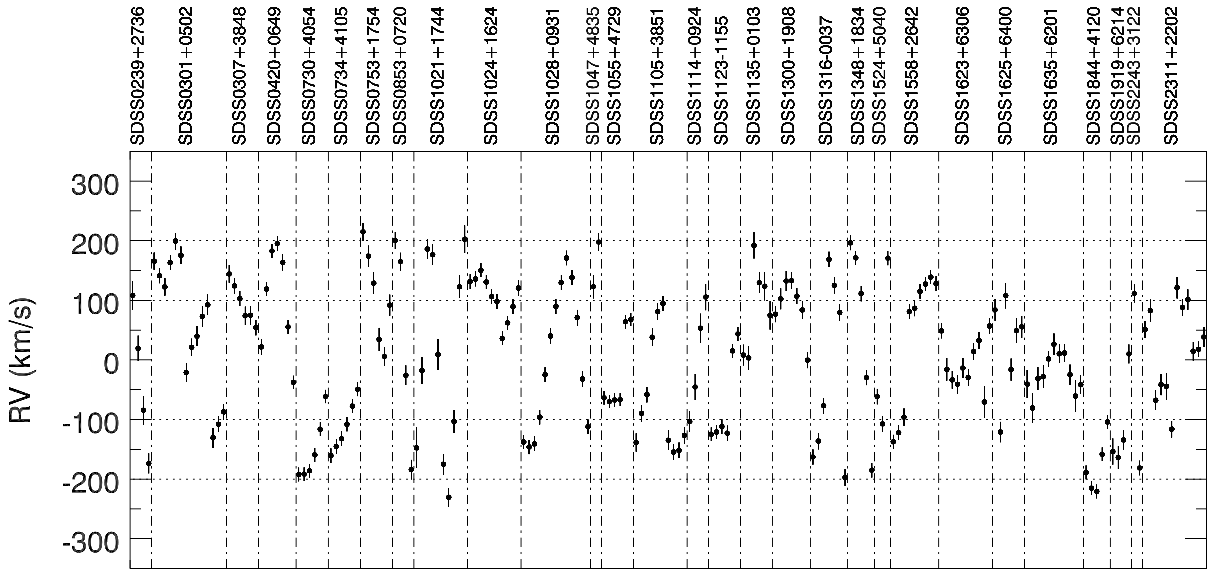

Figure A.1: Radial velocities of the Na absorption doublet for the 29 PCEBs.

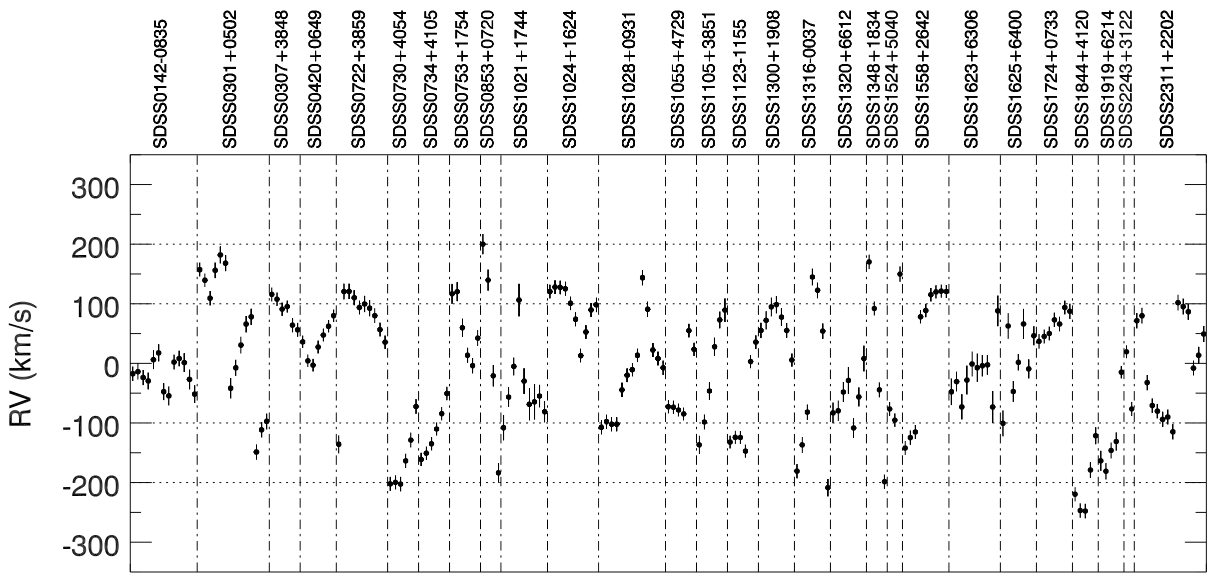

Figure A.2: Radial velocities of the Hα, emission line for the 28 PCEBs.

Table A.3: continued.

System	Type	$T_{\rm eff}$	$\sigma_{T_{\rm eff}}$	$\log g$	$\sigma_{\log g}$	$M_{\rm wd}$	$\sigma_{M_{\rm wd}}$	$d_{\rm wd}$	$\sigma_{d_{\rm wd}}$	Sp2	$d_{\rm sec}$	$\sigma_{d_{\rm sec}}$
SDSSJ233856.89+074456.4	DA/dM	9401	316	8.54	0.42	0.94	0.23	172	53	3	443	87
SDSSJ233922.26+074400.3	DA/dM	15071	2504	7.77	0.45	0.49	0.26	603	157	2	615	147
SDSSJ234106.82+083550.3	DA/dM	11835	1280	7.45	0.58	0.35	0.28	619	195	4	462	136

Acknowledgements

Special thanks to Axel Schwope and Matthias Schreiber, since without them I would have not been able to reach this point nor would I have enjoyed the way. I also thank my supervisor Heike Rauer.

Many thanks to the people with whom I've worked during the last years, specially Boris Gänsicke for all his relevant help and contribution to realize my work, and Alberto Rebassa-Mansergas for the discussions and for always offering his help.

Thanks to all the observers that contributed to this thesis: Robert Schwarz, John Southworth, Pablo Rodríguez-Gil, Stelios Pyrzas, Robert Piontek, Matthias Müller, Andreas Rabitz, Martin Bothe, Alexander Kolodzig, Justus Vogel, Daniele Facchino. I gratefully acknowledge the Calar Alto staff, for making the observatory the most comforting place.

I express my gratitude to my teachers from the department of astrophysics in Universidad de La Laguna, becuase of their great lectures, specially to Fernando Moreno Insertis for his lectures on stellar evolution and to Ramón García López for his lectures on instrumentation. Also, I thank the people with whom I studied one or many many years, becoming my friends.

All the people working at the AIP are acknowledged for creating a nice working atmosphere. Many thanks to Justus Vogel, Alena Zwanzig and Daniele Facchino for their mood, the coffee and cigarettes.

Thanks to my friends from Asturias: Almu, Mada, Sonia, Marta, Bruna, Diana, Almu D., María, for teaching me that time and distance can be irrelevant in a friendship.

I thank my mom, although she is not here anymore, for giving me the courage. Also 'mis niñas' Rocio and Covi for their love and beautiful smiles everytime I see them. Thanks to Jorge, for being the best big brother, and to Elena for taking such good care of all of us. Thanks to Bego, for always listening and supporting in the difficult moments. I am very thankful to Carlos for giving me inspiration.

I deeply thank Pierre for his love and the uncountable good moments.

List of publications

Refereed Journals

Schreiber, M. R., et al. 2010, A&A, 513, L7

Abazajian, K. N., et al. 2009, ApJS, 182, 543

Schwope, A. D., Nebot Gómez-Morán, A., Schreiber, M. R., Gänsicke, B. T. 2009, A&A, 500, 867

Thorstensen, J. R., Schwarz, R., Schwope, A. D., Staude, A., Vogel, J., Krumpe, M., Kohnert, J., & Nebot Gómez-Morán, A. 2009, PASP, 121, 465

Pyrzas, S., et al. 2009, MNRAS, 394, 978

Szkody, P., et al. 2009, AJ, 137, 4011

Nebot Gómez-Morán, A., et al. 2009, A&A, 495, 561

Yanny, B., et al. 2009, AJ, 137, 4377

Rebassa-Mansergas, A., et al. 2008, MNRAS, 390, 1635

Staude, A., Schwope, A. D., Schwarz, R., Vogel, J., Krumpe, M., & Nebot Gómez-Morán, A. 2008, A&A, 486, 899

Conference proceedings

Nebot Gómez-Morán, A., Schwope, A. D., Schreiber, M. R., Gänsicke, B. T. 2009, Journal of Physics Conference Series, 172, 012027

Schreiber, M. R., et al. 2009, Journal of Physics Conference Series, 172, 012024

Schreiber, M. R., Nebot Gómez-Morán, A., & Schwope, A. D. 2007, 15th European Workshop on White Dwarfs, 372, 459

Schreiber, M. R., Gänsicke, B. T., Schwope, A. D., Southworth, J., Nebot Gómez-Morán, A., & Rebassa-Mansergas, A. 2007, VI Reunion Anual Sociedad Chilena de Astronomia (SOCHIAS), 46

Curriculum Vitae

Name	Ada Nebot Gómez-Morán
Born	September 17, 1979 in Oviedo
Nationality	Spanish
Marital status	Single

Sept. 1985-July 1993	Primary School at Colegio Público La Luna, Oviedo
Sept. 1993-July 1998	Secondary School at Instituto Alfonso II El Sabio, Oviedo
Oct. 1998-July 2002	1st degree in Physics at Universidad de Oviedo.
Oct. 2002-Feb. 2006	Diploma in Physics with concentration in Astrophysics at Universidad de La Laguna.
Since April 2006	PhD studies in astrophysics at the Technische Universität Berlin, supervisor: Axel Schwope